

**Muon-Induced Backgrounds in the
DM-Ice17 NaI(Tl) Dark Matter Detector**

By
Antonia J. F. Hubbard

A dissertation submitted in partial fulfillment of
the requirements for the degree of

Doctor of Philosophy

(Physics)

at the
UNIVERSITY OF WISCONSIN-MADISON
2015

Date of final oral examination: May 07, 2015

The dissertation is approved by the following members of the Final Oral Committee:

Reina Maruyama, Assistant Professor, Yale University, Physics

Albrecht Karle, Professor, University of Wisconsin, Physics

Francis Halzen, Professor, University of Wisconsin, Physics

Justin Vandenbroucke, Assistant Professor, University of Wisconsin, Physics

Michael DuVernois, Senior Scientist, University of Wisconsin

Peter Timbie, Professor, University of Wisconsin, Physics

© Copyright by Antonia J. F. Hubbard 2015

All Rights Reserved

MUON-INDUCED BACKGROUNDS IN THE DM-ICE17 NAI(TL) DARK MATTER DETECTOR

Antonia J. F. Hubbard

Under the supervision of

Professor Albrecht Karle at the University of Wisconsin – Madison

Assistant Professor Reina Maruyama at Yale University

The DM-Ice experiment uses NaI(Tl) to directly search for the annual modulation expected from a WIMP dark matter signal. The DAMA NaI(Tl) experiment has observed a modulation, consistent with dark matter, that has been excluded by other experiments. No background model has been able to successfully explain the DAMA signal. To definitely confirm or deny the dark matter interpretation of this modulation, a NaI(Tl) experiment with different backgrounds must be run. Detecting this modulation requires the observation of rare, single-keV nuclear recoil signals. DM-Ice17, the first of three generations of detectors in the DM-Ice experiment, has run with 17 kg of NaI(Tl) in the South Pole ice since December 2010. DM-Ice17 has proved the feasibility of running such an experiment in the South Pole ice. DM-Ice17 continues to take data while R&D is underway with the second-generation DM-Ice37 detector. Once background levels ideal for a WIMP search are achieved, the full-scale, 250 kg DM-Ice250 detector will be commissioned. As a direct detection dark matter experiment in the Southern Hemisphere, the full-scale experiment will have a unique capability to disentangle the WIMP modulation from seasonal variations.

This work focuses on the data analysis of the DM-Ice17 detector, with particular emphasis on muon-induced backgrounds. Muons, identified by their energy deposition and pulse shape, are observed by DM-Ice17 to modulate annually with a 14% fractional amplitude. The highest energy muon events in the crystal induce a long-lived phosphorescence. When this occurs, the detector rate rises significantly, and a cascade of low energy events appears over tens of seconds. The possible contribution of these events to dark matter searches in NaI(Tl) is explored. DM-Ice17 is located within the volume of the IceCube Neutrino Observatory, allowing the analysis of events coincident between the two detectors. These events validate the DM-Ice17 muon tag and provide a novel confirmation of the reported resolution of IceCube reconstructions. They provide additional information that is particularly useful for low energy events in IceCube. This study is particularly relevant given the growing interest in the deployment of scintillators with PINGU.

In this thesis, I present an overview of dark matter theory (Chapter 1) and candidates (Chapter 2), followed by the current status of the experimental dark matter field (Chapter 3). Special emphasis is given to NaI(Tl) dark matter experiments and their development. The mechanics of scintillation are discussed

(Chapter 4), including the nature of long-lived phosphorescence, followed by a description of DM-Ice (Chapter 5). The data analysis of DM-Ice17 is discussed (Chapter 6), with particular attention given to the energy calibration. The muon and muon-induced backgrounds in DM-Ice17 are presented (Chapter 7), including details of the observed modulation and muon-induced phosphorescence in the low energy region. The observation of muon events coincident with IceCube is discussed (Chapter 8), and finally the status of DM-Ice37 detector (Chapter 9) and the conclusions from the DM-Ice17 detector (Chapter 10) are presented.

*I dedicate this work to my grandparents.
Their integrity, intelligence, and love have built an incredible family,
and their shadows fall far longer than they'll ever know.*

ACKNOWLEDGMENTS

First thanks go to my advisors, Reina and Albrecht, who guided me and pushed me to turn cool observations into developed analyses. I am eternally grateful for their excitement, support, and curiosity. I have relished building the DM-Ice17 engine with Matt, Walter, and Zack, who have grown from my co-workers, to my partners in crime, to my brothers. I am certainly better off from our time together, both professionally and personally. The input and expertise of the wider DM-Ice collaboration has been deeply appreciated in the development of this work, and the staff at Boulby, in addition to their professional abilities, are some of the friendliest colleagues I've had the pleasure of meeting.

WIPAC is a contagiously positive, curious, and driven place to do science, and a number of people were incredibly helpful along the way. Thanks to Dipo and Dawn for being my guides through IceCube processing; Marcos and Segev for helping to get the veto off the ground; Ben Riedel for gruffly answering my endless stream of IceCube questions; Naoko for honestly providing (usually solicited) life and physics advice; Paolo for sharing his bottomless knowledge of muons; Jon Dumm for introducing me to IceCube and teaching me diplomacy, and Kim for making bureaucracy painless.

Three years of this work were supported by the NSF Graduate Fellowship. I would like to gratefully acknowledge both this fellowship and travel awards that I have received; few things are more fulfilling than exchanging ideas with people passionate about their work. A profound experience for one person is often an insignificant conversation for another, and in this vein, I would like to thank Reina and Karsten for always treating me as a person and not a machine; Cynthia Phillips and Ian McLean for sparking my interest in research; Karoly Holczer for guiding me to particle physics; Stefan Westerhoff for guiding me to DM-Ice; Janet Conrad for her serious interest in my work, and the WNSL group at Yale for welcoming me completely.

And finally, thanks to my friends and family. My parents continue to be a source of deep encouragement and easy laughs. My sister, whose love of life and nature is so inspiring, reminds me to get outside. All my friends have tremendously supported me and kept me in line, especially my ladies Jo, Livi, Savage and Amy; my forever-grad school roomie Zig; my flower boys Rickard, Henric, Goat, Duff, and Carlos, and everyone I know I must be forgetting. Deepest thanks to Logan, who has supported me so incredibly thoroughly, and who continuously reminds me that we do what we do because it's fun.

TABLE OF CONTENTS

	Page
ABSTRACT	i
LIST OF TABLES	ix
LIST OF FIGURES	xi
1 Cosmological Composition	1
1.1 Λ CDM	1
1.1.1 Cosmological Evolution	2
1.1.2 Current Universe	3
1.2 Observational Cosmology	4
1.2.1 Cosmic Microwave Background	4
1.2.2 Baryon Acoustic Oscillations	5
1.2.3 Big Bang Nucleosynthesis	7
1.2.4 Rotation Curves	7
1.2.5 Large Scale Structure	9
1.2.6 Gravitational Lensing	9
1.2.7 The Bullet Cluster	10
2 Dark Matter Candidates	12
2.1 The Standard Model of Particle Physics	12
2.2 Dark Matter Characteristics	13
2.2.1 Baryonic Matter	13
2.2.2 Cold Dark Matter	13
2.3 Preferred Candidates	14
2.3.1 WIMPs	14
2.3.2 SUSY Dark Matter	15
2.3.3 Warm Dark Matter	17
2.3.4 Axions	17
2.4 MOND	17
3 Dark Matter Detection	19
3.1 Collider Production	19
3.2 Indirect Detection	19
3.3 Direct Detection	21
3.3.1 Annual Modulation	22
3.3.2 Diurnal Modulation	22
3.3.3 Spin Dependence of Interaction	24
3.3.4 Techniques: Shielding Backgrounds	24
3.4 Status of the Direct Detection Field	25
3.4.1 Low Mass WIMPs	29

	Page
3.5 NaI(Tl) Experiments	31
3.5.1 DAMA	32
3.5.1.1 Experiments	32
3.5.1.2 Results	34
3.5.1.3 Result Controversy	36
3.5.2 NaIAD	38
3.5.3 ANAIS	39
3.5.4 KIMS	41
3.5.5 SABRE	42
3.6 Future of Direct Detection	42
4 NaI(Tl) Scintillation Mechanisms	44
4.1 Inorganic Scintillators	44
4.1.1 Primary Ionization	45
4.1.2 Charge Migration and Thermalization	48
4.1.2.1 Self-Trapping	50
4.1.3 Extrinsic Luminescence: Activation Centers	51
4.1.3.1 Quenching	53
4.1.4 Competing Processes	54
4.1.4.1 Intrinsic Luminescence	55
4.1.4.2 Energy Losses	55
4.1.5 Characteristics	56
4.1.5.1 Temperature Dependence	56
4.1.5.2 Transparency	57
4.1.5.3 Resolution	58
4.1.6 Defect Production	58
4.1.6.1 Production Mechanism	59
4.1.6.2 Production Efficiency	60
4.1.6.3 Effects on Scintillation	60
4.2 NaI(Tl) Crystals	61
4.2.1 Crystal Growth	61
4.2.2 Scintillation Mechanism	62
4.2.2.1 Emission Timescale	64
4.2.3 NaI(Tl) Characteristics	66
4.2.4 Phosphorescence	70
4.2.4.1 Experimental Observation	72
5 DM-Ice	77
5.1 Experimental Concept	77
5.2 DM-Ice17	80
5.2.1 Assembly and Deployment	83
5.2.2 Electronics	85
5.2.3 Waveforms	87
5.2.4 Detector Characteristics	88
5.2.4.1 Livetime	88
5.2.4.2 Stability	89

	Page
5.2.4.3	Timing Resolution 91
5.2.4.4	Energy Resolution 92
5.2.4.5	Saturation 93
6	DM-Ice17 Data Analysis 94
6.1	Data Processing 94
6.1.1	Waveforms 94
6.1.2	Noise Removal 96
6.2	Energy Calibration 98
6.2.1	Boulby Calibration 98
6.2.2	PSL Calibration 99
6.2.3	Characteristic In-Ice Lines 100
6.3	Cosmogenic Activation 104
6.4	Alpha Analysis 106
6.5	Simulation 107
7	Analysis of Muon Events 111
7.1	Atmospheric Muons 111
7.1.1	Annual Modulation of Muon Rate 114
7.1.2	Rate Through DM-Ice17 118
7.2	Muons in DM-Ice17 119
7.2.1	Identification 119
7.2.2	Observed Modulation 121
7.2.3	Energy Deposition 124
7.3	Muon-Induced Phosphorescence 125
7.3.1	DAQ Saturation and Deadtime 129
7.3.2	Phosphorescence Implications for NaI(Tl) Experiments 130
8	IceCube Muon Coincidence 133
8.1	Coincidence Concept 133
8.2	IceCube 133
8.2.1	IceCube Data 135
8.2.1.1	Muon Filter 136
8.2.1.2	sDST NChannel 138
8.2.1.3	sDST MinBias 138
8.3	Coincidence Algorithm 139
8.4	Results 140
8.4.1	Coincidence Rates 140
8.4.2	IceCube Misreconstruction Rates 141
8.4.3	Impact on IceCube Reconstructions 148
8.4.3.1	Timing 148
8.4.3.2	Direction 149
8.4.3.3	Energy 152
8.4.3.4	Track Location 153
8.4.4	Future Study 155

	Page
9 Towards DM-Ice250	156
9.1 DM-Ice37	156
9.1.1 Fermilab Run	157
9.1.2 Boulby Run	160
9.2 DM-Ice250	165
9.3 DM-Ice Experiment	165
10 Conclusions	167
LIST OF REFERENCES	169
GLOSSARY	185
APPENDICES	
Appendix A: Underground Laboratories	187
Appendix B: Neutron Background	188
Appendix C: IceCube Coincident Events	193

LIST OF TABLES

Table	Page
3.1 NaI(Tl) Dark Matter Experiment Comparison	31
3.2 NaI(Tl) Contamination Levels Attained	32
3.3 DAMA Modulation Parameters	35
4.1 NaI(Tl) Scintillation Parameters	69
4.2 Experimental NaI(Tl) Phosphorescence Results	73
5.1 DM-Ice17 Channel and PMT Saturation Energies	93
6.1 Calibration functions for ATWD Channels	102
6.2 NaI(Tl) Quenching Factor Measurements	106
6.3 DM-Ice17 Simulation Components	109
7.1 Muon Radiative Energy Loss Parameter	112
7.2 Muon Flux by Location	119
7.3 DM-Ice17 Muon Modulation Parameters	122
8.1 Expected DM-Ice17 - IceCube Coincidence Rates	138
8.2 Accidental Coincidence Between DM-Ice17 and IceCube	140
8.3 Coincidence Result Summary: 2012 - 2014	141
8.4 Coincidence Results by Filter: 2012 - 2014	143
8.5 Misreconstruction Rate Comparison	143
8.6 Zenith Misreconstruction Rate Comparison	145
8.7 Energy Misreconstruction Rate Comparison	146
8.8 Distance Misreconstruction Rate Comparison	147
9.1 Laboratory Background Comparison	161

Table	Page
A.1 Comparison of Dark Matter Laboratories	187
B.1 Neutron Propagation Example	191

LIST OF FIGURES

Figure	Page
1.1 CMB Sky Map	5
1.2 BAO Power Spectrum	6
1.3 M33 Rotation Curve	8
1.4 LSS Data-Simulation Comparison	9
1.5 Gravitational Lensing	10
1.6 The Bullet Cluster	11
2.1 Standard Model of Particle Physics	12
2.2 Dark Matter Candidate Parameter Space	15
2.3 WIMP Density Evolution	16
2.4 Supersymmetric Partners	16
3.1 Hints of Dark Matter from Indirect Detection Experiments	20
3.2 Spin-Dependent Limits	20
3.3 Expected Dark Matter Interaction Rate	21
3.4 Expected WIMP Flux Annual Modulation	23
3.5 Expected WIMP Flux Diurnal Modulation	23
3.6 Electronic and Nuclear Recoil Separation	25
3.7 Direct Detection Experiments, Arranged by Readout Channel	26
3.8 CRESST Result	27
3.9 CoGeNT Result	28
3.10 CDMS-II Si Result	29
3.11 Spin-Independent Limits	30

Figure	Page
3.12 DAMA/LIBRA Experimental Setup	33
3.13 DAMA/LIBRA Multi-Crystal ^{40}K Veto	34
3.14 DAMA/LIBRA Energy Spectrum	35
3.15 DAMA/NaI and DAMA/LIBRA Combined Modulation Data	36
3.16 DAMA/LIBRA Modulation Amplitude Energy	37
3.17 NaIAD Experimental Setup	38
3.18 NaIAD Spectrum	39
3.19 ANAIS Experimental Setup	40
3.20 ANAIS-25 Spectrum	40
3.21 KIMS CsI(Tl) Limits	41
3.22 KIMS NaI(Tl) Spectrum	42
3.23 Potential SABRE Experimental Setup	43
4.1 Inorganic Scintillator Band Structure	45
4.2 Processes in Inorganic Scintillators	46
4.3 Atomic organization of Inorganic Scintillators	48
4.4 Scintillation Process	49
4.5 Luminescence Center Processes	51
4.6 Pair Density Quenching	54
4.7 Temperature Dependence of NaI(Tl) Light Response	56
4.8 Formation of Stable Defects	59
4.9 Crystal Growth Methods	62
4.10 NaI(Tl) Emission Wavelengths	64
4.11 Tl Concentration Dependence of NaI(Tl) Light Yield	67
4.12 NaI(Tl) Light Response	68
4.13 NaI(Tl) Nuclear Quenching Factor	68
4.14 Trap Configuration	71

Figure	Page
4.15 Long and Super-long Observed Phosphorescence Decays	74
4.16 Observed ANAIS Phosphorescence	75
4.17 Observed 45 Day Phosphorescence	76
5.1 Comparison of the DAMA Modulation and the Borexino Muon Modulation	77
5.2 DM-Ice17 Detector	79
5.3 DM-Ice37 Detector	79
5.4 DM-Ice250 Detector	80
5.5 DM-Ice Sensitivity: Null Result	81
5.6 DM-Ice250 Sensitivity: Observed Modulation	81
5.7 South Pole Experiments	82
5.8 DM-Ice17 Detector Assembly	84
5.9 DM-Ice17 Shipment to the South Pole	85
5.10 DM-Ice17 Transport at the South Pole	85
5.11 DM-Ice17 Det-2 Hole Deployment	86
5.12 DM-Ice17 Mainboards	87
5.13 DM-Ice17 Scintillation Waveform	88
5.14 DM-Ice17 Temperature Stability	89
5.15 DM-Ice17 Light Yield Stability	90
5.16 DM-Ice17 Timing Resolution	91
5.17 DM-Ice17 Energy Resolution	92
6.1 High and Low Energy Waveforms	94
6.2 Waveform Corrections	95
6.3 Toroid Waveform Correction	95
6.4 Noise Waveform: EMI	96
6.5 Noise Waveform: Thin Pulse	96
6.6 Effect of Noise Removal on the DM-Ice17 Spectrum	97

Figure	Page
6.7 Boulby Calibration Experimental Setup	98
6.8 Boulby Calibration Data	99
6.9 PSL Calibration Experimental Setup	99
6.10 PSL Calibration Data	100
6.11 DM-Ice17 Energy Spectrum	101
6.12 Calibration Functions	102
6.13 DM-Ice17 Low Energy Spectrum	103
6.14 Comparison of Low Energy and High Energy Calibration Functions	104
6.15 DM-Ice17 Cosmogenic Activation: ^{125}I	105
6.16 DM-Ice17 Cosmogenic Activation: ^{54}Mn	105
6.17 Pulse Shape Discrimination	107
6.18 Bi-Po Waveform	107
6.19 Data-Simulation Comparison: Alpha Region	108
6.20 Data-Simulation Comparison: Gamma Region	109
6.21 Data-Simulation Comparison: Low Energy Region	110
7.1 Atmospheric Muon Spectrum	111
7.2 Depth Dependence of Atmospheric Muon Flux	113
7.3 Depth Dependence of Muon Spectrum	114
7.4 Correlation of Muon Flux and Atmospheric Temperature	116
7.5 Energy Dependence of Muon Modulation	117
7.6 Muon Phase Uncertainty	117
7.7 Correlation Functions of Muon Flux and Temperature	118
7.8 Characteristic Gamma, Alpha, and Muon Pulse Shapes	120
7.9 Muon Cut: PSD	120
7.10 Muon Cut: Energy Deposition	121
7.11 DM-Ice17 Muon Identification	122

Figure	Page
7.12 DM-Ice17 Muon Flux	123
7.13 Muon Modulation in DM-Ice17 and IceCube	124
7.14 Simulated Muon Energy Deposition	125
7.15 Observed Muon Energy Spectrum	126
7.16 Phosphorescence Event	126
7.17 Phosphorescence Identification	127
7.18 Pulse Height of Phosphorescing Muons	128
7.19 Comparison of Phosphorescent Decays	128
7.20 Phosphorescence Spectrum	129
7.21 FADC Muon Waveform	129
7.22 Deadtime Corrections	130
7.23 DAQ Saturation Corrections	131
7.24 Time Dependence of Phosphorescence Event Rate	132
8.1 Cherenkov Emission	134
8.2 Arrangement of South Pole Experiments	135
8.3 IceCube Atmospheric Muon Event	136
8.4 IceCube Depth-Dependent Detection Efficiency	137
8.5 Coincidence Result Summary 2012 - 2014	142
8.6 MuEx Energy Estimator	142
8.7 Reconstructed Energy of Coincident Events	144
8.8 Rate of Zenith Misreconstruction	145
8.9 Rate of Energy Misreconstruction	146
8.10 Rate of Distance Misreconstruction	147
8.11 Coincident Detector Time Difference	148
8.12 Det-2 Azimuthal Geometry	149
8.13 Reconstructed Coordinates	150

Figure	Page
8.14 Difference in Reconstructed Coordinates	151
8.15 Reconstructed Energy	152
8.16 Difference in Reconstructed Energy	153
8.17 Reconstructed Distance of Closest Approach	154
8.18 Difference in Reconstructed Distance of Closest Approach	155
9.1 DM-Ice37 Experimental Setup at FNAL	157
9.2 DM-Ice37 FNAL Calibration Data	158
9.3 DM-Ice37 Muon Identification	159
9.4 Crystal Contamination Comparison	159
9.5 DM-Ice37 Phosphorescence at FNAL	160
9.6 Boulby Underground Laboratory	162
9.7 Laboratory Background Comparison	163
9.8 DM-Ice37 Experimental Setup at Boulby	163
9.9 Background Improvement at Boulby	164
9.10 Projected DM-Ice250 Experimental Setup	165
Appendix	
Figure	
B.1 Target Mass Dependence of Neutron Production	188
B.2 Produced Neutron Spectrum	189
B.3 Simulated DM-Ice17 Neutron Energy Deposition	192
C.1 Coincident Event Examples	193
C.2 Coincident Event: Both Reconstructions Pass	194
C.3 Coincident Event: Both Reconstructions Fail	194
C.4 Coincident Event: DM-Ice17 Seed Fails	195
C.5 Coincident Event: DM-Ice17 Seed Fails	195

Chapter 1

Cosmological Composition

1.1 Λ CDM

Λ CDM describes the universe from the Big Bang to the present day, where it contains complex structure at a variety of scales and is expanding at an ever-accelerating rate. Λ CDM is comprised of six variable parameters: baryon density, dark matter density, dark energy density, scalar spectral index, curvature fluctuation amplitude, and reionization optical depth [1]. These parameters are fit to match observations of rotation curves, gravitational lensing, the Cosmic Microwave Background, Baryon Acoustic Oscillations, supernovae redshifts, Big Bang Nucleosynthesis, and Large Scale Structure. See §1.1.1 for a timeline of cosmological evolution as understood by the Λ CDM model and §1.2 for the observational evidence of this model, including evidence for dark matter, which is the focus of this work.

Λ CDM emerged as the preferred cosmological framework from a combination of astronomical observations and theoretical predictions. The theory first emerged from Vesto Slipher’s 1912 observation of Doppler shifts showing that all spiral galaxies are receding away from Earth [2]. This peculiar observation was explained in 1927 by Georges Lemaître to be a result of an expansion of the universe. Lemaître also postulated the occurrence of the Big Bang, observing that if the universe’s expansion is extrapolated back in time, a point is reached where all mass is concentrated into a “primeval atom”, where and when space-time came into existence [3]. Lemaître’s theory was bolstered in 1929 when Edwin Hubble derived Hubble’s law from measurements of the distances to galaxies with known redshifts. Seeing that galaxies further away were receding away from Earth at a faster velocity, he proposed the relation:

$$v = H_0 D \tag{1.1}$$

where v is the recessional velocity of the galaxy, D is its proper distance from the observer, and H_0 is the Hubble constant [4].

The Big Bang model was only widely favored after the discovery of the Cosmic Microwave Background (CMB). Previously, a large fraction of scientists supported the steady-state model over the theory of universal expansion to explain observations. The steady-state model proposed that new matter was constantly being created, leading to the observations that could otherwise be interpreted as the universe’s expansion. This model implies that the universe should look roughly the same at any point in time, in direct contrast to the Big Bang model, which predicts a hotter, denser universe in the past. The debate between the steady state and Big Bang models was settled in 1964 with the discovery of the CMB (see §1.2.1), which was predicted by the Big Bang model and had no explanation in the steady state model. Additional observations developed the Big Bang model into the modern understanding of Λ CDM (see §1.2). Most recently, the Planck satellite released measurements of the cosmological parameters describing the nature of the universe. The values were based on 15.5 months of observation and added to a long line of observational support for the Λ CDM model of the universe. The model derives its name from the predicted cosmological components, which the recent Planck observations measure to be $4.82 \pm 0.12\%$ normal matter, $25.82 \pm 0.69\%$ dark matter (CDM), and $68.5 \pm 1.7\%$ dark energy (Λ) (see §1.1.2) [5].

1.1.1 Cosmological Evolution

The current interpretation of Lemaître’s “primeval atom” is the Big Bang: that moment in space-time when density and temperature approach infinity and the laws of physics break down. Out of this Big Bang 13.798 ± 0.037 billion years ago [5] came a hot, dense, expanding universe governed by a hypothesized unified force, whose symmetry was quickly broken as the Universe expanded and cooled. Shortly after the Big Bang, a phase transition ushered in the inflationary period. During this period ($10^{-37} - 10^{-32}$ s old), the volume of the universe expanded by a factor of 10^{78} and left a signature of gravitational waves on the CMB [6]. This indicates that the entire observable universe was at one point close enough to be causally connected, leading to the isotropic and homogenous universe observed today (see §1.1).

After this period of rapid inflation, the universe continued to expand and cool, creating the proper conditions for the formation of subatomic particles. A hypothesized process referred to as baryogenesis likely took place directly after inflation, leaving a small excess of quarks and leptons over anti-quarks and anti-leptons and leading to the observed dominance of matter over anti-matter [7]. As expansion continued and typical particle energies kept dropping, symmetry-breaking phase transitions in the $10^{-12} - 10^{-6}$ s old epoch led to the four fundamental forces (gravitational, strong, weak, electromagnetic). From 10^{-6} s to 1 s old, conditions were right for quarks to combine into hadrons, and this era also saw the freeze out of neutrinos (see §2.3.1 for a discussion of the freeze out mechanism). Leptons continued to form until the universe was 10 s old [8].

With the subatomic particles formed, the universe cooled to the proper conditions for the formation of nuclei and, much later, atoms. Roughly 3 – 20 minutes into the universe’s expansion, the temperature was right for protons and neutrons to undergo nuclear fusion into nuclei during the age of Big Bang Nucleosynthesis (BBN, see §1.2.3). During this time, all free neutrons were locked into nuclei and a series of nuclear processes led to the production of light elements: hydrogen, deuterium, helium, beryllium, and lithium. As described in §1.2.2, the ratio of photons to baryons during this period dictated the ratios of the abundances of these elements and places a limit on the fraction of baryonic matter (see §2.1) in the universe. When the universe was roughly 380,000 years old, the temperature was right for atomic formation and photon decoupling, ushering in an era known as recombination. The universe was opaque to photons because they could not travel far without hitting a charged particle, but once electrons and nuclei began to form atoms, free particles became bound, and the mean free path of photons increased. Photons were thus able to decouple from matter and travel freely, forming the CMB (see §1.2.1). Pressure waves in the electron-baryon plasma were embedded in the CMB as Baryon Acoustic Oscillations (BAO, see §1.2.2).

At this point, slightly denser regions in the universe gravitationally attracted more matter, transforming into the astronomical structures observed today (see §1.2.4, §1.2.5). The current universe also contains dark matter and a dominant fraction of dark energy that is driving the expansion of the universe at an increasingly accelerated pace (see §1.1.2).

1.1.2 Current Universe

Astronomical observations reveal a universe, consistent with Λ CDM, that is both flat and expanding [5]. Flatness refers to the universe having Euclidean geometry, associated with a critical density, ρ_c , and expanding forever at a decelerating rate that asymptotically approaches zero. With a dark energy component, however, the expansion may, in fact, continue. The critical density condition, Ω_0 , is equal to one for a critically dense universe:

$$\Omega_0 = \frac{\rho}{\rho_c}, \quad \rho_c = \frac{3H_0^2}{8\pi G} \quad (1.2)$$

where H_0 is the Hubble constant at present (67.3 ± 1.1 km/s/Mpc) and G is the gravitational constant. As described in §1.1, Λ CDM is governed by the Friedmann-Lemaître-Robertson-Walker (FLRW) metric, which dictates the evolution of the universe. The FLRW equations for a flat universe return:

$$\left(\frac{H}{H_0}\right)^2 = \Omega_r(1+z)^4 + \Omega_m(1+z)^3 + \Omega_k(1+z)^2 + \Omega_\Lambda \quad (1.3)$$

where H is the Hubble parameter (H_0 at present), z is the redshift, Ω_r is the present fraction of radiation, Ω_m is the present density of matter, Ω_k is the curvature of space, and Ω_Λ is the dark energy fraction [9]. The redshift, z , can be understood as the stretching of wavelengths from the universe’s expansion. Redshifts are higher for objects moving faster away from the observer, so an object’s redshift can be used to measure its

distance away in the expanding universe, with highly redshifted objects occurring far away in both space and time. Redshift can thus be used as a cosmological measure of distance and time. In terms of temperature relative to present temperature, T_0 :

$$\frac{T}{T_0} = 1 + z \quad (1.4)$$

The variations in z dependence of the components in Equation 1.3 predict that they have evolved differently in time. The $(1 + z)^4$ dependence of radiation density indicates that while it currently makes up a small fraction of the universe, $\Omega_r \sim 0.00005$, it dominated the early ($<4.7 \times 10^4$ years old) universe [8]. The radiation-dominated era gave way to the matter-dominated era ($<4.7 \times 10^4 - 9.8 \times 10^9$ years old), with matter density following a volume dependence of $(1 + z)^3$. As visible matter is observed to have $\Omega_{vm} = 0.0482 \pm 0.0012$, a contribution from additional “dark” (non-visible) components is required to reach the total matter contribution of $\Omega_m = 0.315 \pm 0.017$. The curvature of space evolves as $(1 + z)^2$, but it is taken to be equal to zero in the flat universe scenario. The $\Omega_k = 0$ condition, as a result of the early inflation of Universe, is akin to the Earth appearing flat to human observers who are so much smaller than it is. The current universe ($>9.8 \times 10^9$ years old) is dominated by dark energy, which comprises the $\Omega_\Lambda \sim 0.69$ component and is independent of z .

A combination of observational evidence points to two dark components: dark matter and dark energy (see §1.2). Dark matter, described in depth in Chapter 2, behaves like matter but does not interact with light and is thus invisible to traditional photon astronomy. Dark energy, by contrast, is thought of as a fluid with a negative pressure that does not dilute as the universe expands. It promotes repulsion and drives the acceleration of the universe’s expansion. It may also be identified with the energy density of the vacuum, although its observed density is orders of magnitude lower than predicted for the vacuum energy. The vacuum energy density is understood to be the energy density arising from empty space not really being empty, but filled with virtual particles that are coming in and out of existence [9]. While dark matter is predicted to follow the dilution of all matter with the universe’s expansion, dark energy will dominate in the later universe as it is free of z -dependent dilution. The current composition of the universe is believed to consist of $31.5 \pm 1.7\%$ matter (4.9% ordinary matter and 26.8% dark matter), $68.5 \pm 1.7\%$ dark energy, and a nearly negligible amount of radiation [5].

1.2 Observational Cosmology

1.2.1 Cosmic Microwave Background

The Cosmic Microwave Background (CMB) is comprised of radiation from the period of recombination ($z = 1000$, $t = 3.8 \times 10^5$ years old) when photons decoupled from baryons (see §1.1.1). CMB photons come from

the opaque wall at the surface of last scattering and are indicative of perfect blackbody with a temperature of 2.73 K. The CMB sky map is shown in Figure 1.1.

The nature of the CMB implies the existence of both an early inflationary period and non-baryonic dark matter. The CMB's isotropy and homogeneity provide evidence for the inflationary period as distant regions in the CMB would otherwise not be causally connected (see §1.1.1). The small anisotropies in the CMB developed into present day structure, but these fluctuations are an order of magnitude too small ($\frac{\delta\rho}{\rho} \sim 10^{-5}$) to have produced current structure without a dark component. A gravitationally-interacting, non-baryonic dark matter particle that decoupled from radiation and collapsed earlier than baryonic matter is required for modern structure to be consistent with CMB anisotropy levels [10]. Fluctuations in the dark matter fluid grew and then collapsed while the baryon-photon fluctuations continued to oscillate. At decoupling, the baryons fell into the potential wells of this non-interacting fluid. So while baryons and photons decoupled at $z = 1000$, dark matter fluctuations could collapse closer to $z \sim 10,000$ without tension with CMB fluctuation measurements.

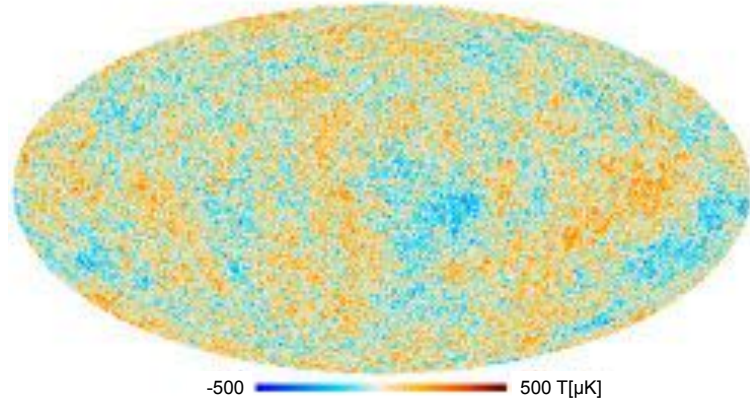


Figure 1.1: CMB sky map from the Planck satellite, showing small ($\sim \leq 500 \mu\text{K}$) temperature fluctuations in the blackbody temperature. Red and blue regions correspond to hot and cold fluctuations, respectively. These fluctuations are too small to form present day structure without a dark component that froze out prior to baryon-photon decoupling. Figure from [10].

1.2.2 Baryon Acoustic Oscillations

Baryon Acoustic Oscillations (BAO) are sound waves, imprinted on the CMB, whose sizes constrain cosmological parameters. These waves arose from small density fluctuations in the early Universe. A gravitational fluctuation will collapse unless its thermal pressure can counter its self-gravity. Density fluctuations smaller than the Jeans length (the distance a sound wave can travel in the collapse timescale) do not collapse,

supported by pressure, and propagate as sound waves. Those fluctuations larger than the Jeans length larger will collapse. Before photon-baryon decoupling, the speed of sound was almost the speed of light, and all causally-connected fluctuations were sound waves. There could be no gravitational collapse because a sound wave could traverse the entire causally-connected region before collapse (i.e., $t_{collapse} = t_{universe}$). After decoupling, however, the speed of sound decreased and collapses could occur. When photons were released to free-stream, the sea of sound waves was frozen as a pattern of CMB temperature fluctuations, with the largest wavelengths being the size of the sound horizon at decoupling. The predicted observation is thus a maximum wavelength that serves as a “standard ruler” and higher overtones of this fundamental frequency, observed at the corresponding angular scales (see Figure 1.2).

The shape of the BAO power spectrum, shown in Figure 1.2, is model-dependent and provides insight into the shape and composition of the Universe. Dark matter played a significant role in BAO structure, with the perturbing overdensity gravitationally attracting increasing amounts of dark matter as the photon-baryon plasma oscillated before decoupling. Observations by Planck [11], WMAP [12], ACBAR [13], BOOMERanG [14], and CBI [15] are consistent with a flat ($\Omega = 1$) universe composed of $\sim 30\%$ matter, of which $\sim 5\%$ is baryonic matter. Recent results from Planck, shown in Figure 1.2a, exhibit a non-baryonic dark matter signature in all peaks of the power spectrum that are in clear disagreement with models without a dark matter fraction, shown in Figure 1.2b. Dark matter density fluctuations are not expected to oscillate: they are pressureless and slowly collapse rather than oscillate as sound waves. However, the gravitational potential wells from these dark matter fluctuations will influence the temperature fluctuations seen in the CMB, with more dark matter corresponding to deeper wells.

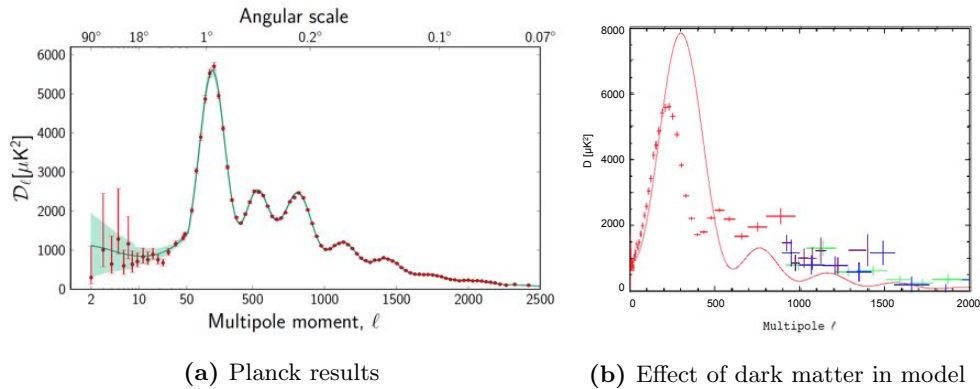
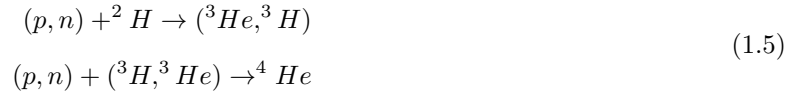


Figure 1.2: Power spectrum from Planck (left, [11]) showing evidence for CDM in each peak. The peak heights imply $\Omega_m \sim 0.3$ and $\Omega_b \sim 0.05$ [11]. Figure 1.2b is illustrative of the tension between models without dark matter (right, red line) and observation, using older data from WMAP (red), ACBAR (green), BOOMERanG (purple), and CBI (blue). Figure from [16].

1.2.3 Big Bang Nucleosynthesis

Light elements were formed during Big Bang Nucleosynthesis (BBN), and their abundances constrain the baryonic fraction of the universe. BBN began at roughly 3 minutes after the Big Bang (at $T \sim 0.1$ MeV), at which point deuterium could survive photon disruption to form higher elements. Before this point, any newly-formed deuterium was destroyed by photons with higher energies than its binding energy. During BBN, protons and neutrons fused to form the light elements: hydrogen, deuterium, helium, beryllium, and lithium. Heavier elements were formed later from stellar interiors and supernovae. BBN lasted until the universe was 20 minutes old and cooled below the point of nuclear fusion (just below 100 keV). The elemental abundances were then fixed, aside from the decay of BBN products; the current abundance of light elements is thus dependent on production during BBN.

The ratio of light elements produced during BBN is sensitive to the initial conditions and motivates a non-baryonic dark matter component. The rate depends primarily on the neutron-to-proton and baryon-to-photon ratios. The neutron-to-proton ratio is relevant because neutrons decay to protons until expansion outpaces these reactions (at $T \sim 0.7$ MeV, where $\frac{n}{p} = \frac{1}{7}$). Neutrons after BBN are all locked into nuclei. The baryon-to-photon ratio dictates whether deuterium will survive to produce He. While most protons stayed uncombined as H nuclei, those participating in BBN reactions generally ended up in ${}^4\text{He}$, and the higher the baryon-to-photon ratio, the more reactions will occur, converting more deuterium to ${}^4\text{He}$:



BBN did not convert all deuterium to ${}^4\text{He}$ because expansion reduced the density enough to cut the conversion short. As a result, deuterium concentrations are very sensitive to initial conditions. In order to create the amounts of deuterium and ${}^4\text{He}$ observed, a large amount of the matter in the universe must be non-baryonic, or there would be less deuterium. This motivates a non-baryonic dark matter component, and Λ CDM-based BBN predictions are in good agreement with observations of roughly 75% H, 25% He, 0.01% deuterium, and trace amounts of Be, Li.

1.2.4 Rotation Curves

The first evidence for dark matter — although it was not interpreted as such at the time — came from Jan Oort, who in 1932 observed that the kinematics of Milky Way stars above the galactic plane implied 50% more mass in the galactic disk than was seen in luminous stars [17]. Oort’s conclusion, however, was that the missing mass must be from interstellar gas, dust, and low-mass stars that his telescope could not see. The next year, Fritz Zwicky studied the Coma cluster’s kinematics and, assuming the galaxies all had mass-to-light ratios similar to the Sun’s, concluded that many galaxies in the cluster were moving too fast for

the observable amount of matter in the cluster, and they should have escaped. Using the virial theorem¹ to determine the expected mass of the cluster, he concluded that only 10% of the kinematically-required mass in the Coma cluster was coming from luminous stars [18]. He termed the remaining mass “dark matter” and is credited as the first person to postulate its existence. Such discrepancies were also seen in observations by Babcock in 1939 [19] and Schwarzschild in 1955 [20], each of whom studied Andromeda (M31). As telescope technology improved, these results kinematic discrepancies remained, culminating in Vera Rubin’s famous high resolution measurements of the optical emission lines from hydrogen and nitrogen in the late 1970s [21]. These confirmed that optical region rotation curves are flat to the visible edge of spiral galaxies. Modern observations showing this disagreement in the M33 galaxy are shown in Figure 1.3 [22].

Measurements in non-optical wavelengths confirmed these discrepancies. Observations past the optical center of galaxies became possible with the advent of radio astronomy in the 1950s. Observations of the 21-cm line were particularly useful for mapping abundant neutral hydrogen and showing that the rotation curves of spiral galaxies stayed flat past the optical region. In the 1970s, the first X-ray satellites went up and mapped hot gas in galaxy clusters. While they observed that there was much more hot gas than stellar mass in these structures, they were still far from fitting the rotation curves without at least 80% of the mass still belonging to a dark component, as shown in Figure 1.3 [9].

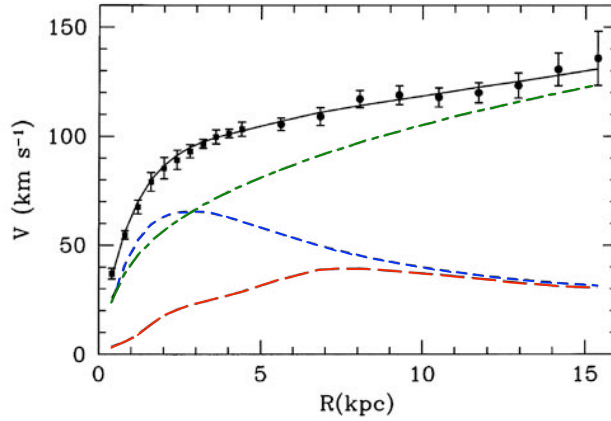


Figure 1.3: Observations of the M33 galaxy’s rotation curve (data points) are shown with the best fit model (black continuous line), which includes dark matter, the visible stellar disk (blue short dashed line), the gas contribution (red long dashed line), and the dark matter contribution (green dashed dotted line). The discrepancy between data and the visible matter curve increases at greater distance from the galactic center, implying a greater dark matter contribution in the outer regions of the galaxy. Figure from [22].

¹In a galaxy with stars of mass m_i at distances from the center of mass r_i : $\sum_i \langle KE_i \rangle = \sum_i \sum_j \left\langle \frac{Gm_i m_j}{r_{ij}} \right\rangle$

1.2.5 Large Scale Structure

Large Scale Structure (LSS) measurements provide evidence for Cold Dark Matter (CDM, see §2.2.2) through their agreement with simulations containing a CDM component. LSS observations map each galaxy brighter than a chosen threshold and convert its redshift to a distance. The field began in 1977 with the Center for Astrophysics (CfA) Redshift Survey [23] and has progressed to the current Sloan Digital Sky Survey, which has mapped over 1.5 million spectra to date, shown in Figure 1.4a [24]. LSS measurements have revealed a surprisingly inhomogeneous matter distribution that matches simulations containing CDM so well at multiple length scales that they are indistinguishable from data, as illustrated in Figure 1.4, which contains both data (top, left) and simulation (bottom, right). The Hot Dark Matter (HDM, see §2.2.2) simulations do not contain enough small scale structure, as shown in Figure 1.4b.

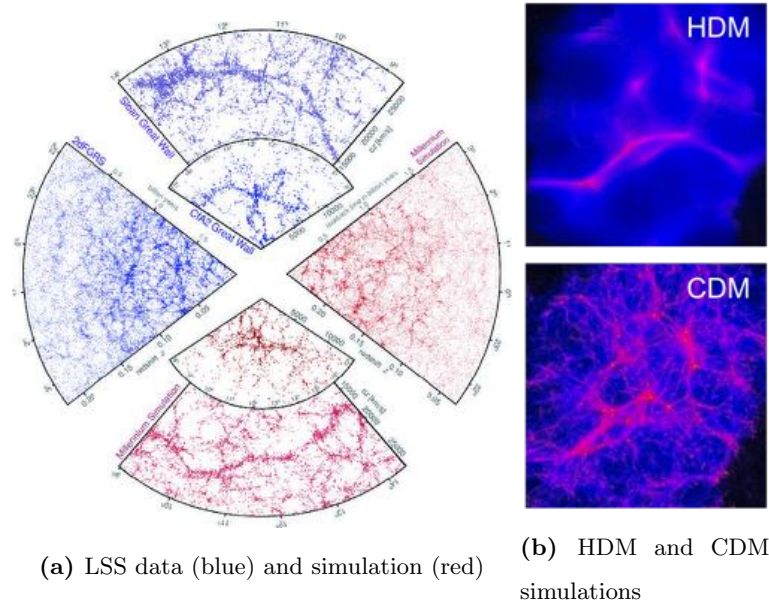


Figure 1.4: Left: LSS, as observed by the Sloan Digital Sky Survey [24] by converting redshifts to distance (top, left). Figure from [25]. Numerical simulations (bottom, right) reproduce this inhomogeneity extremely well when CDM is included. Right: Comparison of simulations with HDM and CDM. Smaller substructure cannot be reproduced with HDM. Figure 1.4b credit: ITP, University of Zurich.

1.2.6 Gravitational Lensing

Gravitational lensing describes the gravitational field of a large mass as it deflects the path of a nearby photon, modifying the apparent flux and shape of the original astronomical source, as shown in Figure 1.5. Gravitational lensing was first used to detect dark matter in 1979, when two images of the same quasar,

separated by $5.7''$, were observed [26]. The advantage of dark matter detection through lensing is the lack of equilibrium assumptions (virial, hydrostatic) of other methods. It does, however, confirm that these are generally good assumptions because lensing data agrees well with the results of other methods. Gravitational lensing has confirmed other measurements, provided insight into the nature of dark matter (see §1.2.7), and is consistent with a dark matter fraction $\Omega_{DM} \sim 0.2 - 0.3$ and baryon fraction $\Omega_b \sim 0.05$.

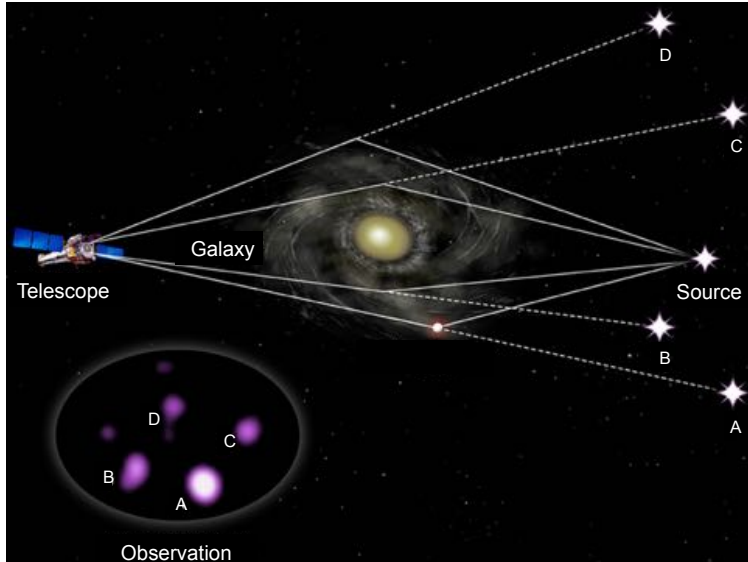


Figure 1.5: Dynamics of gravitational lensing. As photons from an astronomical source are deflected by the modification of space-time due to a large mass (here, a galaxy), observations of the source are distorted. Here, the telescope observes five sources at varying locations, as shown in the inset in the lower left corner. Figure from [27].

1.2.7 The Bullet Cluster

The merging of two galaxy clusters to form the Bullet Cluster (1E 0657-558), shown in Figure 1.6, was observed in the optical (by Hubble, Magellan, Very Large Telescope), in the X-ray (by Chandra [28]), and with gravitational lensing [29]. The optical observations studied the two colliding galaxy concentrations — a main cluster and a smaller sub-cluster. The X-ray observations studied the hot gas, noting that the smaller X-ray component had the bow shape indicative of a supersonic gaseous collision and that the hot gas had merged closer together than the visible galaxies. Combined, these show good evidence that this was a high-velocity collision of two clusters. The galaxies as defined by their visible matter are essentially collisionless, so they pass directly through each other relatively uninhibited. The gas, which is the dominant visible matter component, interacts electromagnetically, colliding and decelerating. As for the dark matter, the

gravitational lensing found that most mass followed the matter concentration, not the gaseous concentration. This implies that dark matter is present, and it is essentially collisionless and dissipationless.

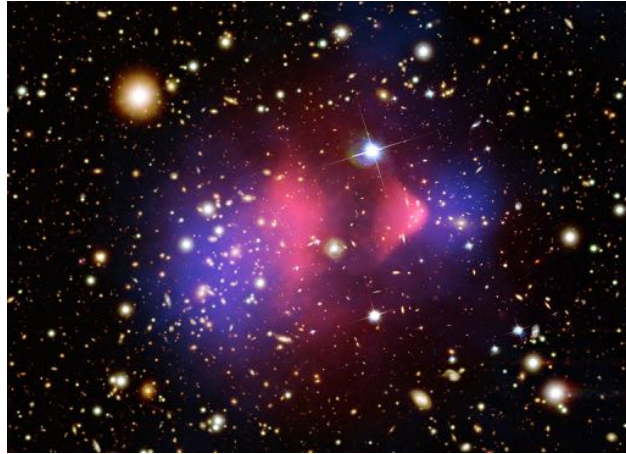


Figure 1.6: The Bullet cluster collision, observed in the optical, in the X-ray (pink), and with gravitational lensing (blue). The hot gas observed with X-rays are more centrally located, having interacted during the collision between the main galaxy cluster and the smaller sub-cluster. The galaxies and the dark matter, however, passed through virtually collisionless. Figure from <http://apod.nasa.gov/apod/ap060824.html>

Chapter 2

Dark Matter Candidates

2.1 The Standard Model of Particle Physics

The Standard Model (SM) of particle physics describes a universe comprised of fermions interacting with each other via fields mediated by bosons. The elementary particles recognized by the SM are shown in Figure 2.1. They are divided first into two categories: fermions, which have a spin of $\frac{1}{2}$ and obey the Pauli exclusion principle, and bosons, which have integer spin and are not restricted by the Pauli exclusion principle.

u	c	t	γ
d	s	b	g
ν_e	ν_μ	ν_τ	Z
e	μ	τ	W
			H

Figure 2.1: SM particles, divided into bosons (blue) and fermions. Fermions are further divided into quarks (red) and leptons (yellow, green), with neutrinos in yellow. None of these SM particles fulfill the requirements of a dark matter particle, which must therefore be a particle beyond the SM.

Fermions are divided into quarks (red in Figure 2.1) and leptons (yellow and green). Quarks (up, down, charm, strange, bottom, top) are the only particles to interact with all four fundamental forces: electromagnetic, weak, strong, and gravitational. They are never found free, but rather confined in compound systems: baryons comprised of qqq and mesons of $q\bar{q}$. Within the leptons are the three generations of neutrinos (ν_x), which only interact weakly, while the other leptons (e, μ, τ) also interact electromagnetically. All fermions have associated antiparticles of equal mass and opposite charge.

The bosons are divided into the gauge bosons (γ , g , Z , W) and the Higgs boson (H). The gauge bosons mediate the fundamental forces, with the photon (γ) mediating the electromagnetic force, gluons (g) mediating the strong force, and the Z and W bosons mediating the weak force. The hypothesized graviton is believed to mediate the gravitational force.

While very successful in describing the physical world, the SM does leave some open questions, and the search for physics beyond the SM is a prodigious experimental effort. Notably, there are no SM explanations for gravity (including general relativity), dark matter, dark energy, neutrino masses, or the matter/anti-matter asymmetry. A supplement to the SM, supersymmetry, is discussed in §2.4.

2.2 Dark Matter Characteristics

Dark matter candidates must fulfill certain characteristics that no SM particle can fulfill. They must be massive enough to match observations of gravitational anomalies (§1.2.4) and structure formation (§1.2.5), eliminating photons, gluons, and neutrinos as candidates. They must be electromagnetically neutral or interactions with light would be observed, and these particles would not be “dark” (§1.2.4). This precludes the charged leptons (e , μ , τ), quarks, and W bosons from being good candidates. As dark matter cannot be baryonic (§1.2.3), compound particles built of quarks are further prohibited. Dark matter particles must be stable, not having decayed since their formation in the early universe, in order to match relic density. This condition eliminates the Z and Higgs bosons as candidates. In addition, a good dark matter candidate leaves stellar evolution unchanged, and is compatible with constraints from self-interaction, direct searches, and astrophysics (§1.2). In addition, possible detection methods are required for to experimentally probe the existence of dark matter.

2.2.1 Baryonic Matter

A number of methods have been used to constrain the baryon fraction of the universe, sampling from different redshifts and converging on a baryonic fraction of $\Omega_b = 0.05$. This is far from the required amount of total matter in the universe ($\Omega_m = 0.315 \pm 0.017$ [5]), and dark matter is understood to be the remaining fraction of matter. This constrains it to be non-baryonic. The baryonic fraction is determined by measurements of BBN (§1.2.3), BAO (§1.2.2) and the CMB (§1.2.1). In addition to these constraints, Massive Compact Halo Objects (MACHOs) were ruled out by microlensing (point-source approximated gravitational lensing) experiments that showed they make up less than 10% of dark matter, if any [30].

2.2.2 Cold Dark Matter

Cold and Hot Dark Matter (CDM, HDM) refer to particles to dark matter candidate particles that were non-relativistic and highly relativistic, respectively, at decoupling. At decoupling, HDM would have been

able to free stream to the horizon at roughly the speed of light (e.g., neutrinos). This theory does not agree with observed structure formation because the LSS observed today (§1.4) would be washed out. Fluctuations smaller than the free streaming distance (i.e., that distance where $KE < mc^2$) would be erased, leading to a top-down structure formation model where large galaxy clusters form first, and galaxies afterwards. This is problematic because very high redshift galaxies have been observed. By contrast, CDM does not erase small fluctuations in the LSS and is compatible with high redshift galaxies. It predicts a bottom-up structure formation in which small structures form first and then merge into larger structures. Applying CDM theory to galaxies, a flat rotation curve can be produced by constraining the mass as a function of radius: $M(r) \propto r$. This implies that dark matter begins to dominate in the outer galactic regions. The inner galactic regions agree well with classical theory, so there does not appear to be much dark matter where the disk is bright. The free parameters used to match observation are the asymptotic halo rotational velocity, the core radius, and the mass-to-light ratio of the visible disk. CDM does run into problems when describing the smaller galactic scales, as described in §2.3.3, although CDM proponents attribute these discrepancies to a poor understanding of galaxy formation [31].

2.3 Preferred Candidates

A number of theoretically-motivated dark matter candidates have been proposed, spanning orders of magnitude of mass and interaction phase space, as shown in Figure 2.2. The theoretically preferred candidates and subject of the current experimental efforts, WIMPs and axions, are described in §2.3.1 and §2.3.4, respectively.

2.3.1 WIMPs

Weakly Interacting Massive Particle (WIMP) dark matter candidates meet the criteria outlined by CDM and return the correct relic density under the assumption that they are weakly interacting. In the early universe ($T > m_{\text{WIMP}}$), WIMP particles and antiparticles were continuously being produced and annihilated until the universe cooled below the temperature of WIMP production, and WIMPs froze out. After the freeze out, dark matter numbers decreased because of self-annihilation until the dark matter density became low enough that annihilation was very rare. The dark matter abundance then stabilized, implying that the current density of dark matter is dependent upon the annihilation cross-section, as shown in Figure 2.3. If the cross-section is that of the weak interaction ($\sim 10^{-37} \text{ cm}^2$), the correct relic density is predicted. This is known as the “WIMP miracle.” The remaining chapters of this work will assume a WIMP dark matter candidate.

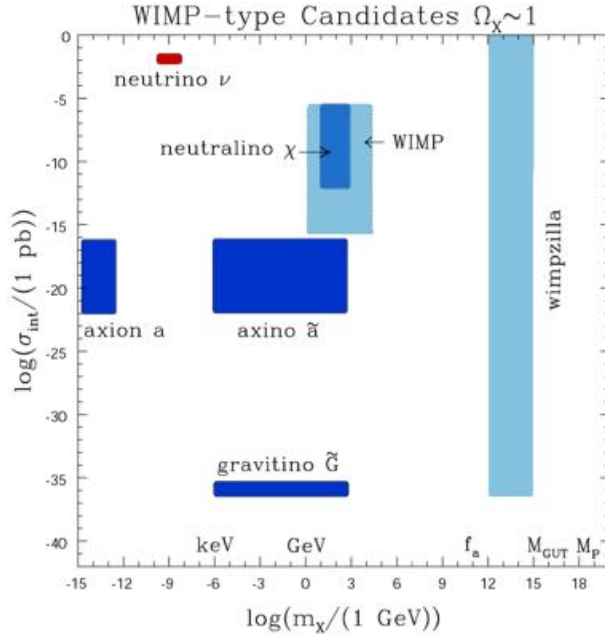


Figure 2.2: Parameter space of theoretically-motivated dark matter candidates, with particle mass on the x-axis and interaction cross-section on the y-axis. The WIMP (and neutralino) and the axion are preferred candidates, while the neutrino and the WIMPzilla have been excluded. Figure from [32].

2.3.2 SUSY Dark Matter

Supersymmetry (SUSY) proposes a symmetry between fermions and bosons that involves supersymmetric partners for all SM particles, as shown in Figure 2.4, one of which may comprise dark matter. Each SUSY particle is heavier than its SM partner and differs in spin by $\frac{1}{2}$. SUSY predicts that in the early universe, supersymmetric partners were in equal abundance to SM particles. By the time the temperature fell below 100 GeV, all of the supersymmetric partners except the lightest had decayed, leaving the SM particles. The lightest SUSY particle would be stable due to a postulated new symmetry, R-parity (P_R), that replaces the conservation of baryon (B) and lepton (L) number and motivates a stable SUSY partner:

$$P_R = (-1)^{2s+3B+L} = (-1)^{2s+3(B-L)} \quad (2.1)$$

where s is spin. SUSY predicts that all SM particles have $P_R = 1$ while SUSY partners have $P_R = -1$. The lightest SUSY partner, assuming R-parity conservation, would have nothing to decay to and would therefore be stable.

From this model emerges a WIMP candidate: the Lowest Supersymmetric Particle (LSP). The most popular SUSY WIMP candidate is the neutralino, which is a linear combination of neutral supersymmetric

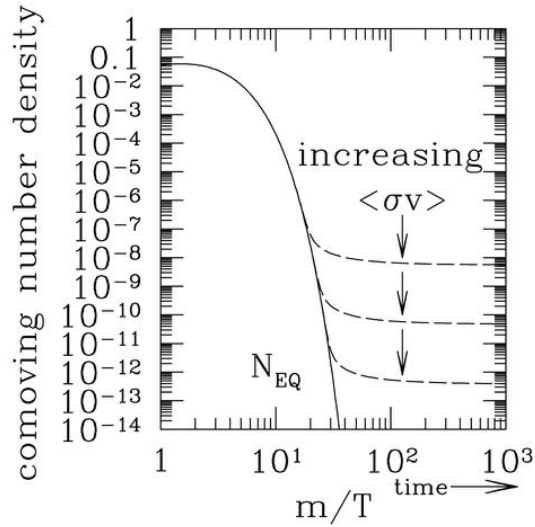


Figure 2.3: WIMP abundance in the expanding universe. After the WIMP freeze out, dark matter density decreased due to self-annihilation until the universe cooled enough that annihilation was rare. At this point, the WIMP abundance stabilized. The correct density is predicted if the annihilation cross-section is that of weak interaction. Figure from [33].

u	c	t	γ	\tilde{u}	\tilde{c}	\tilde{t}	$\tilde{\gamma}$
d	s	b	g	\tilde{d}	\tilde{s}	\tilde{b}	\tilde{g}
ν_e	ν_μ	ν_τ	Z	$\tilde{\nu}_e$	$\tilde{\nu}_\mu$	$\tilde{\nu}_\tau$	\tilde{Z}
e	μ	τ	W	\tilde{e}	$\tilde{\mu}$	$\tilde{\tau}$	\tilde{W}
			H				\tilde{H}

Figure 2.4: SM particles and their SUSY super partners. SUSY partners provide a new class of WIMP candidates, including the neutralino.

particles. The LSP is likely to be the lightest neutralino, a quantum mixture of three SUSY particles with the same quantum numbers: the zino (the Z boson's SUSY partner), the photino (the photon's SUSY partner), and the higgsino (the Higgs' SUSY partner). The neutralino is expected to have a mass of 10 – 10000 GeV [9].

2.3.3 Warm Dark Matter

Warm Dark Matter (WDM) proposes, as the name implies, an intermediate scenario between HDM and CDM. WDM theorizes that dark matter is comprised of ~ 2 keV particles that were light enough at decoupling to free stream for a non-negligible distance that was much smaller than the causally-connected region. They then became non-relativistic and behaved identically to CDM, matching CDM-consistent observations [34]. The success of CDM on a large scale can thus be integrated into the WDM theory, while inconsistencies on the sub-Mpc scale can be explained by the WDM suppression of structure on this and smaller scales [35]. WDM improves dark matter predictions for smaller galaxies, although it requires the inclusion of quantum mechanical effects at small (<100 pc) length scales [34]. The most popular WDM candidate is the sterile neutrino, which is a hypothesized right-handed neutrino that only interacts gravitationally [34]. WDM searches are underway, notably from X-ray telescopes (e.g., Chandra [36]) and the XMASS LXe detector [37].

2.3.4 Axions

Axion dark matter was first postulated following the unexpected observation that the strong interaction appears to respect CP symmetry, as evidenced by the neutron's lack of electron dipole moment. To resolve this, a quasi-symmetry was proposed that is respected at the classical level but is spontaneously broken by an axion field [38]. The axion is predicted to have a mass inversely proportional to the vacuum expectation value that spontaneously breaks CP symmetry.

The Axion Dark Matter eXperiment (ADMX) has been searching for axions through the photons that are predicted to arise from axions scattering off of virtual photons in a magnetic field [39]. The frequency of the resulting photons will depend on the axion mass. ADMX looks for these photons using a finely-tuned radio-frequency cavity at low temperature. ADMX ran from 2008 - 2010 at Lawrence Livermore National Lab, then moved to the University of Washington. The running temperature was also decreased during this upgrade, from ~ 1.2 K to ~ 400 mK, with plans to lower down to 100 mK to reduce noise [40]. A second detector, ADMX-High Frequency (ADMX-HF) is being built to search in the higher frequency (higher mass) axion signal regime. ADMX-HF, located at Yale University, is smaller than ADMX to probe the higher frequency regime [40]. The axion mass space still has unexplored phase space, but it is severely constrained to within 1 - 100 μ eV, with significant mass in that region excluded by beam dump experiments, the longevity of red giants, supernova 1987a, and most stringently, ADMX [30].

2.4 MOND

While dark matter theory explains observational discrepancies by postulating a new particle, it may be the interaction itself that requires modification. This was the original basis for MOdified Newtonian

Dynamics (MOND). At the core of MOND is the correction:

$$F = m \frac{a^2}{a_0} \quad (2.2)$$

in the low acceleration regime ($a < a_0 \sim 10^{-10} \text{ m/s}^2$). [9].

MOND succeeds in yielding a flat galaxy rotation curve in the large radius/low acceleration limit, predicting the difference between low surface brightness and high surface brightness rotation curves. MOND, however, breaks down on the galaxy cluster scale, where it requires a dark component to match observation. It can explain galactic observations, but does not explain lensing, cosmology, structure formation or the CMB, and it has cosmological implications that we do not observe (e.g., discrepancies in the BAO power spectrum, galaxy cluster dynamics, gravitational lensing, high redshift galaxy haloes [41]) . At present, MOND still requires dark matter to be consistent with observation.

Chapter 3

Dark Matter Detection

3.1 Collider Production

A lepton collider like the Large Hadron Collider should be able to produce WIMPs and detect them as missing energy in an event. In such a search, undetected pair-produced squarks or gluinos will decay down to the neutralino, leading to the missing energy and momentum [42].

3.2 Indirect Detection

WIMP indirect detection experiments search for an excess of dark matter annihilation products in those areas (solar core, Earth's core, Galactic Center) where dark matter annihilation is most likely to occur. These experiments have observed a number of inconclusive hints but no definitive signals. Positron detectors, which aim to detect dark matter by observing an anomalously high positron-to-electron ratio, have produced the most notable results. An unexplained positron excess above 10 GeV is observed by the Alpha Magnetic Spectrometer (AMS, [43]), Payload for Antimatter Matter Exploration and Light-nuclei Astrophysics (PAMELA, [44]) and Fermi [45] space-based detectors, as shown in Figure 3.1. The Advanced Thin Ionization Calorimeter (ATIC) adds to this data with an observed excess of the combined electron and positron flux [46]. The Wilkinson Microwave Anisotropy Probe and Planck photon detector satellites have observed a haze about the Galactic Center, which may be from radio synchrotron emission from electrons and positrons spiraling in the galactic gravitational field as a result of dark matter annihilation [12, 47]. By contrast, the Very Energetic Radiation Imaging Telescope Array System (VERITAS [48]) and the High Energy Stereoscopic System (HESS [49]) cosmic ray shower detectors have not seen anything. The IceCube Neutrino Observatory (IceCube, see §8.2) has set the best spin-dependent limits, as shown in Figure 3.2, after observing no excess of neutrinos from the galactic center [50] or solar core [51].

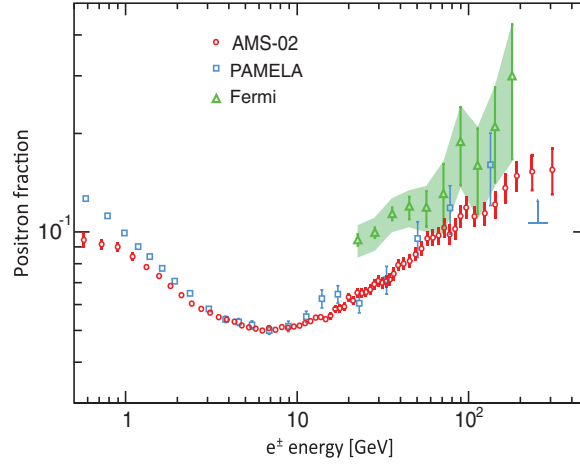


Figure 3.1: Potential hints of dark matter annihilation from indirect detection signals. A high energy positron excess has been observed by AMS [43, 52], PAMELA [44], and Fermi [45], implying a positron source, potentially from dark matter annihilation. Figure from [52].

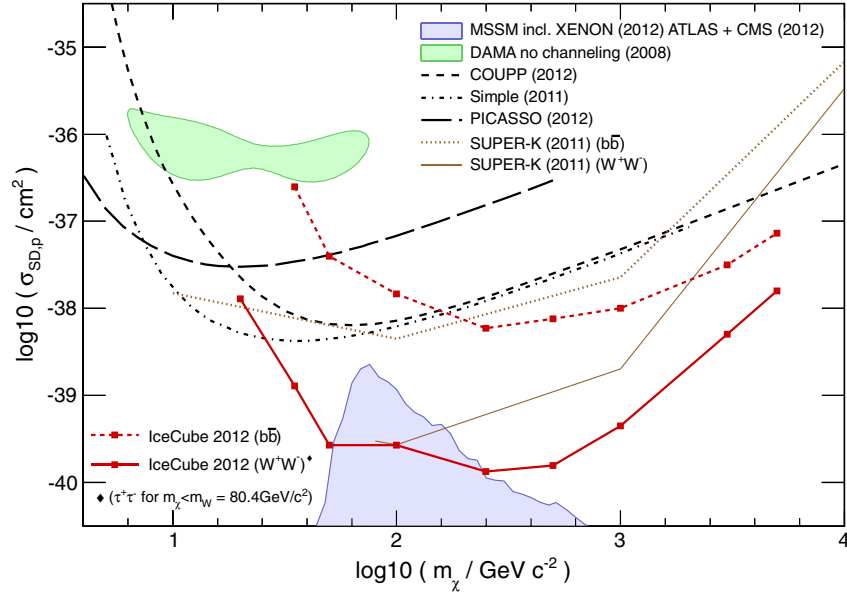


Figure 3.2: Current limits in the spin-dependent WIMP search, with the most stringent limits coming from IceCube [51]. DAMA, KIMS, Simple, and PICASSO are direct detection experiments (see Figure 3.7), while Super-K and IceCube are indirect detectors that observe Cherenkov light. The IceCube limits will improve as the detector has grown from the 79 strings shown here to 86 strings of PMTs and continues to run smoothly. Figure from [51].

3.3 Direct Detection

Direct detection experiments aim to observe the recoil of an atomic nucleus from the scattering of an incoming WIMP. The expected WIMP flux is a product of the galaxy being modeled as a disk rotating through a dark halo. This model predicts an effective WIMP wind of ~ 200 km/s and a WIMP flux on Earth, Φ_χ , of:

$$\Phi_\chi \sim 10^5 \frac{100 \text{ GeV}}{M_\chi} \text{cm}^{-2} \text{s}^{-1} \quad (3.1)$$

where M_χ is the WIMP mass [30]. When a WIMP scatters off of a target nucleus of mass M_A , the nucleus recoils with an energy, E_R :

$$E_R = \frac{\mu_{\chi A}^2 v^2}{M_A} (1 - \cos \theta), \quad \mu_{\chi A} = \frac{M_\chi M_A}{M_A + M_\chi} \quad (3.2)$$

where $\mu_{\chi A}$ is the reduced mass, v_0 is the WIMP speed, and θ is the scattering angle [53]. As an estimate of the energy scale of interest for detection, the average recoil energy for $v_0 = 220$ km/s and $M_\chi = M_A = 50$ GeV/ c^2 is 15 keV:

$$\langle E_R \rangle = \frac{\mu_{\chi A}^2 v_0^2}{M_A} = \frac{1}{2} M_\chi v_0^2 = 15 \text{ keV} \quad (3.3)$$

Both the maximum recoil energy and the average recoil energy are at their largest when the target mass is close to the WIMP mass. The recoil energy spectrum is expected to fall exponentially with energy; the number of the events with energy E_R behaves as $e^{-E_{\text{thresh}}/E_R}$, where E_{thresh} is the threshold energy. A low detection threshold is thus critical to detect as many events as possible, as shown in Figure 3.3.

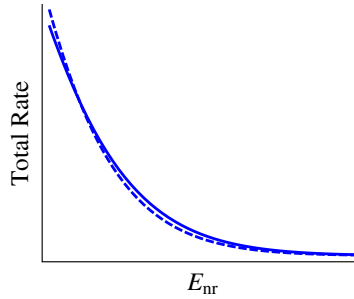


Figure 3.3: Expected rate of dark matter interaction during the times of maximum and minimum rate (see §3.3.1) as a function of energy. A low threshold is critical for direct detection experiments because most events are expected in the low energy region. Figure from [54].

The differential rate of interaction (counts/kg/day/keV) in a detector is derived from the number of interactions per nucleon and the number of nuclei in the material:

$$\frac{dR}{dE_r} = \frac{\rho_0}{M_\chi M_A} \int_{v_{min}}^{v_{max}} v f(v) \frac{d\sigma_{\chi A}}{dE_R}(v, E_R) dv, \quad (3.4)$$

where ρ_χ is the local WIMP density, $\sigma_{\chi A}$ is the WIMP-nucleus cross-section, $\frac{d\sigma_{\chi A}}{dE_R}(v, E_R)$ is the differential cross-section, and $f(v)$ is the WIMP velocity distribution. The minimum velocity, v_{min} , is the minimum velocity that can produce a recoil of energy E_r and is thus limited by the detector threshold, and v_{max} is limited by the local escape velocity. Current experiments have already limited the expected WIMP-nucleon interaction rate to <1 event/(kg · day).

3.3.1 Annual Modulation

The WIMP flux on Earth is expected to modulate throughout the year due to annual changes in the effective galactic velocity of the Earth. This arises from the combination of the Earth's two orbits: one around the Sun and the other, together with the Sun, around the center of the galaxy. As seen in Figure 3.4, the Earth should see a WIMP maximum in June, when its motion around the Sun is in the direction of the galactic rotation velocity (increasing its effective velocity with respect to a galactic halo WIMP). Likewise there should be a WIMP minimum in December when the Earth's velocity is directed against that of the galactic orbit, decreasing its effective velocity. The Earth's velocity in the galactic frame is:

$$v_e(t) = v_\odot + v_\oplus \cos \gamma \cos \omega(t - t_0) = 232 + 15 \cos \left(2\pi \frac{t - 152.5}{365.25} \right) \quad (3.5)$$

where v_\odot is the Sun's velocity with respect to the galactic halo; v_\oplus is the Earth's velocity around the Sun with an inclination of 60.2° with respect to the galactic plane; $\omega = \frac{2\pi}{1 \text{ yr}}$ is the frequency of the orbit around the Sun, and t_0 is that time when the Earth's galactic speed is maximal, in early June [55]. These calculations predict a WIMP signal that modulates with a one year period and has a maximum in early June. In addition, a WIMP signal should be found only in the expected WIMP-induced recoil signal region, should be a single-scatter event, and should modulate with an amplitude $\leq 7\%$.

3.3.2 Diurnal Modulation

The WIMP flux is predicted to follow a diurnal modulation in addition to the annual modulation. The effective WIMP wind in the galaxy should combine with the daily rotation of the Earth to produce a daily modulation, as shown in Figure 3.5. The modulation, in phase with the sidereal period, will go out of phase with the solar day as the year progresses. Only ~ 10 events would be needed to show that the WIMP signal is not isotropic and determine good information on the WIMP velocity distribution [53].

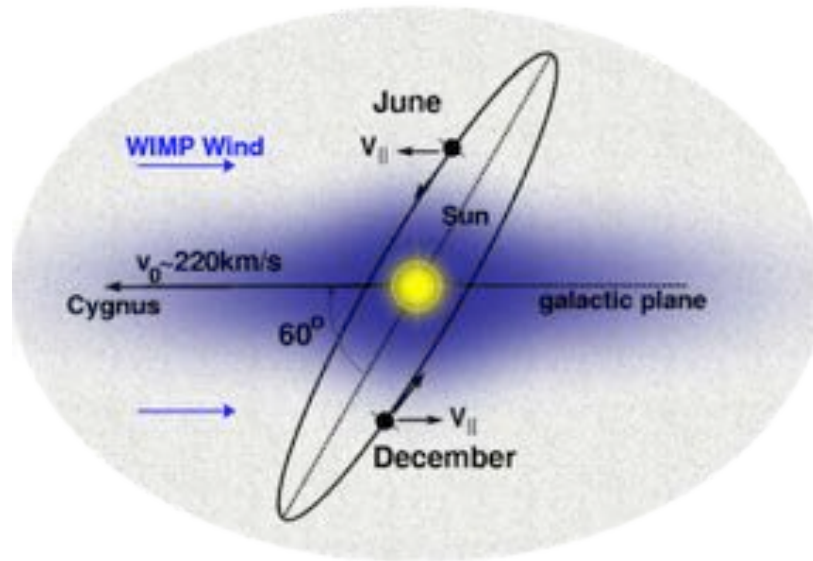


Figure 3.4: Annual modulation mechanism for the WIMP flux on Earth. The modulation is a result of changes in the Earth's galactic orbital velocity due to its orbit about the Sun. The WIMP flux maximum is in June, when the Earth's orbital velocity is aligned with the galactic local velocity, and the minimum is in December, when the Earth's solar velocity goes against the local galactic velocity. The WIMP wind comes from the direction of the constellation Cygnus in the terrestrial frame.

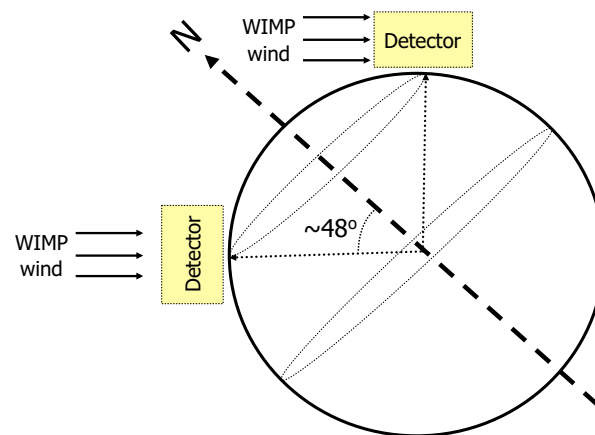


Figure 3.5: Daily modulation in the WIMP flux of terrestrial detectors. The WIMP wind changes direction relative to the detector rotating with a sidereal day period. Only ~ 10 events would be needed to identify the WIMP signal is not isotropic. Figure from [56].

3.3.3 Spin Dependence of Interaction

The WIMP-nucleon interaction may be either spin-independent or spin-dependent, with the spin-independent component from the scalar and vector couplings to quarks, and the spin-dependent from axial-vector couplings [53]. The spin-independent interaction is proportional to the target's atomic mass number, A :

$$\sigma_{SI} \propto A^2 \quad (3.6)$$

Heavy target materials with a large number of nucleons (e.g., Xe^{131}) are preferred for spin-independent searches. Those target materials much heavier than germanium, however, lose coherence and offer only a small increase in overall rate [53]. By contrast, spin-dependent coupling is proportional to the total nuclear spin, J :

$$\sigma_{SD} \propto \frac{(J+1)}{J} \quad (3.7)$$

Nuclei with even numbers of protons have no net proton spin and no spin-dependent sensitivity for the proton interaction, and likewise for even numbers of neutrons and the neutron interaction. Elements with even numbers of both protons and neutrons are not used for spin-dependent searches. Spin-dependent proton and neutron interaction limits are quoted separately, assuming the other interaction is negligible [53]. Many isotopes used for WIMP searches can only search for neutron spin-dependent interactions (e.g., Ge, Si, Xe). Those materials that have odd numbers of protons are not often used as they tend to have higher background levels and lower sensitivity for spin-independent interactions than those materials with an even number of protons.

3.3.4 Techniques: Shielding Backgrounds

Dark matter experiments require low backgrounds to detect such a rare signal, so shielding from the environment, the detector, and even the target is an important experimental factor. Placing experiments deep underground shields them from cosmic ray backgrounds, and additional shielding is used for local environmental backgrounds. As most backgrounds will produce electron recoils rather than nuclear recoils, discrimination between nuclear recoils and electron recoils can reject almost the entire background. Methods for separating electron and nuclear recoils rely on the difference in the velocity of the recoiling object for a given recoil energy, E_R . For $E_R \sim 10$ keV, an electron recoils with $v \sim 0.3c$ while a nucleus recoils with $v \sim 0.0007c$, so the nuclear recoil deposits the same amount of energy over a much shorter track [53]. This can be exploited to separate the recoils by requiring a dense energy deposition to trigger, exploiting pulse timing discrimination, or discriminating on the relative amount of energy in two different channels, as shown in Figure 3.6. Additionally, searching for the annual modulation in the WIMP signal (see §3.3.1) suppresses the interference of backgrounds that do not modulate.

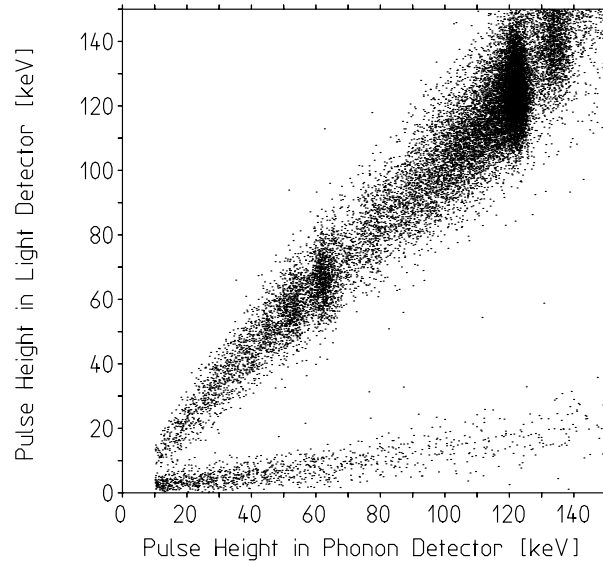


Figure 3.6: Electronic and nuclear recoil separation in the CRESST detector [57]. A two channel readout allows the separation through comparison of signal heights in each channel. The upper band is that of electronic recoils, and the lower band is that of nuclear recoils. Figure from [57].

3.4 Status of the Direct Detection Field

Historically, there have been three dark matter direct detection techniques: ionization (using semiconductors and noble liquids/gases), scintillation (using inorganic crystals and noble liquids/gases), and calorimetry (using cryogenic detectors). Recent experiments have made great strides in background rejection and event identification by integrating multiple readout channels, as shown in Figure 3.6. Three new fields combine multiple detection methods: dual-phase liquid noble gas time projection chambers (TPCs) using scintillation and ionization (e.g., LUX); cryogenic scintillators using scintillation and calorimetry (e.g., CRESST); and cryogenic solid-state detectors using scintillation and calorimetry (e.g., CDMS). Figure 3.7 sorts current and recent direct detection experiments by readout channel. An extensive list of current, former, and future experiments is provided in Appendix A. For information on NaI(Tl) and CsI(Tl) experiments, see §3.5.

Chicagoland Observatory for Underground Particle Physics (COUPP): COUPP is a superheated liquid bubble chamber that uses ionization to search for WIMPs. It is designed such that bubbles from small energy depositions will collapse while bubbles from the energy-dense nuclear recoils remain. These detectors do not observe gamma events, and they use acoustic sensors to reject alphas. They are particularly useful for

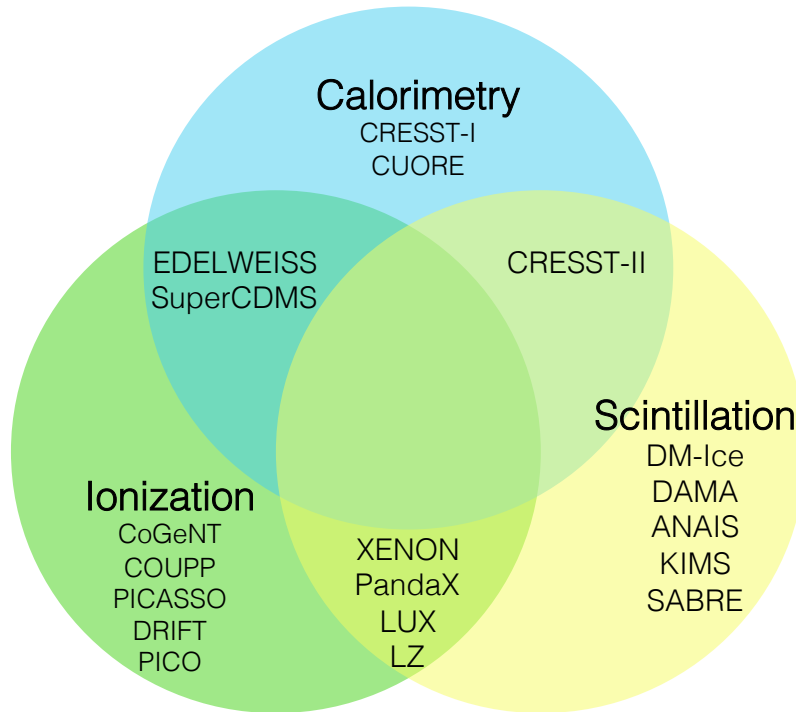


Figure 3.7: A survey of select direct detection dark matter experiments, characterized by their readout channels. Improved background rejection and WIMP identification is possible with multiple readout channels. See Figures 3.2 and 3.11 for the results of these experiments.

spin-dependent searches, as shown in Figure 3.2. The most recent results from the 4.0 kg COUPP CF_3I bubble chamber used 553 kg days of data in which twenty candidate events were observed. Only 5.3 background events were expected, but upon unblinding an unidentified background was found in the data sample. The limit, shown in 3.2, does not include any background elimination as the source was not understood, so the limit assumes that all twenty events are dark matter candidate events [58].

Directional Recoil Identification From Tracks (DRIFT): DRIFT-II is a directional detector looking for two modulations in the dark matter signal: annual and daily. Gas target TPCs like DRIFT are run at low pressure to provide long enough recoil tracks, and gases are typically chosen to allow spin-dependent searches. Electron recoils are rejected by their long track length. The DRIFT-II detector has a 0.8 m^3 gas TPC fiducial volume containing a mixture of CS_2 and CF_4 gases. Their latest results came from 47.4 live-days, but upgrades and improvements are underway to provide competitive limits [59], and a 3.5 year long study of backgrounds has shown promising improvements in background identification and rejection [60].

Cryogenic Rare Events Search with Superconducting Thermometers (CRESST): CRESST-II is a cryogenic scintillator that measures both phonons and scintillation light, allowing the rejection of photons and surface events. Phonons are collected by detecting vibrations in the lattice of the crystal with excellent energy resolution. Combined phonon and crystal scintillation signals are used for discrimination, although this cuts on the WIMP energy since only high-energy WIMPs should produce any detectable light. Additionally, signals that produces phonons but not photons could be mistaken for WIMPs. CRESST-II results are in tension with one another - the positive signal came from 730 kg days of running CaWO_4 with eight crystals of ~ 300 g each and found 67 events in the region of interest with a background expectation of ~ 45 events [61]. These events are shown in Figure 3.8, and the resulting phase space of the observation is shown in Figures 3.11a and 3.11b. Two CRESST-II results following this signal have excluded it. The first exclusion used 47.9 kg days of commissioning run data and a new acceptance region [62]. Three events were observed, consistent with background expectation. The latest CRESST-II result uses 29.35 kg days of exposure from a new, cleaner crystal and improved background rejection. These results, shown in Figure 3.11, are particularly sensitive to the low mass region.

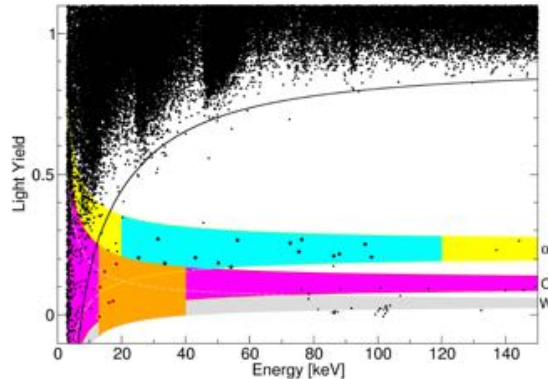


Figure 3.8: Data shown from one CRESST-II module. Events with a light yield ~ 1 are electron and gamma backgrounds. The shaded areas indicate the recoil regions for alpha (yellow), oxygen (magenta), and tungsten (grey) events. The acceptance region is in orange, with a pure alpha population in blue. 67 background events were seen across the 18 modules, with an expectation of ~ 45 events, leading to a 4σ excess. Figure from [61].

Coherent Germanium Neutrino Technology (CoGeNT): CoGeNT is a 440 g Ge ionization detector that is particularly competitive in the low mass regime (see Figure 3.11b). CoGeNT's most recent annual modulation search over 1,129 live days of data found a 2.2σ modulation in the 0.5 - 2.0 keVee range. The modulation, with a fraction amplitude in the 35% - 62% range, was fit with both a floating period and a fixed one-year period. The floating period was optimized to be 350 ± 20 days while the phase of the

fixed-period fit is 102 ± 47 days, creating a modulation that is compatible in phase, but not in amplitude, with the DAMA data (see §3.5.1), as shown in Figure 3.9 [63]. A previous analysis of this positive result [64] and the resulting state of the dark matter field are shown in Figure 3.11.

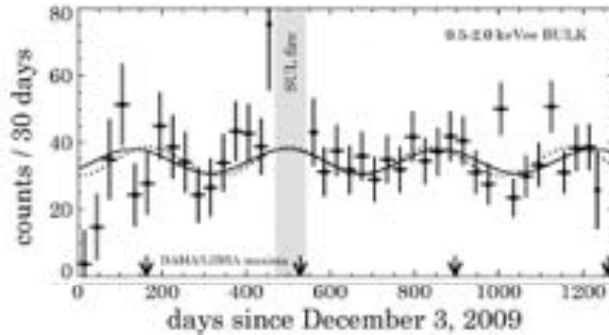


Figure 3.9: Modulation results from CoGeNT, showing a 2.2σ significant modulation. The curves are the best fits to the modulation data with a fixed (solid) and floating (dotted) period. The phase is consistent with that of the DAMA modulation, but the amplitude is $\sim 4 - 7$ times too large [63]). The grey band corresponds to downtime due to a fire in the laboratory. Figure from [63].

DAMIC: DAMIC is a Ge CCD detector that uses ionization to search for WIMPs. It is particularly sensitive in the low mass (<10 GeV) regime as it can operate down to a 0.5 keV_r threshold. The first run limit, from a 107 g-day exposure of a 0.5 kg detector, is shown in Figure 3.11b [65]. A 5 kg detector is currently running but has yet to release results.

Cryogenic Dark Matter Search (CDMS): The CDMS experiment is upgrading from CDMS-II to SuperCDMS. CDMS-II used 4.6 kg of cryogenic Ge and 1.2 kg of cryogenic Si for ionization and phonon detection. SuperCDMS is running with fifteen 0.6 kg Ge crystals and no Si component yet, although it will be added (see §3.6). The standard Ge analysis from SuperCDMS ran on 577 kg days and found eleven candidate events, consistent with the background expectation of $6.1_{-0.8}^{+0.2}$ events and an additional 0.098 ± 0.015 counts from neutrons [66]. The limit from this null result is shown in Figure 3.11. SuperCDMS also performed a low-energy Ge analysis, CDMSlite, using a single 0.6 kg Ge crystal over 6.3 kg-days with an emphasis on a low threshold. The results of this analysis are shown in Figure 3.11 [67]. The latest CDMS-II Si results used 140.2 kg-days of data and saw three events with an expected background of 0.7 events, which may hint, to 3σ , at a WIMP of ~ 8.6 GeV [68], as shown in Figure 3.10. These Si results complicate the suite of positive WIMP signals, as shown in Figure 3.11.

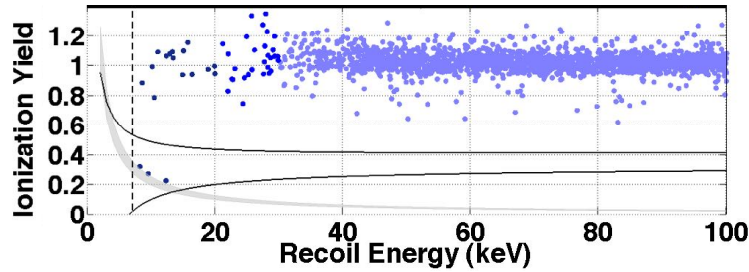
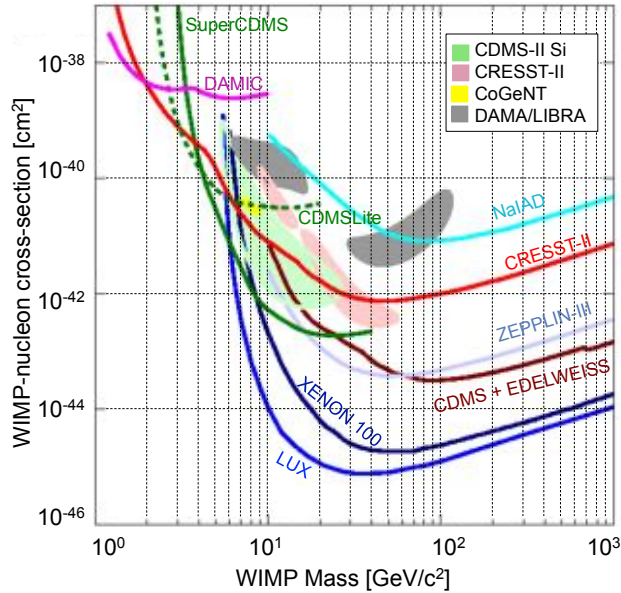


Figure 3.10: Events passing cuts from the CDMS-II Si analysis. Three candidate events were observed with a background expectation of 0.7 events, indicating a 3σ hint of WIMP interactions. Figure from [68].

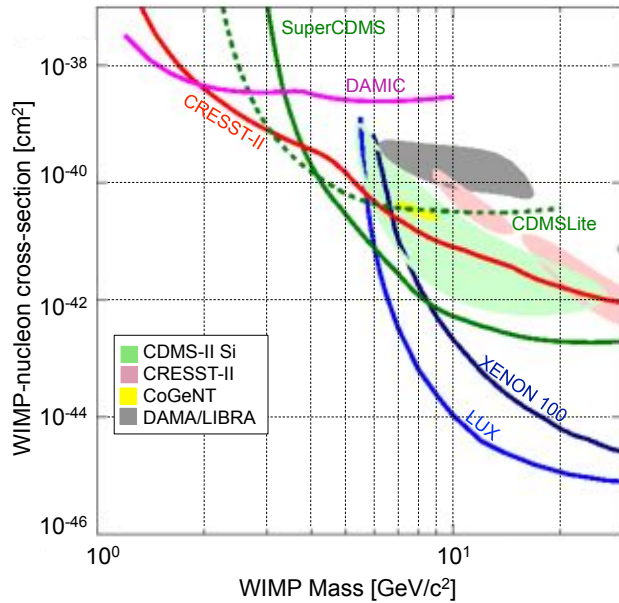
The Large Underground Xenon dark matter experiment (LUX): LUX is a dual phase xenon TPC that offers the most stringent limits across much of the spin-independent WIMP mass range. Dual phase noble detectors take advantage of the faster speed and lower ionization yield of nuclear recoils to separate them from electronic recoil backgrounds. The LUX limit was the result of seeing 3.1 ± 0.2 events in the region of interest over 85.3 live days with a 118 kg fiducial volume, consistent with the background expectation of 2.6 ± 0.6 events [69]. The resulting limits are shown in Figure 3.11.

3.4.1 Low Mass WIMPs

Low-mass WIMPs have been proposed as a way to ease the tension between experimental results. Low-mass WIMPs are argued to be consistent with indirect detection hints (e.g., the “WMAP haze,” gamma rays from the Galactic Center) and direct detection from DAMA, CoGeNT, and CRESST-II [76]. Tension with xenon experiments can be attributed to a poor understanding of the response of liquid xenon to low-energy nuclear recoils or from differing couplings of WIMPs to protons and neutrons. Current observations may be consistent with a light (7 - 12 GeV) WIMP, a $\sim 10^{-26}$ cm³/s annihilation cross-section and a $\sim 10^{-41}$ cm² spin-independent elastic scattering WIMP-nucleon cross-section [76].



(a) Current limits to 1000 GeV.



(b) Current limits to 30 GeV.

Figure 3.11: Best limits for spin-independent direct detection dark matter experiments. The 1 - 10^3 GeV mass range is shown in Figure 3.11a, with the most stringent limits set by LUX [69]. Also shown are limits from XENON100 [70], combined CDMS and EDELWEISS [71], ZEPLIN-III [72], CRESST-II [62], DAMIC [65] and NaIAD [73] and positive indications from CoGeNT [74], CDMS-II Si [68], CRESST-II [61], and DAMA/LIBRA [75]. Figure 3.11b shows the low mass range, from 1 - 30 GeV. It includes the results from DAMA/LIBRA (3σ C.L.), CoGeNT (99% C.L.), CRESST-II (2σ), and CDMS-Si (90% C.L.). Exclusion limits from null results are also shown (90% C.L.) from DAMIC, XENON100, SuperCDMS, CDMSLite, and CRESST-II.

3.5 NaI(Tl) Experiments

NaI(Tl) experiments are optimal to investigate the strong dark matter-like signal observed by the DAMA experiment (see §3.5.1), which has yet to be verified by other experiments. A complementary group of NaI(Tl) experiments is maturing from prototype detectors to active development of large-scale experiments with the ability to definitely test this signal. An experimental comparison of past and current NaI(Tl) dark matter experiments is shown in Table 3.1, with their full-scale detectors listed in the right-hand column. Large mass and overburden, combined with a low threshold and background rate, increase sensitivity to a potential dark matter signal.

Table 3.1: NaI(Tl) Dark Matter Experiment Comparison. Experiments in progress have not published all parameters; these unreleased values are designated by the - symbol. Unknown parameters of future experiments have been left blank.

Experiment	Mass	Time	Depth	Analysis	LE rate	Status
Detector	[kg]	[years]	[m] ([m.w.e.]	Threshold [keV]	~5-10 keV [dru]	
DM-Ice17 [77]	17	2011 –	2450 (2200)	4	7.9±0.4	Running; upgraded
DM-Ice37	37	2014 –	1070 (2850)	-	-	Running, current R&D
DM-Ice250	≈250					Planned
DAMA/NaI [78]	87.3	1996 – 2002	1400 (3400)	2	≈1-2	Completed; upgraded
DAMA/LIBRA [79]	242.5	2003 – 2010	1400 (3400)	2	≈1	Completed; upgraded
DAMA/LIBRA-phase2 [80]	242.5	2011 –	1400 (3400)	-	-	Running
NaIAD [73]	51	2000 – 2003	1070 (2850)	4	≈8	No longer in operation
ANAIS-0 [81]	9.6	2009 – 2012	850 (2450)	2	2-3	Completed; upgraded
ANAIS-25 [82, 83]	25	2012 – 2015	850 (2450)	1	3-4	Completed; upgraded
ANAIS-37 [83]	37.5	2015 –	850 (2450)	-	-	Running, current R&D
ANAIS-250 [83]	≈250		850 (2450)			Planned
KIMS NaI(Tl) [84]	32.2	2013 –	700 (2000)	<2	3	Running, current R&D
KIMS NaI(Tl) [85]	≈200		700 (2000)			Planned
SABRE [86]	≈50		1400 (3400)			Planned

Current experimental efforts focus heavily on the development of low background crystals. A combined effort from DM-Ice, ANAIS (see §3.5.3), KIMS (see §3.5.4) and the Alpha Spectra crystal growing company has produced the results compiled in Table 3.2. SABRE (see §3.5.5) is in development with a separate crystal growing company. The purification and growth techniques that produced the DAMA crystals are proprietary and may not be disclosed or used in the development of current crystals. Contamination numbers

in Table 3.2 are separated for crystals (above the line break) and powders (below). Crystal contamination is derived from the analysis of the alpha energy spectrum. Bismuth-Polonium decays provide a definitive energy scale, and ^{40}K can be tagged using its beta shoulder and coincidence between the 3 keV and 1460 keV peaks. Powder contamination is derived from high purity germanium (HPGe) and Inductively Coupled Plasma Mass Spectrometry (ICPMS) detection methods. HPGe is a non-destructive method that identifies radiation through ionization observed in the germanium detector. ICPMS ionizes the sample with a charged gas and uses mass spectrometry to measure the ions emitted.

Table 3.2: NaI(Tl) Contamination Levels. Certain isotopes, designated by the - symbol, have not been released, although they are constrained by the total alpha rate.

Experiment	^{40}K	^{232}Th	^{228}Ra - ^{208}Tl	^{238}U	^{234}U , ^{234}Th	^{226}Ra - ^{214}Po	^{210}Po
Crystals	mBq/kg	$\mu\text{Bq/kg}$	$\mu\text{Bq/kg}$	$\mu\text{Bq/kg}$	$\mu\text{Bq/kg}$	$\mu\text{Bq/kg}$	$\mu\text{Bq/kg}$
DAMA [87]	0.6	8.5 ± 0.5	8.5 ± 0.5	4.4 ± 0.7	15.8 ± 1.6	21.7 ± 1.1	24.2 ± 1.6
DM-Ice17 [77]	17	10	160	17	140	900	1500
DM-Ice37	<2	-	-	-	-	-	<2100
ANAIS-0 [81, 88]	12.7 ± 0.5	13 ± 5	35 ± 4	75 ± 5	75 , 23 ± 7	98 ± 4	188 ± 5
ANAIS-25 [82, 83]	1.25 ± 0.11	2.0 ± 0.8	2	10 ± 2	-	10	3150
KIMS NaI 1 [85]	1.25	<12	<13	<7	-	<0.3	3280 ± 10
KIMS NaI 2 [85]	1.49	2 ± 1	2	<12	-	<1.5	1760 ± 10
KIMS NaI 3 [85]	0.78 ± 0.07	-	-	-	-	-	$\leq 2290 \pm 30$
KIMS NaI 5 [85]	1.24 ± 0.1	-	-	-	-	-	$\leq 470 \pm 10$
Powders	^{40}K	T-chain	U-chain				
	[mBq/kg]	$[\mu\text{Bq/kg}]$	$[\mu\text{Bq/kg}]$				
DAMA [87]	3.1	81.3	246.9				
SABRE SML [86]	0.37	<1,600	<2,470				
SABRE SA [86]	$0.56 (0.11)$	<6,900	<6,170				

3.5.1 DAMA

3.5.1.1 Experiments

Dark MATter (DAMA) is a NaI(Tl) dark matter experiment searching for the expected annual modulation in the WIMP signal (see §3.3.1). DAMA has run at the Laboratori Nazionali del Gran Sasso (LNGS, 3400 m.w.e.) in three phases and has released the data from the first two phases, which combined for a total exposure of 1.33 ton·yr over 14 years [89]. The run phases are comprised of:

- **DAMA/NaI (1996 - 2002)**: DAMA/NaI ran with nine 9.70 kg ($10.2 \times 10.2 \times 25.4 \text{ cm}^3$) crystals in a 3×3 array for a total mass of 87.3 kg [90]. It collected data over seven annual cycles for a total exposure of 295.2 kg-yrs. DAMA/NaI observed evidence of an annual modulation consistent with a WIMP signal in the 2-4 keV range to 5.0σ significance (see Table 3.3 and Figure 3.15) [55].
- **DAMA/LIBRA-phase1 (2003 - 2010)**: DAMA/LIBRA upgraded the DAMA/NaI setup with new PMTS and 242.5 kg of lower background NaI(Tl) crystals. It was comprised of twenty-five 9.70 kg ($10.2 \times 10.2 \times 25.4 \text{ cm}^3$) crystals in a 5×5 array, shown in Figure 3.12. DAMA/LIBRA collected data over seven annual cycles for a total exposure of 1.04 ton-years. The observed 8.1σ modulation in the 2-4 keV range is consistent with the WIMP signal observed by DAMA/NaI (see Table 3.3 and Figure 3.15) [89]. The combined DAMA/NaI and DAMA/LIBRA modulation reaches 9.5σ from 2-4 keV [89].
- **DAMA/LIBRA-phase2 (2010 - present)**: The DAMA/LIBRA-phase1 detector was upgraded with higher quantum efficiency PMTs, lowering the software threshold from 2 keV to 1 keV. Data collection began in December 2010, and a data release is anticipated after five years of data has been collected. Additional electronics upgrades are both planned and in progress [80].

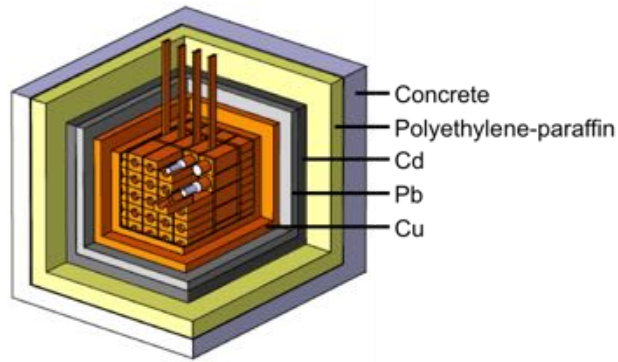


Figure 3.12: DAMA/LIBRA experimental setup. NaI(Tl) crystals are arranged in a 5×5 array, surrounded by multiple layers of shielding (from the inside out): Cu to shield X-rays, Pb to shield gammas, Cd to absorb neutrons, polyethylene-paraffin to moderate neutrons, and concrete to moderate neutrons. All materials were counted and selected for low radioactivity. The Cu box and installation housed within it are continuously flushed with nitrogen and kept at a slight overpressure to prevent radon contamination. Figure from [87].

The DAMA experiments use extremely clean NaI(Tl), which is a strong asset for a low background search. Running with multiple crystals allows a multi-crystal ^{40}K identification that is valuable in the region of interest, as shown in Figure 3.13. The ^{40}K isotope has a 10.7% branching ratio to decay to ^{40}Ar , producing

a 1460 keV gamma and a ~ 3 keV X-ray or Auger electron in the process. For a ^{40}K decay in a crystal in the array, the 3 keV particle will stop in the host crystal while the 1460 keV gamma will escape into a neighboring crystal, creating the correlation shown in Figure 3.13. This correlation allows the calibration and removal of these ^{40}K background events in the region of interest.

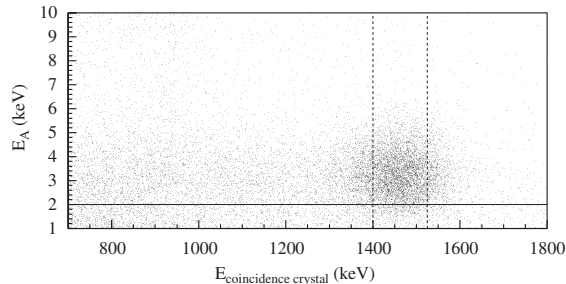


Figure 3.13: Multi-crystal veto of low energy ^{40}K events [87]. The host crystal will register the 3 keV gamma while the 1460 keV gamma escapes to the neighboring crystal. ^{40}K events can be both calibrated and removed with this technique, as shown in Figure 3.14. Figure from [87].

The DAMA modulation data sample is processed with two treatments: the first is a $500\ \mu\text{s}$ deadtime imposed after each event, and the second is the removal of noise and multiple-hit events. The deadtime is designed to reject afterglow (see §4.2.4), Cherenkov events, and Bismuth-Polonium decays, in which a short-lived daughter decays quickly following the initial interaction [87]. PMT noise in single-hit events is identified by its fast time distribution; it decays on the order of tens of ns (compared to the 230 ns scintillation decay time). The spectrum after these cuts indicates a low background (1 dru¹) data sample, as shown in Figure 3.14. The background contamination improvements in the upgrade from DAMA/NaI to DAMA/LIBRA are visible in the decreased background rate in the spectrum.

Potentially-varying components are continuously monitored in the experiment. The energy threshold, PMT gain, and electronic line stability are monitored using the routine calibrations, position and resolution of internal lines, and hardware rate stability. Neutron calibration runs are taken with a ^{241}Am source every 7-10 days, and the position and resolution of the 46 keV ^{210}Pb peak is regularly monitored [55,87]. Additionally, radon levels in the installation, the pressure of the nitrogen, and temperature are also tracked [55].

3.5.1.2 Results

The DAMA/NaI and DAMA/LIBRA cumulative exposure resulted in a $9.5\ \sigma$ annual modulation signature in single-hit events in the 2-4 keV energy range with a 0.0190 ± 0.0020 dru amplitude, a 0.996 ± 0.002 year

¹1 dru = 1 count/keV/kg/day

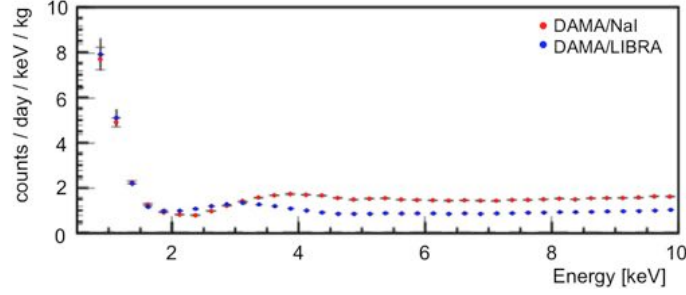


Figure 3.14: Energy spectrum in the region of interest for each of the published DAMA experiments [53]. The DAMA/NaI backgrounds are roughly twice as large as that of DAMA/LIBRA above 4 keV. A similar two-fold shift in modulation amplitude between the two experiments is observed, as shown in Table 3.3. Figure adapted from [78, 79].

period, and a May 14th ± 7 day maximum [89]. For comparison, the expected WIMP modulation should have a $\leq 7\%$ amplitude with a one year period and a June 2nd maximum. The results for each detector and for three energy ranges of interest in the combined dataset are shown in Figure 3.15 and Table 3.3.

Table 3.3: Modulation observed by the DAMA experiments over 14 annual cycles [89]

	Exposure [kg·yr]	Amplitude [dru]	Period [yr]	Phase (t_0) [day]	C.L
DAMA/NaI 2 - 4 keV	295.2	0.0252 ± 0.0050	1.01 ± 0.02	125 ± 30	5.0σ
DAMA/LIBRA 2 - 4 keV	1040	0.0178 ± 0.0022	0.996 ± 0.002	134 ± 7	8.1σ
NaI + LIBRA 2 - 4 keV	1330	0.0190 ± 0.0020	0.996 ± 0.002	134 ± 7	9.5σ
2 - 5 keV	1330	0.0140 ± 0.0015	0.996 ± 0.002	140 ± 6	9.3σ
2 - 6 keV	1330	0.0112 ± 0.0012	0.998 ± 0.002	144 ± 7	9.3σ

The 2-4 keV region has the highest modulation amplitude, as expected from a WIMP signal (see §3.3) and shown in Figure 3.16. No modulation was observed in the multiple-hit dataset or at energies above 6 keV, as shown in Figure 3.16, consistent with expectation for a dark matter signature. Comparison of the DAMA/NaI and DAMA/LIBRA results show a consistent phase and period, although differences in the amplitude have been the subject of discussion because the modulation amplitude decreases when the total

background rate above 4 keV decreases between DAMA/NaI and DAMA/LIBRA (see §3.5.1.3). The phase space that the DAMA signal corresponds to has been ruled out by other experiments (see Figure 3.11), leading to the tension discussed in 3.5.1.3.

3.5.1.3 Result Controversy

The DAMA signal has not been observed by other dark matter experiments that use different detector media, and tension in the field has increased as new experiments continue to report conflicting phase space

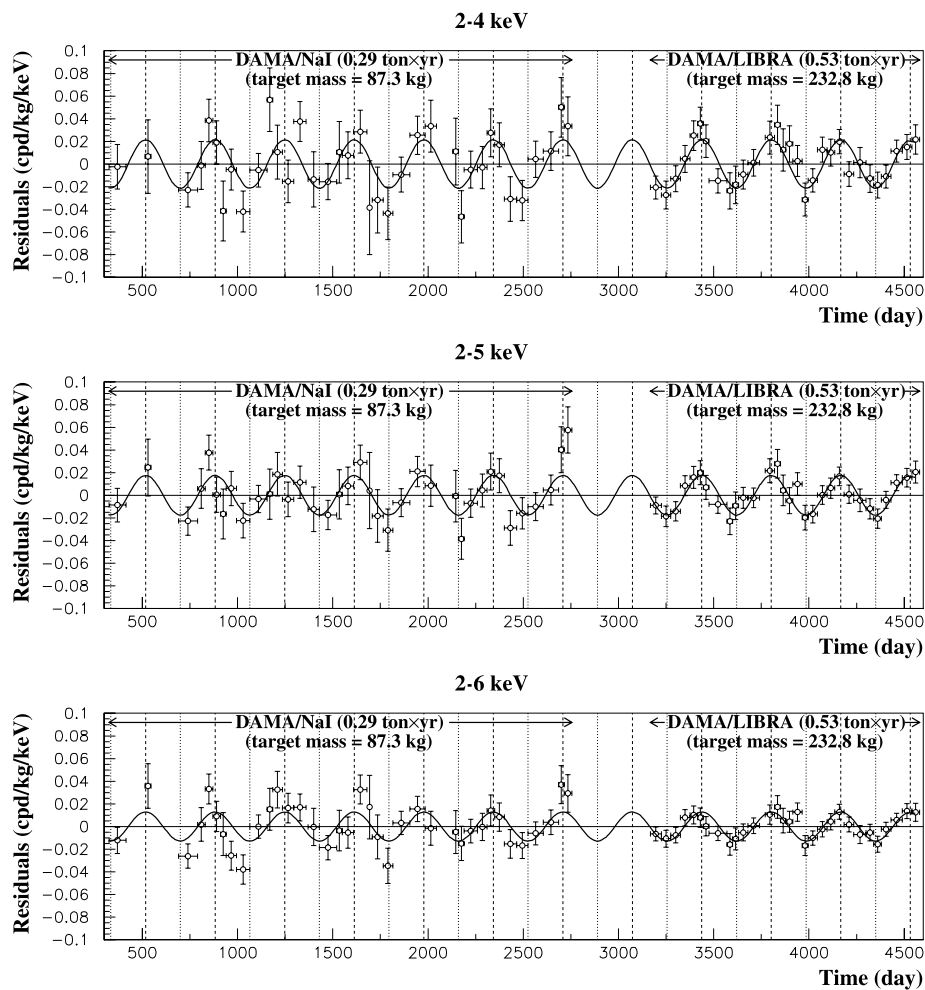


Figure 3.15: Annual modulation results from the first 11 annual cycles of DAMA/NaI and DAMA/LIBRA-phase1 [79]. This does not include the final year of data from [89]. The best fit in the 2-4 keV region over the entire 14 annual cycles corresponds to a 0.996 ± 0.002 year modulation period with a phase of May $14^{th} \pm 7$ days, consistent with the WIMP hypothesis to 9.5σ . Figure from [89].

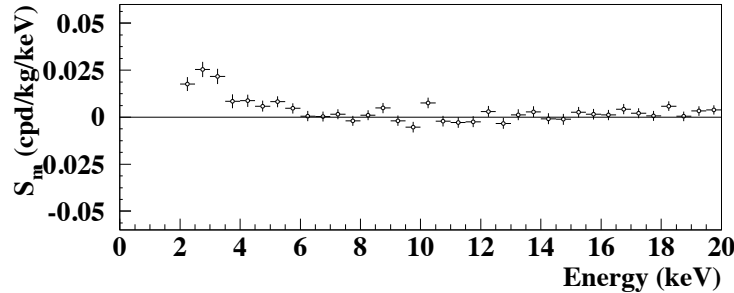


Figure 3.16: Modulation amplitude as a function of energy in the DAMA/LIBRA results. No modulation is observed above 6 keV, consistent with expectation for a WIMP signal. Figure from [89].

limits (see Figure 3.11). Attempts to ease the tension either explain away positive signals as modulating backgrounds [91, 92] or modify expected dark matter interactions to be consistent with the results from different technologies [63, 93]. Modulating backgrounds proposed to explain the DAMA signal have included, among others, seasonal variation in: ambient temperature, muon flux, spallation neutrons from muons in the surrounding rock, scintillator phosphorescence, potassium X-rays, solar neutrinos, and effectiveness of PMT noise cut. DAMA has rebuked many of these proposals, and their rebuttals, in turn, have been debated (see for instance [53, 91, 94]).

The muon background has often been proposed as the source of the DAMA signal because it is known to modulate. Muon production is dependent upon the temperature in the atmosphere, as described in §7.1.1, so the Northern Hemisphere muon flux modulates with a maximum in late June, as measured at LNGS by the Borexino experiment [95]. This puts the modulation out of phase to roughly 3σ [92], and its measured amplitude at LNGS is smaller than the DAMA modulation. Recent proposals have sought a muon-induced modulation in line with the DAMA signal through additional conditions. A second modulating background can combine with the muon background to produce a modulation whose phase is dependent on the relative amplitudes of the components, easing the discrepancies of both phase and amplitude [96]. Such a second modulation has yet to be successfully discovered [97]. The amplitude disagreement may be remedied if muons induce low energy cascades, known as afterglow or phosphorescence, which would amplify the signal. As shown in §4.2.4, there is not much known about long-lived phosphorescent states in NaI(Tl). Muons deposit enough energy in the DAMA crystals – unaccounted for by other output channels – to produce a significant long-lived phosphorescence, and only a small fraction of the deposited energy would be required to produce a significant number of long-lived signals [92]. The proposed effect also diverges from previous attempts to link the DAMA signal to the atmospheric muon modulation by removing the neutron as the moderator of the interaction. The delayed muon emission hypothesis is challenged by Borexino, which has measured the

average muon modulation phase to be June 28th ± 6 days and hence follow, rather than lead, the phase of the DAMA signal [95]. It should be noted that the imperfect sine functional form of the muon modulation leads to increased error in phase measurements. The only consensus to date is that DAMA has been comprised of incredibly clean, calibrated experiments that see a modulation that has yet to be accounted for by a conventional background.

3.5.2 NaIAD

The NaI Advanced Detector (NaIAD) experiment was a NaI(Tl) dark matter experiment that ran in the Boulby laboratory (2850 m.w.e.) from 2000 - 2003. It included the two crystals that make up the DM-Ice17 detector (see Chapter 5). An set of anomalously fast background events were observed that was ultimately determined to be due to implanted surface contamination [98,99]. This was verified by a study of the DM70-Saclay crystal, which emitted anomalously fast pulses until 2002, when it was unencapsulated, polished, and reintegrated to the detector. Running again from 2002-2003, this crystal no longer emitted fast pulses [73].

The NaIAD detector was comprised of seven NaI(Tl) crystals for a total mass of 55 kg. Two crystals were encapsulated, and the remaining five were unencapsulated. Each crystal was kept in a sealed copper box flushed with nitrogen to protect it from radon and humidity in the atmosphere, as shown in Figure 3.17 [100]. Daily calibration data was taken with a 2 hr exposure to a ⁶⁰Co source [73]. One crystal was removed from the final dataset due to its small mass (4 kg) and large background in the region of interest (15 dru), leaving a total active mass of 51 kg for a total exposure of 44.9 kg·yr [73]. Pulse shape discrimination was used to distinguish electronic and nuclear recoils, although the experiment was not able to distinguish between them below 4 keV, limiting its power to make a statement on the DAMA signal [73]. No WIMP-consistent nuclear recoils were observed in the 4-10 keV region, as shown in Figure 3.18.

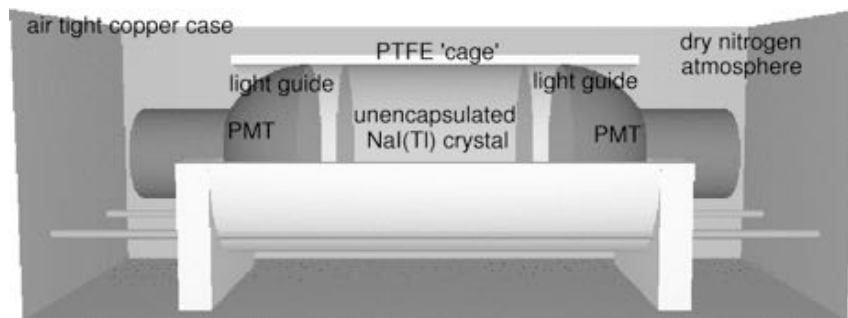


Figure 3.17: Schematic of a single NaIAD crystal module. Crystals were housed in sealed copper boxes flushed with nitrogen to protect them from water and radon in the air. A total of seven crystals were run. Figure from [100].

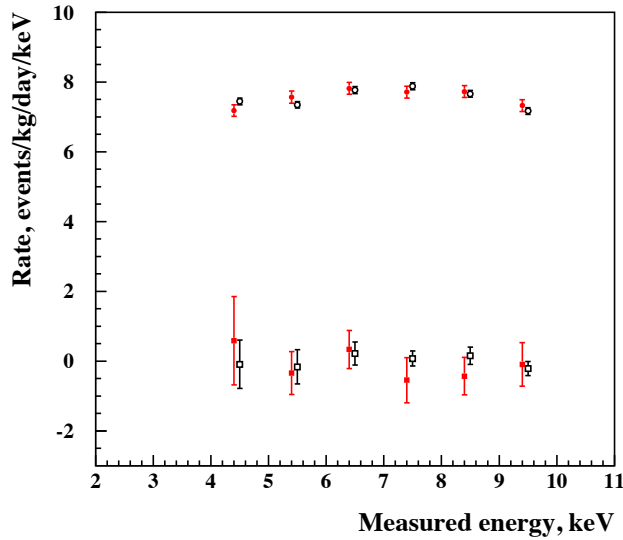


Figure 3.18: Spectrum in the region of interest from the NaIAD experiment [73]. Data shown is from two runs with the DM74 crystal. Total background rates are shown along with the nuclear recoil rate with 90% C.L. error bars. The 1 keV-wide data points are offset to for increased visibility. Figure from [73].

3.5.3 ANAIS

The Annual Modulation with NaI(Tl) Scintillators (ANAIS) experiment is a NaI(Tl) detector at the Laboratorio Subterráneo de Canfranc (LSC, 2450 m.w.e.) designed to test the DAMA results. The detectors are designed in four planned phases, with the first two phases complete and the third phase currently running:

- **ANAIS-0:** ANAIS-0 ran with one 9.6 kg ($4'' \times 4'' \times 10''$) crystal from September 2011 - December 2012 for background studies and the development of filtering algorithms (Figure 3.19, left) [81].
- **ANAIS-25:** ran with two 12.5 kg ($4.75'' \varnothing \times 11.75''$) crystals (Figure 3.19, second from left). It ran from December 2012 - March 2015 for performance and backgrounds studies. Improved light collection allowed more precise contamination level measurements (Figure 3.19, middle) [82].
- **ANAIS-37:** ANAIS-37 is running with both ANAIS-25 crystals and an additional 12.5 kg crystal (Figure 3.19, second from right) [83]. Running began in March 2015, and data has yet to be released. Improved purification and growing techniques of the new crystal are expected to lower contamination levels.
- **ANAIS-250:** ANAIS-250 will be divided into 20 modules for a total mass of 250 kg (Figure 3.19, right).

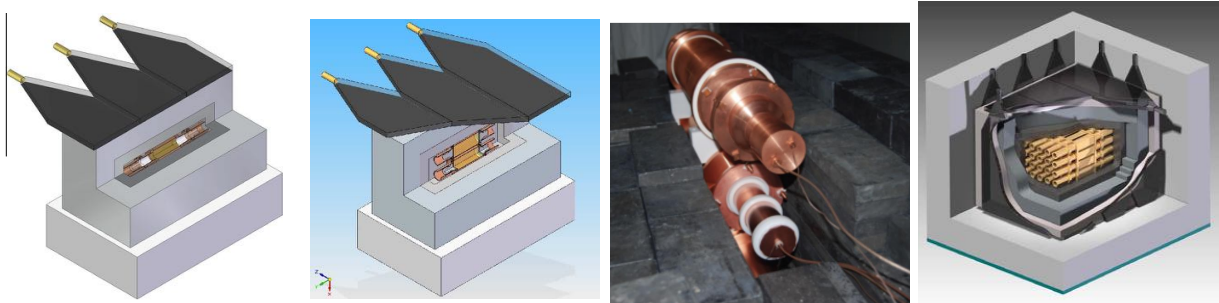


Figure 3.19: Experimental setup of all four phases of the ANAIS experiment, from left: ANAIS-0, ANAIS-25, ANAIS-37, and ANAIS-250. Figures from [81–83].

The ANAIS-0 and ANAIS-25 detectors have shown encouraging results. A study of the uranium and thorium chain contamination was performed through alpha analysis, while the potassium contamination studies were done by looking for coincidence between 3 keV and 1460 keV events in neighboring crystals. Three cuts were made on the ANAIS-25 analysis data: rejection of events with anomalous baselines estimates, multiple-hit events, and rejection of events with fewer than 5 (3) peaks in Detector-0 (1) [82]. Low contamination levels were achieved, as shown in the energy spectrum near the region of interest is shown in Figure 3.20. While crystal R&D continues, the background levels in ANAIS-25 are low enough to perform a successful dark matter search if required. DM-Ice is working with ANAIS, KIMS (see §3.5.4) and the Alpha Spectra crystal company to continue improvement in NaI(Tl) backgrounds (see Table 3.2). See §4.2.4 for a discussion on the ANAIS phosphorescence results.

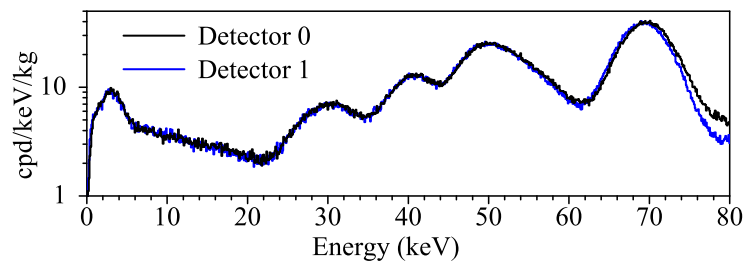


Figure 3.20: Low energy region of the ANAIS-25 spectra from both 12.5 kg NaI(Tl) detectors. Improved purification and growing techniques have lowered background levels, and good agreement is shown in the light response between the detectors. Figure from [82].

3.5.4 KIMS

The Korean Invisible Matter Search (KIMS) is a combined CsI(Tl) and NaI(Tl) dark matter experiment located in the Yangyang Underground Laboratory (Y2L, 2400 m.w.e.). The CsI(Tl)-only phase ran with a 3×4 ($8 \times 8 \times 30$ cm³) crystal array for a total of 103.4 kg. The crystals contain ¹³³Cs and ¹²⁷I and are sensitive to both spin-independent and spin-dependent interactions. Pulse shape discrimination provides separation of electronic and nuclear recoils. The array is housed within layers of shielding, from the inside out: 10 cm copper; 5 cm polyethylene; 15 cm lead; 30 cm liquid scintillator mineral oil [101]. The trigger condition requires a $2 \mu\text{s}$ coincidence between the PMTs on a crystal to minimize noise, and a 50 ms deadtime is imposed after muon events. Results from a 67.19 kg·yr exposure of this detector placed a 0.0098 dru 90% C. L. upper limit on the nuclear recoil rate in the 3.6-5.8 keV region (corresponding to the 2-4 keV region in DAMA). This result rejects the iodine recoil channel of the DAMA signal, as shown in Figure 3.21 [101].

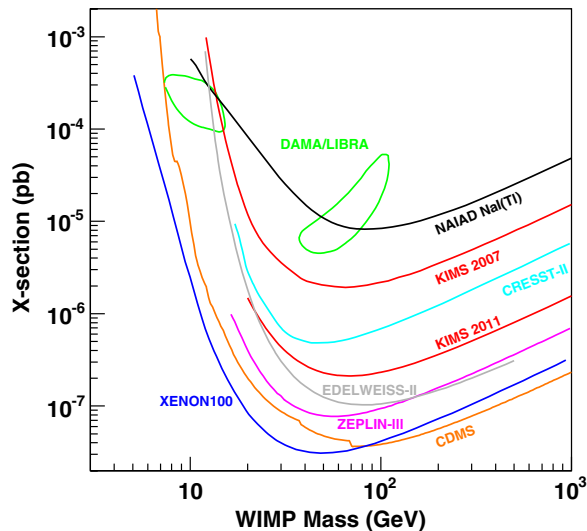


Figure 3.21: CsI(Tl) results from KIMS rejected the iodine recoil source of the DAMA modulation. Figure from [101].

The development of a KIMS NaI(Tl) effort has opened the possibility of commenting on the Na recoil channel of the DAMA signal. KIMS is part of the combined crystal development effort, the results of which are shown in Table 3.2. The NaI(Tl) effort has observed a large light yield of 15 photoelectrons/keV, and contamination developments continue to yield cleaner crystals [84]. The current KIMS NaI(Tl) crystals have achieved backgrounds of roughly 3 dru and a threshold below 2 keV, as shown in Figure 3.22. See §4.2.4 for a discussion on the KIMS phosphorescence results.

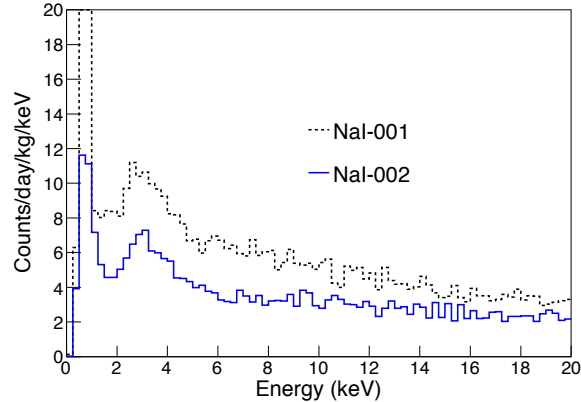


Figure 3.22: KIMS NaI(Tl) spectrum, with low contamination levels (~ 3 dru) and a threshold below 2 keV. Figure from [84].

3.5.5 SABRE

The Sodium iodide with Active Background Rejection Experiment (SABRE) is a NaI(Tl) development project focusing on the growth of NaI(Tl) crystals with low ^{40}K contamination and the design of a well-shielded experiment. The first phase of the project will minimize the ^{40}K concentration in NaI(Tl) crystals through purity improvements to the powder and improved growing techniques, and the second phase will work towards a dark matter measurement. The experiment will consist of a 10 kg NaI(Tl) crystal in a 2 ton liquid scintillator tank that will efficiently veto background events. The experiment has proposed to run inside the DarkSide50 LAr tank at LNGS (3400 m.w.e.), as shown in Figure 3.23 [102]. The DarkSide50 setup allows for crystal insertion next to the cryostat (white cylinder in Figure 3.23), placing the detector within the spherical liquid scintillator tank (4 m diameter). This tank is nested within a 11 m \times 10 m water shield, and PMTs line the outside of both the veto tank and the water shield. Progress made in powder purification is promising, with SABRE powder achieving an order of magnitude less ^{40}K than that of DAMA, as shown in Table 3.2. As the only experiment proposing insertion into a liquid scintillator veto, SABRE will provide a nice complement to the other NaI(Tl) dark matter searches.

3.6 Future of Direct Detection

The next generation of direct detection experiments will be larger, quieter detectors with the potential to verify the positive signals observed by the current generation. The noble liquid detectors will continue to grow in size, with XENON 1T [103], Panda-X [104], LZ [105] and DarkSide [106] preparing dual-phase tonne-scale experiments. The CoGeNT experiment will upgrade to become CoGeNT-4 (C-4), comprised of

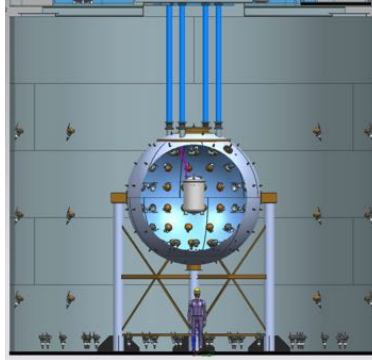


Figure 3.23: Potential location of the SABRE detector within the DarkSide50 liquid scintillator veto [102]. The SABRE detector would be housed in the 4 m liquid Ar sphere at LNGS, outside of the cryostat (white cylinder). The entire setup is housed in a 11 m \times 10 m water tank. Figure from [102].

four larger, cleaner Ge crystals with new multi-crystal analysis capabilities [107]. SuperCDMS will move from Soudan to SNOLAB, increasing both its overburden and the size of its detector from 9 kg Ge to 98 kg Ge and 12 kg Si, allowing further investigation into the Si signal of CDMS-II [108]. The CRESST and EDELWEISS collaborations are combining their expertise to design the European Underground Rare Event Calorimeter Array (EURECA), a multi-target tonne-scale cryogenic experiment [109]. COUPP has upgraded from 4 kg to 60 kg of CF_3I , expecting to set stringent limits in both spin-dependent and spin-independent dark matter searches with three years of data [110]. The COUPP and PICASSO [111] collaborations have merged to run PICO-2L, a C_3F_8 bubble chamber currently in its initial 2L size, and they plan to upgrade to a 250 L detector [112].

A better understanding of the high significance DAMA result (see §3.5.1) will emerge from the NaI(Tl) efforts underway. These experiments may discover a new systematic modulating background or a dark matter-like signal, providing valuable information in either scenario. The combination of four detectors (DM-Ice, ANAIS, KIMS, SABRE) will complement one another to produce a definitive result. With DM-Ice operating in the Southern hemisphere and SABRE operating within a liquid scintillator, a cooperative data comparison will be particularly effective.

Chapter 4

NaI(Tl) Scintillation Mechanisms

4.1 Inorganic Scintillators

Inorganic scintillators are used in particle physics experiments because of their relatively linear energy response and fast decay times. The energy deposited by incident particles produces scintillation light from the de-excitation of electrons and excitons within the target's electronic band structure, as shown in Figure 4.1. Electrons in the valence band are bound at lattice sites, while electrons in the conduction band are free to migrate about the crystal. Electrons can be excited to the conduction band when energy is deposited in the crystal, leaving holes in the valence band. The band gap fills the energy difference between the top of the valence band and the bottom of the conduction band, equal to the energy required to free an outer shell electron in the target material; there are no electrons in the band gap of a pure, undoped crystal. Doping agents are added to scintillators to encourage radiative decay within a desired wavelength range. In an undoped crystal, the de-excitation of the electron back to the valence band with the emission of a photon is an inefficient process; in addition, the emitted photon is likely to be reabsorbed by the crystal [113]. The addition of the doping agent introduces electronic energy levels (“activation centers”) in the band gap, as shown in Figure 4.1. The electron-hole pairs recombine at these activation centers, exciting it and leading to the scintillation photon upon its decay to ground. In the case of DM-Ice, sodium iodide (NaI) is doped with a $\sim 10^{-3}$ mole fraction of thallium (Tl) for this purpose (see §4.2).

Light emission is the product of a series of processes, shown in Figure 4.2: first, the crystal absorbs ionizing radiation, releasing primary electrons, holes and photons. In the event of a neutral particle interaction, the target nucleus is excited and leads to atomic excitation upon its de-excitation. The interactions of the primaries in the material leads to the production of secondary electrons, holes and photons, which interact and lose energy until the electron-hole pairs have the energy of the band gap. The energy of the electron-hole pairs is then transferred to the activation centers, which emit the scintillation light. It has been experimentally verified that the activator site, rather than the host lattice, is primarily responsible for the scintillation. Inorganic scintillator emissions match the emissions of the activator ions [115], and photon

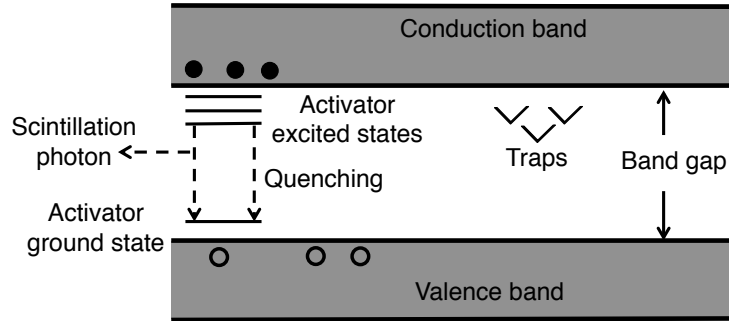


Figure 4.1: Inorganic scintillator crystal band structure. Deposited energy excites electrons from the valence to the conduction band, leaving holes in the valence band. Doping agents are added to the pure crystals to create activator centers, which have multiple levels in the band gap. The electron-hole pair will recombine at an activation center and excite it. The center will then decay down to ground, releasing the scintillation photon characteristic of the detector material [114].

emission from pure alkali halide scintillators is known to be very weak, although it does exist and is described in §4.1.4.1 [115, 116]. NaI(Tl) detectors are specifically addressed in §4.2.

4.1.1 Primary Ionization

The scintillation mechanism begins with the absorption of energy from the incident particle. This process varies by incident particle type. Photons interact via the photoelectric effect, Compton scattering, or pair production, while charged particles deposit energy by scattering off of atomic electrons (and, to a lesser extent, nuclei). In each of these interactions, the incident particles excite and ionize the target atoms. By contrast, neutral particles excite the target atomic nucleus through scattering and absorption, and the nucleus induces the ionization of the atom during its de-excitation. Neutral particle interactions produce photons or charged particles, and the scintillation mechanism follows that of other incident particle types from that point.

Photon interaction probabilities depend on the energy of the incident particle. At low energies (≤ 100 keV), the photoelectric effect is the dominant interaction. An incoming photon of energy E_γ interacting with an electron of binding energy E_b will eject an electron with energy $E_e = E_\gamma - E_b$. When the photon energy falls below the binding energy of a particular shell, the change in the detector response is observable in the light response of the scintillator (see §4.2). At higher energies (100 keV - 5 MeV), Compton scattering becomes the dominant interaction. It yields a photon of energy $E'_\gamma = \frac{E_\gamma}{1 + (E_\gamma/m_e c^2)(1 - \cos \theta)}$ and an electron of energy $E_e = E_\gamma - E'_\gamma$ for scattering angle θ . Pair production can occur above the energy threshold of the interaction, equal to 1.02 MeV ($2m_e$). At the highest energies (> 5 MeV), pair production is the most likely interaction.

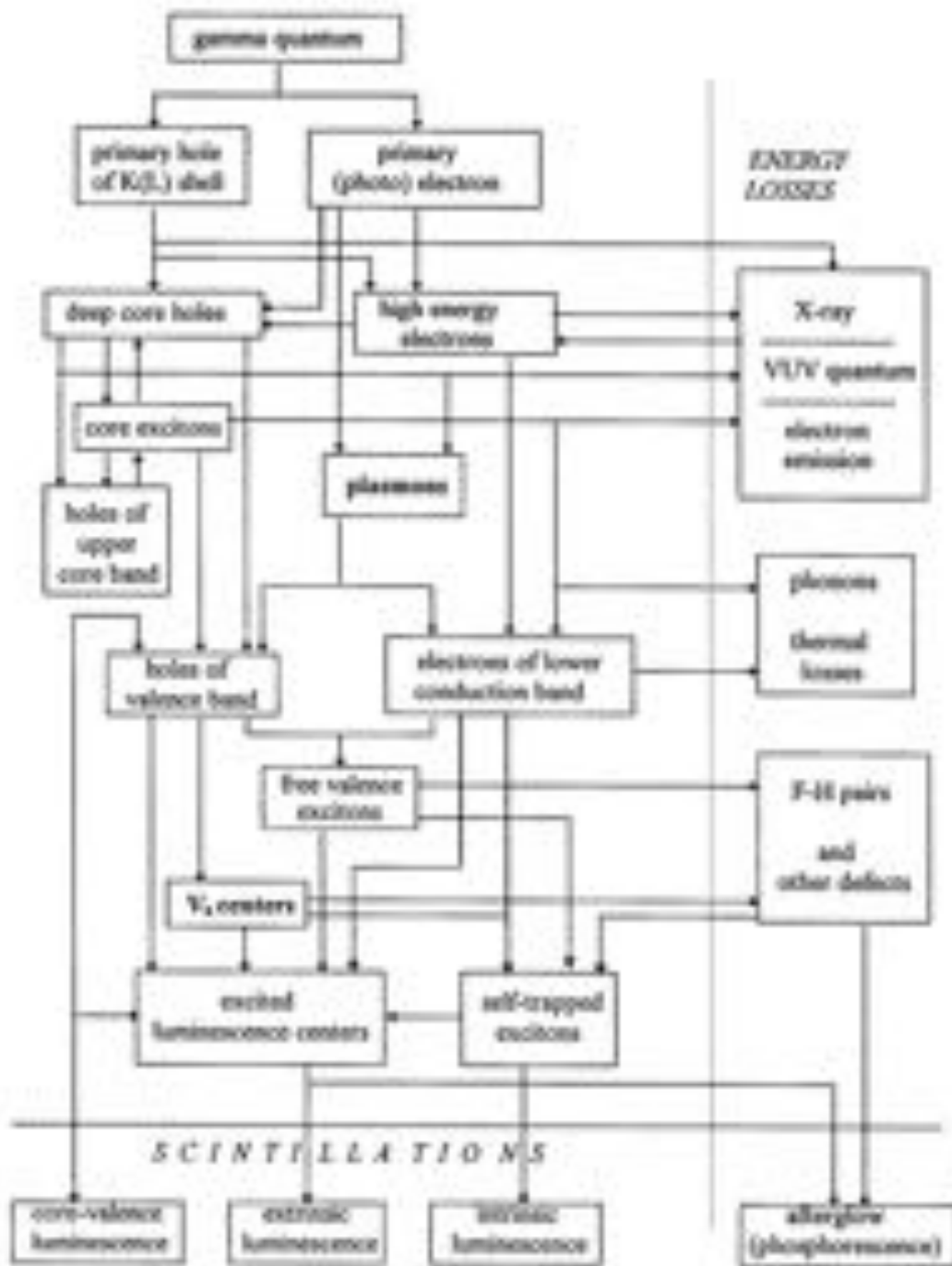


Figure 4.2: Processes in inorganic scintillators following ionizing radiation. Figure from [115].

For each of these processes, nearly all of the photon's energy is absorbed by the crystal. In the photoelectric effect, that energy which is not imparted into the electron (i.e., the binding energy of the shell) is emitted as an X-ray or Auger electron when electrons from the outer shells fall into the newly-formed vacancy. In Compton scattering, secondary photon interactions lead the regaining of most of the imparted energy as the photon is absorbed. In pair production, all of the photon's energy is imparted to the pair.

Charged particle processes depend on the nature of the incident particle. Energy loss, $\frac{dE}{dx}$, is given by the Bethe-Bloche equation (Equation 4.1), and nuclear scattering interactions are expressed by the Rutherford equation:

$$-\left\langle \frac{dE}{dx} \right\rangle = Kz^2 \frac{Z}{A} \frac{1}{\beta^2} \left[\frac{1}{2} \ln \frac{2m_e c^2 \beta^2 \gamma^2 T_{max}}{I^2} - \beta^2 - \frac{\delta(\beta\gamma)}{2} \right] \quad (4.1)$$

where $K = 4\pi N_A r_e^2 m_e c^2$; z is the charge of the incident particle; Z and A are the atomic number and mass of the target, respectively; $\beta = \frac{v}{c}$; m_e is the electron mass; γ is the Lorentz factor; T_{max} is the maximum kinetic energy that can be imparted to a free electron in a collision; $\delta(\beta\gamma)$ is the density effect correction [1]. At high energies, electrons will interact via bremsstrahlung as well, with radiative losses dominating above 10s of MeV [1, 117]. The ionization power of heavy charged particles is equal to the power of electrons of the same velocity times the square of the charge (given by the z^2 term in Equation 4.1) and mass (given by the T_{max} term in Equation 4.1), leading to a nearly completely ionized track for heavy charged particles. Energy loss density increases with charge and mass, while light output decreases correspondingly due to quenching (see §4.1.3.1).

Neutral particles do not directly ionize the scintillator. They transfer energy to a target atomic nucleus through nuclear scattering and absorption, and the nucleus produces the ionization [114, 117]. Below 10 MeV, nuclear scattering is primarily elastic and is a roughly constant function of target atomic mass, A : $\sigma_n = 4\pi(1.4 \times 10^{-13} A^{1/3})^2$. For a discussion on the nuclear quenching factor, see §4.1.3.1.

Further examination of an incoming photon illustrates how primary electrons are ejected: an incoming photon ($h\nu$) will create a hole in an inner shell (usually the K-shell) of an atom and free an electron. The ionization of some atom, A , in a solid may be represented as the absorption of the photon and emission of a free electron:



In the case of an arbitrary shell interaction, the electron will be ejected with an energy of $E_e = h\nu - E_i$, where E_i is the binding energy of the shell level. When a binding-shell energy threshold is crossed, the number and energies of electrons produced shifts with respect to the other side of the threshold; gammas of energy less than E_K can only excite electrons in the L- and M- shells (see §4.2).

4.1.2 Charge Migration and Thermalization

The relaxation of the atom with a hole in the inner shell, A^+ , leads to a cascade of radiative and non-radiative transitions on a $10^{-15} - 10^{-13}$ s timescale, depending on the energy of the initial interaction [115]. The cascade begins when the incident particle has ionized an atom, and the atom can relax radiatively (with the emission of a photon) or non-radiatively (with the generation of a second electron in Auger electron production). Ionizing radiation will generally produce a hole in the inner (K-shell) of the atom and an energetic electron. The L→K-shell transition includes the ejection of an M (or L)-shell electron to the conduction band with a kinetic energy of $E_K - (E_L + E_M)$, or an X-ray that can be absorbed and produce new electronic excitation. A cascade of electron-hole pairs is produced as the secondary X-ray photons and electrons propagate; secondary photons can be absorbed by other atoms to yield new holes and free electrons, and secondary electrons will lead to more ionization: $A + e^- \rightarrow A^+ + 2e^-$. The ionization cascade continues until the electron-hole pairs fall below the ionization threshold, E_t , and cannot cause further ionization:

$$E_t = \frac{9E_g}{7 - \frac{m_e}{m_h}} \quad (4.3)$$

In ionic crystals, $m_h \gg m_e$, leading to $E_t = \frac{9E_g}{7}$. After ionization, the incident, primary, and secondary electrons are indistinguishable.

Small energy losses in the electron-electron relaxation stage arise from the escape of secondary electrons and the creation of F- and H-centers, shown in Figure 4.3 [115] (see §4.1.2.1). F-centers are anion vacancies that capture electrons; these deep traps are stable electronic defects that remove the electron from the scintillation process. Similarly, H-centers (or V_k centers) occur when a hole is shared between two neighboring anions into an X_2^- molecule (e.g., I_2^- in NaI(Tl)). In this discussion, H-centers and V_k centers will be treated the same; the nuances of their differences will be neglected.

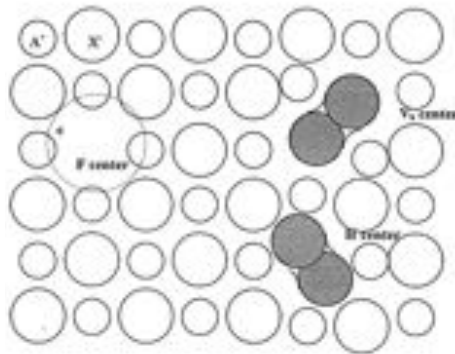


Figure 4.3: Atomic organization in inorganic scintillators. F- and H-centers are lattice vacancies that trap charge carriers, removing them from the scintillation process. Figure from [115].

After electron-electron thermalization, the electron-hole pairs thermalize in the electron-phonon stage. During this time, electrons move to the bottom of the conduction band, and holes move to the top of the valence band until the electron-hole energies are equal to the band gap energy of the crystal, as shown in Figure 4.4. The total number of electron-hole pairs, N_{eh} , remains constant during this stage. It is proportional to the amount of energy absorbed by the crystal, E_γ , and the average energy required to create a single electron-hole pair, ξ_{eh} : $N_{eh} = \frac{E_\gamma}{\xi_{eh}}$. Production energy in ionic crystals is proportional to the band gap energy, E_g : $\xi_{eh} \sim (1.5 - 2.0)E_g$ [115].

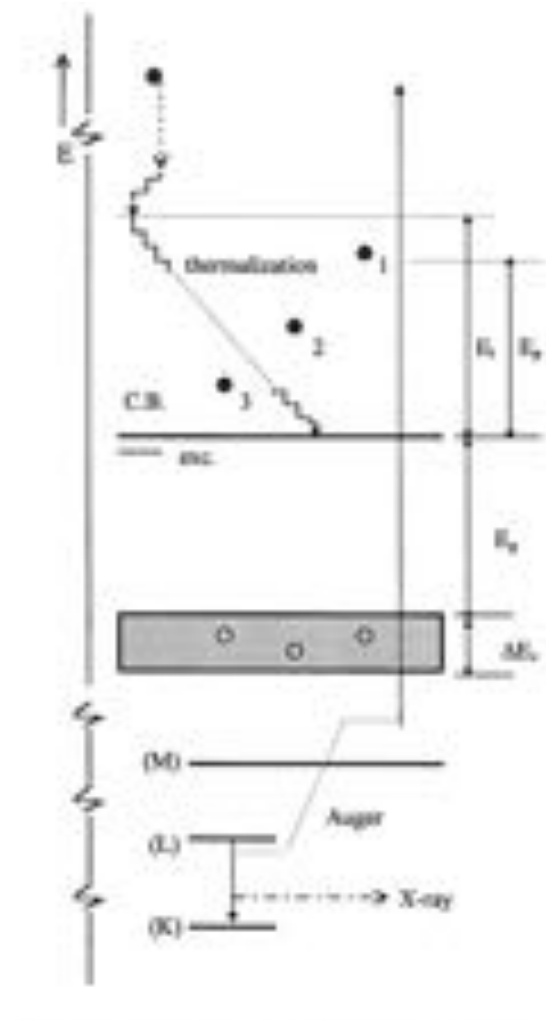


Figure 4.4: Inorganic scintillator scintillation process. Primary ionization is converted to a cascade of electron-hole pairs that thermalize until their energy is equal to the band gap energy. They can then interact with the activator center to produce luminescence [115].

The time and length of phonon relaxation depends on how much energy the electron needs to lose before reaching the top of the conducting band; a constant energy distribution between the bottom of the conduction band and the ionization threshold is assumed. The entire thermalization stage occurs over 10^{-12} - 10^{-11} s, during which time the pairs migrate over a characteristic length of 10^2 - 10^3 nm [115]. Scattering centers, both intrinsic to the crystal and introduced by impurity defects, limit migration. The scattering cross-section of point defects is the geometrical cross-section for neutral defects and the Rutherford cross-section for charged defects [115]. This stage is the highest source of energy loss, with phonon emission releasing over 30% of the absorbed energy. When the electron's energy falls below the phonon energy, it becomes a thermal carrier and can be captured at a luminescence center or a trap.

4.1.2.1 Self-Trapping

Self-trapping during the electron-phonon relaxation stage introduces more complexity to the scintillation process and induces a potential loss mechanism (see §4.1.6). Self-trapping occurs when a hole is shared between two neighboring anions, forming an X_2^- molecule (i.e., V_k center). The formation process requires a hole to reach the top of the valence band and localize at an ion ($X^- \rightarrow X^0$), which polarizes the environment. Axial relaxation leads a neighboring ion to share the hole, creating a self-trapped hole (STH). STHs form within 10^{-12} - 10^{-11} s, which is smaller than the electron lifetime in the conduction band, so most holes get trapped in V_k centers in a pure crystal [115]. They are formed during irradiation and vanish after emission (see §4.1.4.1). Hole self-trapping competes with activator center interactions in doped crystals, introducing a loss mechanism and a channel for scintillation of a different timescale than traditional fluorescence. Above the delocalization temperature (58 K in NaI(Tl)), V_k centers move through the crystal by jumping between neighbor sites, and they can jump to an activator center and participate in scintillation [115,118]. Thermally-induced V_k center motion is controlled by the diffusion coefficient (D_0) and the mobility (μ):

$$\frac{D_0}{\mu} = \frac{k_B T}{e} \quad (4.4)$$

The long lifetime of X_2^- allows significant motion. In addition to X_2^- motion, a hole can release from a V_k center, run across a number of lattice sites as a valence band hole, and fall into another potential well to form another V_k center.

Self-trapped excitons (STEs) are formed when a V_k center captures an electron. Axial relaxation affects valence excitons, forming $(I_2^+)^*$ molecules. Luminescence from these self-trapped holes and excitons is described in §4.1.4.1.

4.1.3 Extrinsic Luminescence: Activation Centers

Scintillation characteristics are determined by the interactions in the activation centers. The activation center is excited through the capture of an electron and hole, capture of an exciton, or impact excitation by an energetic (“hot”) electron. The electron is more mobile than the hole, and will generally recombine first. Exciton excitation is less common. Hot electron excitation requires a large doping agent concentration: the average hot electron interacts every 10^{-15} - 10^{-14} s, which corresponds to a travel distance of 1 - 10 nm between scatters [115]. Energy losses in this stage are dependent on the spatial distribution of electrons and holes in relation to the activator centers: if both electrons and holes are adjacent to the activator ion, recombination is effective. If they are further from the activator, the electron and/or hole may be captured by a trap, as described in §4.1.2.1 and §4.1.6. The charge carriers may also be captured in shallow traps that will allow thermal release and eventual recombination on a longer timescale, as discussed in §4.2.4.

Excitation occurs first from the minimum of the ground band to the excited band, as shown in Figures 4.1 and 4.5. The absorption transition, designated as AC in Figure 4.5, allows the excitation from the ground state (aAa') to the excited state (bBb'). The $(Tl^{+})^*$ decays down to the minimum of the excited band (CB), then down to ground with a photon emission (BD), then to the minimum of ground (DA). Quenching occurs when the curves are close (FF₁).

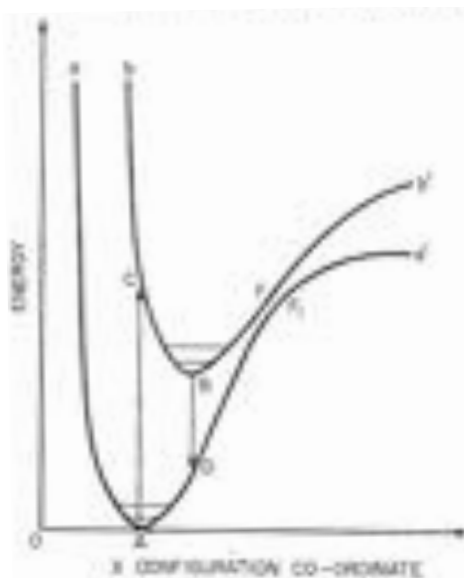


Figure 4.5: Configuration of luminescent center. Designated are the ground state, aAa'; the excited state, bBb'; absorption transition, AC; luminescent transition, BD; internal quenching, FF₁. Figure from [117].

The duration of the scintillation pulse is a function of the rise (τ_R) and decay (τ) times. For an interaction producing N_{eh} electron-hole pairs, the scintillation pulse, $J(t)$, is expressed as [115]:

$$J(t) = \frac{N_{eh}}{\tau - \tau_R} \left[e^{-t/\tau} - e^{-t/\tau_R} \right] \quad (4.5)$$

For multiple decays, each of which produce $N_{\gamma i}$ photons and have a characteristic decay time of τ_i , Equation 4.5 is expanded to include the sum of all decay components of the form $\frac{N_{\gamma i}}{\tau_i} e^{-t/\tau_i}$. A discussion of decay time in NaI(Tl) is provided in §4.2.

The absolute scintillation yield, N_γ , is fundamentally the product of the number of photons per electron-hole pair (α) and the number of electron-hole pairs: $N_\gamma = \alpha N_{eh}$. It can be described in more detailed terms as a function of the linear electron density ($\rho(x)$), which runs over all electron tracks in the scintillation event:

$$\rho(x) = \frac{1}{\xi_{eh}} \cdot \frac{dE}{dE/dx} \quad (4.6)$$

$$N_\gamma = \int_{track} \alpha(\rho) \cdot \rho(x) dx \quad (4.7)$$

The number of photons per electron-hole pair can be expressed in terms of T , the transport efficiency of the pair energy to the activator center, and q , the quantum efficiency of the activator center: $N_\gamma = TqN_{eh}$. The quantum efficiency, q , is defined as the relative probability of a radiative transition: $p_r/(p_r + p_{nr})$. In the absence of quenching, $q \rightarrow 1$ and $T \simeq \alpha$. Quantum efficiency is measured by direct activator photoluminescence. Transport efficiency, which represents migration losses, is more difficult to measure.

The quality of scintillation output is quantified through scintillation yield (i.e., number of emitted photons per energy input) and efficiency (i.e., energy output per energy input). Experimental efforts aim to maximize both yield and efficiency. If N_γ photons are emitted due to ionizing radiation of energy E_γ , the scintillation yield is quantified as:

$$L_R = \frac{N_\gamma}{E_\gamma} = \frac{\alpha N_{eh}}{E_\gamma} = \frac{\alpha}{\xi_{eh}} = \frac{\alpha}{\beta E_g} \quad (4.8)$$

If the emitted photons have an average energy $\langle h\nu_r \rangle$, the conversion efficiency is:

$$\eta = \frac{\langle h\nu_r \rangle N_\gamma}{E_\gamma} = \frac{\alpha}{\beta} \cdot \frac{\langle h\nu_r \rangle}{E_g} \quad (4.9)$$

The probability of radiative recombination at a luminescence center (activator or V_k) is modeled as a system known as a recombination sphere. This model assumes that all holes are captured by the luminescence center, and all electrons are in the conduction band. Some electrons will enter the recombination sphere, drawn by Coulomb attraction, while others will diffuse out of it, escaping the attractive force. The sphere radius, R_r , is therefore that distance from the hole center where the Coulomb energy equals the electron thermal energy:

$$R_r = \frac{e^2}{4\pi\epsilon_0\epsilon_s k_B T} \quad (4.10)$$

R_r is a product of the material, varying from 3.5 nm (BGO) to 12 nm (RBI) [115]. If the distance between the hole and the electron after relaxation (ΔL_{eh}) is smaller than the recombination sphere radius, radiative recombination will occur. ΔL_{eh} is a product of the thermalization lengths of the electron and holes. If $\Delta L_{eh} > R_r$, the probability of radiative recombination is:

$$P = \frac{R_r}{\Delta L_{eh}} \quad (4.11)$$

due to the possibility of the electron entering the recombination sphere via thermal diffusion. Recombination spheres completely overlap at a center concentration of $\sim 10^8/\text{cm}^3$, corresponding to a maximum light yield in NaI(Tl) at a Tl concentration of $\sim 10^{18}/\text{cm}^3$ (0.015 mol%) [115].

4.1.3.1 Quenching

Quenching reduces the light output of an event due to the high ionization density or nuclear interaction of the incident particle. Ionization density quenching occurs because scintillation light output depends on the number of excited luminescence centers, which itself depends on the positions of charge carriers relative to the luminescence centers and traps, the mean migration length of the carriers, and their energies. The range of maximum efficiency corresponds to the region in which ionization areas begin to overlap (i.e., overlapping recombination spheres) but have not yet saturated the volume. In a low ionization density event, the density of electron-hole pairs along the track is much lower than the number of luminescence centers. The light output in this region increases with energy and ionization density as more pairs are created near the luminescence centers [115]. As ionization density increases, all luminescence centers within the range of the ionization track are excited and the response is saturated, leading to a small decrease in light output with incident energy. This is because an electron captured by a luminescence center can be removed from the center by another fast electron, decreasing the total number of excited centers [115]. High ionization density events observe a significantly quenched response, as shown in Figure 4.6. High ionization density events are associated with alpha and muon events. For instance, in NaI(Tl), 16 MeV electrons have an ionization density of $\frac{dE}{dx} = 0.97 \text{ MeV/cm}$, while 5.15 MeV alphas have $\frac{dE}{dx} = 1280 \text{ MeV/cm}$ [115]. Below the quenching density, $\alpha \propto \rho_{\phi}^{0.2}$, increasing from the added number of carriers involved in recombination at luminescence centers [115]. At an incident flux density of $\rho_{\phi q} \geq 10^{23} \text{ eV/cm}^2\cdot\text{s}$ (corresponding to a pair density of $n_{eh} \simeq 10^{20}/\text{cm}^3$ and a track density of 0.68 pairs/nm), all activator centers are involved in luminescence and photon production efficiency, and $\alpha(\rho_{\phi})$ is at its maximum ($\simeq 1$). As ρ_{ϕ} continues to increase, both the luminescence yield and rise time begin to decrease. All activator centers are occupied, and the remaining pairs cannot contribute to scintillation. Electron-hole pairs are lost to non-radiative recombination, thermalized within a 24 nm radius around the ionization track. The number of photons per electron hole pair in the regime follows $\alpha \propto \frac{1}{\rho_{\phi}}$, and ΔL_{eh} is less than the average distance between activator centers. With activator depletion, V_k

centers can recombine both radiatively and non-radiatively with electrons; the ratio of intrinsic luminescence (see §4.1.4.1) to total luminescence increases monotonically with ρ_ϕ [115]. Pure NaI also observes quenching at high ionization density, possibly due to exciton-exciton collisions destroying the exciton population non-radiatively [115]. Alternative non-radiative decay channels may also become more efficient at high ionization, decreasing light output. One such effect may be radiation shaking, in which elastic strain from F- and H-center pair annihilation induces non-radiative transitions at the luminescence centers [115].

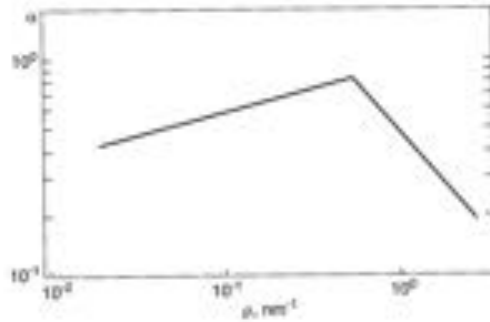


Figure 4.6: Energy transfer efficiency, α , as a function of electron-hole pair density, ρ , in NaI(Tl). Quenching is observed above the critical density, $\rho_\phi = 0.67$ pairs/nm. Figure from [115].

The response of scintillators to nuclear recoils depends on the nuclear quenching factor, which characterizes the difference in light response to nuclear and electronic recoils. For measurements in NaI(Tl), see §4.2.3. Because NaI(Tl) is sensitive only to electronic energy emission, the quenching factor indicates the percentage of energy loss that goes into ionization as the recoiling nucleus collides with electrons and other nuclei [119]. Quenching measurements will be affected if ion channeling – wherein an incoming ion recoils in a direction close to the symmetry plane of the crystal – is a significant effect. During channeling, the ion stays within the open “channels” between rows of lattice atoms and increases the apparent quenching factor. Channeling has not been observed to affect light response, but it is an active area of investigation [120,121].

4.1.4 Competing Processes

Interactions that are not governed by the activation centers compete with the traditional scintillation channels, reducing and altering light output. Intrinsic luminescence produces scintillation in pure NaI and, while significantly less common than Tl-mediated scintillation (<10% of total emitted light), it also occurs in NaI(Tl). Energy losses due to traps, quenching, and phonons are also present, reducing light output. Minimizing the occurrence of these competing processes optimizes fluorescent light output.

4.1.4.1 Intrinsic Luminescence

Intrinsic luminescence occurs without the use of the doping agent; this is the only type of scintillation in a pure, undoped crystal. Intrinsic luminescence arises from self-trapped exciton (STE) interactions. A conduction band electron and a V_k center can form a STE, which decays to a photon:



This luminescence is effective at low temperatures (≤ 100 K), where V_k centers are immovable. At higher temperatures, nonradiative processes dominate, and intrinsic luminescence is severely reduced. Intrinsic luminescence emits in two bands, referred to as the σ and π bands, that differ in polarization with respect to the molecular axis of the STE. The σ (π) band is oriented parallel (perpendicular) to the STE axis. Emission from the σ band occurs on a timescale < 10 ns. By contrast, the π band has a lifetime of $\mu\text{s} - \text{ms}$ [115]. While σ band emission will be read out with the Tl-mediated emission, π band emission will appear as a long-lived emission.

4.1.4.2 Energy Losses

Traps and quenching centers interact with charge carriers to reduce scintillation efficiency. Quenching centers thermally dissipate excitation energy, and traps contain metastable levels in which electrons will either acquire thermal energy to return to the conduction band or decay to the valence band in a radiationless transition (e.g., electron capture). The separation of created electron-hole pairs increases with ionizing radiation energy, thereby increasing the probability of electron capture by traps [115]. Activation and quenching centers are the result of the doping agent, while traps are due to crystal defects [117].

Primary energy losses are due to imperfect quantum efficiency (q), imperfect transfer efficiency to the activator center (T), and thermalization losses. Energy efficiency can be expressed in terms of these components:

$$\eta = \frac{\langle h\nu \rangle}{E_g} \cdot \frac{Tq}{\beta} \quad (4.13)$$

Electron-hole pairs lose energy to phonons during migration. Thermal losses (E_{fl}) in the electron-electron relaxation stage are small. Because $m_h \gg m_e$, the electron gets most of the momentum upon creation, and hole thermalization includes little thermal loss. The electron-hole pair production energy is thus:

$$\xi_{eh} = E_g + \langle E_e \rangle + \langle E_h \rangle + E_{fl} \quad (4.14)$$

$$= 1.8E_g + E_{fl} \quad (4.15)$$

in ionic crystals when losses due to thermalization and phonon generation in the ionization stage are taken into account. When the incident energy is greater than two times the band gap energy ($h\nu > 2E_g$), two electron-hole pairs can be created, so luminescence can be greater than one.

Charge carriers can also migrate to the surface and either recombine at the surface (radiatively or non-radiatively) or leave the surface entirely through electron emission. Taking these surface losses into account, the measured quantum efficiency, $q_e h\nu_i$, can be derived from the quantum efficiency of volume recombination (q_e), the reflection and absorption coefficients (R and k , respectively), and the migration length of charge carriers (L):

$$q_e(h\nu_i) = \frac{1 - R(h\nu_i)}{1 + k(h\nu_i)L} \cdot q_e(h\nu_i) \quad (4.16)$$

This value is experimentally determined and varies by detector and geometry.

4.1.5 Characteristics

Scintillator experiments require stability, large signal transmission, and precise resolution for optimal performance. Inorganic scintillators have optimal temperature ranges for maximized performance, and crystal purity is a driving factor for both signal transparency and detector resolution.

4.1.5.1 Temperature Dependence

Temperature affects scintillation quantum efficiency, charge carrier mobility, and phonon interactions. A linear response function requires a stable light output, where stability is characterized by the relative response temperature coefficient:

$$\alpha_T = \frac{L - L_0}{L_0(T - 300)} , \quad L_0 = L(300 \text{ K}) \quad (4.17)$$

where L is the light response at temperature T , in units of emitted photons/MeV of energy absorbed. This temperature coefficient, which convolves the temperature dependence of the response components, is 0.22 - 0.95%/K in NaI(Tl) [115]. The temperature dependence of the response in NaI(Tl) is shown in Figure 4.7, with a maximum light output around 20°C.

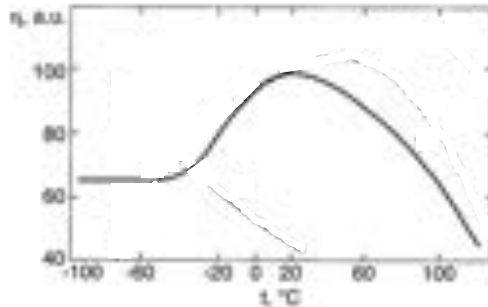


Figure 4.7: Temperature dependence of light response in NaI(Tl) [122]. The inset focuses on the region on interest with respect to dark matter experiment operating conditions [115].

The temperature dependence of the quantum efficiency, derived from direct excitation experiments, can be expressed in terms of a quenching constant (C) and the energy for non-radiative quenching processes to occur (E_q), both of which are experimentally-derived:

$$q(T) = \frac{p_r}{p_r + p_{nr}} = \frac{1}{1 + Ce^{-E_q/k_B T}} \quad (4.18)$$

The probability of radiative decay (p_r) is not temperature dependent, but the probability of non-radiative decay (p_{nr}) is proportional to $e^{-E_q/k_B T}$. At low temperatures ($k_B T \ll E_q$), the probability of radiative decay dominates. Excitonic luminescence (see §4.1.4.1) follows the temperature dependence of quantum efficiency [115]. Doped crystals have an intricate temperature dependence due to the participation of traps complicating the transfer efficiency.

Thermal quenching reduces scintillation intensity and decay time. This quenching occurs because electronic states are sensitive to the positions of nearby ions; both absorption and emission spectra are dependent upon the equilibrium positions and vibrations of these ions. The electron-phonon interaction leads to a separation in the minimum location of the ground and excited states along the so-called Q-axis, which represents the mean distance between the luminescence center and the surrounding ions. This creates a shift between the emission and absorption bands of the center and affects the interaction of the center with vibrational modes known as the Stokes shift [115]. Additional thermal quenching, known as “intercenter” quenching, allows non-radiative decay at the activation center. During intercenter quenching, excited electrons can thermally reach the crossing point, F, shown in Figure 4.5. These thermal quenching events create a large number of phonons. Quenching equations can also describe deep traps from other impurities [115].

4.1.5.2 Transparency

For a photon to be emitted from an inorganic scintillator, it must be optically transmitted. Detector transparency depends on the absorption and scattering processes in the detector. The absorbed scintillation light is given in terms of the absorption coefficient, k [cm^{-1}], and the path length, x :

$$J = J_0 e^{-kx} \quad (4.19)$$

The path length can be greater than the crystal length due to reflections. Emitted light can undergo reabsorption by the crystal or absorption by impurities or defects. Fundamental absorption is due to the properties of the crystal (e.g., band gap energy, activator) and cannot be reduced; it varies between 0.8 - $0.85 E_g$ in ionic crystals [115]. Transmission is determined by the extinction coefficient, defined as the sum of absorption and scattering coefficients. Transmission requires that $h\nu < E_g$, which limits emission efficiency [115]. The maximum light output for an ionic crystal, for $\alpha = 1$ [115]:

$$L_{max} \simeq \frac{0.5 \times 10^6 \text{ photons}}{E_g \text{ MeV}} \quad (4.20)$$

A high energy transmission edge corresponds to the fundamental absorption and exciton creation. Impurity absorption depends on the concentration of impurities and point defects, which is dictated by crystal growth effects [115]. Activator self-absorption and high energy absorption production of intrinsic luminescence are minimized by a large Stokes shift. Bulk light scattering, due to crystal impurities of different indices of refraction, adds to the bulk absorption if the center is greater than 0.1-0.5 μm . Transparency limitations contribute to decreased resolution.

4.1.5.3 Resolution

Energy and time resolution are determined by the physical characteristics of the crystal and the scintillation mechanism. Energy resolution is defined as $R[\%] = \Delta E/E$, where ΔE is the full-width, half-max of the given peak. It is limited by statistical fluctuations of photons from the scintillator. These fluctuations are driven by transfer efficiency, inhomogeneity and nonuniform transmission of the crystal, and non-proportionality of the response. Inhomogeneities in the crystal (i.e., local variations in activator concentrations and imperfections) lead to a difference in the number of photons produced based on the incident location of the ionizing particle. Nonlinearities in the light output are due to the number and energies of produced secondaries, which vary by process (e.g., Compton edge). Additional detector nonlinearities are due to the non-uniformity of the PMT photocathode, variation of PMT quantum efficiency with wavelength, and non-uniform optical coupling. Each of these can be suppressed during construction. Additional uncertainty arises from imperfect reflectivity of the reflector surrounding the crystal.

4.1.6 Defect Production

Ionizing radiation creates damage to the crystal, forming point defects and color centers. Radiation damage is a complex process that involves the crystal as well as any defects or impurities, and the tolerable dose to a detector is referred to a radiation hardness. Damage changes the optical and scintillation properties during and after a large dose, and it can be nonuniform due to inhomogeneous impurity concentrations that develop during the growth process. Degradation in light output has been linked to decreased transmission rather than decreased luminescence following radiation damage [115]. Because a low melting point produces more perfect crystals (see §4.2), radiation hardness improves with better growing techniques. In NaI(Tl), radiation hardness is $\simeq 10^3$ rad, corresponding to a radiation length of $\simeq 2.6$ cm [115].

Hardness is strongly influenced by the V_k center production efficiency, which is a product of the ionic structure and crystal structures. V_k centers distort the crystal lattice and encourage the formation of color centers (see §4.1.6.1). It should be noted that some crystals are observed to recover transmission over time, exhibiting a near perfect recovery after thermal bleaching at high temperatures, or exposure to UV or visible light from minutes to hours at a particular wavelength [115].

4.1.6.1 Production Mechanism

Defect production is observed in ultrasoft X-ray (40 – 300 eV) experiments, which show that quantum efficiency increases with energy until it levels off around 70 eV, implying a nonradiative defect production mechanism or Auger electron emission [115]. The primary method of defect production is imagined in terms of the “knock-on mechanism,” by which an incident particle collides elastically with a lattice atom or ion. The maximum amount of kinetic energy that can be imparted to the lattice ion, T_m , will affect the defect production efficiency. T_m is determined by the energy of the incident particle, E , and the masses of the incident particle and lattice ion, M_1 and M_2 , respectively. It can also be written in terms of the atomic mass number, A , of the ionic atom:

$$T_m = \frac{4M_1M_2E}{(M_1 + M_2)^2} \left(1 + \frac{E}{2M_1c^2} \right) \simeq 2147.7E \left(\frac{E + 1.022}{A} \right) \quad (4.21)$$

To produce a defect, the lattice ion must receive enough energy to displace it from its lattice site to an interstitial site. To do so, the imparted kinetic energy must be greater than the threshold displacement energy of defect creation. If this condition is not met, radiation damage cannot occur from the elastic collision.

Defects are produced in pure crystals as well as in doped crystals, indicating that defect production mechanisms are present in the lattice. Strong self-trapping in ionic crystals leads to strong electron-phonon coupling that induces a local distortion [115]. Defects develop mostly in the anion sub lattice because STHs localize on anions, so the cation sub lattice is more stable against radiation damage. Stable F- and H-center defects form primarily via: $V_k + e \rightarrow (STE)^* \rightarrow F + H$, as shown in Figure 4.8. A neighboring pair of F-H centers is created if the translational motion of a moving STE covers at least half the interatomic distance, separating the the charges enough to form defects [123]. For the defects to stabilize, the separation

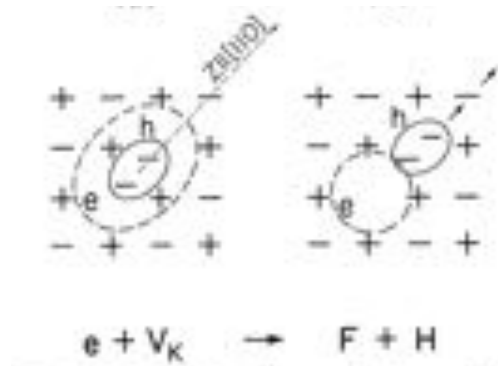


Figure 4.8: Formation of stable defects from STE motion. Figure from [123].

of F- and H-centers must be such that the F-center electron wave function has a negligible overlap with the H-center [123].

Once the unstable F-H pair is created, the H-center moves dynamically. H-center motion is temperature- and crystal structure-dependent and can propagate for up to 10 ms. If the distance between the H- and F-centers is small enough that they are spatially-correlated, recombination is immediate, and no thermal activation is needed. During thermal migration, the H-center completes a number of jumps and rotates to propagate. Following these stages, the H-centers interact with defects and impurities, and stabilize [115]. The efficiency of F-center creation through exciton defect production is dependent upon impurity content and temperature. Some impurities increase the formation rate while other decrease it. At low temperatures (≤ 100 K), H-centers are stable, while above 100 K, the interstitial ion is mobile [115].

4.1.6.2 Production Efficiency

F-H pair formation competes with the other STE decay channels, both radiative and non-radiative (i.e., thermal loss). F-H pair production is most efficient around 300-400 K, below which the thermally-activated processes are not preferred and above which, the H-center can be released from sites and traps and become mobile. At high temperatures, F- and H-centers can recombine, restoring the original crystal configuration [115]. The number of stable F-centers formed (N_F) is proportional to the number of electron-hole pairs created (N_{eh}) and the production efficiency of F- and H-centers per electron-hole pair (η_F). The production efficiency is a product of the number of primary F-H pairs/electron-hole pair (η_F^P), the probability of H-center removal from the F-center area (f_{FH}), and the probability of stabilization of the H-center (f_t) [115]:

$$N_F = N_{eh}\eta_F = N_{eh}\eta_F^P f_{FH} f_t \quad (4.22)$$

The energy required to form a defect is given by the energy of the incident particle (E_γ) and the energy to generate an electron-hole pair (ξ_{eh}):

$$E_{FH}^P = \frac{E_\gamma}{N_{eh}\eta_F^P} = \frac{\xi_{eh}}{\eta_F^P} \quad (4.23)$$

The energy of stable F-H pairs is roughly 100 eV for many alkali halides at room temperature, and it gets larger at low temperatures as H-centers get less mobile [115]. After formation, F-H pair separation is four lattice sites, corresponding to a stable pair configuration with a lifetime of $10^4 - 10^6$ [115].

4.1.6.3 Effects on Scintillation

Defect production is a competing mechanism to scintillation, and the number of produced defects increases with radiation dose. Color centers are formed, in which lattice defects produce absorption bands in the optical transmission spectrum of the crystal and absorb scintillation photons. Traps are produced from

inhomogeneities in the crystal due to chemical or structural defects. They can induce phosphorescence (see §4.2.4) because electrons or holes trapped at inhomogeneities during irradiation can be thermally released and recombine with previously trapped charge partners. Radioactivation is also possible, particularly under irradiation by hadrons, but in most environments this is not a concern because the activated isotopes decay faster than they accumulate [115].

Degradation changes efficiency, the emission spectrum and decay time. Optical transmission, T , can be expressed in terms of the incident (J_0) and transmitted (J) intensities:

$$T = \frac{J}{J_0} \quad (4.24)$$

The attenuation length over thickness d is given by [115]:

$$L_\lambda = \frac{d}{\ln(J_0/J)} = \frac{d}{\ln(1/T)} \quad (4.25)$$

A nonuniform concentration of impurities in the crystal leads to nonuniform radiation damage from traps and color centers. This non-uniformity arises from the growth process, when impurities concentrate near one side of the ingot. The inhomogeneity induces differences in the light output along the length of the crystal after irradiation, even if good uniformity before irradiation was observed [115].

4.2 NaI(Tl) Crystals

Thallium-doped sodium iodide (NaI(Tl)) is used in scintillator dark matter searches (see §3.5) for its combination of a fast time response, relatively linear response, high light output and pulse shape discrimination capabilities. Current work is underway to improve growing techniques (see §4.2.1), optimize light response (see §4.2.2 and §4.2.3), and fully understand exotic interactions (see §4.2.4).

NaI(Tl) is a NaI lattice doped with small amounts of Tl⁺. The Na component is the cation ²³Na ($Z = 11$), and the I component is that anion ¹²⁷I ($Z = 53$). The Tl⁺ component is primarily from two stable states: ²⁰⁵Tl ($Z = 81$, isotopic abundance of 70%), ²⁰³Tl (isotopic abundance of 30%).

4.2.1 Crystal Growth

NaI(Tl) is grown via the Kyropoulos [124] or the Bridgman-Stockbarger [125, 126] method, which are shown in Figure 4.9. The DM-Ice17 crystals were grown using the Bridgman-Stockbarger method [100]. In this process, the crystal seed is placed in the bottom of an ampoule containing the crystal melt, and the temperature gradient in the furnace is carefully controlled to solidify the crystal from the seed outwards [127]. The melting temperature of NaI(Tl) is 661 °C, and the temperature is to direct the melt and control the dynamics of the growth. The crystal in this method experiences very little stress and is free to expand as needed during the process. The crystal is complete once it fills the ampoule, which can lead to adhesion to

the crucible and cracking at times [128]. In the Kyropoulos method, the seed is lowered into the melt, and the crystal grows downwards while being rotated for greater melt homogeneity, considered finished once it has reached the diameter of the holder [127]. While it avoids the cracking risk, this method is less stable than the Bridgman-Stockbarger. In either method, crystals are grown multiple times to remove impurities. As the crystal grows, impurities are pushed downwards. Once completed, the bottom of the crystal is removed, and the top is used as the seed with the new melt [100].

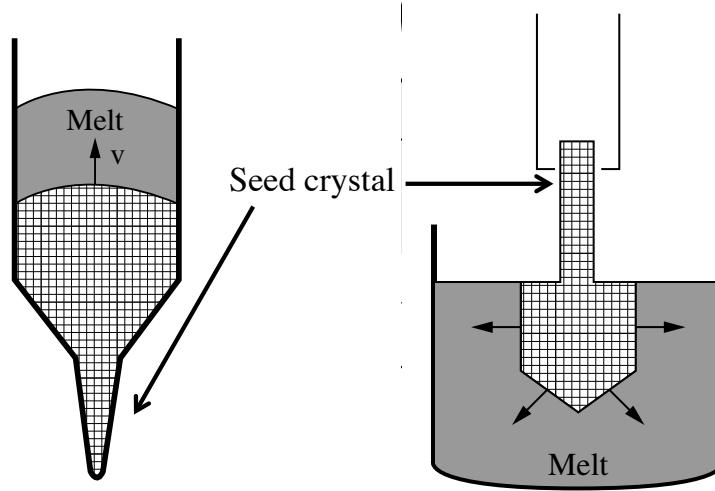


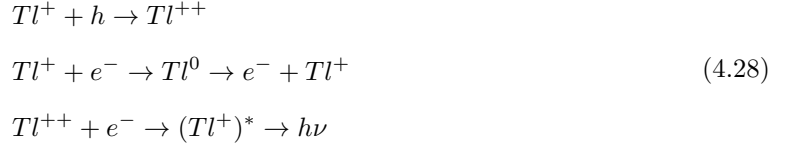
Figure 4.9: Schematics describing the two most common NaI(Tl)-growing techniques - the Bridgman-Stockbarger (left) and Kyropoulos methods (right). DM-Ice17 crystals were grown with the Bridgman-Stockbarger method. Figure from [129].

4.2.2 Scintillation Mechanism

NaI(Tl) activator luminescence occurs through electron-hole recombination, excitonic energy transfer, or hot electron exciton. Each channel is known to occur, with electron-hole recombination strongly dominating. The timescale of each process is explored in §4.2.2.1. In further detail, these luminescence mechanisms are:

- **Electron-hole recombination:** the activator center is excited by consecutive capture of the electron and the hole (Equation 4.26), the hole and the electron (Equation 4.27), or the longer capture and thermal release process (Equation 4.28):





Spectral differences between hole and electron capture (by Tl^0 and Tl^{++} , respectively) are observed at low temperatures but are indistinguishable at room temperature. Low temperature experiments have shown that electrons, being far more mobile than holes, generally reach the activator site first, and hole capture (Equation 4.26) is the dominant recombination mechanism [116, 118, 130].

- **Excitonic energy transfer:** the number of created excitons is only a fraction of the number of created electron-hole pairs. The probability of exciton thermal dissociation increases with temperature, and the lifetime of excitons is smaller than the rise time in NaI(Tl) [115]. During a high energy excitation event, most holes relax to V_k centers or are captured by Tl^+ ions, so the number of created excitons is small. Excitons can be created if a V_k center captures an electron from the conduction band, forming a relaxed exciton, $V_k e$. Excitons transfer energy to the activator centers through reabsorption (radiative) or resonance (non-radiative).
- **Hot electron excitation:** energetic electrons in the cascade may have enough energy to reach the activator state without first creating an electron-hole pair. While electron-hole energy transfer is the dominant scintillation mechanism, inelastic scattering of hot electrons does occur [130].

The Tl^+ decay responsible for scintillation is the $6p^1 6s^1 \rightarrow 6s^2$ transition. Tl^+ has 80 electrons, with two in the outer (sixth) orbital. The ground state electron configuration is 1S_0 , and absorption band measurements illustrate four excitations to each of the lowest excited states, referred to as bands A ($^1S_0 \rightarrow ^3P_1$), B ($^1S_0 \rightarrow ^3P_2$), C ($^1S_0 \rightarrow ^1P_1$), and D (near activator exciton). The absorption bands produce two emission bands visible at low (LHe) temperatures: 330 and 420 nm. The $j=0$ and $j=2$ interactions, corresponding to 3P_0 and 3P_2 , respectively, are forbidden for 1S_0 . The main electronic transition in NaI(Tl) corresponds to the inverse of transition A:



High energy excitation introduces an STE emission at 295 nm as well. Wavelength overlap of the STE and emission and A absorption band allows reabsorption or non-radiative energy transfer, particularly at low temperatures [115]. At room temperature, only the wide 420 nm emission band is observed, corresponding to the main transition. NaI(Tl) is well suited for experimental use because its emission spectrum is compatible with optimal PMT response, as shown in Figure 4.10.

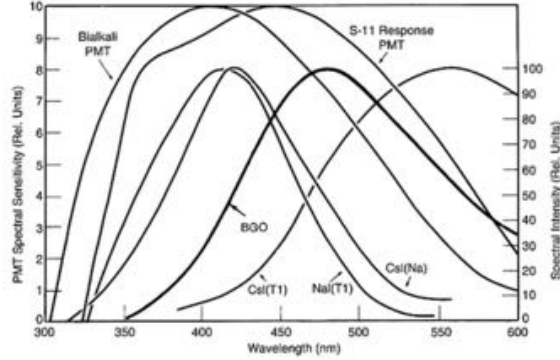


Figure 4.10: The emission band of NaI(Tl), shown in comparison to CsI(Tl), CsI(Na), and PMT response. The NaI(Tl) emission is well-suited for experimental use due to the large overlap in its emission spectrum and optimal PMT response. Figure from [131].

4.2.2.1 Emission Timescale

Recombination processes vary significantly in timescale. The lifetime of $(\text{Tl}^+)^*$, measured to be 220 ± 10 ns, is the timescale generally observed in NaI(Tl) scintillation. Differences in the time required to excite the Tl^+ center lead to decay time shifts [116]. These differences in charge migration time are experimentally determined by observing the Tl^0 (Tl^{++}) absorption band at 620 (312) nm. Electron thermalization and capture occur over 10^{-12} s. Most holes will self-trap, so the hole capture timescale (Equation 4.26) is determined by the timescale of V_k center diffusion. At low temperatures (≤ 100 K), V_k centers are stable, but at higher temperatures, they can diffuse from one site to another and can either recombine with a Tl^0 center or get trapped to form Tl^{++} [115, 116]. The temperature-dependence V_k center capture time is equal to $\tau_h \sim 1$ ns at room temperature. Tl^0 must be stable over this time period for the reaction to occur: $\tau_0 \gg \tau_h$, which has been measured to be true [115, 116, 118].

Electron capture (Equation 4.27) occurs if the hole is created within 25 unit cells (14 \AA) of a Tl^+ ion. In this case, Tl^{++} is promptly formed [116, 130]. This is a non-thermal process and the number of holes trapped by Tl^+ rather than Tl^0 is dependent upon the Tl^+ concentration. In NaI(Tl) with 0.1% molar Tl^+ concentration, 10% of the holes form Tl^{++} centers [116, 132]. For holes created outside of this Tl^+ capture radius, hole trapping is a thermal process.

In the thermal release scenario (Equation 4.28), the timescale is governed by the characteristic time for electrons to be thermally excited from Tl^0 . At room temperature, $\tau_0 \sim 30 - 35 \mu\text{s}$. Tl^{++} is stable over this time [116, 118].

The portion of emission emerging from each recombination process is temperature dependent. Diffusion-limited reactions are modeled using Waite's theory [133], as developed in [116, 118], to determine interaction

rates for each decay channel. The reaction $A+B \rightarrow AB$, where A is diffusing (here, V_k centers) can be described in terms of the diffusion coefficient, $D \simeq e^{E/kT}$ and the capture radius, r_0 [118]:

$$\frac{dA}{dt} = -4\pi r_0 D \left[1 + \frac{r_0}{\sqrt{\pi D t}} \right] AB \quad (4.30)$$

Applying this formulation to V_k centers and thallium ions, the rate of Tl^+ excitation from V_k center trapping on Tl^0 and Tl^+ centers is derived in terms of the number concentrations $V_k(t)$, $Tl^0(t)$, and $Tl^+(t)$. The V_k diffusion constant is $D=1 \times 10^{-5} \text{ cm}^2/\text{s}$ at room temperature, and the capture radius for a V_k center is $r_0 = 58 \text{ \AA}$ at a Tl^0 site, and $r_+ = 14 \text{ \AA}$ on a Tl^+ site. While they are approximated to be zero, alternative interactions are included as well: $G(t)$ describes the loss of V_k centers trapped at non-Tl impurity sites; $H(t)$ describes Tl^+ ions lost to $Tl^+ + e^- \rightarrow Tl^0$; $J(t)$ and $K(t)$ describe Tl^+ production through $Tl^{++} + e^- \rightarrow (Tl^+)^* \rightarrow Tl^+ + h\nu$ and thermal ionization of Tl^0 , respectively. $G(t)$ has been experimentally shown to be a rare process, and $H(t)$, $J(t)$, and $K(t)$ are neglected on the basis of the Tl^0 lifetime being longer than the diffusion timeline [116]. The time evolution of V_k , Tl^+ , and Tl^0 concentrations are thus individually derived:

$$\begin{aligned} \frac{dV_k(t)}{dt} &= -4\pi r_+ D \left[1 + \frac{r_+}{\sqrt{\pi D t}} \right] Tl^+(t)V_k(t) - 4\pi r_0 D \left[1 + \frac{r_0}{\sqrt{\pi D t}} \right] Tl^0(t)V_k(t) - G(t) \\ &= -4\pi r_+ D \left[1 + \frac{r_+}{\sqrt{\pi D t}} \right] Tl^+(t)V_k(t) - 4\pi r_0 D \left[1 + \frac{r_0}{\sqrt{\pi D t}} \right] Tl^0(t)V_k(t) \end{aligned} \quad (4.31)$$

$$\begin{aligned} \frac{dTl^+(t)}{dt} &= -4\pi r_+ D \left[1 + \frac{r_+}{\sqrt{\pi D t}} \right] Tl^+(t)V_k(t) + 4\pi r_0 D \left[1 + \frac{r_0}{\sqrt{\pi D t}} \right] Tl^0(t)V_k(t) - H(t) + J(t) + K(t) \\ &= -4\pi r_+ D \left[1 + \frac{r_+}{\sqrt{\pi D t}} \right] Tl^+(t)V_k(t) + 4\pi r_0 D \left[1 + \frac{r_0}{\sqrt{\pi D t}} \right] Tl^0(t)V_k(t) \end{aligned} \quad (4.32)$$

$$\begin{aligned} \frac{dTl^0(t)}{dt} &= -4\pi r_0 D \left[1 + \frac{r_0}{\sqrt{\pi D t}} \right] Tl^0(t)V_k(t) + H(t) - K(t) \\ &= -4\pi r_0 D \left[1 + \frac{r_0}{\sqrt{\pi D t}} \right] Tl^0(t)V_k(t) \end{aligned} \quad (4.33)$$

These equations converge to model the concentration of excited thallium ions in terms of the mean life of the $(Tl^+)^*$ state, τ :

$$\frac{d(Tl^+)^*}{dt} = 4\pi r_0 D \left[1 + \frac{r_0}{\sqrt{\pi D t}} \right] Tl^0(t)V_k(t) - \frac{(Tl^+)^*}{\tau} \quad (4.34)$$

These equations assume a random distribution of V_k centers and Tl^0 sites, which is under debate [116, 130]. The probability of hole localization near activator centers is greater than the random localization probability, as shown in NaI(Tl) and KI(Tl) experiments. These studies observe 10 (7)% of holes forming Tl^{++} centers in 0.1 (0.07) mol% Tl-doped NaI (KI), while the fraction of Tl^{++} was expected to match the molar concentration [115, 116, 132].

Alternative decay channels are observed to occur as well. Hopping due to self-trapped excitons is postulated to produce decay times on a μs -ms timescale and increasing in prevalence at lower temperatures [134, 135]. More complex Tl sites, such as double thallium ion centers, emit in the same wavelength as that of the traditional thallium emission, but introduce small differences in temperature dependence [136].

If the excited activator state is allowed to transition to the ground state, it will do so with a high probability of photon emission. This decay is the fast fluorescent decay component of scintillation. The temperature-dependent fluorescent decay has a characteristic decay time of 220 ± 10 ns at room temperature. If the electron creates an excited metastable state that is forbidden to decay to the ground state, more energy must be added, generally through thermal excitation, to raise the configuration to a state that can decay down. This metastable state is postulated to emit for long ($\sim \mu\text{s}$ - days) periods of time (see §4.2.4). Scintillation light output is a combination of fluorescence and longer phosphorescence decays, but it is often approximated as a single exponential decay with a fluorescent time constant due to the dominance of this decay channel.

4.2.3 NaI(Tl) Characteristics

NaI(Tl) properties depend on the Tl^+ concentration, temperature, and type of primary interaction. Studies have observed behavior from crystals with low Tl concentrations, which behave like pure NaI, to high concentrations, which exhibit decreased light collection and changes in decay times [137]. Nonproportionality in the detector response depends slightly upon Tl concentration, as shown in Figure 4.11. Scintillation rise time decreases with activator concentration up to 0.03 mol%, and it remains constant around 12 ns from 0.03% to 0.37%. Above 0.03 mol%, the scintillation yield is saturated, as shown in Figure 4.11. This is linked to aggregate Tl^+ centers, which can form deep electron traps that may contribute to longer phosphorescence decays (see §4.2.4). The optimal Tl^+ concentration is thus 0.01% - 0.03%.

Temperature dependence of the light yield has been observed, consistent with an Arrhenius temperature dependence. The relative amplitudes of competing processes, Q_i , from the activation energy E and temperature T , can be modeled as [134]:

$$\frac{Q_1}{Q_2} \sim e^{-\frac{E}{kT}} \quad (4.35)$$

This model implies that changes in the light yield and decay time with temperature may be due to competing processes in the charge transport to the Tl^+ centers (as described in §4.1) [134], or the thermal release of traps at different temperatures [115]. Comparisons of pure and Tl-doped NaI indicating the dominance of lattice structure mechanisms in the low temperature < 50 K light yield [122]. NaI(Tl) is highly efficient compared to other scintillators with a 22% absolute scintillation efficiency. NaI(Tl) is observed to emit 38,000 photons/MeV absorbed, corresponding to $38,000 \times 5.9 \text{ eV} = 0.22 \text{ MeV}$ for 22% efficiency. While highly efficient for a scintillator, this implies significant loss to non-fluorescence channels (e.g., phonons).

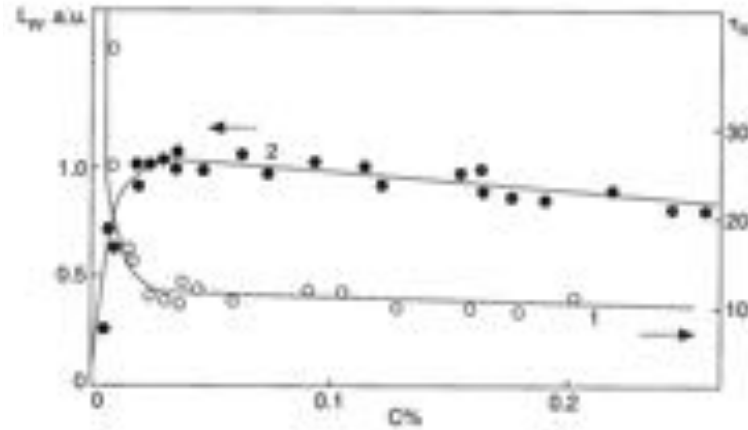


Figure 4.11: Effect of varying Tl concentration on light yield (filled circles, left axis) and scintillation rise time (open circles, right axis). Saturation above 0.03% mol is observed. Figure from [115].

NaI(Tl) light response is generally linear, but it deviates from linearity in specific emission regimes, as shown in Figure 4.12. The output above ~ 100 keV can be approximated as linear, while the low energy output is distinctly nonlinear as the result of the binding energy K- and L-edges in iodine (see §4.1.1). Gamma interactions below 100 keV are dominated by the photoelectric effect, and when the photoelectron ejected is just above the K-shell energy (33 keV), it has very little kinetic energy and there is a small response. When the photoelectron is just below the K-energy, K-shell ionization is not possible and L-shell ionization takes its place, leaving more kinetic energy for the electron since the binding energy of the L-shell is lower. The photoelectrons ejected at this point thus create a higher response. The same is true at the 5 keV L-shell boundary; the M-shell binding energy is 1 keV [114]. Sodium contributions, with a smaller cross-section than iodine, are generally neglected above 5 keV. Similarly, the photoelectric cross-section for electrons in iodine outside of the K-shell is less than 15% of the K-shell electron cross-section [115]. Removing the K- and L-shell drops from consideration, maximum light response is observed between 20 and 50 keV. Response nonproportionalities are similar between pure NaI and NaI(Tl), indicating a phenomenon intrinsic to the crystal [115]. The inclusion of traps has been shown to decrease light output, but it does not change the overall shape of the light yield [115]. See §6.2 for a discussion on the calibration of DM-Ice. The response below 20 keV is sensitive to the surface treatment of the crystal. A cleaved surface produces a 10 - 13% higher light output than a polished crystal in this energy regime [115].

Both nuclear and high ionization density (e.g., alpha, muon) interactions are quenched (see §4.1.3.1). The nuclear quenching factor is energy dependent, and the dark matter energies of interest are of particular experimental interest, as shown in Figure 4.13 [120]. The DAMA NaI(Tl) experiment uses quenching factors

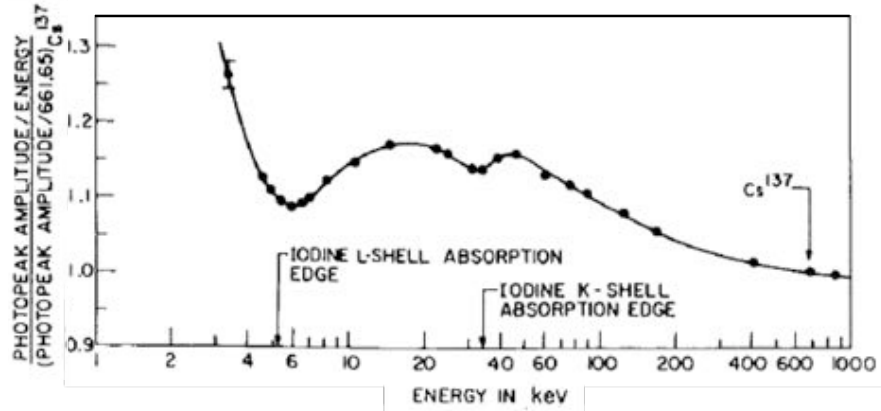


Figure 4.12: NaI(Tl) light response illustrating a nearly linear light response above 100 keV and a nonlinear response below this, primarily as a result of the K- and L-shell absorption edges. Figure from [114].

of $q_{Na} = 0.30 \pm 0.01$ (averaged over 6.5 - 97 keV_{nr}) and $q_I = 0.09 \pm 0.01$ (averaged over 22 - 330 keV_{nr}) [90]. Dedicated quenching measurements have varied, with the recent measurements yielding an sodium quenching factor at ~ 10 keV of 6% [120] to $\sim 30\%$ [138] and at ~ 800 keV_{nr} of $21 \pm 4\%$ [139] to $\sim 30\%$ [140]. Iodine recoils are $\sim 8\%$ [138, 140]. A precise understanding of the quenching factors is required to understand a WIMP nuclear interaction.

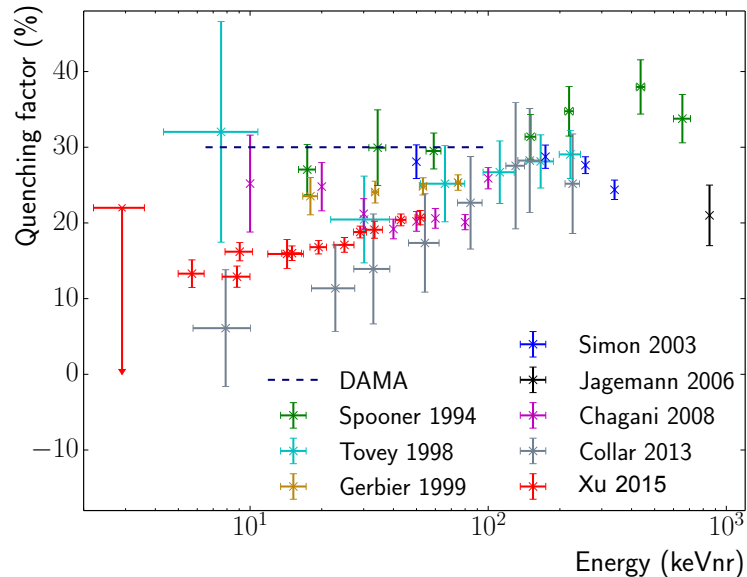


Figure 4.13: A summary of NaI(Tl) quenching factor measurements. Figure from [141].

A compilation of NaI(Tl) parameters is shown in Table 4.1:

Table 4.1: NaI(Tl) Scintillation Parameters

Symbol	Physical Parameter	Value
Z_{eff}	Effective atomic number	45.8
A_{eff}	Effective mass number	111
X_0	Radiation length of electron	2.57 cm
R_e	Mean path of a 2.18 MeV electron	3.5 mm
X	Coefficient of backscattering of electron ($E_e < 0.5 MeV$)	0.37 au
α/β	Quenching factor	0.44
a	Lattice constant	6.47 Å
E_g	Band gap width	5.9 eV
T_m	Melting temperature	661°C
	Solubility in cold water	184.0 g/100cc
L_R^1	Photon yield	38,000 γ /MeV
τ_1	Decay time	230 ns
λ_m	Emission wavelength	415 nm
D	Density	3.67 g/cm ³
$\frac{1}{\mu}$	Absorption coefficient	3.05 cm
n	Index of refraction	1.85
T_d	Delocalization temperature	58 K
D_0	Diffusion coefficient	1×10^{-5} cm ² /s
μ	Mobility	1×10^{-3} cm ² Vs
ξ_{eh}	Electron-hole pair creation	13.7 eV
τ_{Tl+}	Decay time of photoluminescence	220 ns
τ_1	Decay time of γ -scintillation	250 ns
τ_R	Rise time of γ -scintillation	40-50 ns
	Lifetime of V_k centers	10-100 ns
	Lifetime of Tl ⁰	15 ns

4.2.4 Phosphorescence

In addition to fluorescent scintillation, NaI(Tl) decays with multiple longer-lived components, collectively known as phosphorescence or afterglow. The precise mechanisms of phosphorescent decay are not well understood, but they include long-lived metastable activator states and trapping on crystal defects. Traps are due to defects and impurities in the crystal, both intrinsic and induced by irradiation. The intensity, spectral composition and decay time of phosphorescence are all products of the purity of the raw material, crystal pulling conditions (see §4.2), heat treatment, and doses of irradiation [115]. Irradiation-activated traps can form new phosphorescence centers in the detector.

Differences in experimental results indicate numerous decay channels. The light sum is expressed in terms of scintillation intensity, $J(t)$:

$$S(t) = \int_0^t J(t) dt \quad (4.36)$$

$$J(t) = J_1 \left(e^{-t/\tau_1} - e^{-t/\tau_R} \right) + J_2 e^{-t/\tau_2} \quad (4.37)$$

NaI(Tl) emission is modeled with a finite rise time (τ_R) and two decay times (τ_i), each with intensity contribution J_i . 90% of light is emitted within 1 μ s [115].

Two conventional decay channels produce long-lived decays: STE emission (Equation 4.12) that lasts for μ s-ms, and the long-lived recombination channel (Equation 4.28) that produces μ s-long decays. The decay of Tl^0 and Tl^{++} absorption follows charge migration and is described in terms of the concentration of centers created during irradiation, n_0 , and the activation energy of center decay, E_a :

$$J(t) = \frac{J(0)}{(1 + at)^2}, \quad a = \frac{c \cdot n_0}{1 + e^{E_a/kT}} \quad (4.38)$$

where c is a constant. The activation energy for Tl^0 (Tl^{++}) in NaI(Tl) is 0.18 ± 0.02 (0.24 ± 0.002) eV [115]. The temperature dependence of a allows a thermo-stimulated rate estimation; at room temperature, $a^{-1} \ll 10^{-6}$ s for Tl^0 and Tl^{++} centers [115]. A comparison of decays in KI(Tl) and NaI(Tl) illustrates the effect of this channel. A high level of phosphorescence and loss in KI is due to the long time of hole diffusion. The light output of KI(T) at 1 μ s is only 25% that of NaI(Tl), and the difference between the two is a long-lived Tl^0 trap in KI(Tl). Tl^0 should live longer in KI(Tl) than in NaI(Tl) due to the difference in the band gaps widths (6.3 eV versus 5.9 eV) and reduced V_k center mobility. A greater effect is observed through the absence of fluorescence in KCl(Tl) due to the long lifetime of trapped electrons on Tl^0 (band gap of 8.6 eV) and small V_k center mobility [115].

The metastable state interpretation of phosphorescence predicts an electron exciting an activator center to a state that is forbidden to decay to ground. The excited state requires additional energy, generally from thermal excitation, to get raised into a state that can decay. The phosphorescence decay time is then characteristic of the metastable activator state lifetime.

The trap interpretation of phosphorescence can be analyzed to predict reaction rates, trap depths, population of traps and even conditions for equilibrium, which have been experimentally measured [142]. The reaction rate, k_i , of electron trapping is:

$$k_i = s_i e^{-\epsilon_i/kT} \quad (4.39)$$

where s_i is the frequency factor of the transitions from the trap to the luminescent state; ϵ_i is the trap depth; k is the Boltzmann constant; T is the temperature. A configuration diagram that includes trap processes is provided in Figure 4.14, where each state is populated by n_i electrons.

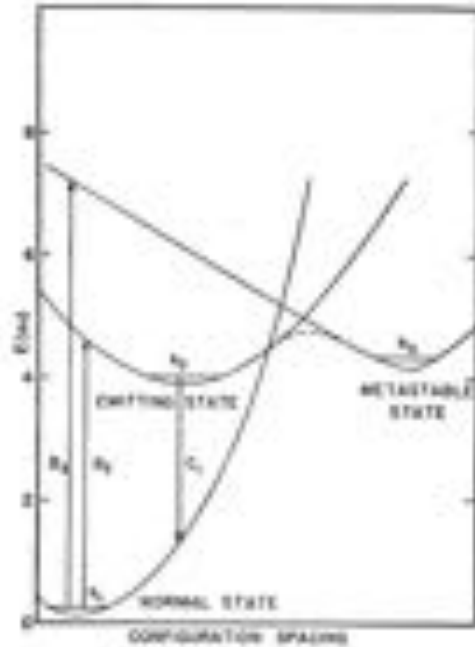


Figure 4.14: Schematic of a trap configuration that could produce long-lived phosphorescence states. Each state contains n_i electrons. Scintillation is a product of the C_1 process. Figure from [142].

Using the notation from the configuration diagram in Figure 4.14, the number of electrons in a given trap under constant irradiation is a function of the rate of electrons being raised to the trap, $B_3 n_1$, minus the reaction rate for the radiationless transition back to ground, k_1 , and the reaction rate for the transition to the luminescent state, k_2 :

$$\frac{dn_3}{dt} = -k_1 n_3 - k_2 n_3 + B_3 n_1 \quad (4.40)$$

where n_3 is the number of electrons in the trap at time t_0 . The analogous equation for the number of electrons in the luminescent state is:

$$\frac{dn_2}{dt} = -C_1 n_2 + B_2 n_1 + \mu_1 k_1 n_3 + (1 - \mu_2) k_2 n_3 \quad (4.41)$$

where n_2 is the number of electrons in the luminescent state at time t_0 ; C_1 is the rate of transition from the luminescent to ground state; B_2n_1 is the rate of electrons being raised into the luminescent state; μ_1 is the fraction of trapped electrons that go to the luminescent state; μ_2 is the fraction of trapped electrons that go to the ground state in a radiationless transition. At a given time, n_3 electrons are in the trap and n_2 electrons are in the luminescent state, having reached that state from either the ground or trap state. In order to predict the signal derived from phosphorescent events, the buildup intensity due to the trap at a given exposure time, t_0 , is derived:

$$I_0(t_0) = DC_1n_2(t_0) = DB_3n_1 \frac{\mu_1k_1 + (1 - \mu_2)k_2}{k_1 + k_2} (1 - e^{-(k_1+k_2)t_0}) \quad (4.42)$$

where D relates the observed intensity to the transition rate from the emitting state to ground. After the source is removed, the phosphorescent state is predicted to decay with the following equation at given time t , following the irradiation over time t_0 :

$$I(t) = I_0(t_0)e^{-(k_1+k_2)t} \quad (4.43)$$

where $I_0(t_0)$ is given in Equation 4.42. The irradiation time can thus alter the relative intensities of the traps produced, and may alter the phosphorescence decay time measurement [142]. Emission, when accounting for traps, can be expressed as an extension of Equations 4.5 and 4.2.4 in terms of the lifetime of the trap, τ_S , the number of trapped carriers, N_S , and the probability of Tl^+ capture, k :

$$J(t) = \frac{N_\gamma}{\tau} e^{-t/\tau} + \frac{kN_S}{\tau_S - \tau} \left(e^{-t/\tau_S} - e^{-t/\tau} \right) \quad (4.44)$$

Roughly 0.3 - 5% of NaI(Tl) emission occurs at $t > 6$ ms [115]. On long time scales ($t > 5\tau$ and $\tau_S \gg \tau$), emission can be simplified to:

$$J(t) = \frac{kN_S}{\tau_S} e^{-t/\tau_S} \quad (4.45)$$

On these time scales, the dominant fluorescent component has decayed, leaving the phosphorescence component of the scintillation as the primary decay channel. Emission is expected to evolve from Equation to Equation , with the phosphorescence time dependent upon the crystal and irradiation conditions. Dependence of the decay at this timescale on the trap dynamics allows investigation into the trap mechanics from the observation of the phosphorescent decay.

4.2.4.1 Experimental Observation

A suite of NaI(Tl) experiments have studied phosphorescence, observing timescales ranging from $1.5\mu\text{s}$ to 45 days, as shown in Table 4.2. Phosphorescent decays have been experimentally induced by cosmic rays, radioactive sources, and UV and visible light. A notable exception to these experimental results is that of

Table 4.2: Long-lived NaI(Tl) Phosphorescence Results. Missing information is designated by -. Values that are assumed from comparison to other data or implied in experimental description are designated by \dagger .

Decay time	Source	Age	T [°C]	Size	Decay	Ref.
$1.5 \pm 0.08 \mu\text{s}$	Radioactive sources	-	room \dagger	$1.5'' \times 1'' \dagger$	40% total light	[143]
70 - 100 ms	Cosmic rays Internal radioactivity	~ 3 yrs	20-22°C	$4'' \times 4'' \times 10''$ 9.6 kg^2	43.43 muons/day 4.4 - 8.7 dru (2 - 20 keV)	[144], [145]
0.15 s	Cosmic rays Radioactive sources	-	room	$1.5'' \times 1''$	9% total light $\sim 600 \text{ p.e.}_{ph}/\text{MeV}$	[146]
$1.7 \mu\text{s}$, 1.0 ms, 0.1 s, 0.65 s	Gammas Alphas	New ³	77 - 290 °C	-	-	[147]
few s	Atmospheric muons	1-3 yrs	-	$5\emptyset \times 7''$ $4.2\emptyset \times 11''$	-	[84]
8 - 10 s	Atmospheric Muons	~ 15 yrs	-20°	$14 \emptyset \times 15 \text{ cm}$	-	§7.3
~ 75 s	Visible light	-	room \dagger	$40\emptyset \times 40 \text{ mm}$	-	[148]
0.23 - 90 min	⁶⁰ Co source	New	29.9 - 52.7°	$2.5 \times 2.5 \times 1 \text{ cm}$	equilibrium	[142]
0.33 - 0.5 s min-hrs	Betatron (3 MeV and 6 MeV)	-	17°	$70 \times 70 \text{ mm}$	Slow $\sim 10 \times$ superslow	[149]
~ 2 hours	⁶⁰ Co	-	room \dagger	$2\frac{1}{2} \times 2''$	-	[150]
Hours - days	UV radiation	-	room \dagger	-	-	[151]
~ 45 days	5 min of visible light	-	$24.5 \pm 0.5^\circ$	$1'' \times 0.16''$	-	[152]

DAMA (§3.5.1), which has not observed phosphorescence in their NaI(Tl) detector but imposes $500 \mu\text{s}$ dead time following all events in order to reject any backgrounds [94].

Select experimental results of particular interest to DM-Ice are summarized here. A number of decay processes likely make up the results observed, as evidenced by the differences in timescale and response:

1. One experiment managed to produce an equilibrium in trap contents and measure the trap depth of six states ranging from 0.23 to 90 minutes. The corresponding trap depths are $0.7 \pm 0.2 \text{ eV}$ to $1.1 \pm 0.2 \text{ eV}$, as determined by observing the change in decay time with temperature, which was consistent with the behavior of a single process being responsible for each trap. The deeper traps were correlated to the longer phosphorescence decay times. These results are consistent with the presence of traps that can

²One of four crystals used in the study

³Grown by the experiment

release trapped electrons to either the luminescent state or back to the ground state. In addition to the six measured traps, it observed evidence for both shorter decay time traps and some lasting for several days, but the intensities of these extreme cases were too low for analysis. As the decays were consistent with experiments using KI(Tl), it was postulated that the traps are a product of Tl interactions (see §4.1.6) [142].

2. A 1981 betatron experiment observed two phosphorescence decays: one on a 0.33 - 0.5 s timescale and the other lasting minutes and even hours, as shown in Figure 4.15a. The sub-second phosphorescent decay was proportional to the intensity of the source, while the long-lived phosphorescent decay was proportional to the absorbed dose, as shown in Figures 4.15b and 4.15c. The shorter phosphorescence decay was an order of magnitude more prevalent than the longer decay [149]. These measurements complement a 1973 experiment that observed the the fluorescent component was proportional to the radiation intensity, while the phosphorescent component was related to absorbed dose. The ratio of phosphorescence to fluorescence light was observed to increase with energy [146].

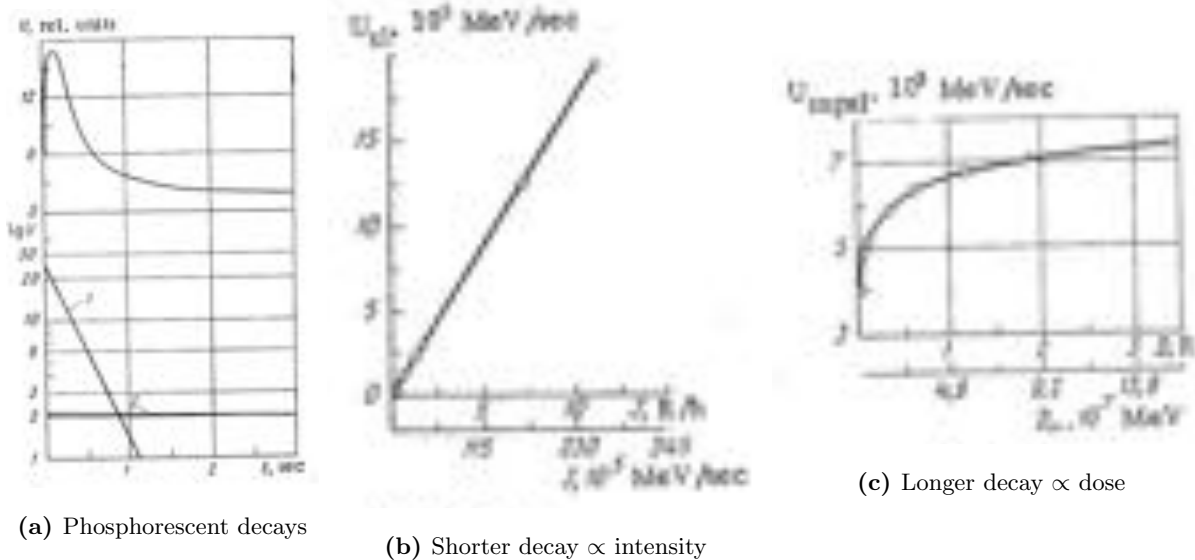
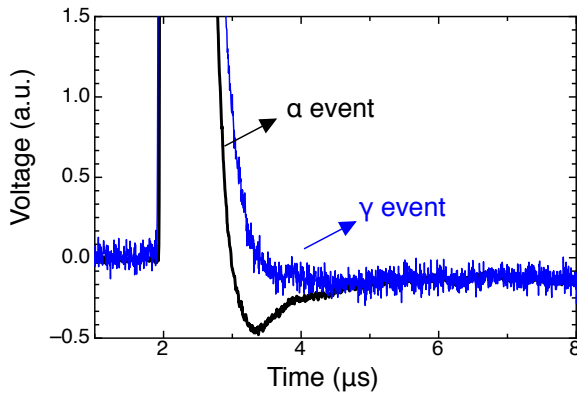


Figure 4.15: Phosphorescent decays, observed to be comprised of two components: sub-second decays, which are proportional to the source intensity, and longer (minutes – hours) decays that are proportional to the absorbed dose. Figures from [149].

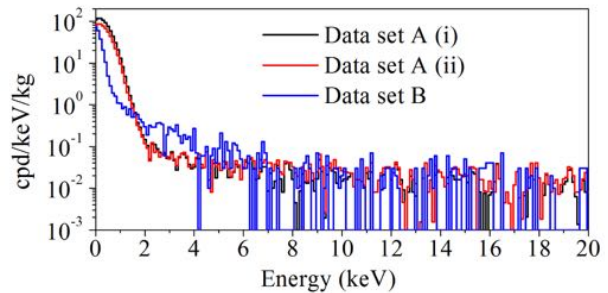
3. A 1961 experiment observed 40% of the NaI(Tl) total light output coming from a 1.5 μ s-long phosphorescent component. The decay time was independent of the Tl concentration in CsI(Tl) measurements,

motivating the conclusion that the observed phosphorescence was due to the crystal rather than the Tl centers [143].

4. The KIMS NaI(Tl) dark matter detector (see §3.5.4) observes a decay component lasting a few seconds following muon events. Two decay components are observed following all events: a 220 ns component and a $1.17 \mu\text{s}$ component that is likely due to longer-lived fluorescent decay channels [84].
5. The ANAIS dark matter detector (see §3.5.3) observes a 70 - 100 ms phosphorescent component in the gamma/muon event sample that is not present in alpha events, as shown in Figure 4.16a [144, 145]. It should be noted that this effect may be due to the electronics circuit, as the motivation for a slow component is the lack of undershoot in gamma/muon waveforms. An excess of events in the 2 - 20 keV region is observed following high energy muon events, contributing 4.39 - 8.65 counts/kg/day to the event rate in the 0.5 s following the muon [144]. Differences across the four crystals used in the study imply that impurities, rather than an intrinsic feature of the Tl^+ centers, are the source of these decays [145].



(a) Long-lived decay in the gamma/muon event sample



(b) Spectrum of phosphorescence events

Figure 4.16: Phosphorescence evidence [145] and phosphorescence spectrum following high energy events in the ANAIS-0 detector. A 4.39 - 8.65 counts/day/kg rate increase is observed in the 2-20 keV region for 0.5 s after a muon interaction. Figures from [144, 145].

6. Saint Gobain, the crystal production company that supplied the DAMA experiment's NaI(Tl), has observed a phosphorescent component that appears as low energy noise in the 6 - 10 keV region over hours and even days following exposure of the crystal to light of wavelengths shorter than, or equal to, the UV range. Phosphorescence eventually decays away upon the return of the crystal to darkness if

there has not been too much exposure; otherwise, the signal can mimic a PMT light leak and eventually lead to irreparable discoloration and color centers that produce light traps (see §4.1.6). Permanent damage can occur after less than an hour of exposure to sunlight [151].

7. The longest-lived phosphorescence measured lasted for roughly 45 days, as shown in Figure 4.17. This measurement was made after a 1968 ^{55}Fe X-ray measurement was observed to maintain a stable background of single photoelectrons in the NaI(Tl) detector. The crystal was left in the dark for several weeks, exposed to room light for five minutes, and then observed to emit the 45-day signal [152].

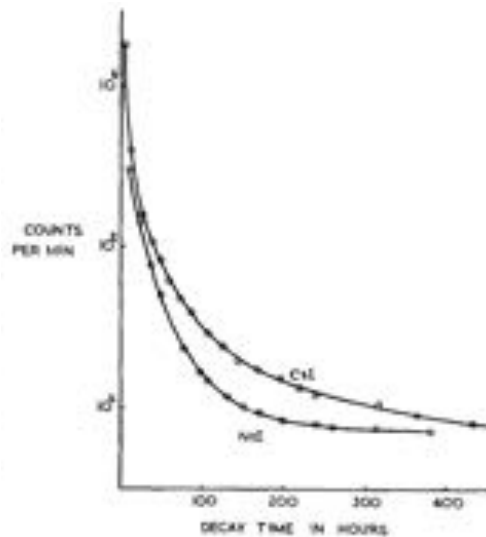


Figure 4.17: Phosphorescence lasting 45 days (right) after a five minute exposure to room light. Figure from [152].

The variation in decay times observed for long-lived phosphorescence in NaI(Tl) indicates numerous decay channels. Metastable activator states and lattice defects are both likely contributors to this phenomenon. The properties of phosphorescence vary between crystals and must be characterized for each crystal individually. It is likely that phosphorescence decay times increase with total absorbed dose over the lifetime of the crystal due to the induction of defects and deeper traps from irradiation. For a discussion on phosphorescence in DM-Ice, see §5.1. For a discussion on the proposed role of phosphorescence in the DAMA signal, see §3.5.1.3.

Chapter 5

DM-Ice

5.1 Experimental Concept

DM-Ice is a NaI(Tl) dark matter detector designed to observe the WIMP annual modulation. As the only direct detection experiment operating in the Southern Hemisphere, DM-Ice has a unique ability to decouple the WIMP annual modulation from that of seasonally-varying backgrounds. While modulating backgrounds from seasonal temperature variations should be perfectly out of phase between the Northern and Southern Hemispheres, the WIMP phase should be consistent between them. As an example of this effect, Figure 5.1 shows the muon rate in the Northern and Southern Hemispheres overlaid with the WIMP maximum reported by DAMA [79]. Operation in the Southern Hemisphere moves this modulating background out of phase with the WIMP signal.

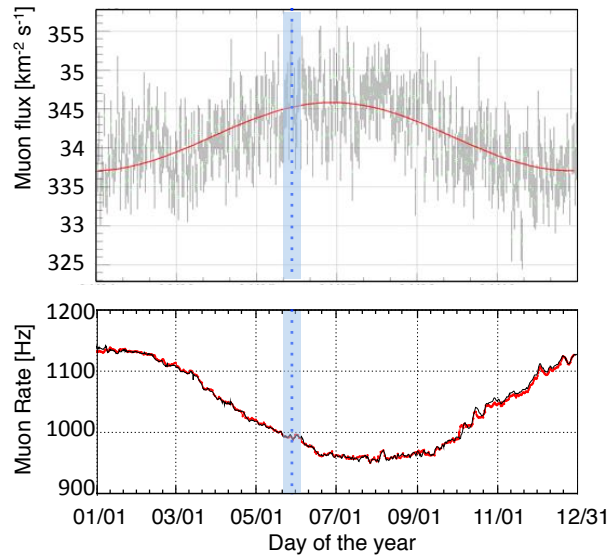


Figure 5.1: The DAMA phase (1σ band, blue) [79], overlaid with the muon rates in the Northern and Southern hemispheres, as measured by Boraxino in LNGS (top, [95]) and IceCube (bottom, [153]). Borexino data is shown with the best fit in red. IceCube data (red) is shown on top of atmospheric temperature (black).

DM-Ice is designed to run in four phases:

- **DM-Ice17:** DM-Ice17 is the DM-Ice prototype, comprised of two 8.47 kg NaI(Tl) crystals in separate pressure vessels, as shown in Figure 5.2. It was deployed in the South Pole ice in December 2010 and has been in continuous operation since then. It is used for background studies and the development of the simulation (§6.5), the modulation analysis (Chapter 6), and the IceCube muon veto (Chapter 8).
- **DM-Ice37:** DM-Ice37 is the DM-Ice R&D detector, comprised of two 18.7 kg NaI(Tl) crystals, as shown in Figure 5.3. They were deployed at Fermilab (FNAL) from April 2014 to November 2014. The detector was moved from Fermilab to the Boulby Underground Laboratory (Boulby) in the UK because Boulby offers a larger overburden and lower environmental radioactivity. The detector has been in continuous operation since deployment at Boulby, and is discussed in depth in §9.1.
- **DM-Ice250 North:** DM-Ice250 North will be the first phase of the full DM-Ice detector. It will run at Boulby within the former ZEPLIN shielding. Figure 5.4a shows the DM-Ice250 North detector in an older configuration, within the former XENON100 shielding. It will be comprised of two 125 kg crystal arrays in separate pressure vessels, each containing seven crystals.
- **DM-Ice250 South:** DM-Ice250 South will run the DM-Ice250 detectors in the South Pole ice after running at LNGS. They will be deployed on strings similar to the DM-Ice17 setup, as shown in Figure 5.4b. Once deployed, the detectors will not be removed from the ice. Development of the full-scale detector is discussed in §9.2.

The sensitivities of DM-Ice17 and DM-Ice250 to a null result are shown in Figure 5.5. The sensitivity of DM-Ice17 precludes an exclusion or confirmation of the DAMA signal, but the full-scale detector will return significant results within two live years of exposure. The DM-Ice17 background values considered correspond to the rates in the region of interest with and without removal of the 3 keV ^{40}K peak (see Chapter 6). The sensitivity of the full-scale detector to a positive signal is shown in Figure 5.6 as a function of live time. The detector will be capable of observing a dark matter modulation to 3σ - 5σ using crystals that are currently available (see Chapter 9). Backgrounds considered for the full scale detector span the range of expected background rates from the sum of the lowest background levels achieved for each contaminating isotope to those levels that are typically available (see §9.1); backgrounds are considered with and without the removal of the low energy ^{40}K peak. DM-Ice17 is not included in Figure 5.6 because its background rates are currently too high to be sensitive to this signal.

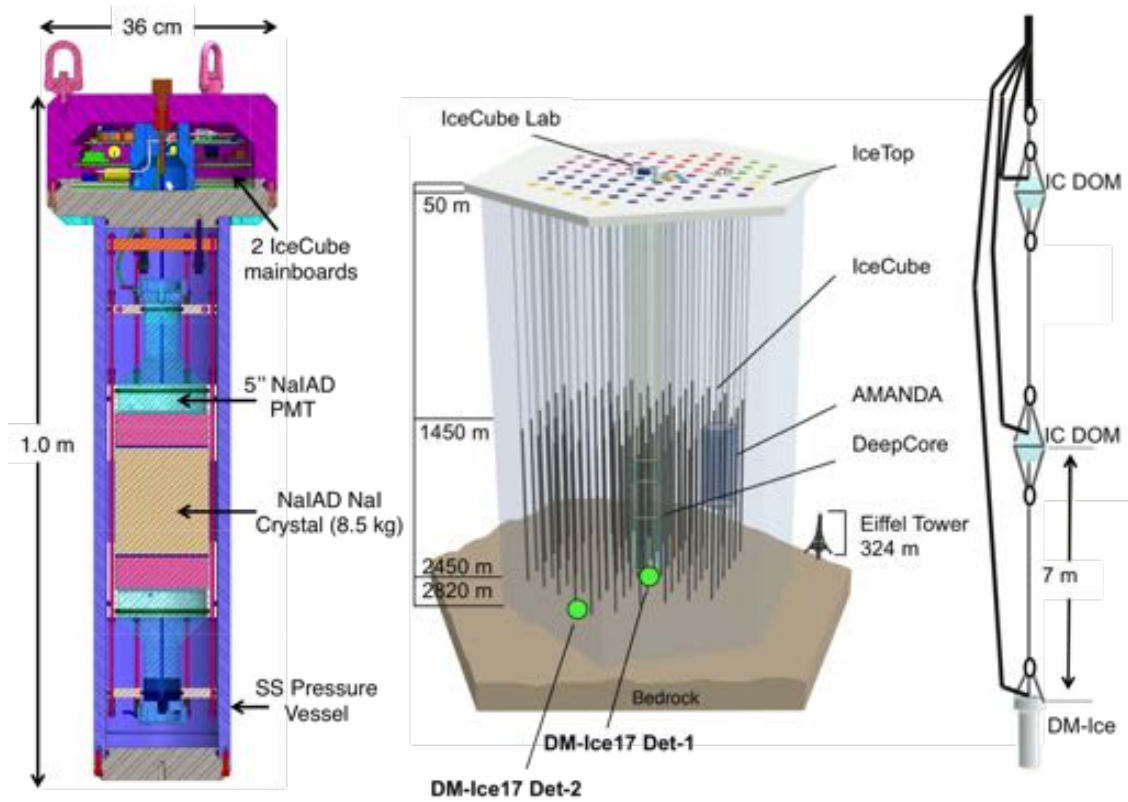


Figure 5.2: DM-Ice17 detector. Two detectors, each containing a 8.47 kg NaI(Tl) crystal coupled to two PMTs, are deployed in the South Pole ice within the volume of the IceCube Neutrino Observatory (Chapter 8).



Figure 5.3: DM-Ice37. Two 18.7 kg NaI(Tl) crystal are deployed at Boulby for R&D. Testing of crystal and PMT contamination are underway to determine the feasibility of currently available components for the full-scale detector. The crystals are housed in a lead castle and continuously flushed with nitrogen.

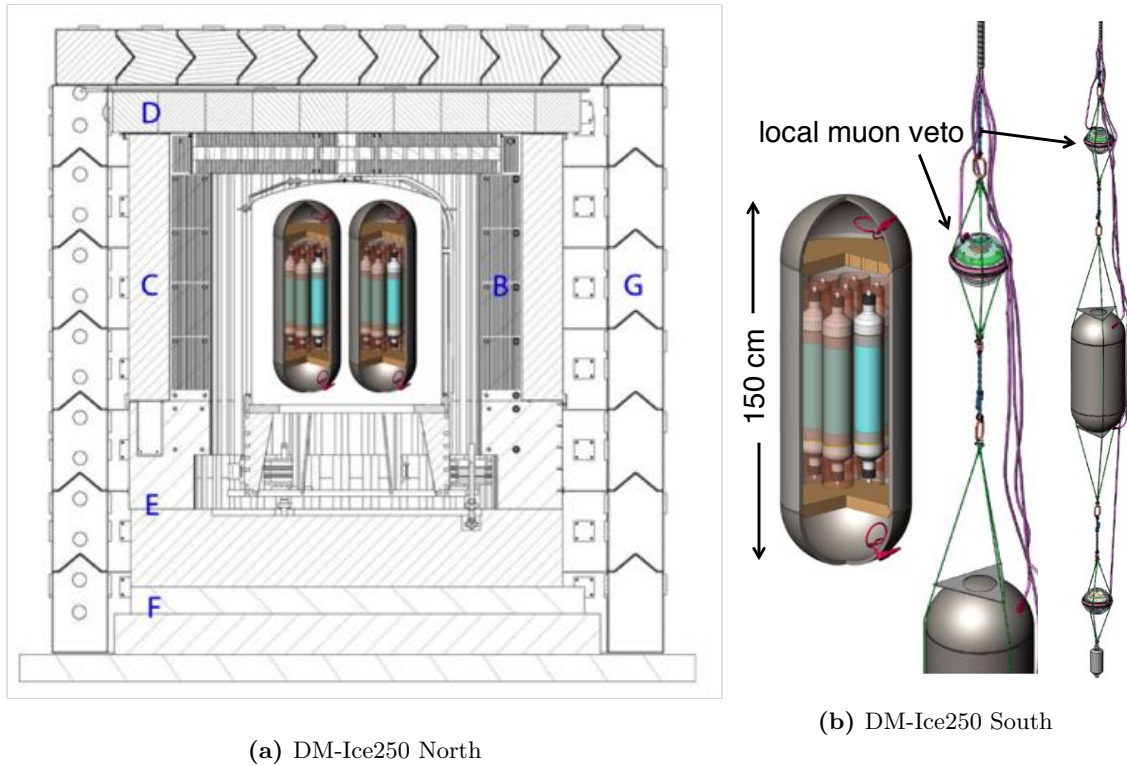


Figure 5.4: Proposed DM-Ice250 North (5.4a) and DM-Ice250 South (5.4b) detector schematics. Each NaI(Tl) crystal is coupled to two PMTs. The setup in the Northern hemisphere will be at Boulby within the former ZEPLIN shielding. The Southern hemisphere detector will run after DM-Ice250 North, placing the same detectors within the volume of the IceCube Neutrino Observatory, which it will use as a muon veto.

5.2 DM-Ice17

DM-Ice17 is operating beneath 2450 m (2200 m.w.e.) of Antarctic ice, roughly 1 km from the geographic South Pole. It was deployed in December 2010, with the final seven strings of the IceCube Neutrino Observatory (IceCube), and it has been in continuous operation since then. The two DM-Ice17 detectors were deployed and permanently frozen on separate IceCube strings, shown in Figure 5.7. Each detector is located 7 m below the deepest IceCube detector on the string. Details on IceCube are provided in §8.2.

DM-Ice17 consists of two identical detectors: Det-1 and Det-2. They each contain a 8.47 kg NaI(Tl) crystal ($\varnothing 14.0$ cm \times 15.0 cm height) wrapped in polytetrafluoroethylene (PTFE) for diffuse light reflection. The crystals were encapsulated within a copper housing with quartz windows on either end, leading to 5.0 cm thick quartz light guides coupled to 5" PMTs, as shown in Figure 5.2 [77]. The entire system was flushed with dry nitrogen. Det-1 contains PMT-1a and PMT-1b, and Det-2 contains PMT-2a and PMT-2b. The

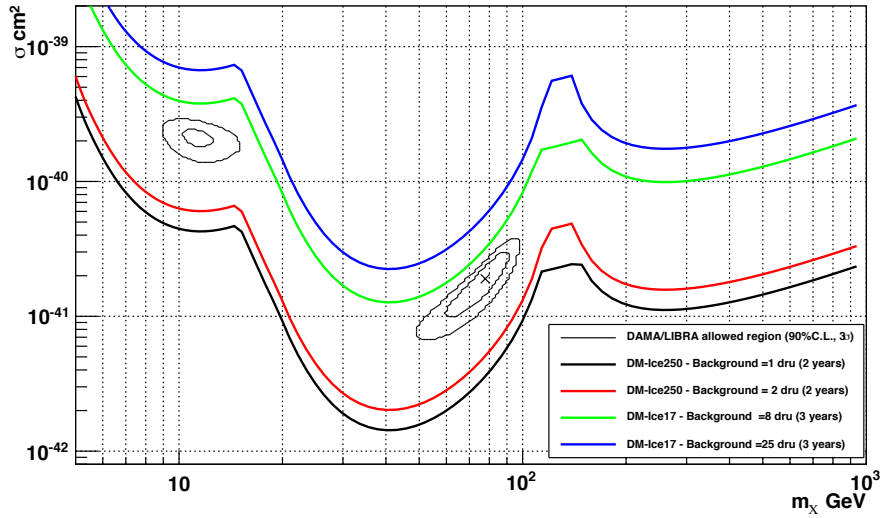


Figure 5.5: Sensitivity of the DM-Ice17 and DM-Ice250 detectors to a null result in the 2 - 4 keV region. DM-Ice17 is considered over three years with 25 dru and 8 dru backgrounds, and DM-Ice250 is considered over two years with 1 dru and 5 dru backgrounds [154]. The DAMA/LIBRA regions are shown in black contours.

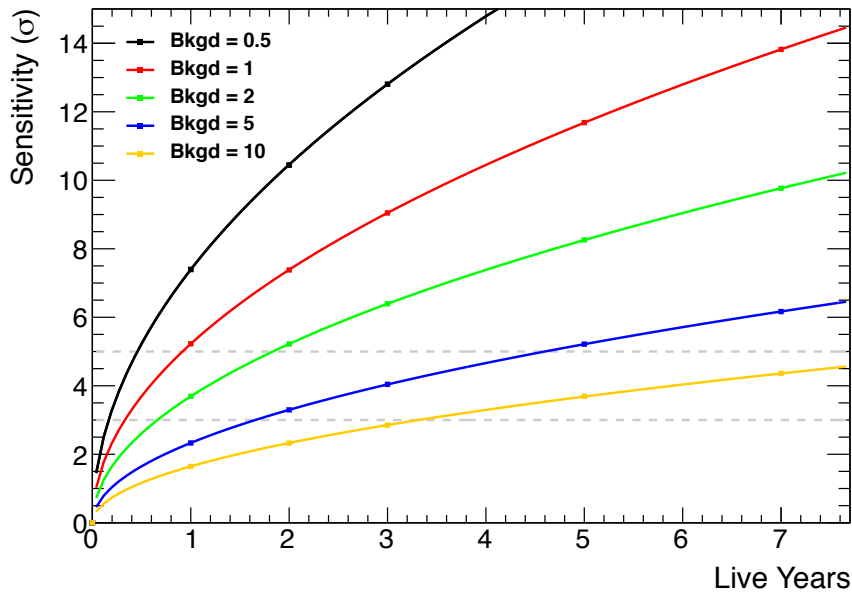


Figure 5.6: Sensitivity of DM-Ice250 to a positive result in the 2-4 keV region as a function of exposure. Background rates of 0.5-10 dru are considered for up to 7 live years of exposure. The 3σ and 5σ levels are shown in dashed grey.

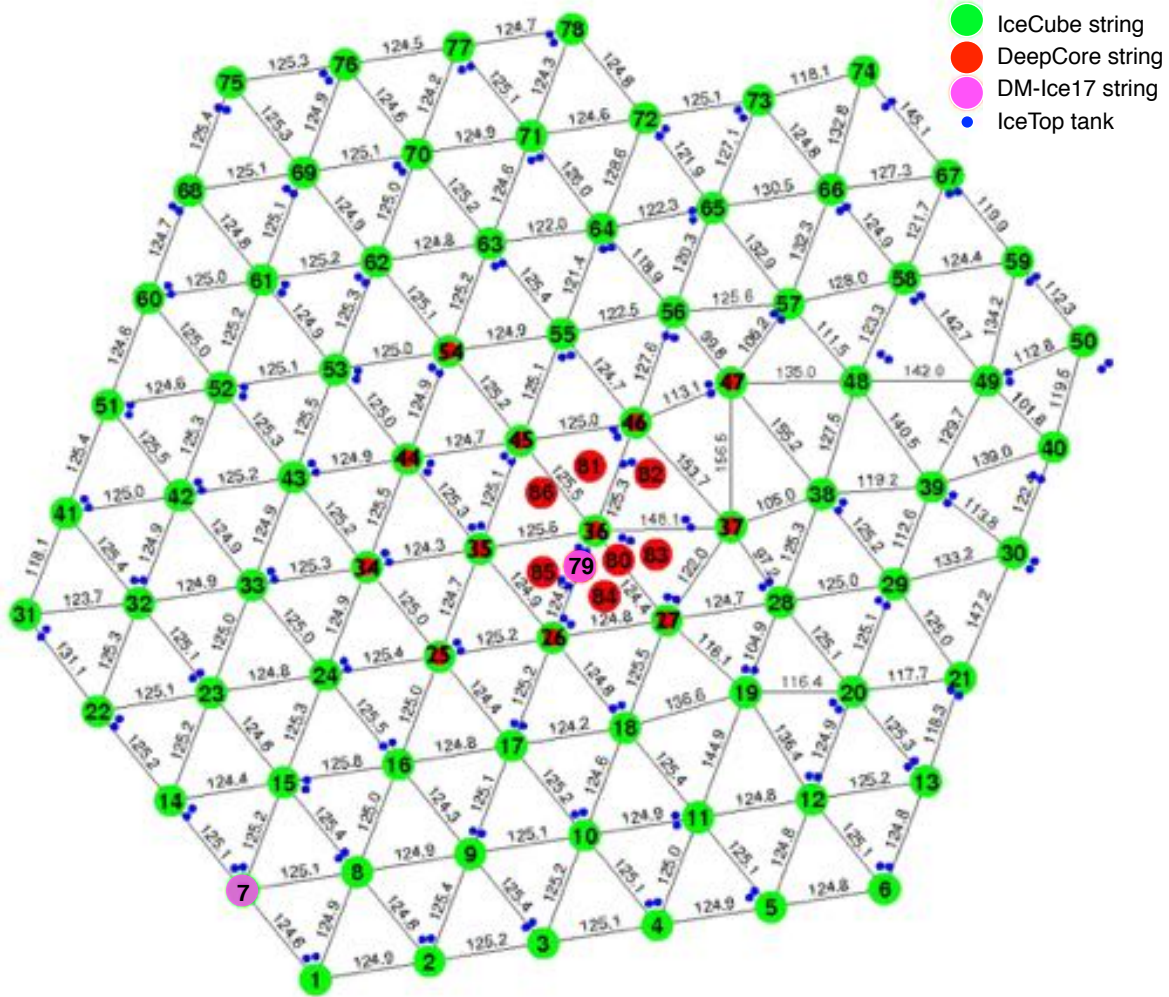


Figure 5.7: Layout of IceCube, DM-Ice17, and IceCube-associated DeepCore and IceTop detectors at the South Pole. DM-Ice17 has one detector on the edge of IceCube, with the other at the center of the detector. Shown are the location of each string and the interstring distances between IceCube strings.

mainboards sit above the top PMT and house the high voltage, electronics, and monitoring hardware. The entire setup is enclosed in a copper-lined stainless steel pressure vessel designed to withstand the pressure of the water column above the detector and the extreme conditions of the deployment process. During deployment, a hot water drill makes a 2450 m-deep water-filled hole in the ice into which the detector is lowered and which refreezes over the period of a day. IceCube has observed pressure spikes exceeding 7000 psi during the deployment and freeze-in period, and the pressure vessel was designed to withstand 10000 psi of external pressure. Details of the DM-Ice17 hardware and deployment can be found in [77].

The prototype hardware is a combination of new components chosen for their low backgrounds and previously-used components that are well-characterized. The crystals, light guides and PMTs are from the former NaIAD experiment, which operated from 2000 to 2003 in the Boulby Underground Laboratory (Boulby, see §3.5.2), and the DM-Ice17 crystals are referred to in NaIAD publications as DM80 and DM81 [155]. The crystals were produced for NaIAD by Bicron and encapsulated by Saint Gobain. The relatively high background rate of these crystals (7.9 ± 0.4 counts/keV/kg/day from 6.5 - 8.0 keV_{ee}) precludes the production of stringent dark matter limits with these detectors, but the crystals are well-characterized detectors suitable for a prototype setup like DM-Ice17 (see Figure 5.5). The NaIAD detector elements were stored in sealed copper boxes at Boulby from run completion in 2003 until retrieval for DM-Ice17 in 2010. Low background counting was performed on the drill water, silicone gel, copper, stainless steel, and PTFE at SNOLAB [77]. Contamination in other components was minimized by selecting vendors known to produce radio-clean devices. Machined components were cleaned with ultra-high vacuum cleaning techniques while the optical components were cleaned with methanol and deionized water. Assembly occurred in the semi-clean room used to assemble IceCube modules.

The South Pole ice environment is highly radio pure. The ice at the depth of DM-Ice17 is 90,000-100,000 years old [156] and contains $\sim 10^{-4}$ ppb ²³⁸U and ²³²Th and ~ 0.1 ppb ⁴⁰K contamination [77]. The contamination is mostly from the 0.1 ppm dust levels in the ice due primarily to volcanic ash depositions. These background levels are orders of magnitude lower than those found in traditional rock mines [157]. The bedrock below the glacial ice is a negligible background, shielded from DM-Ice17 by over 300 m of ice. A summary of contamination in the detector elements and environment is provided in §6.5.

5.2.1 Assembly and Deployment

The DM-Ice17 detectors were assembled at the Physical Sciences Laboratory (PSL) in Stoughton, Wisconsin, as shown in Figure 5.8. Prior to shipment to PSL, the NaI(Tl) crystals were calibrated with source runs while still at Boulby (see §6.2.1) in September 2010. Once in Wisconsin, the crystals were coupled to light guides and PMTs, and the mainboards (see §5.2.2) were added. The entire assembly was then placed into the stainless steel pressure vessels used to mitigate mechanical, thermal, and pressure shock. Now assembled, the detectors were placed in their custom-designed wooden shipping containers. Source runs were performed with the detectors in the shipping containers (see §6.2.2) before shipment to the South Pole.

The detectors were sent from Wisconsin to the South Pole via Los Angeles, Christchurch and McMurdo. Sensors were applied to the shipping containers to monitor the temperature, humidity, and mechanical shock experienced by the detectors [77]. The pressure vessel, insulating layers, and suspension system within the pressure vessel helped to mitigate shock to the crystals. Thermal shock is of particular concern for encapsulated crystals due to differences in thermal expansion coefficients between the crystals and the



Figure 5.8: Assembly of the DM-Ice17 detectors. Clockwise from top left: NaI(Tl) crystals from the NaIAD experiment arrived in Wisconsin in September 2010; the detectors were assembled in September and October 2010 at PSL by first coupling the crystals, light guides, and PMTs; the mainboards were added to the top of the detector; the assembly was placed inside stainless steel pressure vessels and loaded into the shipping containers for transport to the South Pole.

encapsulation materials. Encapsulated crystals should experience no greater a temperature change than $8^{\circ}\text{C}/\text{hr}$; the DM-Ice17 detectors experienced a gradient of less than $3^{\circ}\text{C}/\text{hr}$ during transportation. The crystals traveled first by land from Wisconsin to Los Angeles, California and then by air from Los Angeles to Christchurch, New Zealand. They remained on the surface for two weeks in Christchurch awaiting the flight to McMurdo Station, Antarctica, shown in Figure 5.9 (left). They spent one day at McMurdo before flying to the South Pole Station, as shown in Figure 5.9 (right). Once at the South Pole, the temperature stabilized around the -25°C surface temperature. Det-1 (Det-2) was on the South Pole surface for 15 (10) days awaiting deployment and being tested. The detectors were deployed in the ice as quickly as possible to minimize the time spent at the surface at the South Pole (elevation 2835 m) and minimize cosmogenic activation (see §6.3).

The detectors were transported to the deployment hole sites (see Figure 5.10) and allowed to thermalize in the 19°C deployment tower before being lowered into the hole, passing through the -50° air column in the top ~50 m of the hole before hitting the 0°C water that filled the remainder of the hole (see Figure 5.11). No damage to the detectors has been observed.



Figure 5.9: Shipment to the South Pole. Left: The detectors are shown on the flight from New Zealand to McMurdo Station, Antarctica. Right: The detectors are shown on the flight from McMurdo Station to the South Pole Station.



Figure 5.10: Transporting the detectors to the drilling sites.

5.2.2 Electronics

Each PMT in DM-Ice17 has its own IceCube mainboard and high voltage, as shown in Figure 5.12, remotely controlled through a hub in the IceCube Laboratory (ICL) at the surface. The hubs can be accessed by on-site personnel at any time, or accessed remotely when a satellite connection to the South



Figure 5.11: Deployment of DM-Ice17 Det-2. It was wrapped in an additional layer to further protect against thermal shock. The right-hand figure shows an IceCube module entering the hole directly above Det-2.

Pole is available. The sample rate, high voltage, and threshold can all be adjusted remotely. The PMTs are set to trigger on ~ 0.25 photoelectrons (p.e.), and waveforms are recorded if a 500 ns coincidence condition between coupled PMTs is met. PMT data is sent to the mainboards through a cable, set to equal length to match transit times. The mainboards run a simplified version of IceCube's TestDAQ software [158]. The PMT signals are digitized by the mainboards and sent to the hub. DM-Ice17 power and communication travels along the IceCube signal cables, passing through twisted copper wires. The event time stamps sent to the ICL hub are adjusted for the cable length and synchronized to the IceCube GPS receiver for conversion to universal time. IceCube and DM-Ice17 data have synchronized time stamps. Data is sent via satellite to the University of Wisconsin, Madison for data processing. For further details on the electronics, see [77].

In addition to normal run-taking, the DAQ regularly records monitoring information to verify run settings. Monitored values include, among others: pressure, high voltage (both the chosen setting and the operating value), temperature, and the event rate passing threshold (without the coincidence condition applied). The high voltage (HV) of each PMT was set to 1000 V for both PMTs in Det-1 and set to 1100 (950) V for PMT-2a (PMT-2b). Monitoring data was taken every 2 seconds from January 2011 until February 2012, and has been taken every 60 seconds since. This rate reduction was implemented to reduce the noise associated with the monitoring process, as discussed in §6.1.2.

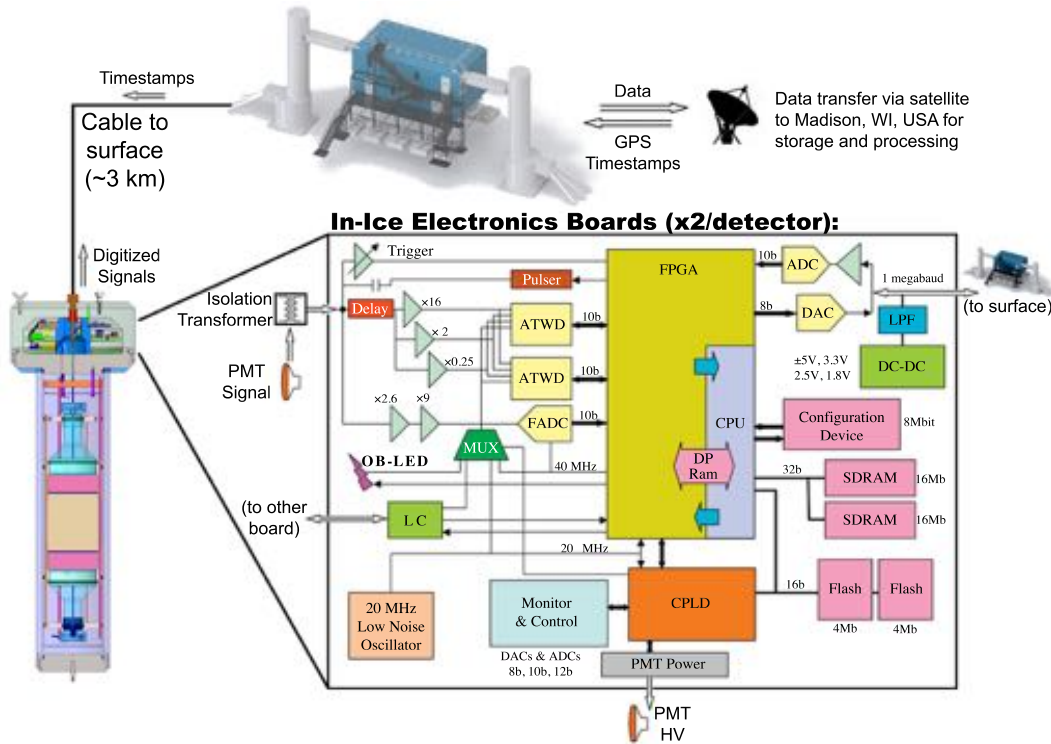


Figure 5.12: IceCube mainboards used in DM-Ice17.

5.2.3 Waveforms

Data is read out separately from each coupled PMT when the proper conditions are met: each PMT must observe a signal that rises above ~ 0.25 p.e., and they both must trigger within 500 ns of each other. Regular runs are taken without the PMT coincidence condition to collect numerous single photoelectron (SPE) events. A light yield of 5.9 ± 0.1 p.e./keV for Det-1 and 4.3 ± 0.1 p.e./keV for Det-2 is determined by comparing the energy of the SPE peak with the 65.3 keV line from cosmogenic ^{125}I .

Waveforms are read out in four channels: three Analog Transient Waveform Digitizer (ATWD) channels and one Flash Analog to Digital Converter (FADC). A typical waveform is shown across all four channels in Figure 5.13. The ATWD channels have roughly 600 ns readout windows, sampling at ~ 200 MHz for a total of 128 data points. The FADC channel has a longer $6.375 \mu\text{s}$ readout window and a 40 MHz sampling rate for a total of 255 data points. Differences in gain across the readout channels expand the detector's dynamic range. Figure 5.13 displays, from the top: ATWD0 ($16\times$ gain), ATWD1 ($2\times$ gain), ATWD2 ($0.25\times$ gain), and FADC ($23.4\times$ gain). ATWD0 is ideal for low energy events, ATWD1 over the gamma and alpha regions, and ATWD2 in the alpha and muon regions where the other channels are saturated (see §5.2.4.5). Combined,

these channels allow the unsaturated readout of events from single photoelectrons (sub-keV energy) to high-energy muon events (tens of MeV). The ATWD channels currently provide better resolution than the FADC channel, so they are used for spectral analysis. Improvements to the FADC waveform treatment are underway to extract more information from its long tail and provide valuable timing and baseline information. See §6.1.1 for a discussion on waveform corrections and processing.

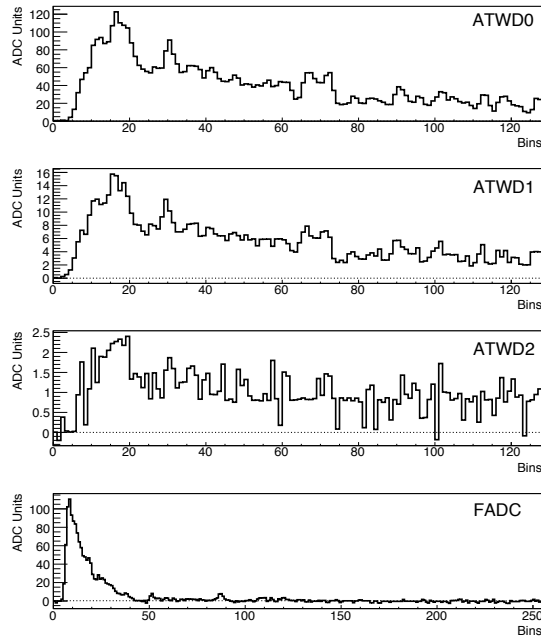


Figure 5.13: A scintillation waveform from PMT-1a in DM-Ice17. The DAQ outputs three ATWD channels (~ 600 ns), each with a different gain, and a FADC channel (~ 6.375 μ s). These waveforms have been baseline- and droop-corrected (see §6.1.1).

5.2.4 Detector Characteristics

5.2.4.1 Livetime

DM-Ice17 data taking began in January 2011 and, with a 99.75% uptime during normal running, has reached an exposure of 51 kg-yrs of data over the first three years of running. Initial runs (January 5, 2011 - June 16, 2011) were used to optimize the run parameters (HV, sampling rate, thresholds, etc.). Stable data taking began in June 2011, and only data from after this point is used for analysis. The small dead time is comprised of the time between runs and a 700 μ s dead time after each event due to waveform digitization. There is a 98.94% (98.92%) uptime in Det-1 (Det-2) if all data is taken into account. The additional downtime

arises from 10 long (>1 hr) dead times due to power outages, test runs, and DAQ errors. These downtimes have all been accounted for and are well understood.

5.2.4.2 Stability

Temperature Stability

Mainboard temperatures, which are monitored every minute, stabilized following an initial freeze-in period. Thermalization is modeled with two exponential time components, as shown in Figure 5.14. A fast freeze-in constant (~ 10 days) was observed as the water in the drill hole froze. A second, slower time constant (~ 50 days) was also observed and is likely due to the dissipation of heat deposited in the nearby ice during the hot-water drilling process. The drop around 160 days corresponds to a change in the PMT high voltage setting that changed the power dissipation, lowering the amount of heat coming off the mainboards. The following discontinuities are associated with power outages in the ICL or the hub lasting over an hour. The temperatures have stabilized, with an RMS of 0.06°C , since the beginning of physics data taking in July 2011. The monitored values are roughly 10°C warmer than the surrounding ice due to the heat dissipated by electronics. The top mainboard, whose temperature sensor is located directly above the DC-DC converter of the mainboard below it, observes a $2\text{-}3^\circ\text{C}$ higher temperature than its partner mainboard. The crystals themselves should exhibit a more stable temperature than the mainboards due to their larger thermal mass and their larger distance from the electronics.

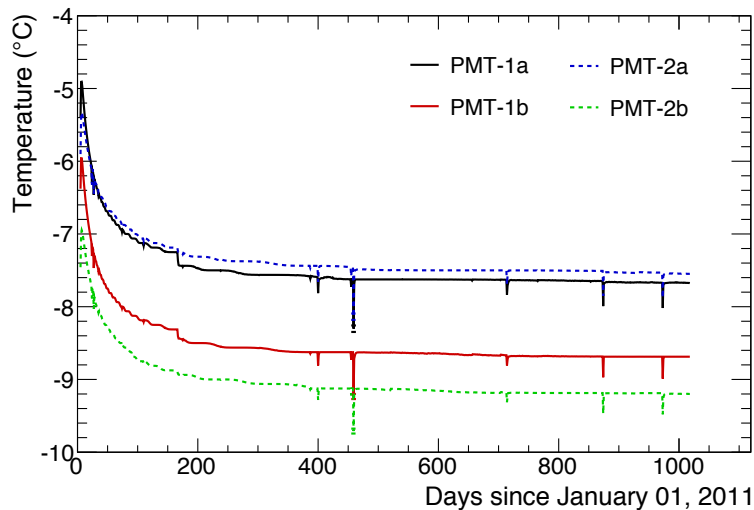


Figure 5.14: Temperature stability, as recorded by DM-Ice17 mainboards. After an initial freeze-in, the temperature has stabilized with an RMS of 0.06°C . Discontinuities are associated with a change in HV settings and power outages.

Light Yield Stability

Stability of the light response is measured by tracking the relative location of a known peak over time. The PMT HV is monitored and has remained stable to within $0.4\text{--}0.7 V_{RMS}$ with the exception of PMT-2b, which shows random variation about the assigned set point. No correlation has been observed between this variation and PMT gain or rate. Figure 5.15 shows the light collection stability of all four PMTs at 609 keV and 46.5 keV, respectively. At 600 keV, there appears to be a small ($<2\%$) light loss over two years, which is likely the result of outdated pedestal corrections (see §6.1.1). Even with this effect, the detector is stable to within 2% at this energy, which is less than the energy resolution, so no time dependence is required in the energy calibration. There does not appear to be any light loss at 45 keV, with fluctuations staying below 2% and no discernible trend.

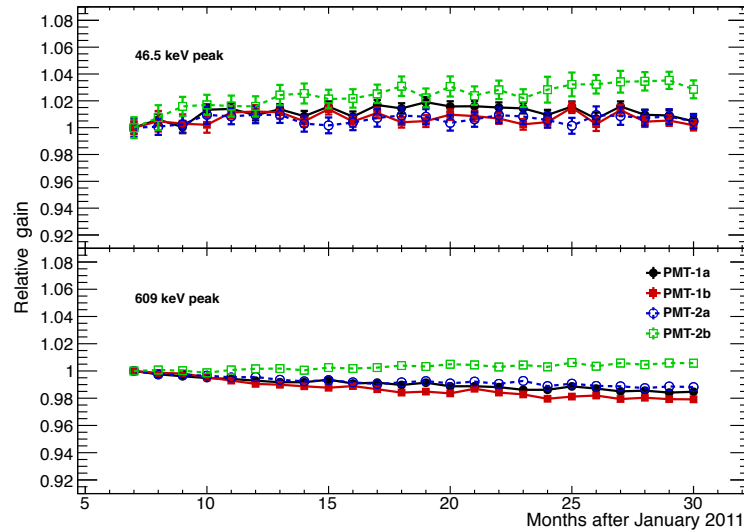


Figure 5.15: Light yield stability of DM-Ice17 PMTs at 46.5 keV (top) and 609 keV. A small light loss is observed at 609 keV, while no trend is discernable at 46.5 keV.

The coincident rate for each detector shows a small decrease over time, while the non-coincident (dark noise) runs show no variation in the PMT trigger thresholds. The coincident rate, which averages to 2.4993 ± 0.0002 Hz in each detector, gradually decreases by 0.027 (0.013) Hz/yr for Det-1 (2). This may be due to the decay of contaminant isotopes, and it is a topic of current investigation.

5.2.4.3 Timing Resolution

Timing resolution is governed by electronics instability, while uncertainty due to the timescale of the scintillation mechanism, readout resolution and crystal size are comparatively negligible. Fluorescent scintillation begins less than a nanosecond after the incident particle interacts in the crystals, as discussed in §4.1 and §4.2. The readout timestamp resolution is 0.1 ns. The crystal length affects the relative timing of the hits in each PMT: those events occurring equidistant from each PMT arrive simultaneously, while those events that occur closer to one end will appear at the closer PMT quicker than its counterpart. This introduces an uncertainty proportional to the length of the crystal, corresponding to 0.5 ns in the 15 cm crystal length. A 10.6 (10.7) ns uncertainty is introduced by differences in the trigger time across coupled PMTs, as shown in Figure 5.16a. This difference is due to variations in the time difference between the trigger and start of the scintillation waveform. Differences in the trigger time between PMTs correspond to differences in the location of the “half-max” (when the waveform rises to half of its full height) time in the waveform from each PMT, as shown in Figure 5.16b. This indicates that the PMTs have observed identical events, but one PMT triggered before the other, due to the electronics rather than effects from the crystal. Large differences in the trigger times (>50 ns) are due to accidental coincidence with SPE noise events that triggers one PMT earlier than the other. Low energy events were removed for this analysis to avoid effects from noise and SPE-like pulses.

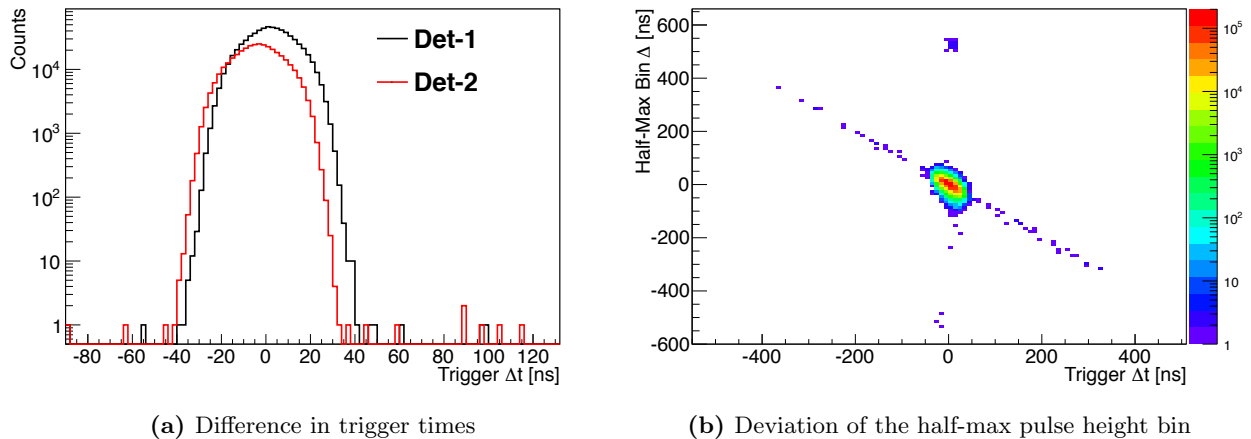


Figure 5.16: Timing uncertainty due to electronics instabilities. Left: Trigger time difference between coupled PMTs, introducing a ~ 11 ns uncertainty. Large (>50 ns) time differences are due to accidental coincidence with SPE events. Right: Correlation between the trigger time difference and the half-max time difference. Events at high half-max and small time difference are due to Bi-Po interactions. Data is from from one month of Det-1 ATWD2. Det-2 shows the same behavior.

5.2.4.4 Energy Resolution

DM-Ice17 energy resolution is derived from the widths of internal contamination peaks. Spectral peaks are fit to a Gaussian curve over a linear background. DM-Ice17 resolution is competitive with that of other NaI experiments, ranging from $\frac{\sigma}{E} = 0.34 \pm 0.06$ (0.57 ± 0.27) at 2.88 keV to $\frac{\sigma}{E} = 0.020 \pm 0.001$ (0.019 ± 0.001) at 2614.5 keV in Det-1 (Det-2), as shown in Figure 5.17. The data presented here is from DM-Ice17 (one month of combined data from both PMTs for each crystal), ANAIS [82], NAIAD [155], DAMA [87], and a small NaI detector [159]. Of particular interest is the improvement in resolution from NAIAD to DM-Ice17, which used the same crystals and PMTs. Improvements in waveform corrections and calibration, as well as a long calibration dataset, are likely the source of this improvement, although it is a topic of ongoing investigation. The poorly resolved line around 12 keV is the result of multiple X-ray peaks being fit as a single line. Resolution at the 3 keV peak may improve as analysis cuts are finalized. Small NaI detectors have increased resolution due to better light collection and greater homogeneity throughout the crystal compared to larger detectors. The DAMA resolution function has a discontinuity around 80 keV, where the DAQ readout channel is switched.

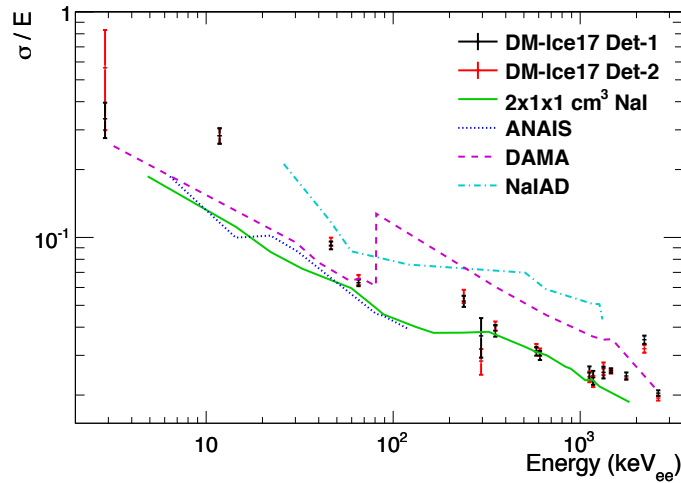


Figure 5.17: Resolution of NaI experiments (DM-Ice17, DAMA, ANAIS, NAIAD, small NaI detector). DM-Ice17 has very competitive resolution. The poorly resolved peak around 12 keV is the result of multiple X-ray peaks making up a peak that was fit as a single line. The discontinuity in DAMA’s resolution function is where they switch readout channels in their DAQ [87].

5.2.4.5 Saturation

Channel and PMT saturation are both observed in DM-Ice17. Channel saturation occurs when an event is too large for a given channel (with its respective gain) to read out. This is a DAQ readout limitation. PMT saturation is the result of a reduced electron output from the photocathode when a high photon input depletes the free electrons in the photocathode valence band.

Saturated events are identified by the saturation-induced alterations induced in the waveform. These pulses are removed from analyses in which they would produce misleading data (e.g., energy spectra). Readout channel saturation is identified by the clear cut off at the top of the waveform. Once the droop correction is applied, this flat top becomes a line but is still clearly unnatural. The saturation energy is unique for each channel of each PMT, as listed in Table 5.1. ATWD2 is not included in the table because it is not observed to saturate with the energies of events observed in DM-Ice17. PMT saturation is identified by the uncharacteristically fast waveforms that it creates. Because energy is defined as the integral of the waveform, PMT-saturated waveforms produce an energy underestimate. These events can be removed using a pulse shape discrimination variable (see §7.2). PMT saturation occurs at those energies listed in Table 5.1. It is only a consideration for muon data because these are the only events that deposit enough energy to saturate the PMTs.

Table 5.1: Saturation energies [MeV]

	Det-1a	Det-1b	Det-2a	Det-2b
Channel Saturation [MeV]				
ATWD0	2.05	1.40	2.90	2.80
ATWD1	8.58	6.83	8.85	13.42
FADC	1.30	1.05	2.50	2.50
PMT Saturation [MeV]				
Percentage of muon events	80%	80%	93%	81%

Chapter 6

DM-Ice17 Data Analysis

6.1 Data Processing

6.1.1 Waveforms

DM-Ice17 extracts waveforms from each PMT when threshold and coincidence conditions are met (see §5.2.3). High energy scintillation events display the characteristic rise and fall times of NaI(Tl), while low energy events are a collection of single photoelectrons (SPEs), as shown in Figure 6.1. The x-axis is in nanoseconds, while the y-axis is in units of charge (ADC units). For a discussion of conversion from ADC units to keV, see §6.2. The light response of Det-1(2) is measured to be $5.9 (4.3) \pm 0.1$ p.e./keV (see §5.2.3).

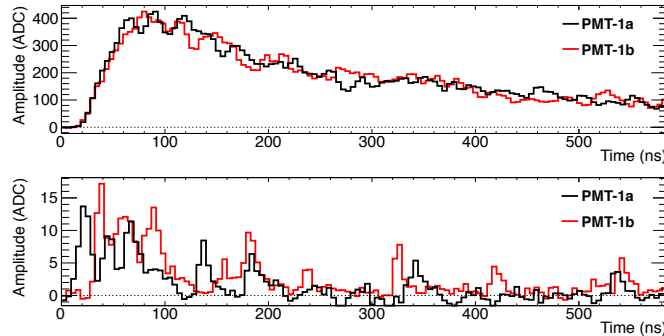


Figure 6.1: High energy (716 keV, top) and low energy (7.4 keV, bottom) waveforms extracted from Det-1. Both waveforms are from the ATWD0 channel. High energy events exhibit characteristic NaI(Tl) decay times while low energy signals become a series of single photoelectrons.

Waveforms are individually treated with three corrections that have been optimized for each readout channel. These are, in order of application:

- **Pedestal subtraction** removes digitizer noise. Regular pedestal runs read out waveforms from each PMT without threshold or coincident requirements, and the waveforms from these hour-long runs are averaged into a waveform characteristic of PMT noise. This average waveform is subtracted from all

coincident waveforms from the corresponding PMT. Pedestal runs are taken every two weeks. The effect of pedestal subtraction is shown in Figure 6.2.

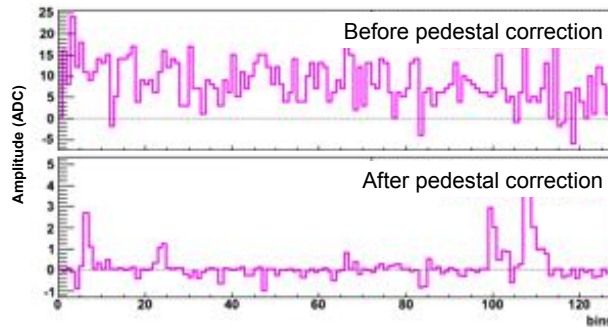


Figure 6.2: Effect of pedestal and baseline corrections on an ATWD1 waveform.

- **Baseline subtraction** corrects for drifting of the zero point in the waveform (i.e., an offset in the y-axis in Figure 5.13). The baseline algorithm records the height of the first bin in every waveform over a 2000s window and finds the mode of the distribution. This value is then subtracted from each bin of all waveforms in the first 1000s of the event sample. This is done separately for each channel of each PMT. Rare miscorrections from this algorithm are adjusted by a secondary baseline correction that brings the baseline closer to a zero starting point.
- **Droop correction** removes waveform alterations induced by electronic components in the DAQ. Waveforms without this correction exhibit an overshoot in the decay tail into negative height values. The effect of droop correction is shown in Figure 6.3.

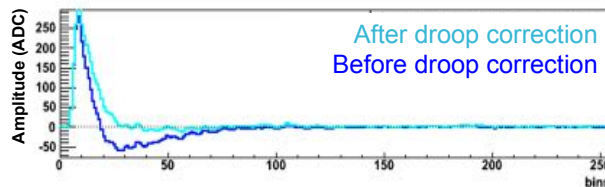


Figure 6.3: Effect of droop correction on an ATWD1 waveform.

6.1.2 Noise Removal

Noise events are identified and removed once waveform corrections have been performed. Three classes of noise are observed:

- **Electromagnetic Interference (EMI) events** are induced by hardware monitoring (see §5.2.2). Lowering the monitoring rate from 0.5 Hz to 0.017 Hz, starting in February 2012, reduced the EMI contribution from 21% (4.5%) to 0.9% (0.2%) of all Det-1 (Det-2) data. EMI events are the dominant source of noise from 2 - 20 keV. A sample EMI waveform is shown in Figure 6.4.

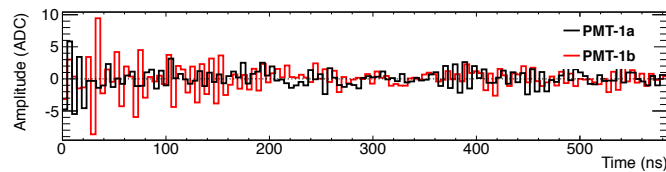


Figure 6.4: EMI waveforms are caused by interference during hardware monitoring. They are identified by their oscillatory nature. These waveforms are from the ATWD0 channels of both PMTs in Det-1.

- **Thin pulses** are likely triggered by interactions in the light guides and PMTs (possibly Cherenkov light ([87], [160])). They are characterized by differences in shape between the PMTs and by their fall time, which is an order of magnitude faster than NaI(Tl) scintillation events. Their waveform shape asymmetry indicates that the event occurs closer to one PMT than the other. An example of a thin waveform is shown in Figure 6.5.

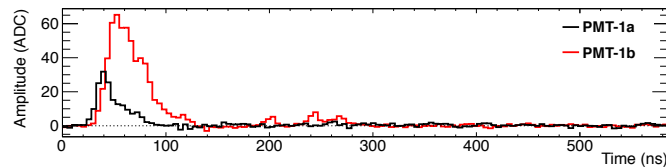


Figure 6.5: Thin pulse events, caused by interactions in the PMTs and light guides, are identified by their fall time, which is too fast for NaI events. Differences in the waveforms between coupled PMTs indicates that the event occurred close to one PMT. These waveforms are from the ATWD0 channels of PMT-1a and PMT-1b.

- **SPE-like noise** events are low-energy, centered at the single photoelectron (SPE) energy level. Their source is an ongoing topic of investigation, but these events trigger both PMTs at a rate of ~ 1 Hz, which is two orders of magnitude larger than expected from accidental coincidence. Thin pulses and SPE-like noise are the dominant sources of noise at sub-keV energies.

Two cuts are designed to remove noise events: an EMI cut and a cut on the number of peaks in the waveform. The EMI cut relies on the EMI cut variable, defined as:

$$\sum_{n=1}^{N-1} [(t_{n+1} - t_n) - (t_n - t_{n-1})]^2 \quad (6.1)$$

where t_n is the n th time bin of the waveform, and N is the end of the waveform. It takes advantage of the oscillatory nature of EMI waveforms to remove them from the event selection with 99.98% efficiency while preserving 99.99% of non-EMI events.

The peak finding cut counts the number of peaks with SPE-like features, requiring four such peaks in each PMT. This effectively places a cut on the minimum number of photoelectrons in the event and eliminates thin pulse events and low energy, SPE-like noise. This cut maintains a 60% signal passing efficiency and a signal-to-noise ratio of 16 down to 4 keV. The cut efficiency below 4 keV is currently under investigation but is shown to remove roughly half of the signal. The net result of these cuts produces the low energy spectrum in Figure 6.6, which shows the low energy signal and noise spectra in Det-1 before and after cuts.

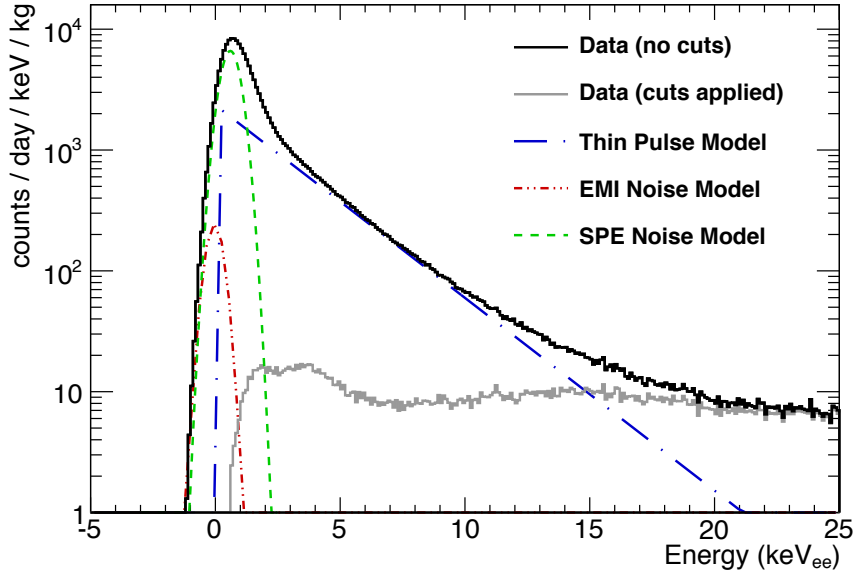


Figure 6.6: Application of noise cuts to the Det-1 low energy ATWD0 spectrum. The spectrum before (black) and after (gray) cuts. Models of the thin pulse, EMI, and SPE-like noise are shown in blue, red, and green, respectively.

6.2 Energy Calibration

6.2.1 Boulby Calibration

The first set of calibration data was taken with the DM-Ice17 crystals before they left the Boulby Underground Laboratory in the United Kingdom (~ 2850 m.w.e. overburden), where they had been stored (see §5.2). These calibration spectra were used as reference for the basic spectral shape and energy calibration estimates. Data was taken at room temperature both inside and outside the NaIAD experiment's lead castle, as shown in Figure 6.7. Both background data and ^{57}Co and ^{60}Co source data were taken, as shown in Figure 6.8. ^{60}Co decays with the emission of two strong gamma lines: one at 1173 keV (branching ratio of 99.85%) and one at 1333 keV (99.98%). ^{57}Co decays with the emission of a 122 keV gamma (85.6%) and a 136.5 keV gamma (10.7%). The calibration spectra for each crystal during these runs is shown with clear peaks from ^{60}Co (red), ^{57}Co (blue), and the 1461 keV gamma line from environmental ^{40}K (black). This data has proven to be a useful reference for both DM-Ice17 calibration and full detector R&D work (see Chapter 10).



Figure 6.7: Setup of Boulby calibration testing. Images, clockwise from top left: one of the copper-encapsulated crystals coupled to PMTs on either end; lowering a crystal into the lead castle; the lead castle setup with the crystal inside; covering the lead castle.

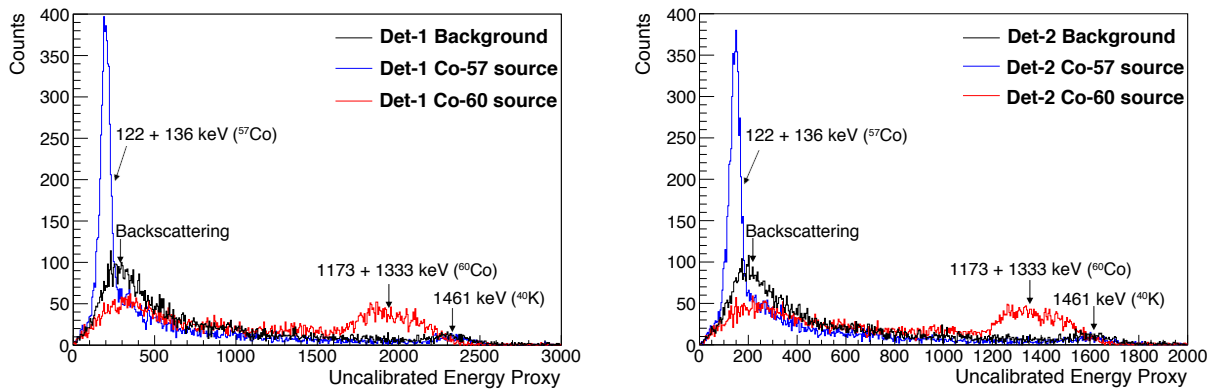


Figure 6.8: Spectra from calibration runs taken with Det-1 (left) and Det-2 (right) at Boulby. The black curve shows the background spectrum, with environmental ^{40}K visible at 1461 keV. The blue curve corresponds to a ^{57}Co source run and the red curve to a ^{60}Co source run. The x-axis is an energy proxy derived from the FADC channel.

6.2.2 PSL Calibration

Calibration data taken directly before shipment to the South Pole was used as a first approximation of the in-ice energy scaling. The data was taken above ground at PSL in Wisconsin (see §5.2.1) at room temperature when the prototype was in its final configuration and already housed in its shipping crate (see Figure 6.9). In addition to background data taking, a ^{207}Bi source was taped to the crate for source runs. ^{207}Bi decays with the emission of three gammas: 570 keV (97.8%), 1064 keV (74.5%), and 1770 keV (6.9%). ^{207}Bi peaks are visible in the calibration data, shown in Figure 6.10. The energy scaling from these runs allowed the identification of internal contamination lines from the in-ice data, which were then used for a more precise and accurate energy calibration, as described in §6.2.3 and §6.3.



Figure 6.9: Setup of PSL calibration runs. The detector was in its final configuration and already in the shipping crate. The ^{207}Bi source can be seen taped to the shipping crate on the right hand side.

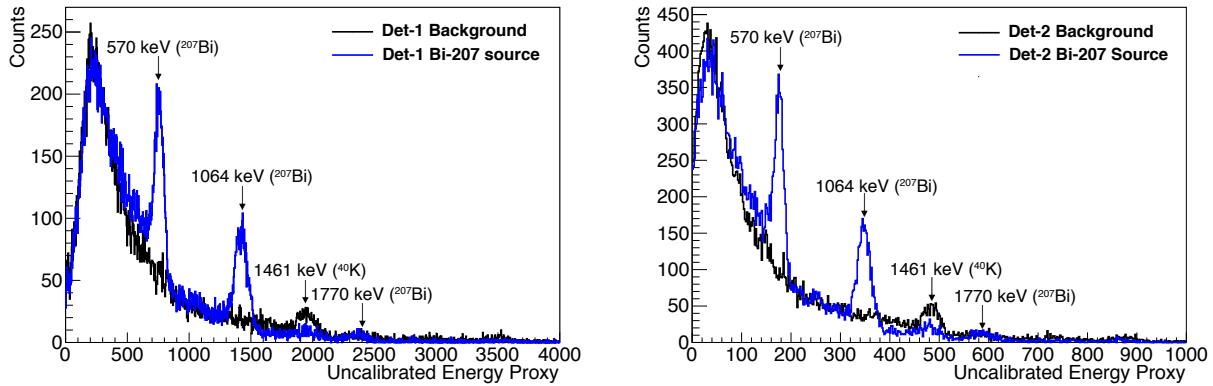


Figure 6.10: Results from the calibration runs done with ^{207}Bi for Det-1 (left) and Det-2 (right) directly before shipment. The two gamma peaks are visible in these uncalibrated ATWD1 spectra. The calibration from this source data was used as the initial approximate calibration in the ice.

6.2.3 Characteristic In-Ice Lines

The energy scaling of in-ice spectra is done using internal contamination lines for calibration. Energy is defined as the sum of all bins in the waveform (see Figure 5.13), which corresponds to integration over ~ 600 ns for the ATWD channels. The approximate energy scaling from source runs performed before deployment (see §6.2.2) allowed the isotopic identification of the lines, and all of the peaks identified in Figures 6.11 were used for calibration. Prominent lines are from the ^{238}U - and ^{232}T -chains, ^{60}Co , and ^{40}K . The insets of Figure 6.11 show the energy spectrum up to the highest energy alpha events while the larger images focus on the gamma region. Alphas were not used for energy scaling because they get quenched (see §4.1 and §4.2). The energy calibration is verified through analysis of cosmogenically-activated isotopes (see §6.3) and comparison with simulation (see §6.5).

Each of the ATWD channels is optimized for use over a particular part of the energy spectrum: ATWD0 is used for low energy events and saturates above 1.4 MeV; ATWD1 is used for gamma and alpha events and saturates above 8.63 MeV; ATWD2 is used for high energy alpha and muon events and is not observed to saturate (see §7.2). Linear calibration functions, parameterized in Table 6.1, were used for each channel because the <100 keV and 100-2800 keV gamma regions, when taken separately, have approximately linear light responses (see §4.2). The PMTs are fit separately due to differences in PMT gain. Their calibration functions are summed and divided by two to produce the combined-PMT spectra shown in Figure 6.11. The calibration functions are of the form:

$$E [\text{keV}_{\text{ee}}] = a + b \times x [\text{ADC counts}] \quad (6.2)$$

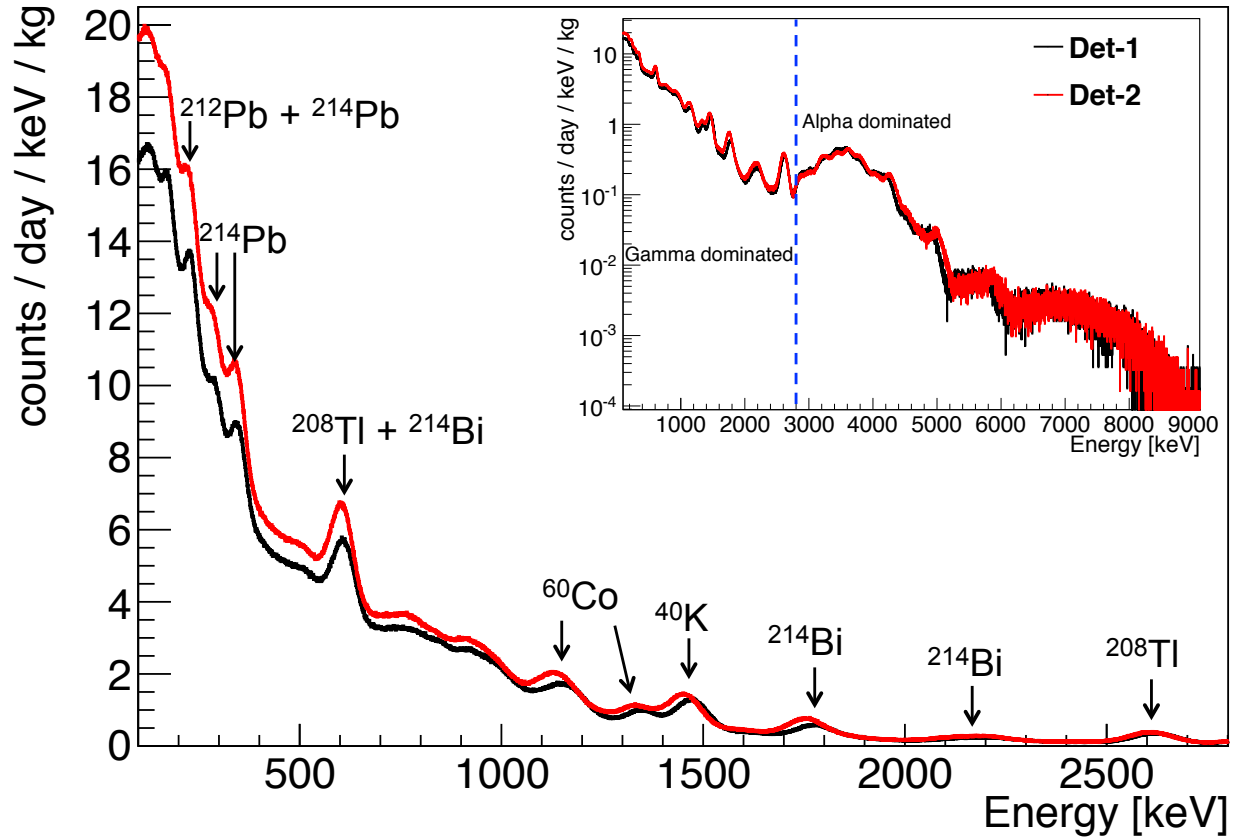


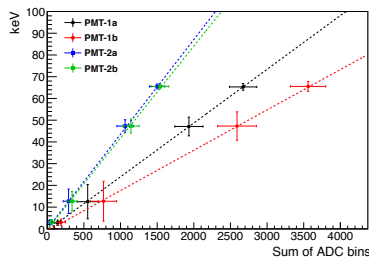
Figure 6.11: Energy spectrum in the 100 - 2800 keV region in ATWD1 for Det-1 (black) and Det-2 (red). All lines used in the energy calibration are labeled. Inset is the ATWD1 spectrum up to the highest energy alphas. This data is from 24 months of data from both PMTs on each crystal. The prominent lines are from the ^{238}U -chain, ^{232}Th -chain, ^{60}Co and ^{40}K .

Figure 6.12 shows the data points and calibration fits for the ATWD channels of each PMT. The x-axis is the integral under the waveform in ADC counts (i.e., the units of the y-axis of Figure 5.13).

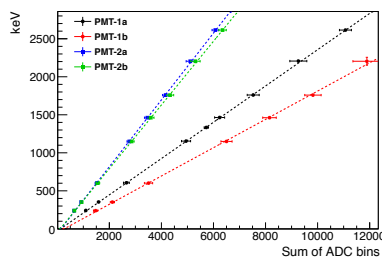
The non-linear light response of NaI (see Figure 4.12) requires that separate energy calibrations be used above and below ~ 100 keV. Figure 6.13 shows the low energy spectra for Det-1 (left) and Det-2 (right), with the peaks used for calibration labeled. The low energy region is studied with the ATWD0 channel, which is also calibrated using Equation 6.2, as parameterized in Table 6.1. Nonlinearities in response are evident in Figure 6.14, where low energy data for each PMT is shown alongside the extrapolation of its high energy calibration. The extrapolation produces a negative intercept, consistent with previous experimental observations [114, 161].

Table 6.1: Calibration functions for ATWD Channels

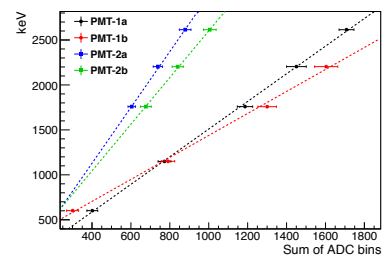
Channel		PMT-1a	PMT-1b	PMT-2a	PMT-2b
ATWD2	a	-27.89 ± 1.5	215.16 ± 1.3	-115.48 ± 14.5	5.33 ± 12.5
	b	1.537 ± 0.001	1.223 ± 0.001	3.11 ± 0.02	2.60 ± 0.01
ATWD1 (>100 keV)	a	-29.79 ± 0.61	-49.26 ± 0.78	-61.36 ± 0.65	-45.93 ± 0.73
	b	0.2386 ± 0.0001	$0.18610 \pm 1 \times 10^{-5}$	0.4393 ± 0.0002	0.4188 ± 0.0002
ATWD0 (<100 keV)	a	-0.7793 ± 0.10	-0.9254 ± 0.10	0 ± 0.1	0 ± 0.1
	b	$0.02473 \pm 6 \times 10^{-5}$	$0.01855 \pm 4 \times 10^{-5}$	$0.04355 \pm 7 \times 10^{-5}$	0.0423 ± 0.0001



(a) ATWD0



(b) ATWD1



(c) ATWD2

Figure 6.12: Linear calibration function of each PMT in DM-Ice17 for the ATWD0 (left), ATWD1 (center) and ATWD2 (right) channels. Each data point is associated with a peak identified in Figure 6.11. ADC bins refers to the integral of the waveform in its original units (i.e., units of the y-axis of Figure 5.13). Alphas are not used in calibration due to quenching.

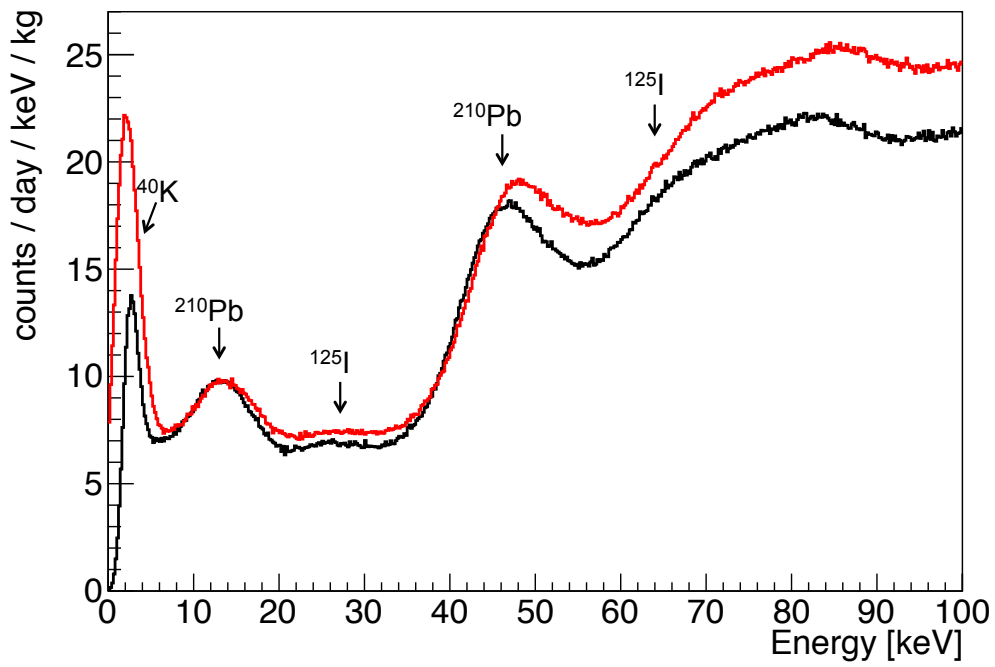


Figure 6.13: The low energy spectrum in ATWD0 from 24 months of data in Det-1(black) and Det-2(red). The cosmogenically-activated ^{125}I lines are visible, as are the ^{210}Pb gamma and surface X-ray peaks. The lowest energy peak is a combination of the 3 keV ^{40}K and noise. The Det-2 peak is higher than the same in Det-1 due to less efficient cuts.

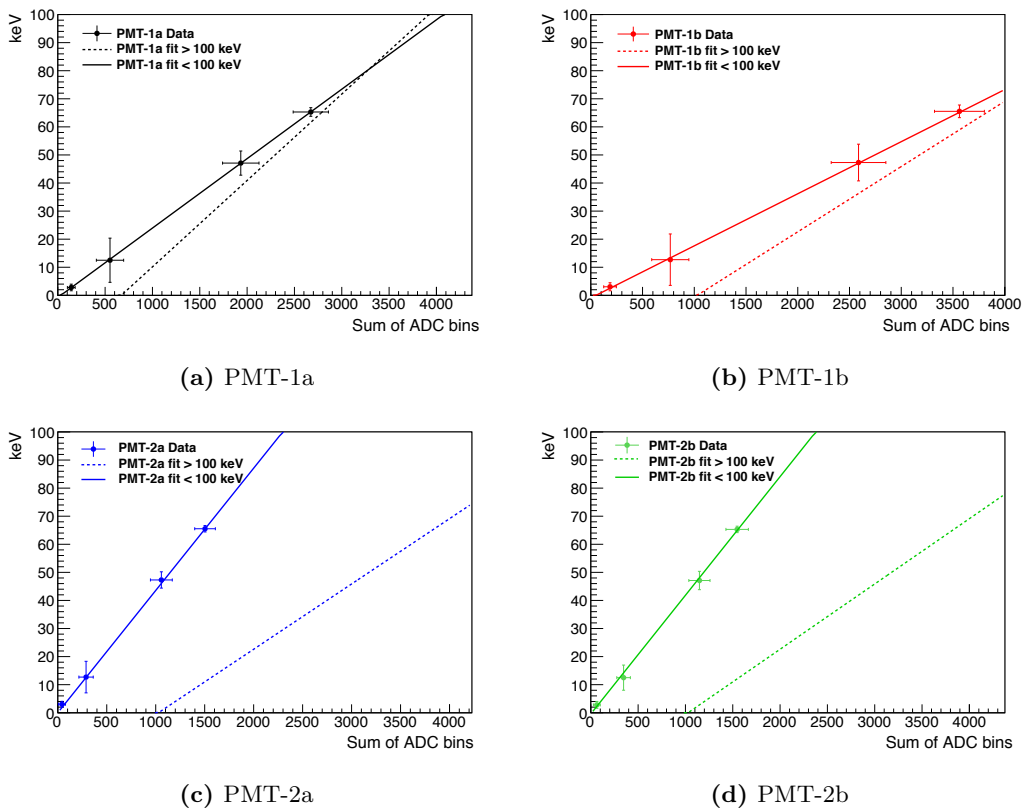


Figure 6.14: Comparison of the low energy calibration functions (solid line) of each PMT (from left: Det-1a, Det-1b, Det-2a, Det-2b), with the extrapolation of the high energy calibration (dotted line). Linear calibration functions are used for each function, but different calibration functions are required for high and low energy regions due to nonlinearities in crystal response. Extrapolation of the high energy waveforms to low energy produce negative intercepts, consistent with literature.

6.3 Cosmogenic Activation

Short-lived, cosmogenically-activated isotopes are valuable calibration tools because their decay times can be used to verify their identity. Observation of these short-lived decays offers an elegant solution to the impossibility of calibration source runs for DM-Ice17. Most notable of these isotopes is ^{125}I ($T_{1/2} = 59.4 \pm 0.01$ days). Figure 6.15 shows the ^{125}I peak decaying away at the expected energy, verifying that the calibration in this region is correct. The identification of the isotope is confirmed by its half-life, measured to be 59.4 ± 2.7 days. Cosmogenically-activated ^{54}Mn is also observed to decay with its expected half life (312 days), as shown in Figure 6.16.

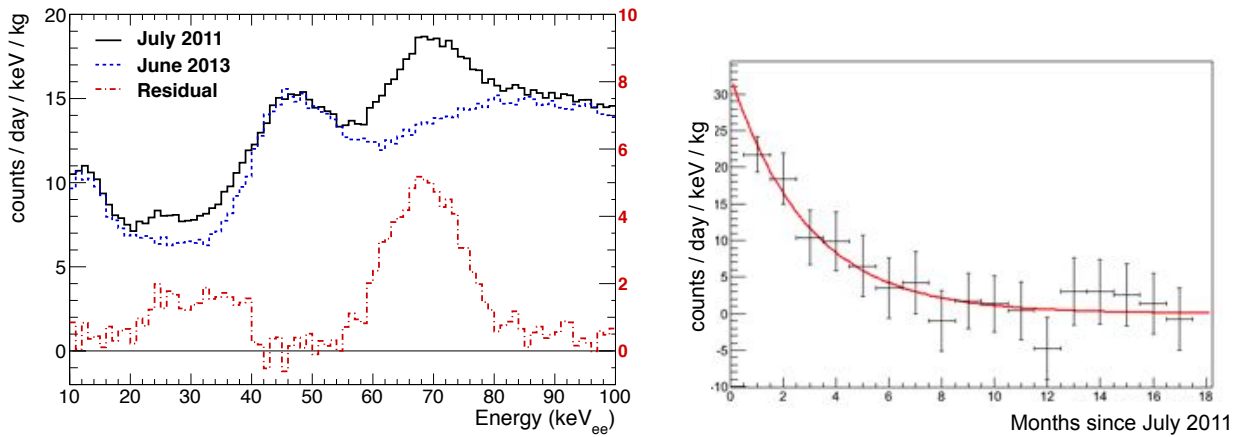


Figure 6.15: Comparison of spectra from July 2011 and April 2012 shows cosmogenically-activated ^{125}I decaying away. Both the sharp gamma peak and broad X-ray peaks are seen in the ATWD0 spectrum from Det-1 (left). The identification of the isotope is confirmed by its 59.4 day half-life (right).

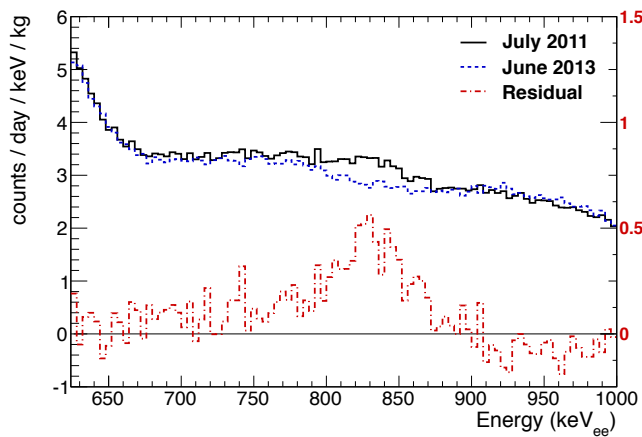


Figure 6.16: Comparison of spectra from July 2011 and June 2013 shows the cosmogenically-activated ^{54}Mn isotope decaying away. The identification of the isotope is confirmed by its 312 day half-life.

While the short-lived, cosmogenically-activated isotopes are useful for DM-Ice17 calibration, cosmogenic activation introduces unwanted internal backgrounds and thus the process must be minimized for DM-Ice250. Activation is more probable at higher altitudes, where the neutron intensity is higher: $I_n(h) = I_0 e^{-h/L}$, where I_0 is the flux at sea level, $L = 148 \text{ g/cm}^2$ is the neutron absorption length, and h is the pressure at altitude A [162]. The cosmogenic activation of components in DM-Ice17 is simulated using the ACTIVIA simulation package. Most activation occurs while the detector is awaiting deployment on the South Pole

surface (9,301 ft above sea level). Minimizing the wait time during this stage of deployment and potentially storing the detectors in the South Pole tunnels 40-50 ft beneath the surface will be sought for DM-Ice250 South. A full discussion of cosmogenic activation in DM-Ice17 is discussed in a publication currently in preparation.

6.4 Alpha Analysis

The internal contamination levels of the crystal due to the ^{238}U - and ^{232}Th -chains are derived from the analysis of alpha events. Alphas are used because they must originate in the crystal or they would have been stopped by other detector components, whereas gammas may originate elsewhere. Alpha events are separated from gammas through pulse shape discrimination (described in detail in §7.2). Alpha waveforms decay faster than gammas, as shown in Figure 6.17. The two event types are represented by Gaussian functions whose tails do not overlap. This separation is consistent with 100% efficiency, with less than one misidentified event expected in the event sample. The green band in Figure 6.17 is due to bismuth-polonium ("Bi-Po") decays. These events, which are part of the ^{232}Th chain, includes a ^{212}Bi isotope that decays to the short-lived ($t_{1/2} = 299 \pm 2 \text{ ns}$) ^{212}Po , which also decays in the readout window, as shown in Figure 6.18. These events display artificially small τ values in Figure 6.17 because a large portion of the alpha event is cut off, suppressing the mean time and the reconstructed energy of the events [77].

The comparison of alphas to simulation (see §6.5) determines that the U-chain and Th-chains are each out of equilibrium, which is not unexpected. The alpha quenching factor (see §4.1 and §4.2) is measured to be $\alpha/\gamma = 0.43 + 0.039 E_\alpha[\text{MeV}]$ for Det-1 and $\alpha/\gamma = 0.47 + 0.034 E_\alpha[\text{MeV}]$ for Det-2, consistent with measurements by DAMA and ANAIS, as shown in Table 6.2. In addition to alpha events, the crystal contamination levels from ^{40}I and ^{129}I are determined by their continuous beta spectra and the comparison of these spectra to simulation.

Table 6.2: NaI(Tl) Quenching Factor Measurements

Experiment	α/β
DM-Ice17 Det-1	$0.435 + 0.039E_\alpha$
DM-Ice17 Det-2	$0.47 + 0.034E_\alpha$
DAMA	$0.467 + 0.0257E_\alpha$
ANAIS	$0.483 + 0.032E_\alpha$

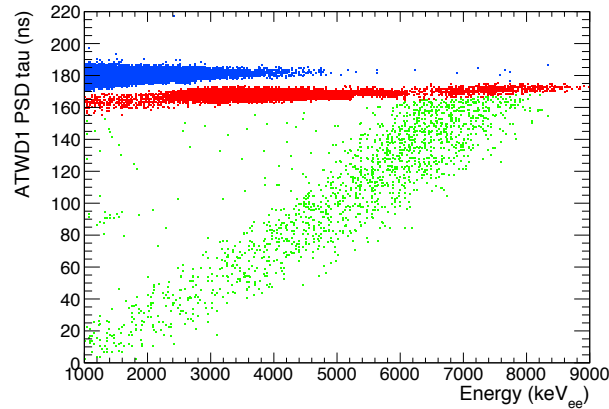


Figure 6.17: Separation of gamma (blue) and alpha (red) waveforms through pulse shape discrimination. This separation is 100% efficient. Green events are Bi-Po decays (see Figure 6.18) in which a short-lived gamma and its alpha daughter are read out in the same waveform, truncating the alpha tail and lowering the pulse shape discrimination variable. Shown is the separation in the ATWD1 channel of Det-1.

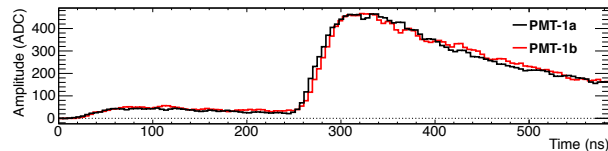


Figure 6.18: Sample waveform from a Bi-Po decay. The ^{212}Bi beta decay is observed, followed by the larger ^{212}Po alpha decay. These events make up the green event sample in Figure 6.17.

6.5 Simulation

Simulation is used to verify the energy calibration and to determine the contamination of detector elements. There is good agreement between simulation and data across the alpha and gamma regions, as shown in Figures 6.19 and 6.20, respectively. The alpha region agreement varies significantly between PMTs, due to uncertainties in the contamination levels and quenching factors. The gamma region shows agreement to within 70%. The DM-Ice17 simulation has been developed using the 4.9.5 release of the Geant4 software package (for details, see [77]). The simulation includes the full detector geometry, hole ice, and Antarctic ice. Crystal contamination levels are derived from analysis of the alpha region and beta shoulders, as described in §6.4; the quartz light guides and PMT contamination levels were estimated from databases and manufacturer specifications; the pressure vessel, PTFE supports, copper plate, silicone gel, and drill ice contamination levels were counted at SNOLAB, and the Antarctic ice studies were extrapolated from

dust levels measured in the Vostok ice core [163]. Table 6.3 compiles the simulated components, isotopes, and the source of contamination levels that feed the simulation. Contributions from the PTFE supports, copper rods, copper plates, silicone optical gel, quartz light guides, drill ice, and glacial ice are found to be negligible. Details of the simulation and contamination levels can be found in [77].

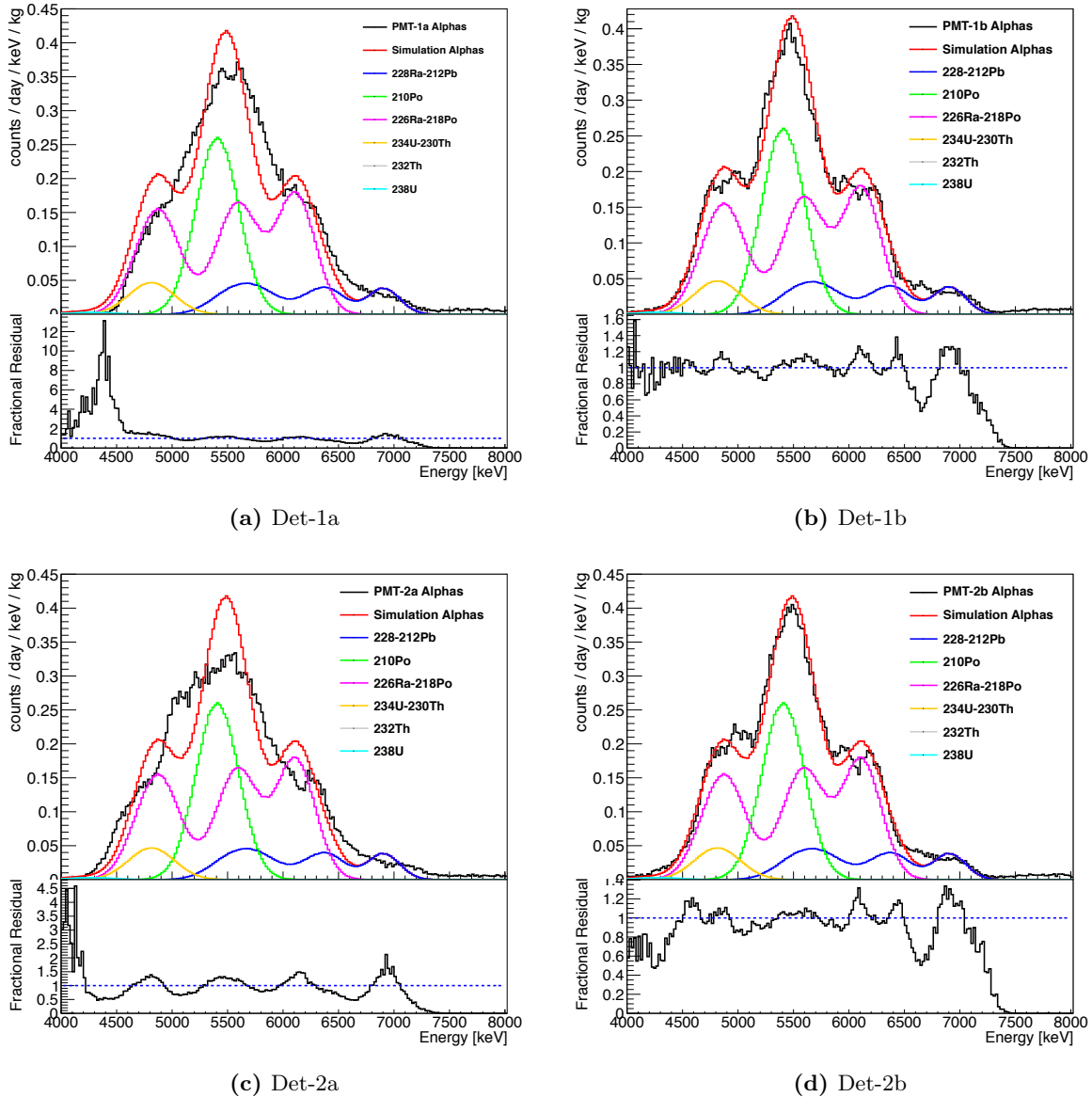


Figure 6.19: Comparison and residuals of the alpha region of each PMT (black) compared to simulation (red). Each PMT is shown individually due to differences in alpha response.

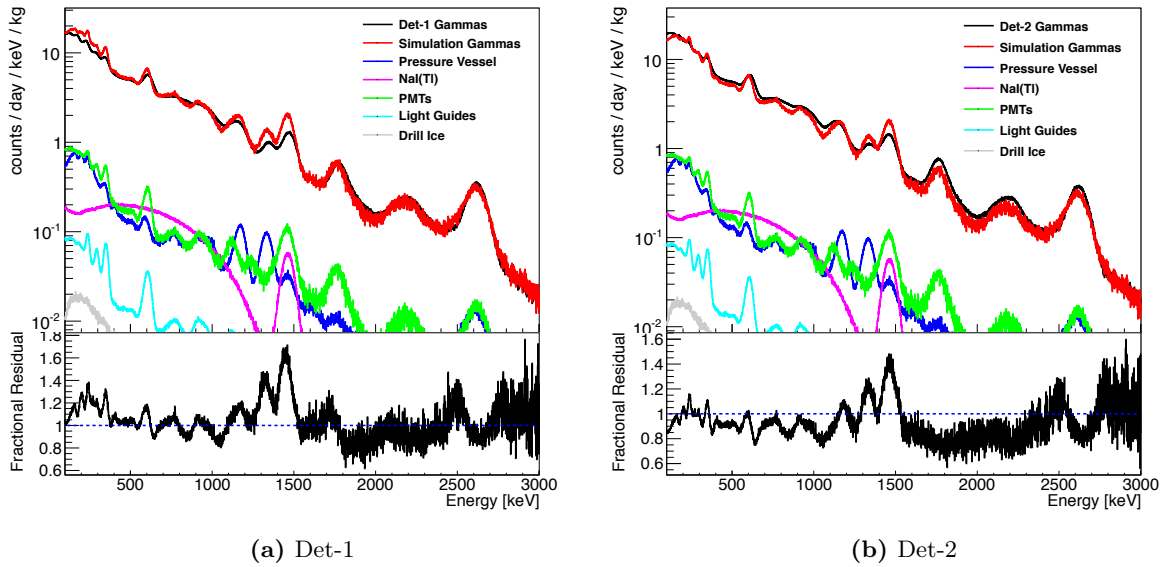


Figure 6.20: Comparison of data and simulation over the gamma region from each detector Agreement is shown over the entire region, indicating an understanding of the energy calibration and contamination levels. Data shown is from the ATWD1 channel.

Table 6.3: Simulation components: simulated isotopes, measurements, and contamination [77]

Component	Simulated Isotopes	Measurement
NaI(Tl) crystal	^{238}U , ^{232}Th , ^{40}K , ^{129}I , cosmogenics	In-ice analysis (see §6.4)
Copper encapsulation	^{238}U , ^{232}Th , ^{40}K , cosmogenics	SNOLAB
Quartz light guides	^{238}U , ^{232}Th , ^{40}K , cosmogenics	Literature
PMTs	^{238}U , ^{232}Th , ^{40}K , cosmogenics	Literature
Pressure vessel	^{238}U , ^{235}U , ^{232}Th , ^{40}K , ^{60}Co , cosmogenics	SNOLAB
Drill ice	^{238}U , ^{232}Th , ^{40}K , ^{235}U	SNOLAB
Antarctic ice	^{238}U , ^{232}Th , ^{40}K	Vostok ice cores

The low energy data is consistent with simulation once cut efficiencies are accounted for. Noise cuts below 4 keV remove roughly half of the data, as shown in Figure 6.21. Data and simulation agree to within a factor of 2.2 (5.2) below 10 keV in Det-1 (Det-2), consistent with expectation based on the cut efficiencies. Above 10 keV, agreement is within 10 (40)% in Det-1 (Det-2). Visible features in the low energy region

include a broad peak around 14 keV from ^{238}U surface contamination of the copper encapsulation, a peak at 3 keV from ^{40}K in the crystal, and noise below 2 keV (see Figure 6.6). A flat background of 7.9 ± 0.4 dru is observed in the 6.5 - 8 keV region, below which the spectrum is dominated by the ^{40}K peak.

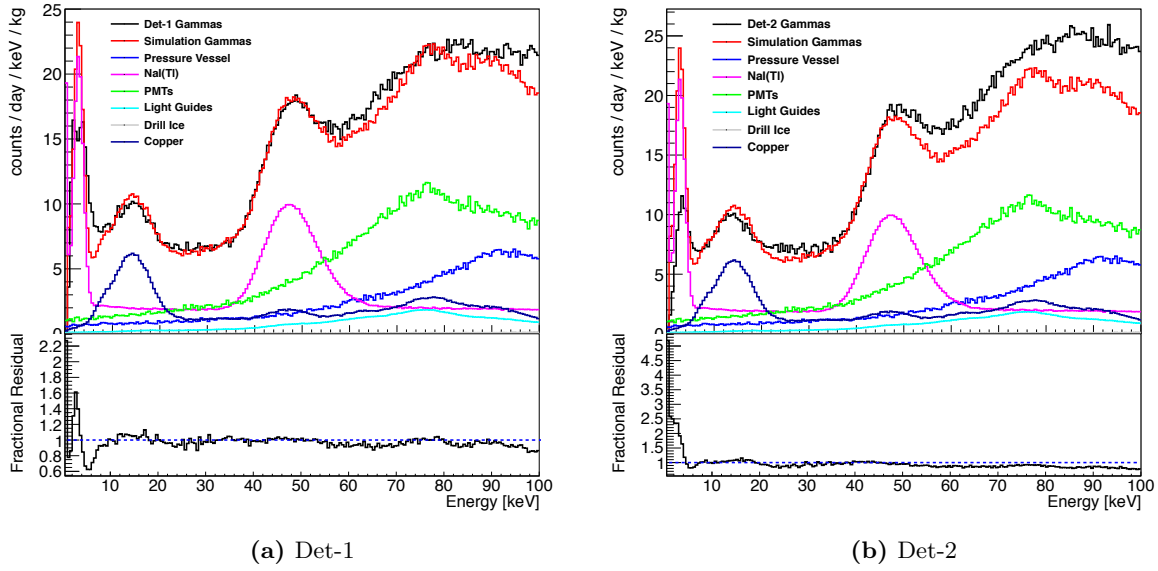


Figure 6.21: Comparison and residual of data and simulation in the low energy region of Det-1(left) and Det-2 (right). Data and simulation are in agreement after accounting for cut efficiencies. Data shown is from the ATWD0 channel.

Chapter 7

Analysis of Muon Events

7.1 Atmospheric Muons

Atmospheric muons are a significant background in underground experiments because they can propagate from their production location in the upper atmosphere to penetrate the Earth's surface and trigger detectors [1]. They are of particular importance in modulation experiments because the muon rate is known to modulate annually. Muons are produced when cosmic rays (predominantly protons) enter the atmosphere and interact with atomic nuclei to produce pions and kaons. These mesons decay to muons if the distance between interactions is long enough (i.e., fewer interactions with other atmospheric particles). Changes in the atmospheric density as a result of seasonal temperature changes lead to variations in muon production, as discussed in §7.1.1 and §7.2.2. The mean energy of muons at the Earth's surface is roughly 4 GeV, increasing with zenith angle, as shown in Figure 7.1 [1].

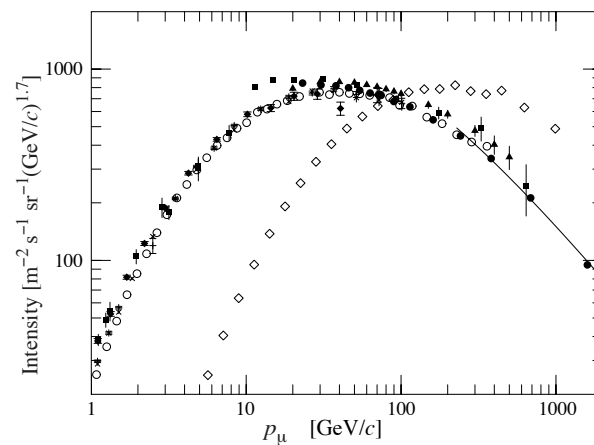


Figure 7.1: Measured atmospheric muon spectrum at sea level for particles produced by cosmic rays with an incident angle of 75° (\diamond) and 0° (each symbol representing a different measurement of the vertical muon flux) [1]. Intensity is defined as $I_\mu = p_\mu^{2.7} dN/dp_\mu$, where p_μ is the muon momentum.

As muons propagate from the upper (~ 15 km elevation) atmosphere to an underground detector, they lose energy through ionization and through radiative processes: pair production, bremsstrahlung, and photonuclear reactions. Only high energy muon will reach underground detectors, and the differential flux of higher energy (>100 GeV) muon is described as [164]:

$$\Phi_{\mu}(E_{\mu}) = \Phi_N(E_{\mu}) \left[\frac{A_{\pi\mu}}{1 + B_{\pi\mu} \cos \theta^* E_{\mu}/\epsilon_{\pi}} + \frac{A_{\kappa\mu}}{1 + B_{\kappa\mu} \cos \theta^* E_{\mu}/\epsilon_{\kappa}} \right] \quad (7.1)$$

where $\Phi_N(E_{\mu})$ is the primary nucleon spectrum at the muon energy, E_{μ} , and the first and second fractional terms correspond to muon production from pion and kaon decays, respectively. $A_{i\mu}$ includes the physics (branching ratio, cross-section, decay distribution) of meson decay to muons, while the denominator terms account for the competition between meson decay and interaction. The denominator terms depend on ϵ_i , the characteristic energy for each channel, and θ^* , the local zenith angle at production, which takes the curvature of the Earth into account. These critical energies correspond to 111 GeV for pions and 823 GeV for kaons at a mean atmospheric temperature of 211 K. Below the critical energy, $E_i = \epsilon_i/\cos \theta^*$, meson decay dominates; above this energy, meson interaction takes over [165]. The temperature dependence of this term drives the muo modulation described in §7.1.1.

Muon energy loss during propagation underground is described in terms of the distance traveled, X :

$$\frac{-dE_{\mu}}{dX} = a + bE_{\mu} \quad (7.2)$$

where a [$MeV \cdot cm^2 \cdot g^{-1}$] is the ionization energy loss parameter, and b [$cm^2 \cdot g^{-1}$] is the fractional energy loss parameter from the sum of radiative processes. a is roughly 2 MeV/cm in ice, while b is an energy-dependent variable, of order $10^{-6} cm^{-1}$, whose precise value in ice increases with energy, as shown in Table 7.1 for a muon in ice ($\rho = 0.9196 \pm 0.0050 g/cm^3$) [1]. Above the critical energy, $\epsilon_c = \frac{a}{b}$, energy loss due to radiation overtakes that due to ionization. For muons in ice, this occurs at several hundred GeV. The muon Minimum Ionizing Particle (MIP) energy, where mean energy loss is at a minimum, is hundreds of MeV, and most relativistic muons interact as MIPs. This energy loss during propagation creates a depth-dependent

Table 7.1: Radiative energy loss parameter (b) for muons of varying energies in ice

E_{μ} [GeV]	b [$10^{-6} cm^{-1}$]
10	1.53
100	2.31
1000	2.92
10000	3.38

energy threshold for muon observations in underground detectors. They lose roughly 2 GeV propagating from the high atmosphere to sea level, and as they propagate underground, lower energy muons continue to get attenuated. Larger depths thus see a lower rate of muons, as shown for water and ice in Figure 7.2. The mean range, X , of a muon with initial energy $E_{\mu,0}$ in a medium is dictated by the attenuation parameters described above [1]:

$$E_{\mu,0} = (E_{\mu} + \epsilon_c)e^{bX} - \epsilon_c \quad (7.3)$$

where E_{μ} is the energy of the muon after it has propagated a distance X in the medium. This equation dictates that a muon must have an energy of several hundred GeV to penetrate 2450 m of ice (2200 m.w.e.). Both the MUSIC and CORSIKA muon simulations predict the average energy of muons at 2200 m.w.e. to be roughly 300 GeV [166, 167]. The depth-dependence of the muon energy spectrum due to the attenuation of low energy muons is shown for the South Pole ice in Figure 7.3. DM-Ice17 is situated at 2450 m, between the red and orange curves [166]. These used hadronic interactions from SIBYLL [168], weighted to the Hoerandel spectrum [169].

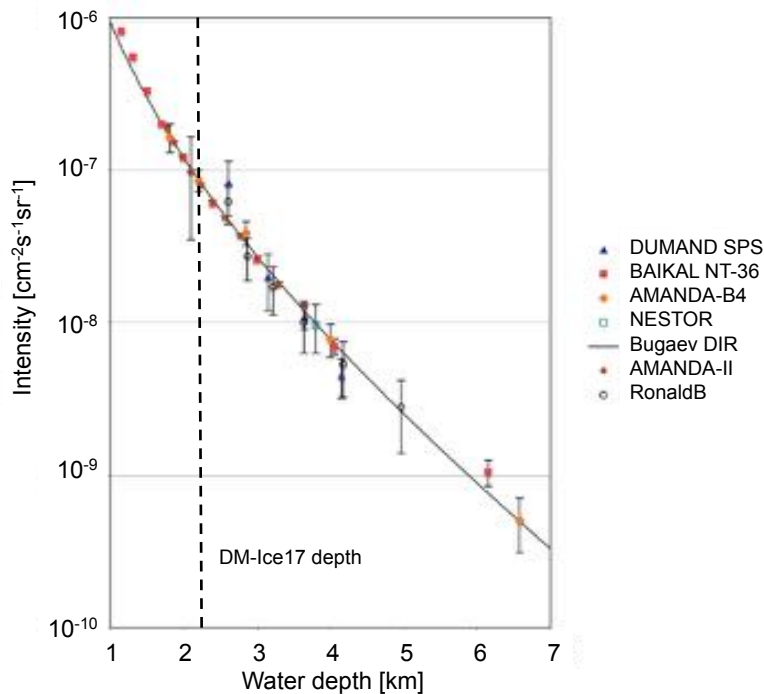


Figure 7.2: Depth dependence of the muon flux in water and ice, as predicted by theory (solid line) and measured by underground particle physics experiments (data points) [170]. The deepest AMANDA point is from the observation of muon flux as a function of zenith angle, which was converted to a depth dependence [171]. The AMANDA detector is located 1500 - 2000 m deep in the ice [172]; IceCube has not released such a figure.

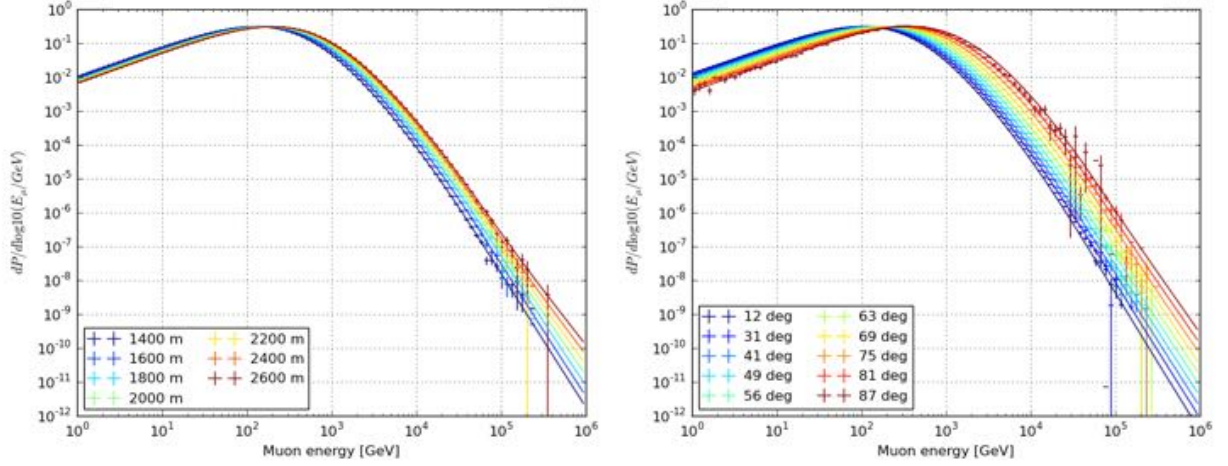


Figure 7.3: The energy distribution of muons as a function of ice depth (left) and zenith angle (right), as determined by the CORSIKA simulation [166]. The depth-dependent plot fixes a zenith angle of 41° (chosen arbitrarily), and the zenith-dependent plot fixes a depth of 1400 m (top of IceCube). DM-Ice17 is located at 2450 m deep. Muon simulations (CORSIKA [166], MUSIC [167]) have predicted the spectral peak at DM-Ice17 depths to be roughly 300 GeV [167].

7.1.1 Annual Modulation of Muon Rate

The atmospheric muon flux seasonally varies due to its dependence on the atmospheric temperature. The higher temperature in the summer, T , lowers the atmospheric density, ρ :

$$\rho = \frac{P}{R_s T} \quad (7.4)$$

where P is the pressure and R_s is the specific gas constant for air. Higher temperatures in the summer increase both the mean free path for atmospheric mesons and the fraction of them that decay to muons. The critical energies for pion and kaon decay to muons at a particular atmospheric depth are inversely proportional to the atmospheric density, driving the temperature dependence of the flux. The muon flux, I_μ , is parameterized as an average muon flux, I_μ^0 , and a modulating flux of amplitude ΔI_μ . It is related to atmospheric temperature through the correlation coefficient, α_μ . The correlation coefficient is dependent upon the energy and zenith angle. It can be derived from the dependencies in Equation 7.1 and expressed as:

$$\alpha_\mu(E_\mu, \theta) = \frac{T}{\Phi_\mu(E_\mu, \theta)} \frac{d\Phi_\mu(E_\mu, \theta)}{dT} \quad (7.5)$$

The correlation coefficient is averaged over zenith angle and expressed in terms of the effective atmospheric temperature to produce the muon flux dependence:

$$\frac{\Delta I_\mu}{I_\mu} = \alpha_\mu \frac{\Delta T}{T} \quad (7.6)$$

Temperature dependence requires the muon flux to follow a roughly sinusoidal function throughout the year, parameterized by the period, T , and the phase, t_0 :

$$I_\mu = I_\mu^0 + \Delta I_\mu = I_\mu^0 + \delta I_\mu \cos\left(\frac{2\pi}{T}(t - t_0)\right) \quad (7.7)$$

The modulation is expected to have a roughly one year period with a maximum rate in the summer. This muon modulation will thus be completely out of phase between the two hemispheres. Figure 7.4 shows the muon flux at the South Pole, as measured by IceCube (top) compared to the flux in the Northern Hemisphere, as measured by Borexino (bottom).

The muon modulation amplitude varies at underground sites due to geographic location and overburden. The modulating muon flux at LNGS (3800 m.w.e.) has been measured by Borexino to be $3.41 \pm 0.01\%$ $\text{m}^{-2}\text{s}^{-1}$ with a $1.29 \pm 0.07\%$ fractional amplitude and a phase of June 28th ± 6 days [95]. IceCube has measured the muon flux at the South Pole (1500-2200 m.w.e.) to be 10% [165]. IceCube sees a higher cosmic ray flux due to its location at the geographic South Pole: the Earth's magnetic field funnels cosmic rays towards the poles, leading to an increase in the observed flux [165]. The increased fractional modulation is due to seasonal variations being maximal at the South Pole, which observes only one sunset and one sunrise per year. Temperature changes are maximized, leading to an increased muon modulation [165]. The muon modulation is known to increase with energy, reaching the fractional modulation of the temperature fluctuation at the highest energies, as shown in Figure 7.5 [173]. The muon modulation though DM-Ice17 (see §7.2.2) is thus expected to be more closer to the temperature fluctuation than that of the entire IceCube detector because it is located at the bottom of IceCube. This means that only the highest energy muon can penetrate to reach DM-Ice17, leading to a modulation that is correlated to higher energy particles that are produced higher in the atmosphere and are more tightly coupled to the temperature modulation amplitude.

Deviations from a sinusoidal modulation limit the quality of a sinusoidal fit to the modulation. These deviations are due to the imperfect sine of temperature variations and differences in the modulation from year to year. These deviations are observed when attempting to fit the IceCube muon modulation from year-to-year, as shown in Figure 7.6. IceCube observes a correlation coefficient (see Equation 7.5) of $0.860 \pm 0.002(\text{stat}) \pm 0.010(\text{sys})$ [165]. Earlier results are shown in Figure 7.7, with effective temperature indicating that the muon fluctuation is extremely coupled to the temperature [153]. The effective temperature assumes an isothermal atmosphere, weighted by layer for muon production. The phase obtained by fitting a sinusoid to the muon rate can vary by over 10 days, depending on the year and range fit, simply due

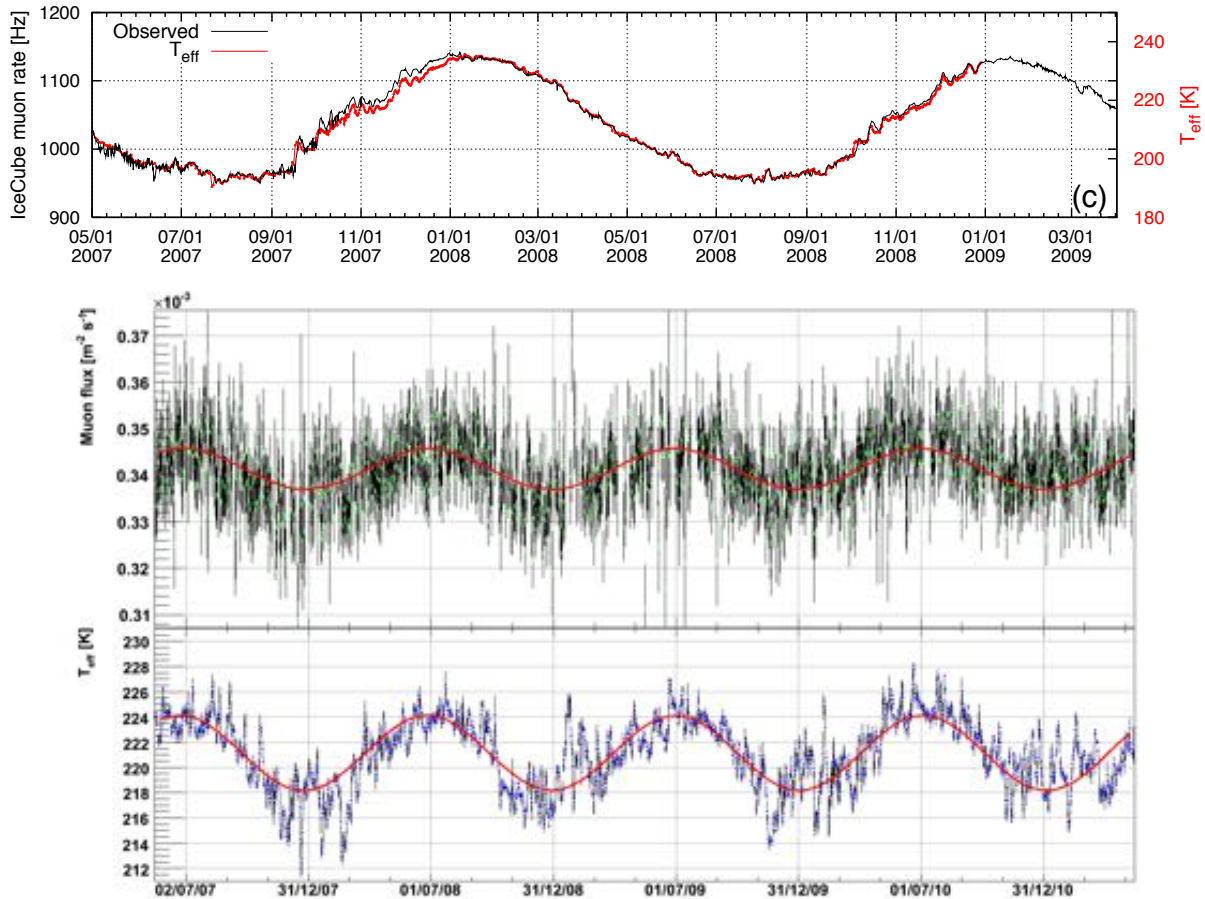


Figure 7.4: Correlation of IceCube (top) [165] and Borexino (middle) [95] trigger rate with temperature. IceCube data is shown, in black, for two years compared to temperature, in red. Borexino is shown in green and black (middle) to temperature in the Northern hemisphere (blue, lower). Both the Borexino and Northern Hemisphere temperature distributions are fit to a sine function, shown in red.

to the nature of the fluctuations. IceCube has not reported a sinusoid fit to the muon modulation due to these considerations. Borexino, with a phase of 28 ± 6 days, observes a $0.93 \pm 0.04(\text{stat})$ correlation coefficient with Northern hemisphere, as shown in Figure 7.7, offset by five days from the temperature maximum on 23 ± 0.4 days, as reported by the European Center for Medium-range Weather Forecasts [95]. The increased correlation at Borexino is expected due to its increased depth. The preferred fit to the Borexino includes two sinusoids to partially account for deviation from a perfect sine; the second sinusoid has a period of 179 ± 2 days and an amplitude of $0.37 \pm 0.07\%$ [95]. With a 45 day separation from the DAMA phase (May

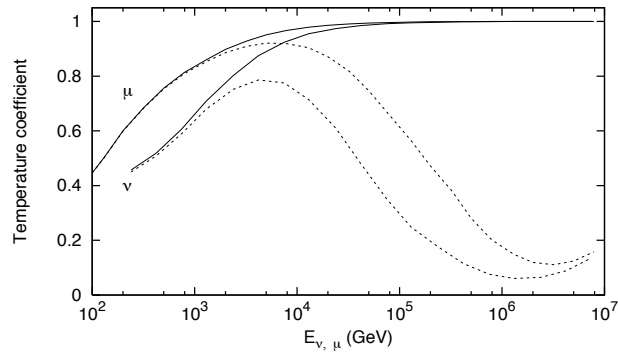


Figure 7.5: Energy dependence of muon modulation. Higher energy muon modulation with a larger fractional amplitude, approaching the temperature modulation at the highest energies. Solid (dashed) lines include (do not include) charmed hadron production. Figure from [173].

14 ± 7 days), the dominant Borexino is out of phase with the DAMA signal to 4.9σ , but the described effect introduces a systematic offset to the phase in the LNGS muon flux.

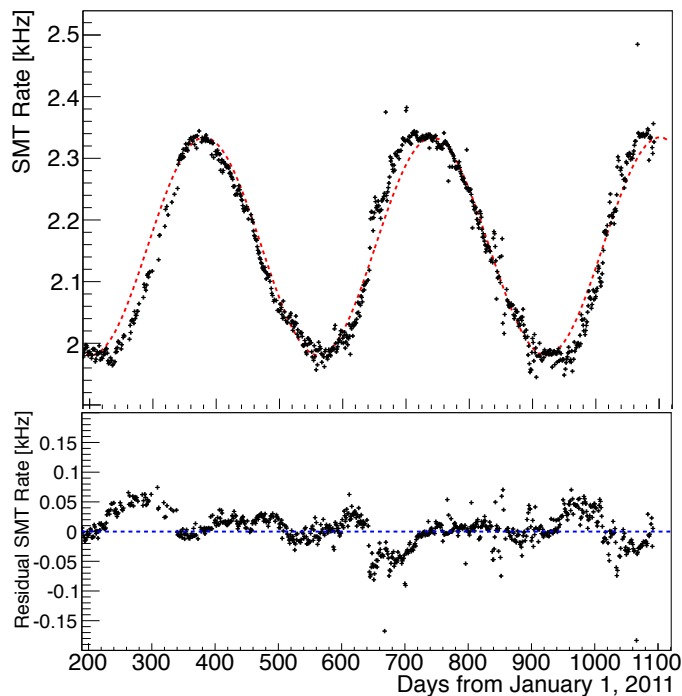


Figure 7.6: Uncertainty introduced by imperfect sine of muon rate modulation. The IceCube trigger rate (top, black) is fit to a sinusoid with a floating period (top, red). The imperfect sinusoid of the modulation is shown in the disagreement on the rising edge of the modulation, visible in the comparison plot (top) and the residual (bottom).

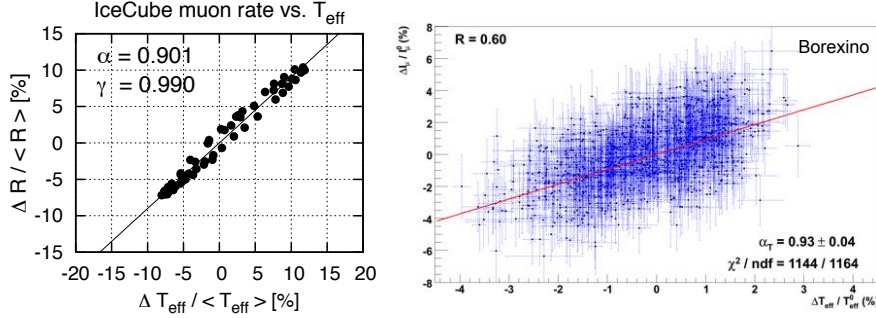


Figure 7.7: Correlation of IceCube trigger rate (left, center [153]) and Borexino trigger rate (right, [95]) with temperature. IceCube has a 90.1% correlation with effective temperature fluctuations in the atmosphere; Borexino has a 93% correlation.

7.1.2 Rate Through DM-Ice17

The rate of muons that pass directly through DM-Ice17 is dependent upon the muon rate at the surface of the ice, the cross-sectional area, and attenuation through the ice overburden. The IceTop water Cherenkov tanks observe a vertical muon rate at the South Pole surface (elevation of 9,300 ft) in December of $176 \pm 1 \mu/\text{m}^2/\text{s}/\text{sr}$ for muons above the IceTop threshold of 335.4 MeV/c [174]. The total muon rate is approximated by integrating over the hemisphere, which spans the zenith range from zero to $\frac{\pi}{2}$. Assuming the flux at zenith angle θ to be:

$$\Phi_{\mu}(\theta) = \Phi_{\mu}(0) \cos^2 \theta \quad (7.8)$$

the integrated downward flux can be determined from the vertical rate [175]. For the South Pole surface, this downward rate becomes:

$$\Phi_{\mu}[\mu/\text{m}^2/\text{s}] = 2\pi \int_0^{\pi/2} 176 \mu/\text{m}^2/\text{s}/\text{sr} * \cos^3 \theta \sin \theta d\theta = 276 \mu/\text{m}^2/\text{s} \quad (7.9)$$

The ice overburden lowers the muon flux at DM-Ice17 by five orders of magnitude. The muon flux underneath 2200 m.w.e. of ice has been simulated to be roughly $1.9 \times 10^{-3} \mu/\text{m}^2/\text{s}$, assuming a minimum muon energy of 1 GeV (see Table 7.2) [167]. Approximating the muon flux as predominantly vertical, the DM-Ice17 crystal cross-section is the surface area of interest. The crystals are 14 cm in diameter, creating a 0.015 m^2 cross-section for each prototype. Because the crystals are optically isolated from the ice, only muons that pass directly through the crystal are observed. This predicts a flux of muons through each crystal of:

$$1.9 \times 10^{-3} \mu/\text{m}^2/\text{s} \times 0.015 \text{ m}^2 = 2.9 \times 10^{-5} \mu/\text{s} \sim 2.5 \mu/\text{crystal}/\text{day} \quad (7.10)$$

Table 7.2 summarizes the muon flux at three locations of interest: sea level, the South Pole surface, and at the DM-Ice17 depth. The minimum momentum considered for the South Pole surface was 335.4 MeV/c, as

measured by IceTop, and 1 GeV/c for the sea level measurements and for the simulations of flux 2000 m.w.e. deep in ice. The higher elevation of the South Pole surface leads to a higher muon flux, and an improvement of five orders of magnitude is provided by the ice overburden of DM-Ice17.

Table 7.2: Muon Flux Comparison (no shielding)

Location	Muon Flux	Minimum Momentum	Reference
Sea level	$70 \mu/\text{m}^2/\text{s}/\text{sr}$	1 GeV/c	[1]
South Pole surface	$176 \mu/\text{m}^2/\text{s}/\text{sr}$	335.4 MeV/c	[174]
South Pole, 2000 m.w.e.	$1.22 \times 10^{-3} \mu/\text{m}^2/\text{s}/\text{sr}$	1 GeV/c	[167]

7.2 Muons in DM-Ice17

7.2.1 Identification

Muons passing through DM-Ice17 are expected at a rate of 2-3 muons/crystal/day, deposit ~ 80 MeV in the crystal (see §7.2.3), and induce scintillation waveforms with a pulse shape similar to that of gamma events. These characteristics combine to form the muon tag. Specifically, muons in DM-Ice17 are identified by their waveform height and their characteristic pulse shape; the height cut separates muons from gammas, while pulse shape discrimination (PSD) separates muons from alphas where their height distributions overlap. This identification is verified through the observed muon rate and coincidence with IceCube (see Chapter 8).

Muons are separated from alphas using PSD. Muons and gammas exhibit a similar pulse shape, while the alpha pulse shapes have a faster decay time, as shown in Figure 7.8. PSD allows the complete rejection of alphas from the muon event selection, with their PSD distributions characterized by two non-overlapping normal distributions, as shown in Figure 7.9. No misidentifications in either direction are expected in the 3.5 yr event sample. The PSD parameter, τ , is defined as:

$$\tau = \frac{\sum_{h_m+100}^{h_m+100} h_i t_i}{\sum_{h_m}^{h_m+100} h_i} \quad (7.11)$$

where h_i is the height of the waveform in bin t_i . To account for small variations in waveform trigger time, the τ sum is taken over 100 bins, starting with the half-maximum bin (“half-max”, h_m). Half-max is defined as the first bin with a height equal to half the height of the waveform. If there are fewer than 100 bins after

half-max, the sum is taken to the end of the waveform. ATWD1 pulse shape discrimination is used because it provides better separation than ATWD2 due to its higher gain. Similarly, single PMT cuts provide better separation than a cut using combined information across both PMTs, so cuts on Det-1a and Det-2a are used for Det-1 and Det-2, respectively.

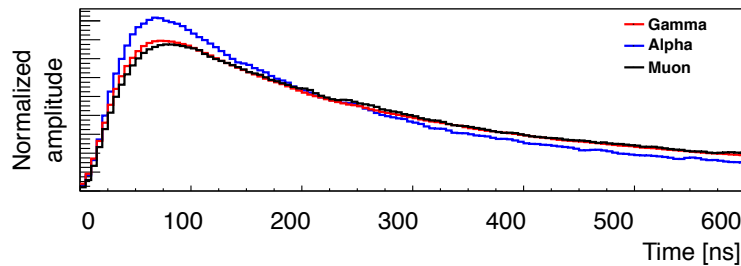


Figure 7.8: Pulse shapes characteristic of muon (black), alpha (blue) and gamma (red) events in the detector. PSD is used to separate alphas from the gamma/muon stream. The shown waveforms represent a normalized average waveform from each event type.

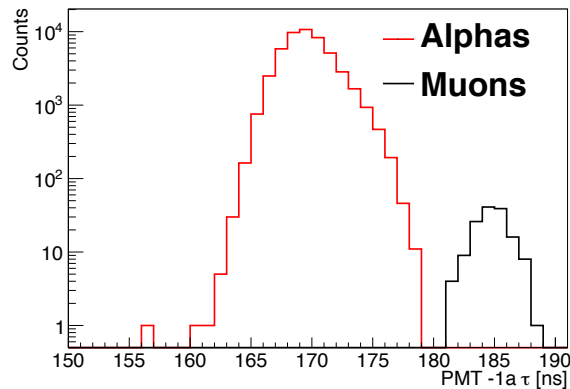


Figure 7.9: Quality of the ATWD1 PSD cut. Alphas (red) are completely removed from the muon event sample (black), and no muons are expected to be misidentified as alphas. Data shown is from one year on Det-1a (left) and Det-2a (right).

Muons produce the highest energy depositions observed in the detector, so their waveform heights are generally larger than those associated with alphas or gammas. Gammas are removed from the muon event sample from a height cut to high efficiency, as shown in Figure 7.10. Fewer than 3 gammas are expected in the muon sample every year, as determined by fitting the gamma spectrum cutoff, although some muons do bleed into the gamma sample. Because the muon energy deposition is proportional to the path length through the

crystals, muons that clip the edge of the detector are indistinguishable from gamma events. These lost events are a small fraction of the muon event sample, as evidenced by agreement between observed and predicted muon rates. ATWD1 waveform height is used for muon identification due to its higher gain. ATWD2 energy calibration is used for analysis because the other channels saturate over the muon energy regime.

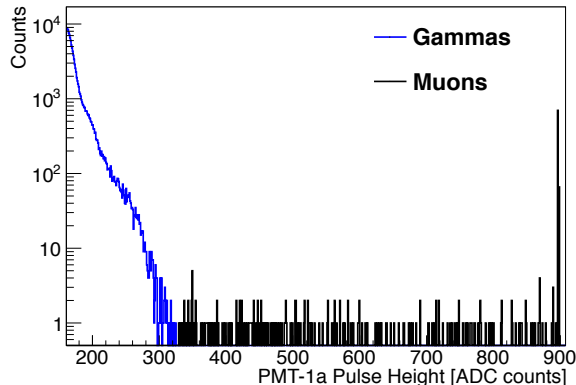


Figure 7.10: Distribution of ATWD1 pulse height separating the gamma (blue) and muon (black) event samples. Data is shown for 1 year of Det-1a (left) and Det-2a (right). Less than three gammas per year are expected in the muon sample.

To be classified as a muon, an event must be tagged by one of two conditions: waveform height or combined height and PSD. The height tag simply requires that the height of the ATWD1 waveform - before droop or baseline corrections - be greater than the highest alphas or gammas, reaching at least 650 (400) in ADC units for PMT-1a (PMT-2a). Alternatively, the PMT-1a (PMT-2a) ATWD1 waveform can be greater than 325 (324), with an ATWD1 τ value greater than 177 (184). Cuts are consistent with 100% alpha rejection, with no misidentified events expected in the event sample over the 3.5 yr data sample. Less than 11 gamma events are expected in the muon sample over 3.5 yr. The distribution of the muon cut parameters for each event type are shown in Figure 7.11.

DM-Ice17 is the only NaI(Tl) dark matter experiment isolating muons using the crystal signal alone. The DAMA/LIBRA detector removes multiple-hit event but does not isolate muons [87, 94], and ANAIS and KIMS use an active scintillator veto. The ANAIS experiment placed active vetoes on top of their lead shielding in both ANAIS-0 [144] and ANAIS-25 [82], and the KIMS array is enclosed in an active veto [84].

7.2.2 Observed Modulation

The muon flux through DM-Ice17 is observed to annually modulate with a $14 \pm 3\%$ fractional amplitude, as shown for both detectors individually and for the combined data sample in Figure 7.12. The muon fluxes

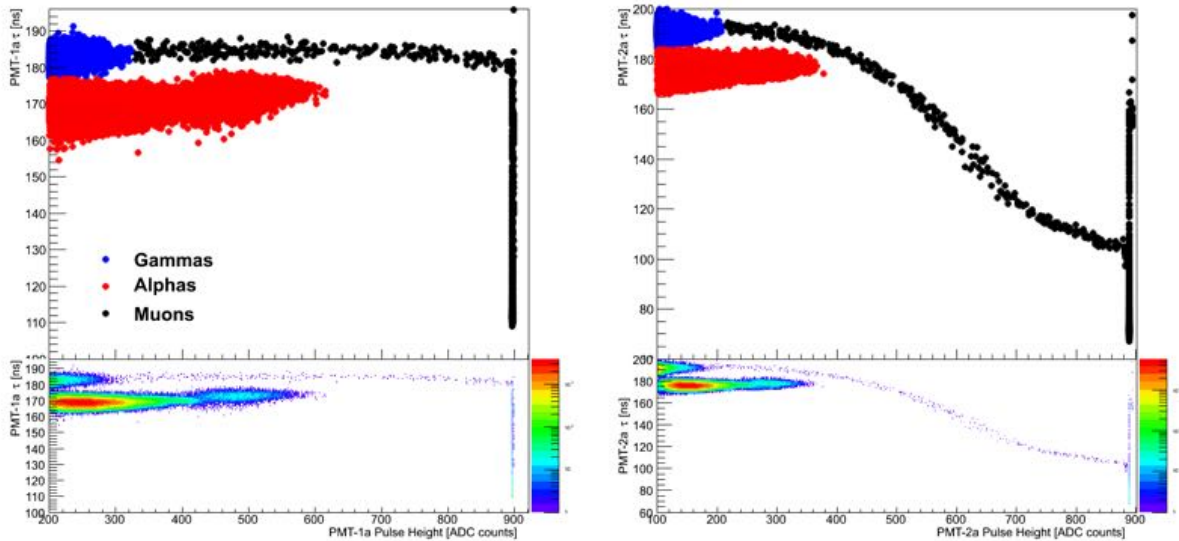


Figure 7.11: Distributions of τ and waveform height for Det-1 (left) and Det-2 (right), classified by event type. The lower images are identical to the upper images, with density shown in the z-axis. Muons are identified by their ATWD2 waveform heights and ATWD1 pulse shapes, which are longer than those from alpha events. PMT saturation is visible in the declining τ value across the muon events (see §5.2.4.5). Single PMTs are used because they provide better event type separation. Bi-Po alpha events have been removed. Data shown is from one year.

through DM-Ice17 over 3.5 years in Det-1, Det-2, and the combined detector are fit to the parameters shown in Table 7.3.

Table 7.3: DM-Ice17 Muon Modulation Parameters

Detector	Average Rate/ Crystal	Modulation Amplitude (Fractional Amplitude)	Period [days]	Phase [days]
DM-Ice17 Det-1	$2.89 \pm 0.05 \mu/\text{day}$	$0.40 \pm 0.07 \mu/\text{day}$ ($14 \pm 2.4\%$)	380 ± 16	January $5^{\text{th}} \pm 11$
DM-Ice17 Det-2	$2.91 \pm 0.05 \mu/\text{day}$	$0.39 \pm 0.07 \mu/\text{day}$ ($13 \pm 2.4\%$)	378 ± 19	December $30^{\text{th}} \pm 14$
Combined	$2.92 \pm 0.04 \mu/\text{day}$	$0.40 \pm 0.05 \mu/\text{day}$ ($14 \pm 1.7\%$)	375 ± 13	January $6^{\text{th}} \pm 9$

All of the above fit parameters have been allowed to float. Fixing the modulation period to one year yields a combined detector muon flux consistent in amplitude but with a shifted phase; the fixed period modulation converges to $(2.92 \pm 0.036) + (0.39 \pm 0.051)$ muons/crystal/day with a phase of January 17 ± 8 days.

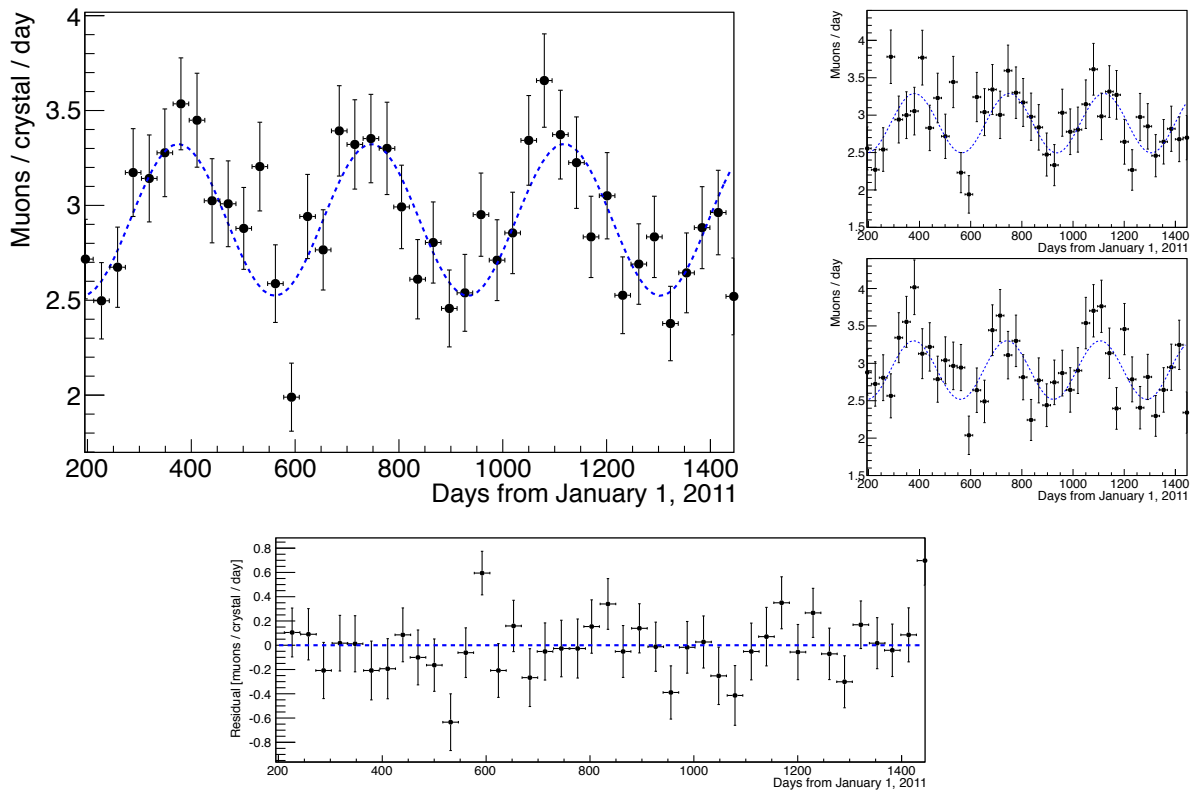


Figure 7.12: Muon flux through both detectors (left) and through Det-1 (top, right) and Det-2 (bottom right) individually. The data is divided into month-long intervals. The annual modulation is consistent across both detectors and fits a $14 \pm 2\%$ fractional modulation with a phase and period consistent with the expected phase in early January and period of roughly one year. The residual from the comparison of the fit to data is shown in the lower plot.

The modulation phase and period are consistent with that observed by IceCube, as shown in Figure 7.13. The muon modulation follows the atmospheric temperature modulation, which deviates from a perfect sine function. The quick rise to the maximum rate and slower decline to minimum rate are visible in the IceCube data in the figure. The DM-Ice muon rate does not have the statistics to observe this deviation from a sine function, but it would be expected to observe the same phenomenon if the rate through the detector provided adequate statistics for such a study. The reduced χ^2 of the DM-Ice17 modulation compared to the fit sine function is 1.34, and scaled to the IceCube data is 1.66. By contrast, the no modulation fit has a χ^2 of 2.79.

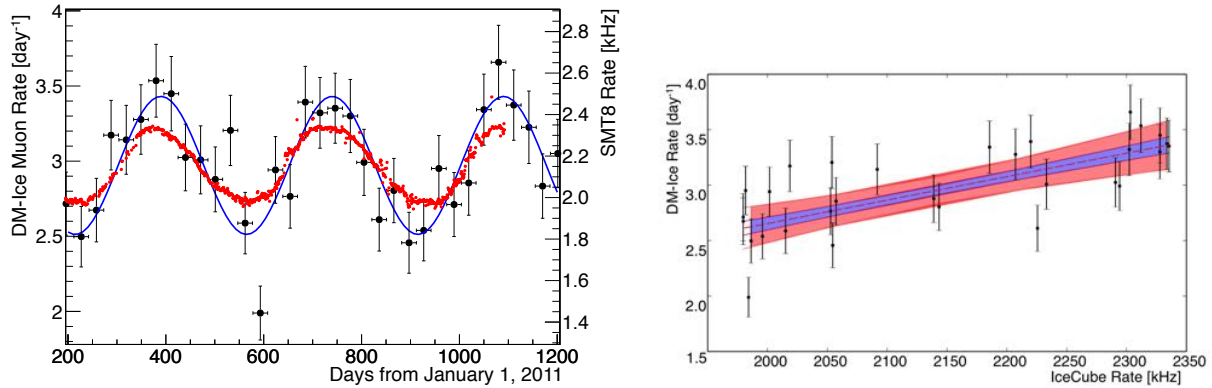


Figure 7.13: DM-Ice muon rate (black circles, left axis) and fit (blue) compared to the IceCube trigger rate (red, right axis). The modulations are consistent in phase and period, with the high statistics in IceCube allowing deviations from a pure sine function to be clearly visible. The muon rate is correlated with the effective temperature of the atmosphere (see §7.1.1 and Figure 7.5). The IceCube data shown in the SMT8 trigger rate (see §8.2.1). Correlation of the two trigger rates is shown on the right, with the best fit given by the red dashed line and 1σ and 3σ contours in red and blue, respectively.

7.2.3 Energy Deposition

The expected muon energy deposition is derived from GEANT4 simulation. Muons of three energies (10 GeV, 100 GeV, 1 TeV) were simulated, starting 0.3 mm above the crystal and propagating downward through the NaI(Tl) detector. The resulting energy depositions in the crystal illustrate that all muons are most likely to deposit the ~ 81 MeV MIP energy, with higher energy muons producing the high energy tail, as shown in Figure 7.14. The inset of Figure 7.14 focuses on the MIP peak, showing the similarity of the distribution across all three muon energies, while the larger image shows the larger higher high energy tail produced by the higher energy muons.

Muon energy depositions appear between 5 MeV_{ee} and 15 MeV_{ee} in Det-1, as shown in Figure 7.15. This implies a large quenching factor when compared to the simulated energy deposition due to the high ionization density of the muon interactions resulting from their large mass. The muons used for energy calculations are those that saturate neither the readout channel nor the PMT. All energy spectra are from Det-1 because the Det-2 PMTs are saturated over the muon region, rendering the gamma calibration meaningless in this regime.

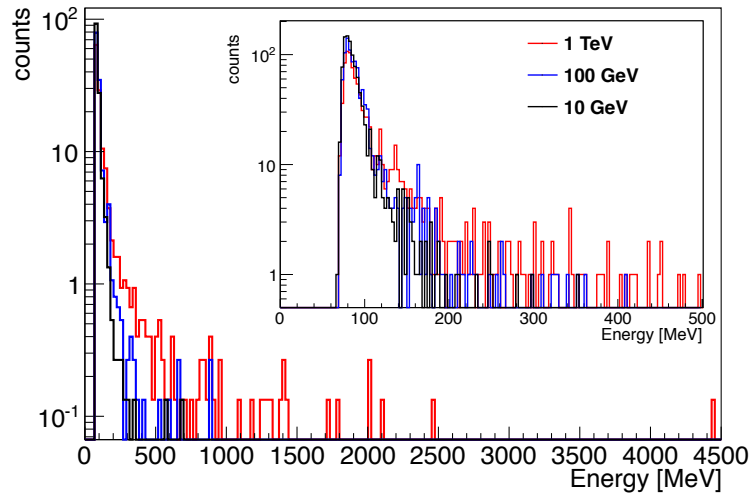


Figure 7.14: Simulated muon energy deposition in DM-Ice17. Three different muon energies (10 GeV, 100 GeV, 1 TeV) were simulated starting at 0.3 mm above the detector. Higher energy muons produce a higher energy tail in their deposited energy spectra, but the ~ 81 MeV MIP interaction dominates the spectrum for all muons. A ~ 81 MeV peak from muon interactions is thus expected in the DM-Ice17 detector, although it is expected to be quenched due to the large ionization density of the muon interaction.

7.3 Muon-Induced Phosphorescence

The highest energy muon events induce long-lived phosphorescence in the DM-Ice17 crystals, observed as prolonged cascades of low energy events (see §4.2.4). Phosphorescence is observed in both normal, local coincidence (“LC”) data and single PMT threshold crossings (“monitoring data”, see §5.2.2), as shown in the example event in Figure 7.16. Rates during this period spike outside of the statistical fluctuations of normal running rates (2.5 Hz LC, 100 Hz monitoring). Rates above 300 Hz in monitoring data have not been observed outside of a phosphorescence event. The increase in the rate rather than the rate itself is used as an additional metric to avoid local statistical fluctuations in the background rate. This is most prominent in comparing data from before and after the monitoring rate decrease that lowered the rate of EMI noise events (see §6.1.2), as shown in Figure 7.17. The increase in the number of events in the 30 s following a muon, relative to the number of events in the 30 s before the muon, illustrates muon behavior, both phosphorescing and non-phosphorescing, as shown in Figure 7.17. Most muons do not phosphoresce, and they are grouped about zero, while phosphorescing muons induce an increase in the 30 s event rate of at least 60 events. This cut combined with a minimum of 135 counts in the 30 s following the muon is used to isolate phosphorescence.

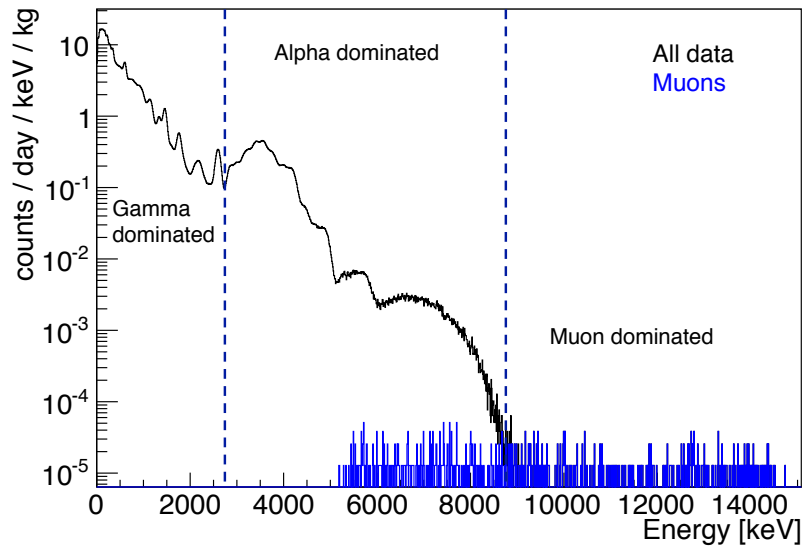


Figure 7.15: The energy spectrum of all events in black, with muons overlaid in blue. A large quenching factor is observed, as evidence through comparison with the spectrum in Figure 7.14. Data is from Det-1; the PMTs in Det-2 are saturated in this regime. Energy is defined as the integrated charge in the waveform (see §6.2).

Both the LC and monitoring rates examine the number of events above threshold in a single PMT with no software coincidence requirement, but LC data must pass a $500 \mu\text{s}$ hardware coincidence.

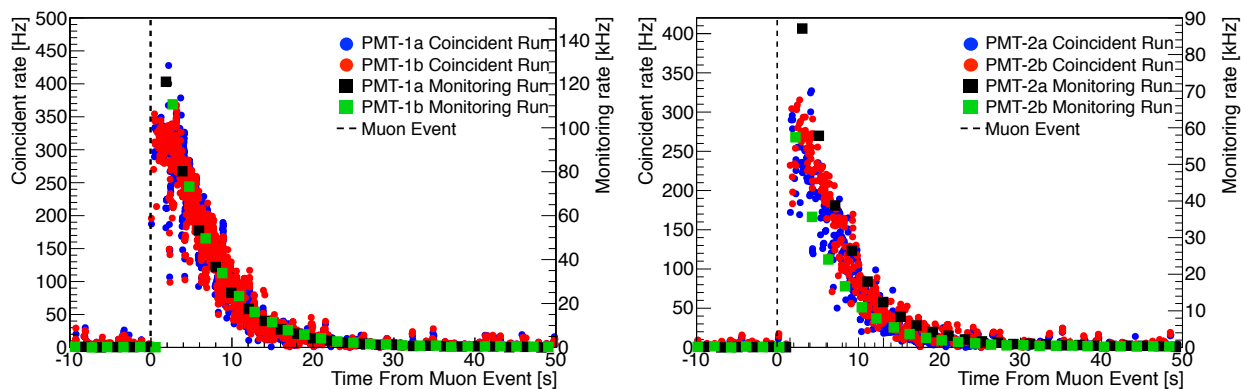


Figure 7.16: Muon-induced rate spike and subsequent decay due to phosphorescence in Det-1 (left) and Det-2 (right). Spikes are observed in both monitoring (green, black) and LC data (red, blue) following a muon event (time indicated by the dashed line). The x-axis is the time in relation to the muon event.

Large phosphorescence events are only induced by the highest energy muons, which are identified as the muons with the highest ATWD2 waveform heights, as shown in Figure 7.18. Phosphorescence exhibits a

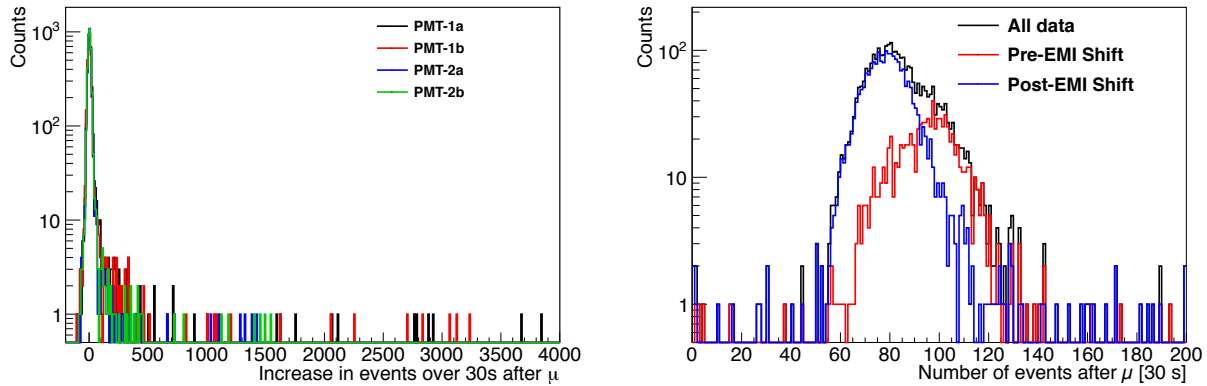


Figure 7.17: Phosphorescence is identified when the trigger rate in the 30 s after a muon event significantly increases (left). Most muons induce no rate increase, as shown in the distribution about zero, while phosphorescing muons induce the high rate tail. The increase in counts rather than the raw counts is used to account for local rate changes. This is particularly evident in the monitoring rate shift that decreased EMI noise events (right). The right hand figure has magnified the region about the central mean for clarity; it represents a subset of the total distribution, which extends to higher values on the x-axis, for PMT-1a. Data shown covers 3.5 years, from July 2011 through December 2014.

characteristic decay time of 9 ± 3 s, consistent in both detectors. Figure 7.19 shows a collection of phosphorescent decays, showing a consistent decay time when DAQ saturation is accounted for (see §7.3.1) and lasting for tens of seconds following a muon event.

Phosphorescence states are dominated by low energy (< 2 keV) events that resemble SPE noise. A single muon can induce hundreds, even thousands, of events in the low energy region. An average increase of 11 events over 30 s follows muon events. These events do not pass the DM-Ice17 noise cuts, as shown in Figure 7.20, which compares the spectrum of phosphorescence events from Figure 7.16 (left) before and after cuts. Of the 886 events in the dark matter region of interest (< 10 keV_{ee}) in the 30 s following the muon event, all but one are removed by standard noise removal (see §6.1.2). Only this event and 14 higher energy events remain, consistent with the expected background rate of non-phosphorescent events over this time period. While phosphorescence has the potential to induce a modulation in the region of interest due to the muon modulation, these events are completely removed from the DM-Ice17 modulation dataset. For a discussion on the potential of phosphorescence to induce a signal in other experimental setups, see §7.3.2.

It should be noted that an additional phosphorescent component may be present on the μ s timescale and observed in the FADC channel, show in Figure 7.21. Because this channel is severely saturated in this

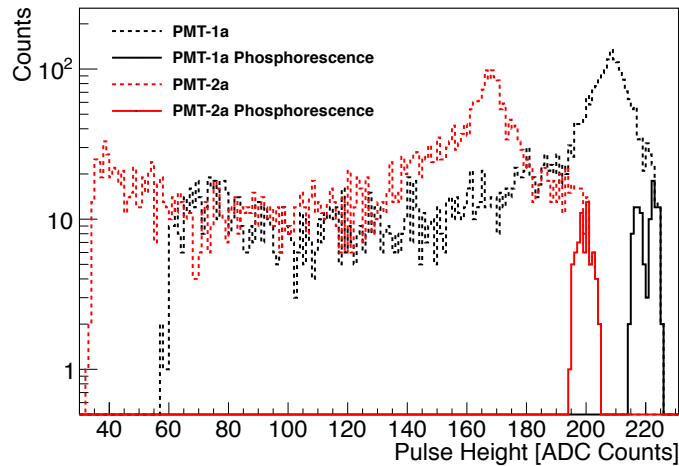


Figure 7.18: Phosphorescence is only induced by the highest-energy muon depositions. The pulse heights for all muons are shown for each detector in the dotted lines, and the subset of muons that induce phosphorescence are shown in solid lines. Black is Det-1a, and red is Det-2a.

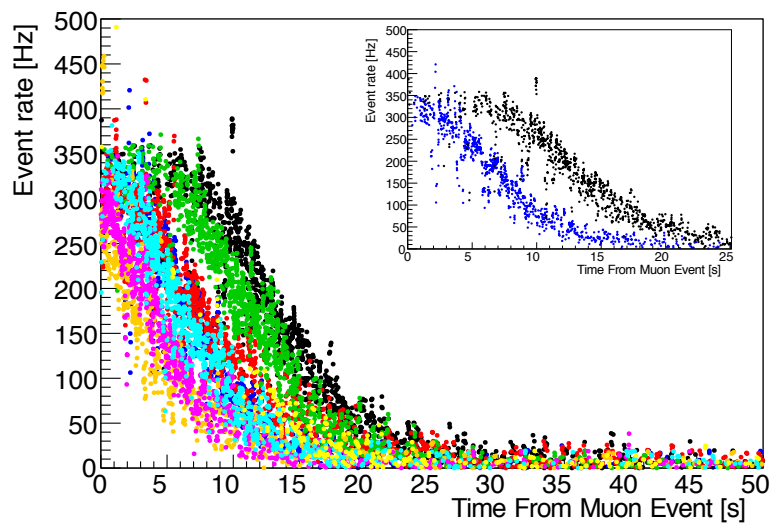


Figure 7.19: Comparison of Det-1 phosphorescent decays. Decays exhibit characteristic time constants of 9 ± 3 s, with some events exhibiting DAQ saturation for a prolonged period of time. The inset shows a phosphorescent event that decays immediately (blue) compared to one that remains at a saturated rate for a prolonged period of time (black). The x-axis is set to zero at the time of the muon event inducing phosphorescence.

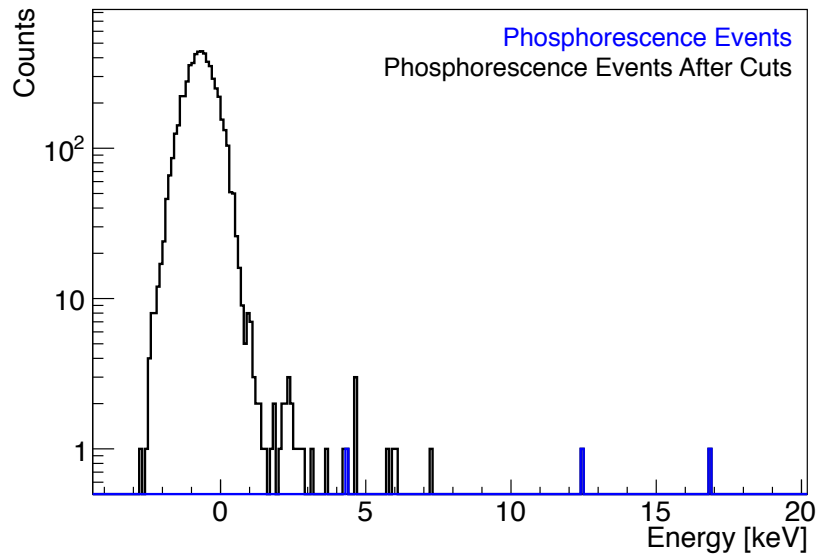


Figure 7.20: ATWD0 energy spectrum of events in the single phosphorescence rate spike in Det-1 from Figure 7.16. 886 events are in the region of interest (<10 keV) and 14 events are above the region of interest. The low energy spectrum extends below zero, which is not shown here. The low energy events match the SPE spectrum well and are all cut in noise removal.

regime, it is unclear whether this effect is due to saturation and waveform corrections or if it is a physical effect. If real, this is likely the product of Tl^0 decay or excitonic luminescence (see §4.2.4).

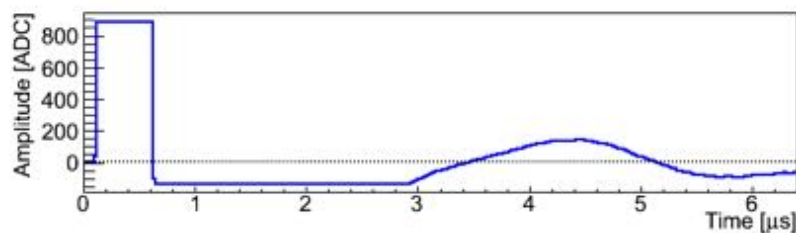


Figure 7.21: Muon waveform in the FADC channel. Muons exhibit a secondary event in the FADC channel, which may be due to a phosphorescence effect or to waveform manipulations. This will be the subject of future study.

7.3.1 DAQ Saturation and Deadtime

Two deadtimes impact phosphorescence rate calculations. The first is the $700 \mu\text{s}$ deadtime following each event. This is the time required for the buffer to clear in the electronics, and it is subtracted from the

livetime in rate calculations. An additional deadtime is only observed during phosphorescence events. In these periods of high rate readout, the detector reads out for ~ 10 ms, then is dead for ~ 20 ms. The precise timing of these deadtimes varies, complicating its removal. A removal algorithm has been implemented that identifies large gaps (>25 ms) in trigger times. It calculates the exact deadtime for that instance and removes it from the livetime. This only occurs for events that pass at least 50 Hz trigger rate, and the correction is only implemented when visible drops in the data are visible during a saturation event. These corrections are applied in Figure 7.22, and a significant increase in reported rate is observed when properly accounting for livetime. DAQ saturation is still visible in this event. In addition to these deadtimes, the nine largest

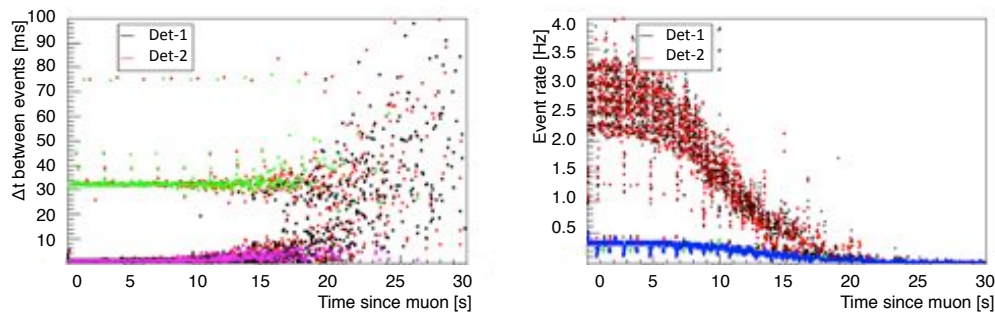


Figure 7.22: Accounting for deadtime. Two event populations are visible in the left image; normal running, with a time between events of less than 10 ms, and events during deadtime, where the time between events jumps to >30 ms. These events, identified in green, are corrected, yielding the points in magenta. This correction increases the observed rate, as shown in the right-hand image. The blue (green) points are the recorded rate before correction; black (red) is the corrected rate.

phosphorescence events peak at a high enough rate to saturate the DAQ. During this time, events in the crystal are occurring faster than the DAQ can process them, leading to a reduced number of data points and a maximum readout rate, as shown in the inset of Figure 7.19. Phosphorescence studies do not require the standard software coincidence applied in DM-Ice17 analysis because DAQ saturation effect limits LC pairing. Phosphorescence decays that saturate the DAQ are consistent with the characteristic phosphorescence decay time once they fall below the saturation level. DAQ saturation is accounted for by fitting the decay after it falls below the saturation rate, and extrapolating the fit back to the time of the muon event. Comparing this fit to the observed rate, the portion of light lost to DAQ saturation is derived, as shown in Figure 7.23.

7.3.2 Phosphorescence Implications for NaI(Tl) Experiments

DM-Ice17 is the latest addition to the suite NaI(Tl) experiments to observe phosphorescence [84,142–152], and it is the first to observe the monitor the number of phosphorescence events evolve over an extended period

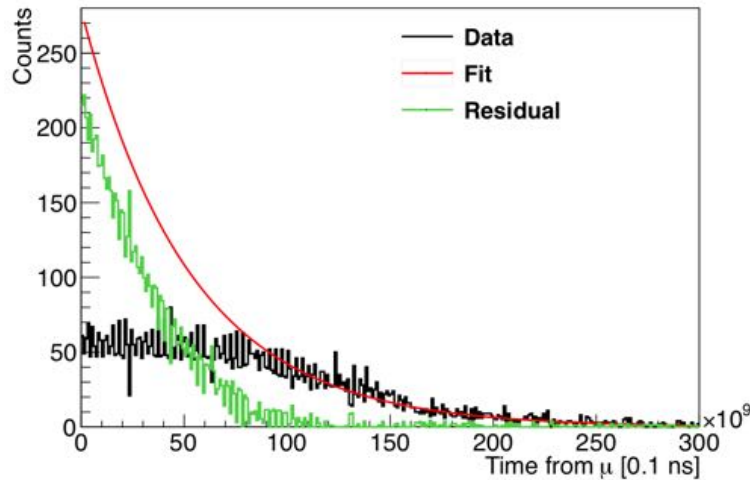


Figure 7.23: Accounting for DAQ saturation. The unsaturated portion of the pulse is fit, and the exponential is extrapolated back to the muon event time. The difference between the observed distribution and the fit indicates the percentage of data being dropped due to DAQ saturation. This event only registered 25% of the modeled signal.

of time. DM-Ice17’s second-scale decay constant falls within the generous range of previous observations that range from microseconds to days (see §4.2.4). As discussed in §4.2.4, decays on the μs -ms timescale can be explained in terms of Tl^0 and excitonic decay, while longer decays are likely the product of metastable state and traps due to crystal defects and inhomogeneities. Phosphorescence increases with the total absorbed dose, and it is likely that the lifetime exposure of a crystal to greater amounts of irradiation contributes to a longer phosphorescence signal. (see §9.1.1). The number of events following a muon in DM-Ice17 traces the muon modulation, as shown in Figure 7.24 (top, left), as expected simply due to normal background rates. No additional modulation is added due to phosphorescence, as evidenced by the lack of modulation in the relative rate in Figure 7.24 (top, right). Additional Monte Carlo analysis has shown a preference for a null result over a phosphorescence modulation for the muon and phosphorescence rates in the DM-Ice17 crystals. Phosphorescence modulation, even without the application of noise removal, is not a significant modulation in the low energy region of DM-Ice17.

Dark matter experiments take care to avoid phosphorescence signals because they have the potential to induce a modulation in the region of interest. This is done by imposing a deadtime following muon events. ANAIS, which observes a 70-100 ms phosphorescence, imposes a 0.5 s deadtime following events greater than 9 MeV; KIMS, which observes a phosphorescence of a few seconds, has a 8 ms deadtime; DAMA is the notable exception as it does not observe phosphorescence, but it imposes a 500 μs dead time following all events that

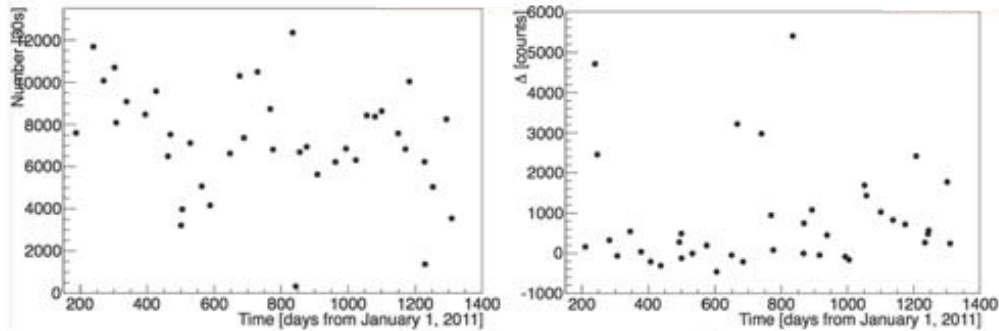


Figure 7.24: Number of events (left) and relative number of events (right) in the 30s following a muon event as a function of time. This rate follows the muon modulation rate, as expected by reading out over a larger period of time. No modulation is observed in the relative number of cuts. It should be noted that phosphorescence events are removed by noise cuts in DM-Ice17 analysis.

may be removing any phosphorescence present [87, 94]. The $700 \mu\text{s}$ deadtime following DM-Ice17 events is not long enough to remove the long-lived phosphorescence observed.

While phosphorescence is not a significant modulation and is efficiently removed in DM-Ice17, it has the potential to induce a significant modulation in DM-Ice250 or similar detectors, such as DAMA, ANAIS, KIMS, and SABRE. Monte Carlo analysis studied the effect of the DM-Ice17 and ANAIS phosphorescence responses in a detector with the DAMA muon rate and low energy background rate. While DAMA rejects muons with the multiple-hit cut, a single crystal effect from the muon like phosphorescence may not be removed. DM-Ice17 does not observe phosphorescence events above 2 keV, indicating that this phosphorescence response cannot produce a signal consistent with that observed by DAMA. The ANAIS phosphorescence does appear in the region of interest, but this signal is over an order of magnitude smaller than the DAMA modulation. The scatter on these events is larger than the expected modulation, and a significantly larger muon rate would be required to produce a signal consistent with the DAMA modulation.

Chapter 8

IceCube Muon Coincidence

8.1 Coincidence Concept

DM-Ice17 is located within the volume of the IceCube Neutrino Observatory, which is both the largest neutrino observatory and the largest muon detector in the world (see §8.2) [176]. It is thus possible to compare the detector event times and study muons observed by both detectors (see §8.3). This coincident data sample provides DM-Ice17 with a verification of the muon tag and provides IceCube with a novel calibration tool because the muon is known to pass through the DM-Ice17 crystal volume (see §8.4).

8.2 IceCube

The IceCube Neutrino Observatory is a cubic-kilometer Cherenkov detector that observes light emitted by energetic charged particles travelling faster than the speed of light in ice [177]. When a charged particle moves faster than light through a medium, it disrupts the electromagnetic field and produces a coherent shockwave. This Cherenkov emission is commonly described as a “sonic boom of light”. The emitted light travels along the characteristic angle of emission, as shown in Figure 8.1. The angle depends on the speed of the particle ($\beta = v/c$) and the index of refraction of the medium (n):

$$\cos \theta = \frac{1}{n\beta} \quad (8.1)$$

A relativistic charged particle in ice has a characteristic emission angle, θ , sharply peaked about 41° . Cherenkov emission is characterized by the Frank-Tamm formula [178], which describes the number of photons, N , emitted as a function of wavelength, λ :

$$\frac{d^2 N}{dx d\lambda} = \frac{2\pi\alpha}{\lambda^2} \left(1 - \frac{1}{\beta^2 n^2(\lambda)} \right) \quad (8.2)$$

where $\alpha \sim \frac{1}{137}$. Emission is peaked at shorter wavelengths, producing a blue light that is detected by photosensors in Cherenkov experiments.

IceCube is comprised of 5160 Digital Optical Modules (DOMs) located between 1450 and 2450 m deep in the ice on 86 strings. The strings are 125 m apart, and DOMs on each string are 17 m apart. IceCube

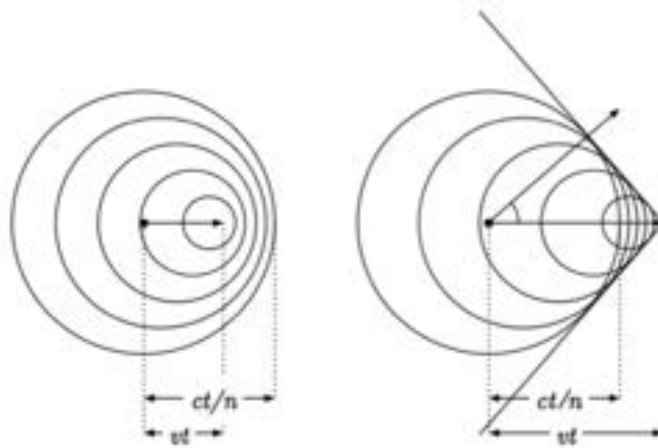


Figure 8.1: Cherenkov emission [179]. A relativistic charged particle moving faster than the speed of light in a medium will produce a coherent shockwave with a characteristic emission angle. Emission appears as a cone of blue light.

is designed to observe the Cherenkov light due to high energy (>100 GeV) neutrino events, but its primary background is from atmospheric muons. Of the ~ 3 kHz IceCube data rate, only ~ 3 mHz are from neutrino events.

IceCube has two associated subdetectors: IceTop [180], which is a cosmic ray detector on the surface, and DeepCore [181]. The DeepCore Low-Energy Extension (DeepCore) is a 401 DOM infill array¹, located in the center of IceCube, that is designed observe low energy events. A combination of 35% higher quantum efficiency DOMs and a more densely-packed DOM array (62.5 m inter-string spacing and DOMs separated by 7 m) allows DeepCore to lower the detector energy threshold and observe events down to 10 GeV. Det-1 of DM-Ice17 is located within this array at the bottom of string 79, as shown in Figure 5.7, and the full-scale DM-Ice detectors will be located as close to the central DeepCore region as possible. Det-2 of DM-Ice17 is located at the edge of IceCube on string 7.

The detection efficiency of IceCube increases with depth, as shown in Figure 8.4. The efficiency at the top of detector is roughly 40%, with IceCube triggering at 2.6-3 kHz for a 6-7 kHz atmospheric muon background. The efficiency increases to 98% at the bottom where IceCube triggers at roughly 1 kHz with a 1 kHz atmospheric muon background. This increase in efficiency is due to muon energy loss in the detector: muons that reach the bottom of IceCube have lost roughly 200 GeV in the detector, triggering DOMs on the way through, while the low energy (“dark”) muons have been stopped.

¹These DOMs are included in the 5160 total DOM array of IceCube.

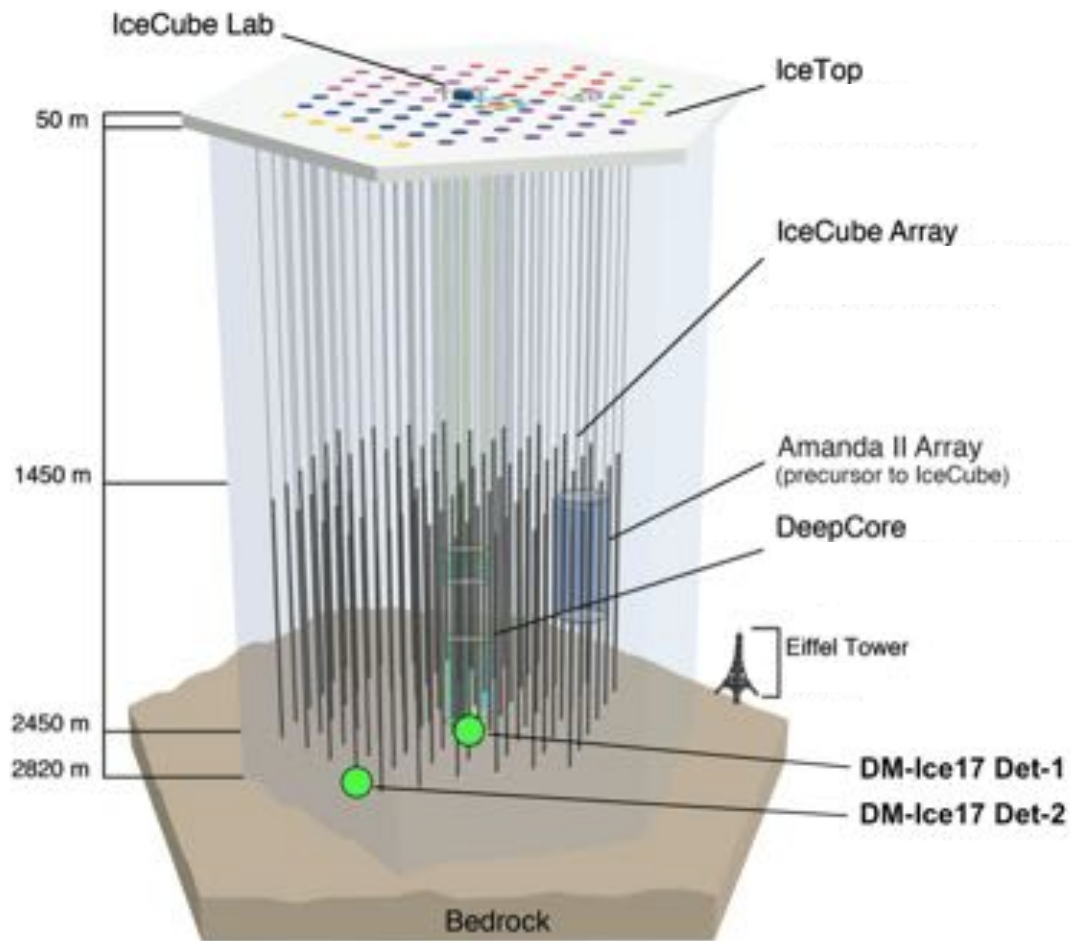


Figure 8.2: The geometric arrangement IceCube, DM-Ice17, DeepCore, and the IceTop detectors on the surface. AMANDA, the predecessor of IceCube, is no longer in operation. The surface color coding refers to the year in which the associated IceCube string was deployed, and the Eiffel Tower is shown for scale. Det-1 of DM-Ice17 is located in DeepCore while Det-2 is located on the edge of IceCube.

8.2.1 IceCube Data

IceCube data is divided into physics streams, each passing specific trigger and filter conditions that are optimized for the interactions they intend to examine. Data is filtered and processed in real time before being transmitted to the Northern Hemisphere for further offline processing. IceCube events are reconstructed with both energy and directional information, as shown for a typical atmospheric muon event in Figure 8.3. DM-Ice17 and IceCube use the same electronics, allowing timing alignment and effective data comparison. The DM-Ice coincidence study uses the Muon Filter (§8.2.1.1), sDST NChannel Filter (§8.2.1.2), and the

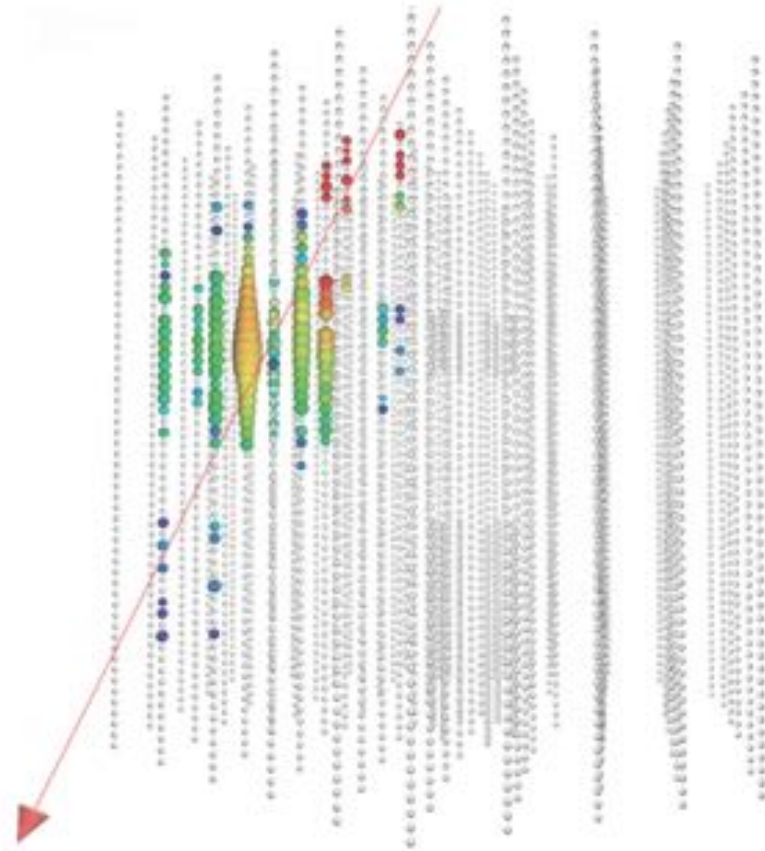


Figure 8.3: A high energy muon event in IceCube. Each dot corresponds to a PMT in the detector, with larger dots indicating larger amounts of charge registered in the PMT. The event colors illustrate the timing of the event, progressing from red (earliest) to blue (latest). The reconstructed track is shown in red. This event topology is characteristic of an atmospheric muon track [182].

sDST MinBias filter (§8.2.1.3), described in Table 8.1. These filters were chosen to optimize the number of atmospheric muons detected while keeping accidental coincidence as low as possible.

8.2.1.1 Muon Filter

The Muon Filter is used for the IceCube neutrino point source and diffuse neutrino analyses. The filter is designed to observe high energy muon events, which tend to reconstruct better due to the higher number of photons deposited. It has a 34.4 Hz rate and triggers on an eight-fold Simple Majority Trigger (SMT8) condition [183]. SMT8 requires that eight DOMs situated as neighbors or next-to-neighbors (known as Hard Local Coincidence, or HLC) fire in $5 \mu\text{s}$ window. The HLC condition lowers the probability of random noise events across the detector triggering an event. Triggered DOMs that do not meet the HLC condition make

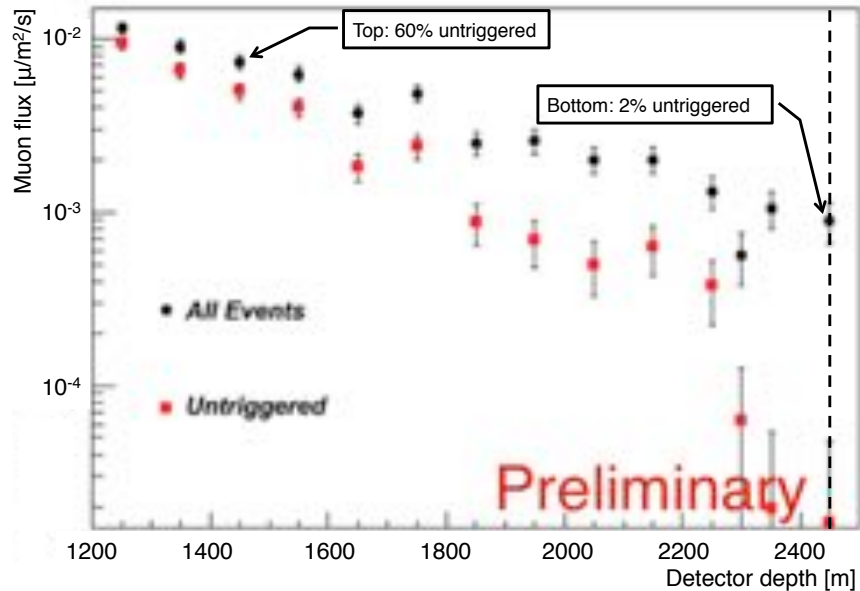


Figure 8.4: IceCube detection efficiency as a function of depth. Efficiency increases from 40% at the top to 98% at the bottom, where DM-Ice17 is located. The efficiency improvement is the result of high energy muons emitting Cherenkov light, while they pass through the detector while low energy muons that do not emit Cherenkov light are stopped before hitting the bottom.

up the Soft Local Coincidence (SLC) dataset. The readout window starts $4\ \mu\text{s}$ before the first HLC hit and continues until $6\ \mu\text{s}$ after the last.

Muon Filter events undergo waveform calibration, extraction, and two types of cleaning: SeededRT and TWC [183]. Seeded Radius-Time (SeededRT) cleaning keeps only those hits that have another DOM trigger within the given radius and time (RT) window around them. It begins with the core HLC events, which are those with at least two other HLC hits in their RT window, and moves out from there. Time Window Cleaning (TWC) takes a sliding $5\ \mu\text{s}$ window and keeps only that window with the most hits. These cuts have been designed to maximize physics retention and noise removal, and they retain over 92% of signal events while removing over 97% of noise events [184]. The events are then reconstructed and tagged as Muon Filter events. The filter has run on all IceCube data overlapping with the running of DM-Ice17. It is expected to be coincident with roughly 4% of the DM-Ice muons, based on the ratio of the filter rate to the atmospheric muon rate. Det-2 has a significantly lower coincidence due to its geometric location.

8.2.1.2 sDST NChannel

The Super Data Storage and Transfer (sDST) filters are designed to keep as many interesting triggered events as possible. Two sDST filters are used in this study, each with a separate criterion for what constitutes an interesting event. The sDST NChannel filter keeps all events in which 25 DOMs fired in the trigger window [185]. This filter has a 431.9 Hz rate, providing a large data sample expected to include over 90% of muons reaching DM-Ice17. Reconstructions are not run in this filter, so they are integrated offline in the DM-Ice17 coincidence processing. This data was not used by any working group in IceCube, and the stream was only available for the 2012-2013 season. It is expected to be coincident with 90-95% of DM-Ice17 muons because those muons that reach DM-Ice17 depth will pass the NChannel condition. Deviation from 100% coincidence is expected due to trigger variation in IceCube; coincident events with the same global trigger may appear too distant in time for coincidence due to the layout of the global trigger. Coincident events make up 10% of the IceCube event population, although only a subset of these will have the time profile to induce non-coincidence.

8.2.1.3 sDST MinBias

The sDST Minimum Bias (sDST MinBias) filter saves every fifth event that passes one of three trigger conditions: SMT8, SMT3, or the String Trigger, in which 5 of 7 vertically adjacent DOMs fire. sDST MinBias has a 454 Hz trigger rate and is used for calibration purposes. As with the sDST NChannel filter, reconstructions in this stream are applied offline during DM-Ice17 coincidence processing. This stream was introduced in May 2012 and is still in use. It is expected to be coincident with 15-20% of DM-Ice muons based on the size of the filter and the condition that it accepts only every fifth event.

Table 8.1: Expected coincidence rates between DM-Ice17 muon stream and IceCube data streams. The data streams were chosen to optimize muon collection and minimize accidental coincidence.

IceCube Data Stream				Expected Coincidence
Name	Trigger Condition	Rate	Years	% of DM-Ice17 muons
Muon Filter	SMT8	34.4 Hz	2011-2014	4%
sDST NChannel	25+ DOMs	432 Hz	2012	90-95%
sDST MinBias	Every 5 th event	454 Hz	2012-2014	15-20%

8.3 Coincidence Algorithm

Muons observed by both DM-Ice17 and IceCube are correlated by the time they trigger each detector. Shared DAQ software and GPS timestamps allow a direct comparison of trigger times in the two experiments. Both timestamps are in Coordinated Universal Time (UTC) (i.e., tenths of nanoseconds since the start of the year). Both the leap day and the leap second of 2012 were applied to both experiments' timestamps.

The coincidence algorithm starts with the trigger time of DM-Ice17 muon events. To minimize data processing time, the coincidence algorithm isolates the IceCube run containing data from the time of the DM-Ice17 muon. A 1.8% IceCube dead time is observed, in which the DM-Ice17 muon occurs while IceCube does not have available offline data. Both hardware deadtime and rejected events contribute to this deadtime. The coincidence algorithm continues by accepting only those IceCube events passing the Muon, sDST MinBias, or sDST NChannel filters and searching for events in which IceCube triggers within $[-1, 6] \mu\text{s}$ of the DM-Ice17 muon. This time window was chosen because a muon takes up to $6 \mu\text{s}$ to pass through IceCube. A $4 \mu\text{s}$ offset is applied in the timing comparison to account for the IceCube readout window padding that records the $4 \mu\text{s}$ before the trigger condition is met.

Coincident events are analyzed and processed to derive relevant reconstruction parameters. All IceCube events are taken from processed ("Level 2") data, but each filter's data has undergone different levels of processing. Muon Filter events have been fully reconstructed; sDST MinBias events have undergone SinglePhotoElectron (SPE) fitting but require MultiplePhotoElectron (MPE) reconstructions; sDST Channel events require both SPE and MPE. Both SPE and MPE are seeded with the result of the Linefit reconstruction. Linefit is computationally fast and an efficient seed for the more precise reconstructions. It ignores ice properties and Cherenkov cone geometry, fitting only the path of light along lines connecting hit DOMs. The SPE fit, also comparatively fast, incorporates ice scattering and Cherenkov geometry, but it reconstructs using only the first photon that arrives at each DOM. MPE is more computationally intensive, but it takes into account the multiple photons in each DOM, and it samples the likelihood space to verify that the minimizer has found a global, rather than a local, maximum likelihood [186]. The analysis thus starts by identifying which reconstructions are already available and runs any missing reconstructions.

All reconstructions are repeated using the location of the coincident DM-Ice17 prototype as the reconstruction seed. The seed is the starting point of any reconstruction. The location of DM-Ice17 is suggested as the starting point, but the reconstruction is allowed to deviate from this location without a penalty. The results from changing the reconstruction seed to the DM-Ice17 coordinates are discussed in §8.4.

A number of reconstruction parameters provide valuable information, notably the distance of closest approach to DM-Ice17, the energy approximation, the zenith, and the azimuth. The distance of closest approach to DM-Ice17 is calculated using the DMIce position and the MPE reconstruction. The x- and

y-coordinates of the DM-Ice17 detector positions are determined by the coordinates for strings 79 and 7, respectively; the z-coordinate is set to the position of the deepest IceCube DOM on the string plus the 7.6 m distance between it and the crystal in each DM-Ice17 prototype. MPE has a resolution of roughly 20 m, which is taken as the maximum acceptable distance for a properly reconstructed event in this study.

Accidental coincidence between the chosen IceCube filters and the DM-Ice17 muon stream is expected in each crystal every 2 months. Events reconstructed as far from DM-Ice17 are more likely to be poorly reconstructed than accidentally coincident, as shown in Table 8.2. The implementation of IceCube noise removal algorithms may remove these events, as discussed in §8.4.4. Using all IceCube data for the study would introduce an accidentally coincident event every 22 days, which is prohibitively large. The accidental coincidence rate also precludes running a search for additional DM-Ice17 muons from the entire DM-Ice17 data sample, even with a smaller IceCube stream like the Muon Filter, without significant cuts on the data, as shown in Table 8.2. The potential for such a study following the development of strict cuts is discussed in §8.4.4.

Table 8.2: Accidental coincidence between the DM-Ice17 muon stream and chosen IceCube filters over a $7 \mu\text{s}$ window. Filters were selected to maximize muon retention and minimize accidental coincidence. Strict cuts would be required to expand the study to all DM-Ice17 or all data through the bottom of IceCube, as shown by the high accidental coincidence rates.

DM-Ice17		IceCube		Accidental Coincidence	
Data Stream	Rate	Data Stream	Rate	Rate	2 yr Expectation
Muon events	$26.6 \mu\text{Hz}$	Muon Filter	34.4 Hz	6.41 nHz (1/4.95 years)	<1
Muon events	$26.6 \mu\text{Hz}$	sDST NCh	432 Hz	80.4 nHz(1/144 days)	5
Muon events	$26.6 \mu\text{Hz}$	sDST MB	454 Hz	84.5 nHz(1/137 days)	5
Muon events	$26.6 \mu\text{Hz}$	All data	$\sim 2.8 \text{ kHz}$	521 nHz (1/22.2 days)	33
All data	2.5 Hz	All at 2450 m	$\sim 1 \text{ kHz}$	17.5 mHz (1/57.1 seconds)	1.1×10^6

8.4 Results

8.4.1 Coincidence Rates

The 2 yr coincidence study found up to 93% of Det-1 DM-Ice muons coincident with IceCube events and an improvement in misconstruction rates of 20% when the DM-Ice17 seed was used. From May 2012 to May 2014, 3978 muons were observed in DM-Ice17. Of those, 1666 (43%) were coincident with IceCube events,

as shown in Table 8.3. The sDST NChannel filter was particularly effective for this study, with 93%(33%) of Det-1 (Det-2) muons coincident with events in this channel. Because it was only available for one of the two years studied, the large percentage of coincident events in this channel is larger than the total coincident rate, in which Det-1 (Det-2) had 55%(30%) coincidence with IceCube over the entire 2 yr dataset, as shown in Figure 8.5 and Tables 8.3 and 8.4, with the latter organizing the results by filter. Coincident rates for each filter are consistent with expectation (see Table 8.1).

Table 8.3: Results of 2012-2014 coincidence study. The first row compiles the numbers of muons observed in DM-Ice17; the next two rows show the number of those muons that have associated IceCube data and the associated dead time; the bottom rows show the number and percentage of events passing the coincidence algorithm.

Result Parameter	Det-1	Det-2	Total
DM-Ice muons	1981	1997	3978
# with IceCube data available	1952	1956	3908
IceCube deadtime	1.5%	2.1%	1.8%
# coincident with IceCube	1072	594	1666
% of DM-ice muons	55%	30%	43%

8.4.2 IceCube Misreconstruction Rates

A comparison of the traditionally-processed (SPE-seeded) MPE reconstruction with that using the DM-Ice17 seed provides valuable information about the quality of reconstructions and the potential to include DM-Ice17 information in calibration studies. Traditionally-processed Level2 MPE reconstructions use SeededRT-cleaned pulses and seed with the result of the SPE fit. The DM-Ice17-seeded MPE reconstructions use these same SeededRT-cleaned pulses, which had to be produced offline in this analysis for the sDST NChannel stream. The DM-Ice17 seed contains the position of the DM-Ice17 detector, which in IceCube coordinates corresponds to (31.25, -72.93, -511.05) for Det-1 and (-334.80, -424.50, -511.26) for Det-2. The other parameters of the seed are from Linefit, run on the SRTInIcePulses. The MuEx energy estimator was used with MPE for energy reconstructions. MuEx reconstructs within a factor of two, with increasing precision at higher energies, as shown in Figure 8.6 [187].

Misreconstructions are identified primarily by their zenith angle, which reconstructs to an unphysical value greater than 90° when the reconstruction fails. In addition to the zenith angle, energy misconstructions are considered misreconstructed below ~ 200 GeV because the muon will lose this much energy as it passes through the detector. The distance of closest approach of the reconstruction to the DM-Ice17 detector should

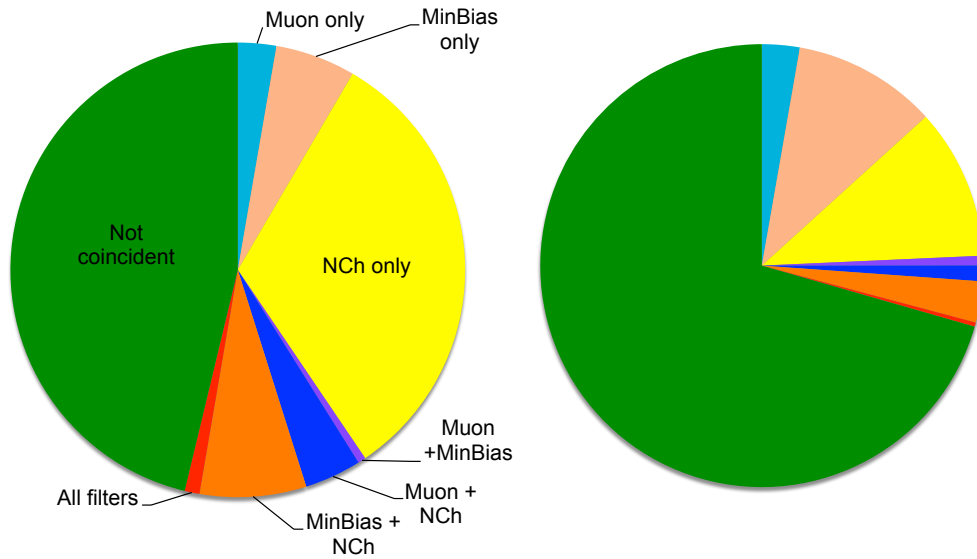


Figure 8.5: Results of DM-Ice17 and IceCube coincidence for Det-1 (left) and Det-2 (right). The sDST NChannel filter was particularly effective in this study. Shown are the number of DM-Ice17 muons that were not coincident (green), coincident with only the Muon Filter (light blue), sDST MinBias filter (beige) or sDST NChannel filter (yellow) as well as those coincident with two filters (Muon and sDST MinBias in purple, Muon and sDST NChannel in dark blue, and sDST MinBias and sDST NChannel in orange) and all three filters (red).

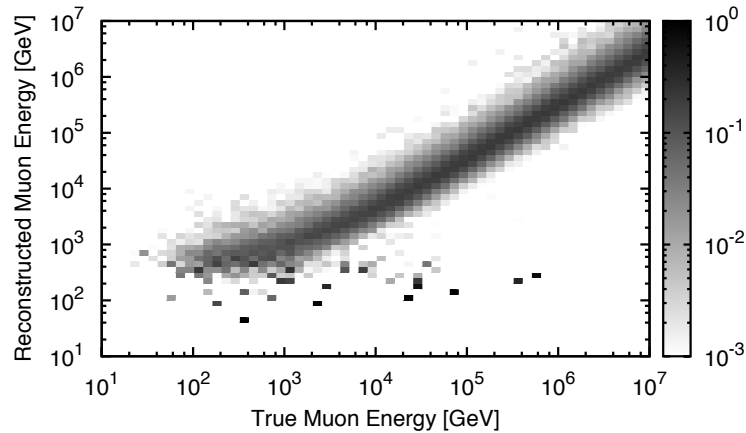


Figure 8.6: Quality of the MuEx energy estimator. Energies reconstruct to within a factor of two, with better agreement at high energies. Figure from [187].

be within the 20m resolution of the MPE reconstruction, and tracks that do not pass within this range are tagged as reconstructions that can use improvement.

Table 8.4: Coincident results organized by filter. The top rows compile the number and percentage of DM-Ice17 muons also observed in IceCube; the following rows show the number and percentage of those muons that coincide with events in the Muon Filter, sDST Channel, and sDST MinBias, respectively. Events passing multiple filters are counted in each filter but only once in the total, so the sum of the total passing events in each filter does not equal the total passing rate reported. *sDST NChannel data is only available for one year, so the percentage of coincidence is for only 2012-2013.

Result Parameter	Det-1	Det-2	Total
# coincident with IceCube	1072	594	1666
% of DM-ice muons	55%	30%	43%
#Muon Filter	166	98	264
% of DM-Ice muons	8.5%	5.0%	6.8%
#sDST NChannel	887	309	1196
% of DM-Ice muons*	93%	33%	63%
#sDST MinBias	295	290	585
% of DM-Ice muons	15%	15%	15%

The DM-Ice17 seed lowers the rate of misreconstruction by 20%, as show in Table 8.5. Due to differences in the event selection between filters, differences in the effect of the DM-Ice17 seed on misconstruction rates across filters illustrate the effect of using DM-Ice17 for particular event types. The difference in event selection is illustrated by the energy distribution of coincident events in each filter, as shown in Figure 8.7.

Table 8.5: Rate of misreconstructions for each MPE reconstruction seed.

Reconstruction	Zenith $>90^\circ$	Energy <200 GeV	Distance >20 m
Det-1 Traditional seed	115	64	139
Det-1 DM-Ice17 seed	44	23	166
Det-2 Traditional seed	145	23	94
Det-2 DM-Ice17 seed	100	28	105
Total Traditional seed	260	87	233
Total DM-Ice17 seed	144	51	271

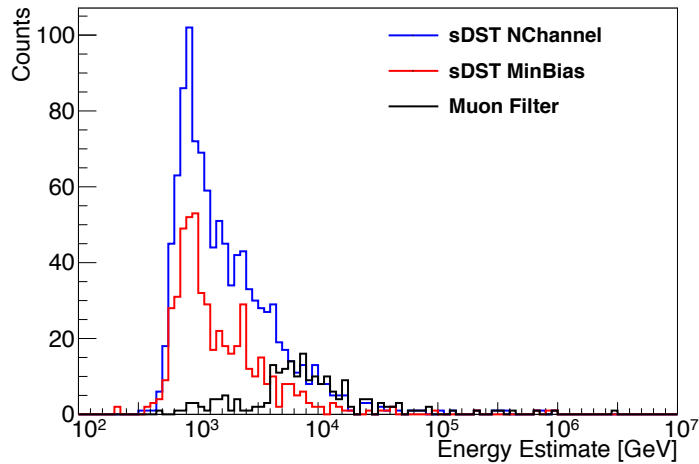


Figure 8.7: Reconstructed energies of coincident events in each filter. Energy reconstructions are from DM-Ice17-seeded MuEx fits. The Muon Filter preferentially selects high energy events while sDST NChannel and sDST MinBias include more low energy events.

The rate of misreconstruction for each filter from the zenith angle is shown in Figure 8.8 and Table 8.6; energy misreconstruction is shown in Figure 8.9 and Table 8.7; large distances of closest approach to DM-Ice17 are shown in Figure 8.10 and Table 8.8. An overall improvement in the number of misreconstructed events as determined by {zenith, energy, distance of closest approach} is observed, falling from {260, 87, 233} events with the traditional seed to {144, 51, 271} with the DM-Ice17 seed. Det-1 successfully reconstructs more often, as expected by its geometric location. The improvement in misreconstruction rates with the addition of the DM-Ice17 seed is significant for the lower energy sDST NChannel stream, while it does not improve events from the higher energy Muon Filter or the sDST MinBias filter. In the sDST NChannel stream, zenith misreconstructions fall from 223 to 72 with the inclusion of DM-Ice17. Of these zenith-misreconstructing events in sDST NChannel, 35 fail with both seeds, 37 newly misreconstruct upon the introduction of the DM-Ice seed, while 188 no longer misreconstruct using the DM-Ice seed. This indicates that the inclusion of the DM-Ice17 seed improves reconstructions for these events, which are primarily low energy events that are difficult to reconstruct. By contrast, in the Muon Filter and sDST MinBias channels, the number of zenith-misreconstructed events goes from 60 to 97 with the introduction of the DM-Ice seed. Of these, 38 fail with both seeds, 59 newly misreconstruct with the DM-Ice seed, and 22 successfully reconstruct only with the DM-Ice seed. This increase in misreconstructions indicates that the DM-Ice seed is less helpful with higher energy events, and the development of a full likelihood reconstruction will be required for improvement with these events, as discussed in §8.4.4.

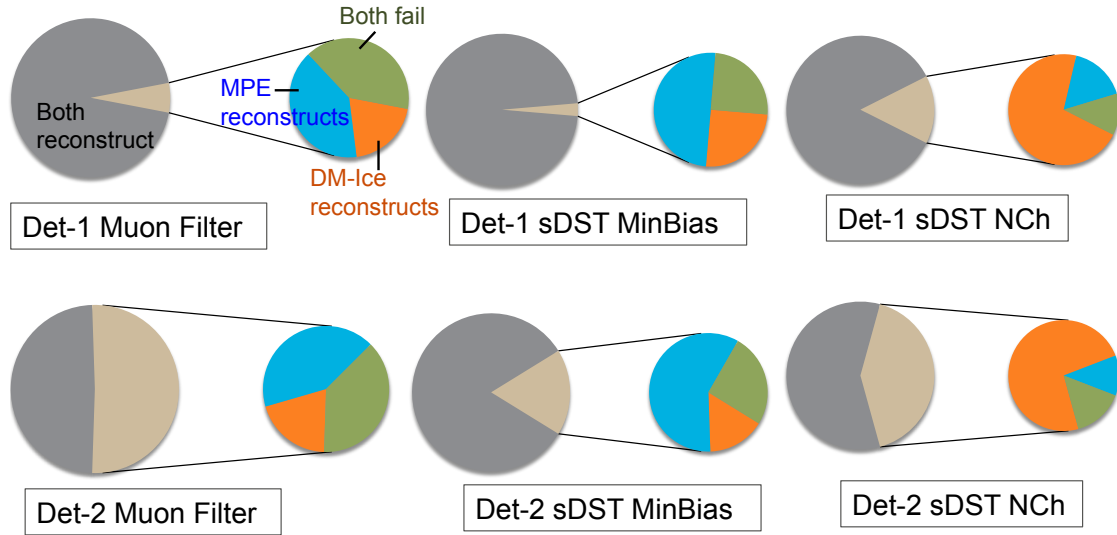


Figure 8.8: Rate of zenith $>90^\circ$ misconstructions for SPE- and DM-Ice17-seeded MPE reconstructions. Significant improvement occurs for the lower energy sDST NChannel filter, while the sDST MinBias and higher energy Muon Filter streams are not improved. The values from these figures are compiled in Table 8.6.

Table 8.6: Zenith misreconstruction rate, by filter. Rates are compared before and after seeding with DM-Ice17. This data is illustrated in Figure 8.8.

	Det-1 (2)	Pass DM-Ice seed	Fail DM-Ice seed
Pass traditional seed	Muon Filter	156 (48)	4 (21)
	sDST MinBias	287 (239)	4 (30)
	sDST NChannel	755 (181)	22 (15)
	Total	926 (387)	24 (56)
Fail traditional seed	Muon Filter	2 (10)	4 (19)
	sDST MinBias	2 (8)	2 (13)
	sDST NChannel	94 (94)	16 (19)
	Total	95 (101)	20 (44)

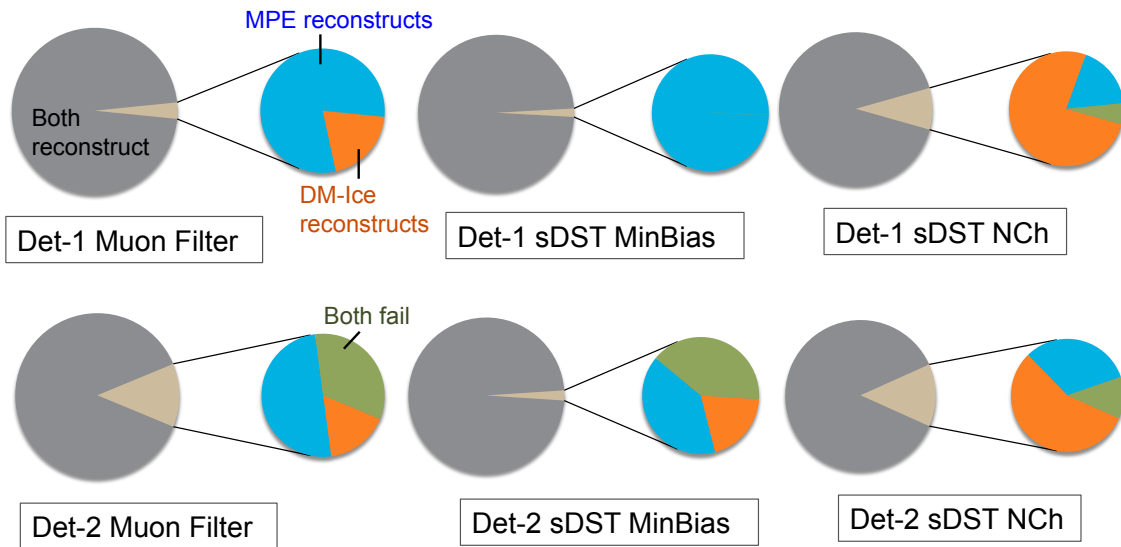


Figure 8.9: Rate of unphysically low energy reconstructions (<200 GeV) for SPE- and DM-Ice17-seeded MPE reconstructions. Zenith misconstructions have been removed. As with the zenith misconstructions, significant improvement occurs for the lower energy sDST NChannel filter, while the sDST MinBias and higher energy Muon Filter streams are not improved. No events in the muon or sDST MinBias filter failed with both seeds. This data is compiled in Table 8.7.

Table 8.7: Energy misreconstruction rate, by filter, before and after seeding with DM-Ice17. This data is illustrated in Figure 8.9.

		Det-1 (2)	Pass DM-Ice seed	Fail DM-Ice seed
Pass traditional seed	Muon Filter		152 (41)	3 (4)
	sDST MinBias		283 (231)	3 (5)
	sDST NChannel		696 (161)	9 (4)
	Total		864 (358)	10 (10)
Fail traditional seed	Muon Filter		1 (1)	0 (2)
	sDST MinBias		0 (1)	1 (2)
	sDST NChannel		46 (13)	4 (3)
	Total		47 (15)	5 (4)

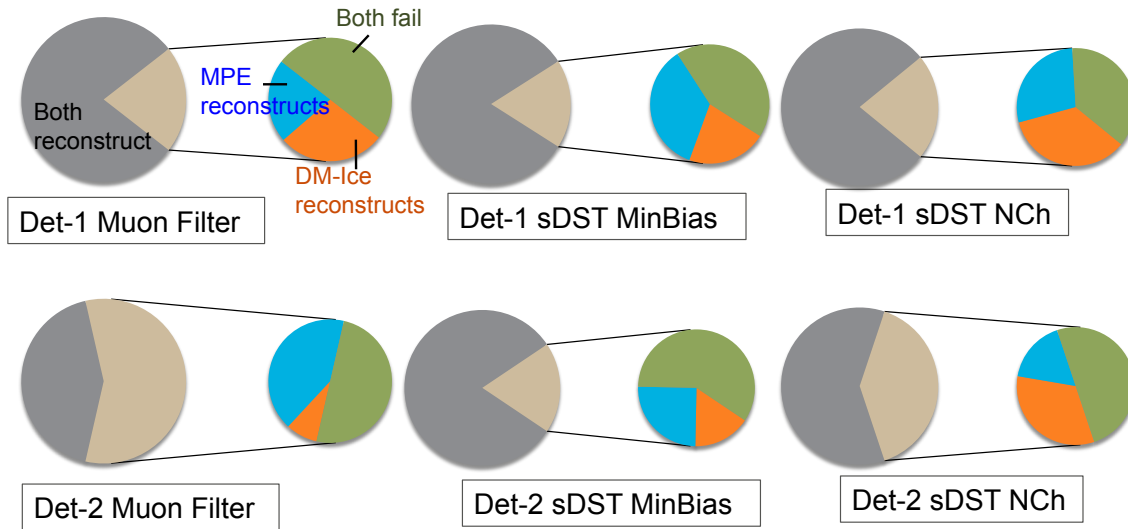


Figure 8.10: Rate of reconstructions passing outside the 20m resolution distance from DM-Ice17 for SPE- and DM-Ice17-seeded MPE reconstructions. The seeds perform similarly, with the DM-Ice17 improving sDST NChannel events the most. Zenith and energy misconstructions have been removed. This data is compiled in Table 8.8.

Table 8.8: Distance misreconstruction rate, by filter, before and after seeding with DM-Ice17. This data is illustrated in Figure 8.10.

	Det-1 (2)	Pass DM-Ice seed	Fail DM-Ice seed
Pass traditional seed	Muon Filter	120 (18)	7 (10)
	sDST MinBias	232 (190)	18 (10)
	sDST NChannel	545 (97)	43 (11)
	Total	678 (257)	56 (23)
Fail traditional seed	Muon Filter	9 (2)	16 (11)
	sDST MinBias	11 (7)	22 (24)
	sDST NChannel	53 (21)	56 (32)
	Total	58 (26)	73 (52)

8.4.3 Impact on IceCube Reconstructions

When both seeds successfully reconstruct, comparing the reconstruction parameters determines the resolution of the reconstructions and verifies that the reconstructions behave as expected. Investigated parameters include the trigger time difference, the reconstructed zenith and azimuth, the reconstructed energy, and the distance of closest approach to the coincident DM-Ice17 detector.

8.4.3.1 Timing

The difference between the DM-Ice17 and IceCube event start times verifies that all events fall within $[-1, 6] \mu\text{s}$, where a positive value indicates that IceCube triggered first. No event triggered DM-Ice17 before IceCube, as shown in Figure 8.11. The timing variable is not reconstruction-dependent, so there is no difference between seeds. The Det-1 timing distribution peaks from $2.5\text{--}4 \mu\text{s}$, indicating that the muons pass through 1 km of IceCube before hitting DM-Ice. The Det-2 distribution peaks near zero and $3.5 \mu\text{s}$, indicating two event populations: “corner clippers” that skim the corner of the detector and trigger both detectors nearly simultaneously, and events that pass through 1.2 km of IceCube before triggering DM-Ice. Differences between the filters are consistent with their trigger conditions, with Muon Filter events preferring high energy events that pass through the entire detector or pass through the edge of IceCube, while the sDST filters see a larger spread in trigger time differences.

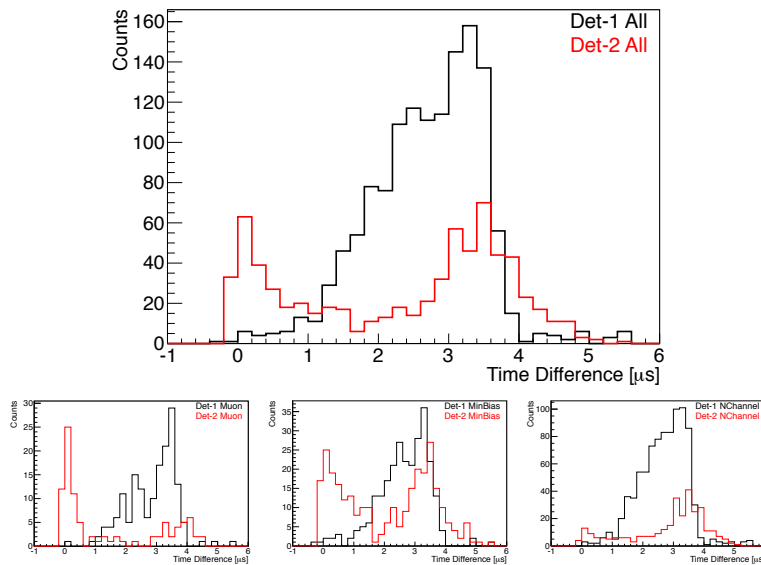


Figure 8.11: Difference in time between DM-Ice17 and IceCube trigger times. Shown is all data (top) and (bottom, from left): Muon Filter, sDST MinBias, and sDST NChannel events. Det-1 is in black, and Det-2 is in red. The $4 \mu\text{s}$ padding offset has been applied.

8.4.3.2 Direction

Zenith and azimuth distributions are in good agreement and consistent with expectation across each seed. No azimuthal dependence is expected for Det-1, and none is observed. An azimuthal asymmetry is expected and observed for Det-2, which only has IceCube on one side of it, as shown in Figure 8.12. The grey region refers to that range with very few events in the azimuth distribution (around 200°), and orange refers to the region with the azimuthal distribution peaks. The azimuthal peaks are associated with the location of IceCube in reference to Det-2. The zenith angle distributions peak between 20° and 55° , as shown in Figure 8.13. The residuals are dominated by the larger number of events in the DM-Ice17-seeded reconstructions due to the lower rate of misconstruction, and the form of the residuals follows that of the distributions. While more muons are expected near vertical ($\theta_z=0$), a larger area is integrated over at higher zenith angles, resulting in the observed distribution.

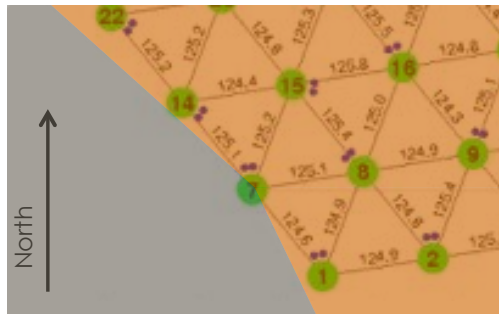


Figure 8.12: Azimuth coordinates of Det-2 in relation to IceCube. Azimuth is defined in polar coordinates with zero to the east. The orange band is where the majority of the events in Figure 8.13 lie, while the grey is where there are few events. This corresponds to the location of the IceCube detector in relation to Det-2.

In addition to changes in the parameter distributions due to the new seed, changes in individual reconstructions have also been investigated. The differences in the reconstructed zenith and azimuth angles are centered about zero for both zenith and azimuth, as shown in Figure 8.14. The distributions each have a gaussian sigma of 0.7° . These values imply a net uncertainty slightly smaller than the quoted resolution of 20 m.

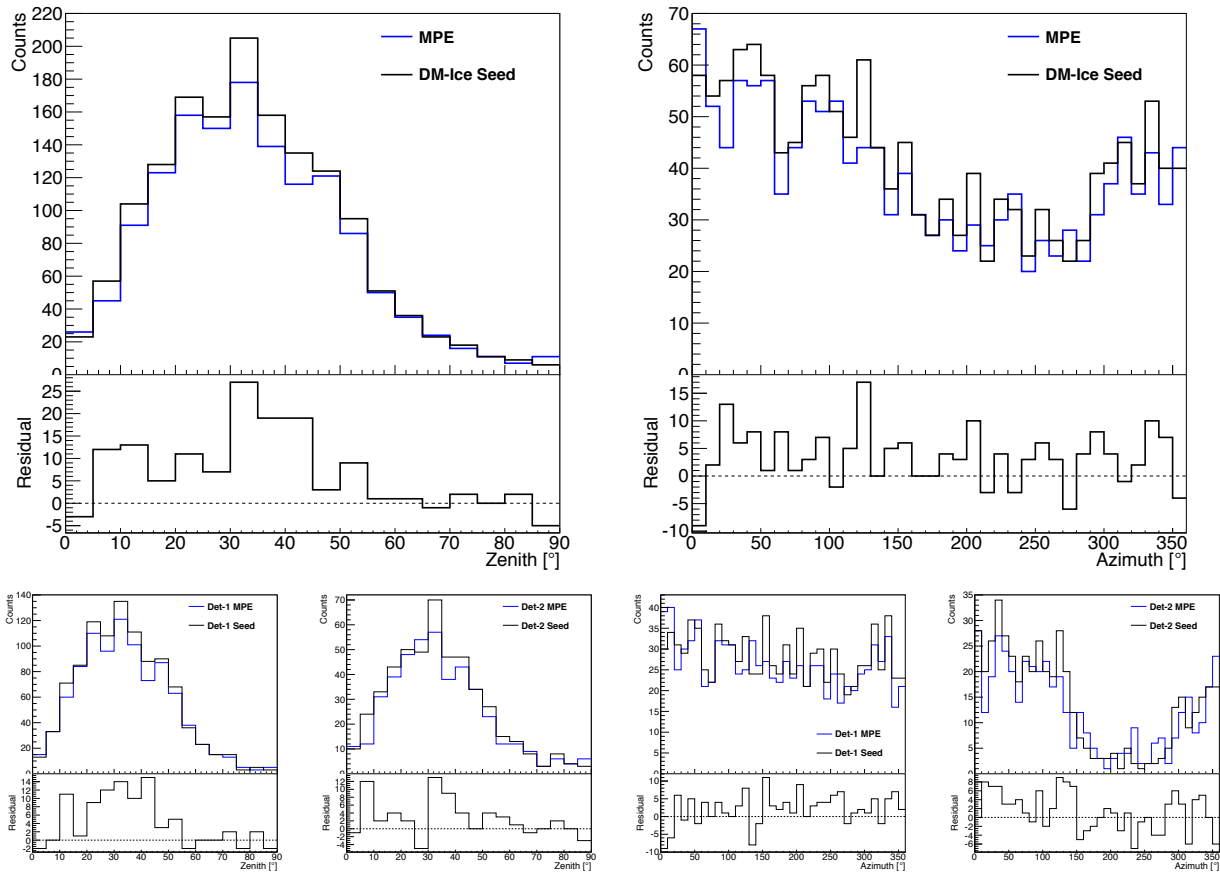


Figure 8.13: Reconstructed coordinates (zenith, azimuth) of coincident events. DM-Ice seeded reconstructions are shown in black, and traditional MPE seeds are in blue. The smaller images show the distributions in Det-1 (left) and Det-2 (right). Good agreement is observed between the seeds. Misreconstructed events have been removed.

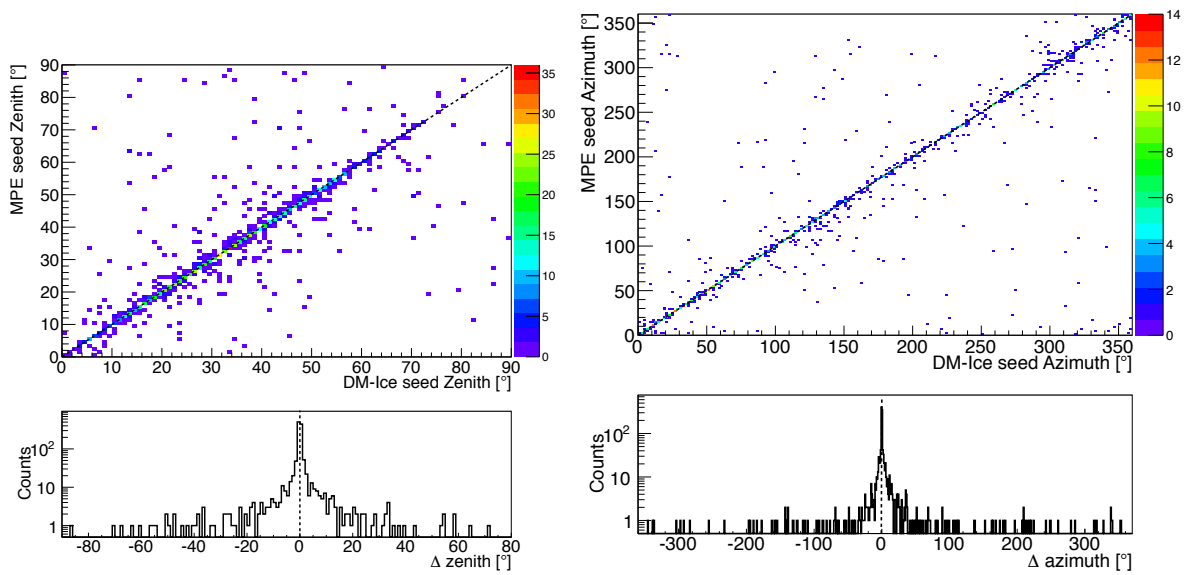


Figure 8.14: Difference in reconstructed coordinates (zenith, azimuth) for each seed. The difference is defined as the DM-Ice seeded reconstruction with the traditional MPE reconstruction subtracted from it. Good agreement, on average, is observed between seeds, as indicated by the distributions clustering about zero. Misreconstructed events have been removed.

8.4.3.3 Energy

IceCube reconstructions provide DM-Ice with muon energy information, and the spectrum of coincident events is consistent with expectation, as shown in Figure 8.15. The IceCube energy threshold is roughly 100 GeV, leading to a decrease in events approaching this energy. The high energy spectral shoulder is due to the combination of filters, as shown in Figures 8.7 and 8.15. These reconstructions validate the assumption that the incident DM-Ice17 muon sample are minimum ionizing particles.

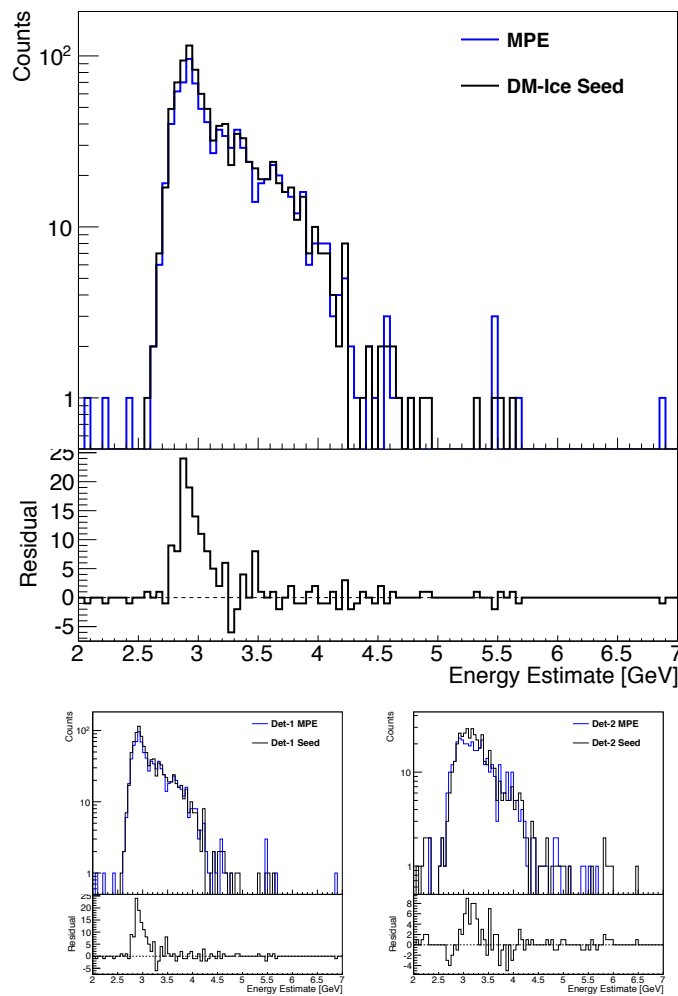


Figure 8.15: Muon energy approximation for those events passing the coincidence condition, as determined by the MuEx energy estimator. The DM-Ice17 seed is in black, and the traditional seed is in blue. The comparison in Det-1 (left) and Det-2 (right) are shown below. Misreconstructed events have been removed. The expected spectrum from simulation is provided in Figure 7.3 .

The difference in the energy distribution is in the positive direction, indicating a net increase in the reconstructed energy with the DM-Ice17 seed, as shown in Figure 8.16. 55% of the events have a higher energy reconstruction with the DM-Ice17 seed. This is expected due to the seed encouraging the track to pass through the bottom of the detector, which occurs for higher energy events. The distribution can be fit with a Gaussian centered about 84 GeV for Det-1 and 187 GeV for Det-2, with a width of $\sigma=600$ GeV. The spread is larger at lower energies, consistent with expectation for the MuEx estimator.

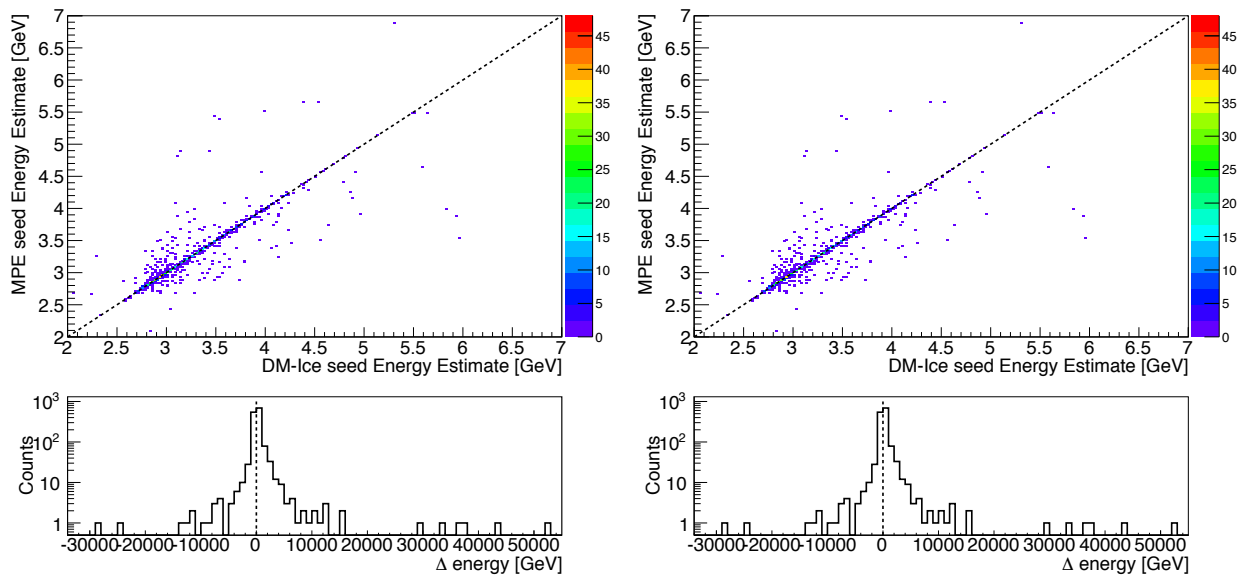


Figure 8.16: Difference in energy reconstruction between seeds. DM-Ice17-seeded events reconstruct, on average, as higher energy. The difference is defined as the DM-Ice seeded reconstruction with the traditional MPE reconstruction subtracted from it. Misreconstructed events have been removed.

8.4.3.4 Track Location

A natural and powerful measure of the quality of the reconstruction is the distance of closest approach of the track to the DM-Ice17 crystal through which the muon passed. An uncertainty of ± 0.5 m is taken for the DM-Ice17 coordinates due to the volume of the crystal, uncertainty in the depth precision, and uncertainty in the x-y coordinates due to movement in the hole during deployment and freeze-in. The MPE reconstruction has a 20 m resolution, so a well-reconstructed event should pass within 20 m of DM-Ice17. In the SPE-seeded sample, $65.4 \pm 2.0\%$ of events are within the reconstruction resolution, while in the DM-Ice17-seeded reconstructions, $72.0 \pm 2.1\%$ of events are within this resolution, as shown in Figure 8.17. Well-reconstructed events are more likely in Det-1 events, where improvement went from $70.6 \pm 2.6\%$

to $78.2 \pm 2.7\%$, as opposed to the small improvement in Det-2, where the distributions are within error of each other, increasing from $60.0 \pm 3.1\%$ to $60.7 \pm 3.2\%$. A small improvement is observed with the DM-Ice17 seed, with 53% events passing closer to the detector, as evidenced in Figure 8.18. The difference distribution is centered about an improvement of 0.06 m with a Gaussian uncertainty of 0.6 m. The events outside of this distance are both poorly reconstructed events and events that contain noise or coincident muons in the detector. These distribution indicate improvement from reconstructions using the DM-Ice17 seed while illustrating that there is room for further improvement, as described in §8.4.4.

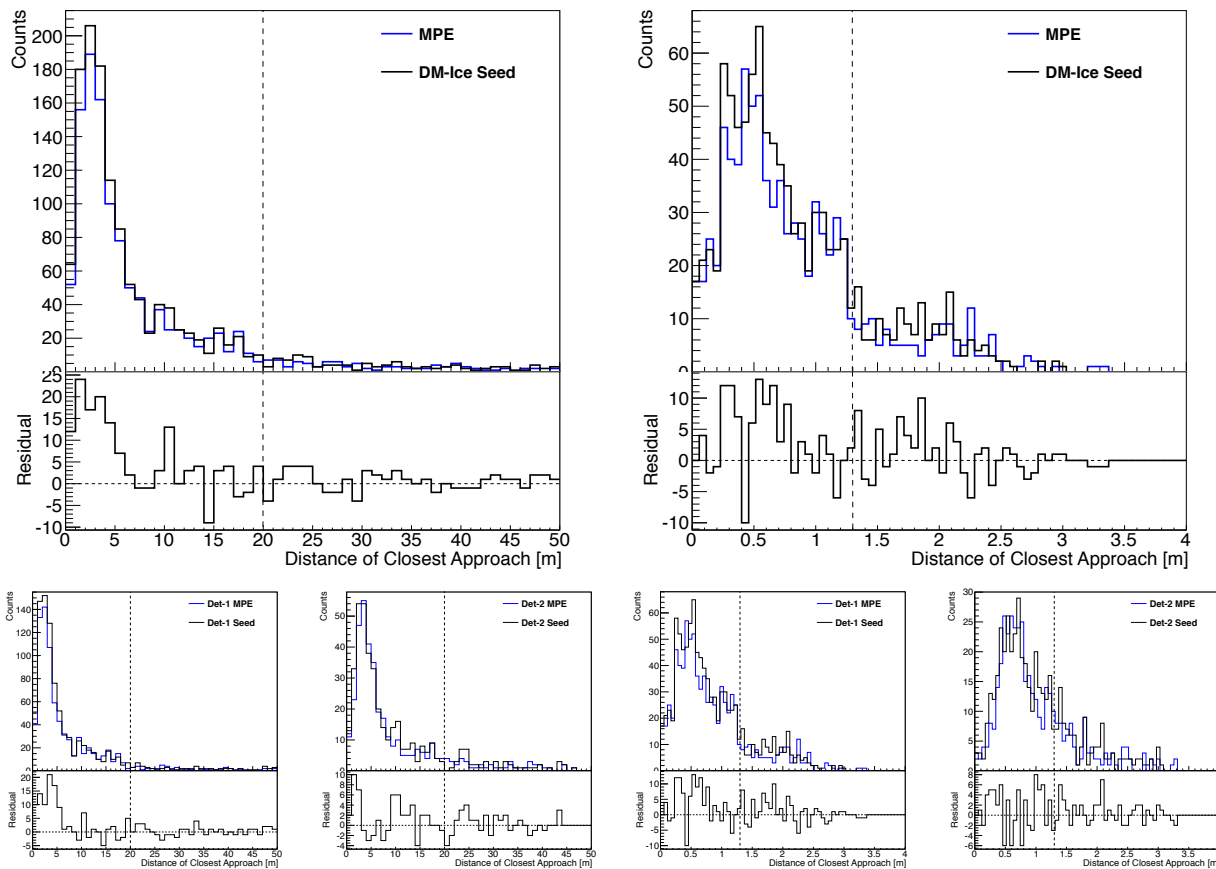


Figure 8.17: Distance of closest approach of coincident events in IceCube to the top of the DM-Ice17 crystal. The DM-Ice17 seed is in black, and the traditionally-seeded MPE reconstruction is in blue. Misreconstructed events have been removed. The right-hand side images show the full distance range, while the left-hand images zoom in on the largest distribution.

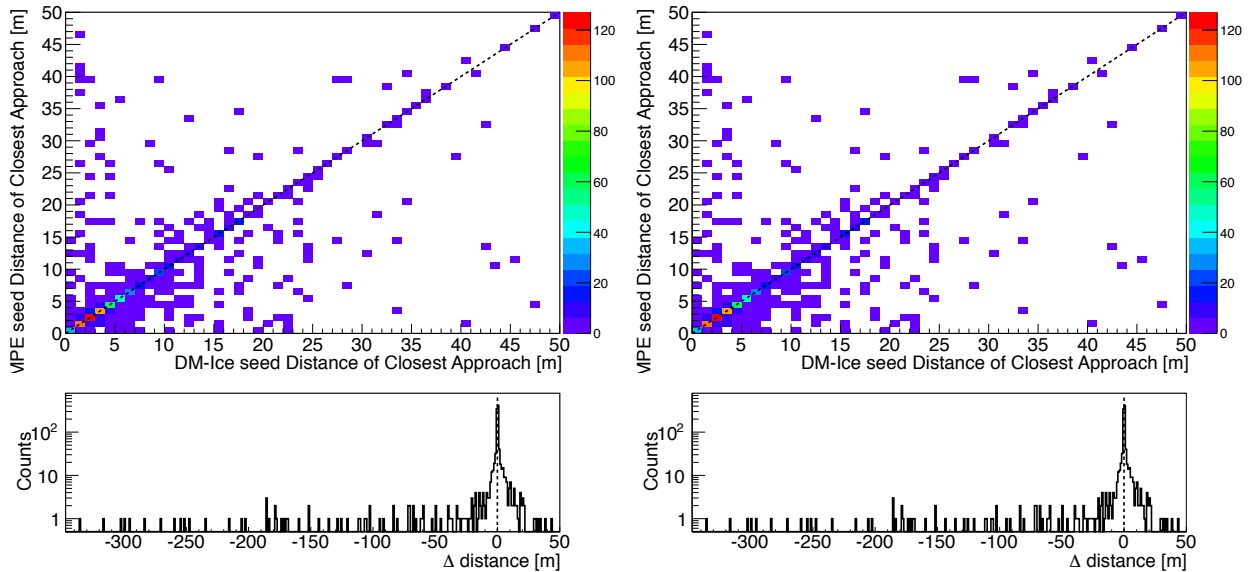


Figure 8.18: Difference in distance of those events passing the coincidence condition. DM-Ice17-seeded events reconstruct, on average, as closer to the DM-Ice17 prototype. The difference is defined as the DM-Ice seeded reconstruction with the traditional MPE reconstruction subtracted from it. Misreconstructed events have been removed.

8.4.4 Future Study

This study validates the DM-Ice17 muon identification and the quoted resolution of IceCube reconstructions. The improvements in low energy reconstructions with the addition of the DM-Ice17 seed illustrate the asset of including scintillators in a low energy Cherenkov detector.

This study is one of many that can be pursued with these coincident events. DM-Ice may be able to use IceCube to identify muons that clip the crystal, appearing in the gamma regime. This study would require location cuts in IceCube and energy cuts in DM-Ice17, but may be able to provide a limit on the number of such clipping events.

The development of scintillators like DM-Ice17 as a calibration tool will be of particular use to the improvement of reconstructions with the Precision IceCube Next Generation Upgrade (PINGU), the next generation Cherenkov detector that will focus on the low energy region. A co-deployment with the full-scale DM-Ice detector would be mutually-beneficial.

Chapter 9

Towards DM-Ice250

With the prototype operating better than projected and returning the information that it was designed to find, progress is being made on the development of the full-scale detector, starting with DM-Ice37. Improvements have been made in the location, crystal purity, PMTs, and electronics. Development will continue to achieve crystal contamination levels lower than those in the DAMA crystals. The full-scale, 250 kg detector will run at Boulby until the deployment of PINGU. DM-Ice250 and PINGU will deploy in the South Pole ice together, providing complementary data that allows DM-Ice to continue to verify its muon veto and that improves the low-energy reconstruction capabilities of PINGU. With experience in detector development, South Pole deployment, and NaI(Tl) dark matter analysis, DM-Ice250 will be ready to deploy at the South Pole on an aggressive timescale once actively running at Boulby.

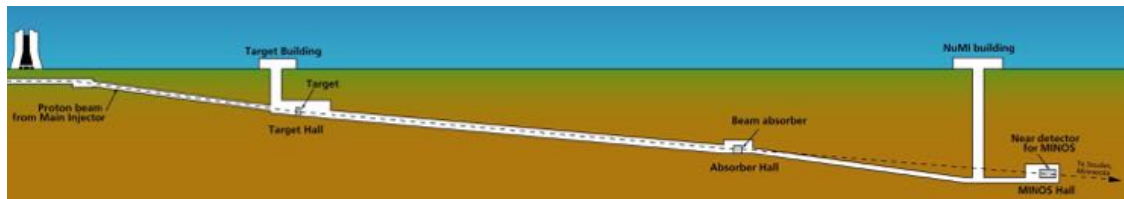
9.1 DM-Ice37

DM-Ice37 is currently running at the Boulby Underground Laboratory in the UK. This phase of the experiment is focused on the development of low-background detector components. A collaborative crystal R&D program is underway to produce NaI(Tl) with the level of background achieved by DAMA (~ 1 count/day/keV/kg in the region of interest). DM-Ice is working with the crystal growing company Alpha Spectra in conjunction with the ANAIS and KIMS dark matter experiments (see §3.5). Significant progress has been made in crystal purification and growth, and DM-Ice will be in the R&D phase until crystals are developed with backgrounds lower than the DAMA crystals. At that point, DM-Ice250 will be commissioned and deployed.

DM-Ice37 is made up of two copper-wrapped 18.3 kg crystals, ($5'' \varnothing \times 15''$) from the Alpha-Spectra company, referred to as AS1 and AS2. The crystals were first run at Fermilab in Illinois (see §9.1.1) from April 2014 - November 2014, then they were sent to Boulby (see §9.1.2). They have been running continuously at Boulby since their installation.

9.1.1 Fermilab Run

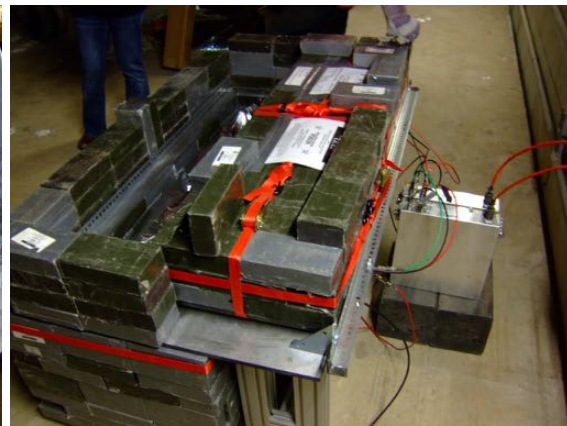
DM-Ice37 testing began at the Fermilab National Accelerator Laboratory. The detectors ran in a lead castle in the MINOS Near Detector tunnel, as shown in Figure 9.1. The crystals were each connected to two R877-100-01 PMTs and wrapped in a mylar bag for light shielding and nitrogen containment. The data was read out in four channels, just as in the ice, with three ATWD channels at three different gains and an FADC channel (see §5.2.2).



(a) MINOS tunnel at Fermilab



(b) DM-Ice test crystals in mylar bag



(c) Lead castle used for testing

Figure 9.1: DM-Ice test setup at Fermilab. Two crystals are located in the lead crystal, each connected to two PMTs for coincidence.

Data from the Fermilab test setup was treated with the DM-Ice17 data processing scheme, including the same waveform corrections. Source runs provided data for energy calibration, as shown in Figure 9.2.

The testing location provided 100 m (225 m.w.e.) of rock overburden [188, 189]. The integrated atmospheric muon flux at this depth is projected to be $0.7 \mu/\text{m}^2/\text{s}$ [190]. This leads to a projected muon flux estimate per crystal of:

$$0.7 \mu/\text{m}^2/\text{s} \times 5'' \times 15'' = 0.07 \mu/\text{m}^2/\text{s} \times 0.048 \text{m}^2 = 120 \mu/\text{hr} \quad (9.1)$$

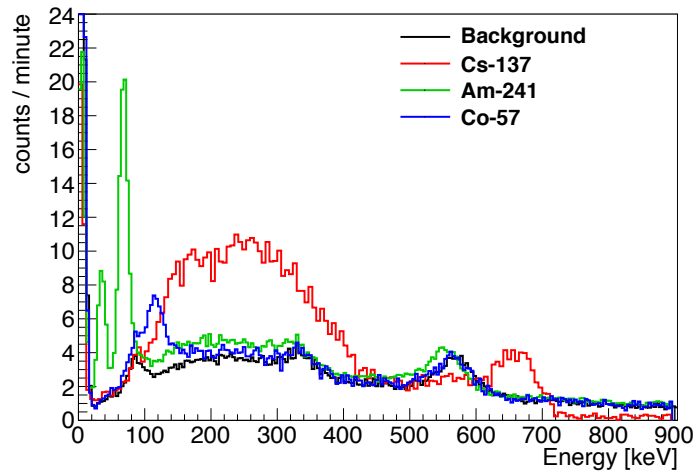


Figure 9.2: Calibration data from Fermilab source runs. Shown is data from the AS2 ATWD1 channel.

Observed muon rates were $\sim 50 \mu/\text{crystal}/\text{hour}$, indicating uncertainty in the expected value and significant overlap of muon events into the gamma region. Gamma, alpha, and muon events were separated using the same parameters as the in-ice analysis, as shown in Figure 9.3. Event type separation was chosen to isolate a pure, rather than a complete, muon sample; the cuts maintain a negligible number of alphas entering the muon sample, less than 0.01% of muon events entering the alpha sample ($\sim 34/\text{yr}$), and less than 0.01 gammas entering the muon sample per year.

Improved contamination levels are evident in the comparison of the Fermilab alpha region with that of the detectors in the ice. Figure 9.4 shows the alpha region from PMT-2b in the ice compared to AS1A's alphas at Fermilab. A 65% reduction in internal contamination (from $5.22 \pm 0.002 \text{ mBq/kg}$ to $1.85 \pm 0.002 \text{ mBq/kg}$) is evident in the reduced alpha flux. Levels of ^{210}Pb remained relatively constant between DM-Ice17 and DM-Ice37, with all other internal contaminants significantly decreased. The ^{210}Pb levels continue to increase in the crystals as ^{222}Rn introduced during exposure to air in the crystal growing process decays. This increase is evident in the increased levels from runs at Fermilab to those at Boulby, as discussed in §9.1.2.

The large background rate at Fermilab forced the experiment to relocate to Boulby, which provides a larger overburden. This large muon rate was, however, beneficial for phosphorescence studies. A roughly 300 ms phosphorescence decay was observed following high energy muon events at Fermilab, as shown in Figure 9.5. The phosphorescence decay time was significantly shorter than observed at the South Pole, fit to roughly 300 ms. This decay is a source of active investigation. The significant decrease in the decay time is consistent with the hypothesis that phosphorescence is due to impurities and defects in the crystal (see §4.2.4). Because a newly-grown crystal was run at Fermilab, it had not received the lifetime of exposure,

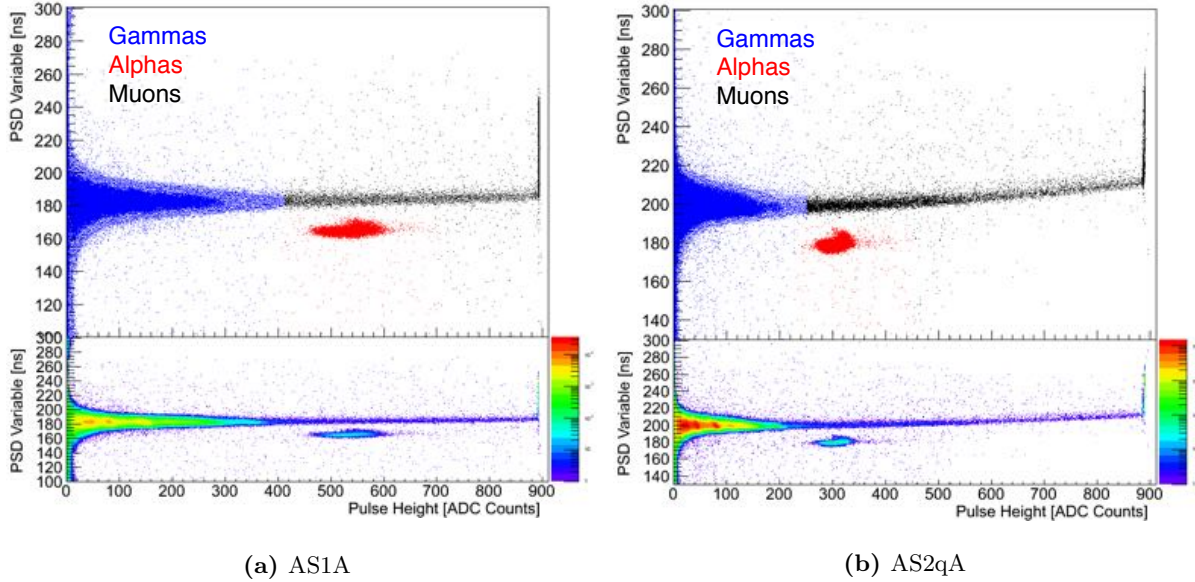


Figure 9.3: Event type separation in each crystal at Fermilab for AS1 (left) and AS2 (right). The bottom figures are identical to the top figures, with the z-axis illustrating the density in each bin.

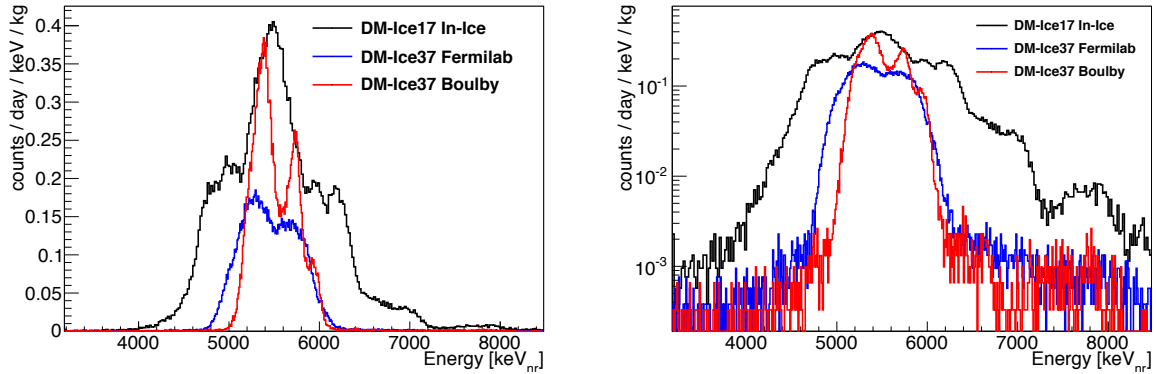


Figure 9.4: Comparison of alpha spectrum between Det-2 in the DM-Ice17 detector (black) and AS1A run at Fermilab (blue) and Boulby (red) (linear, left and log, right). Improved reduction of internal contamination has significantly reduced the alpha rate in DM-Ice37. The increased peak heights at Boulby are due to improved resolution and an increase in the lower level of the ^{238}U -chain as radon continues to decay.

and radiation-induced defects, of the older crystal in the ice. Future studies on both old and new crystals will provide more data for this study.

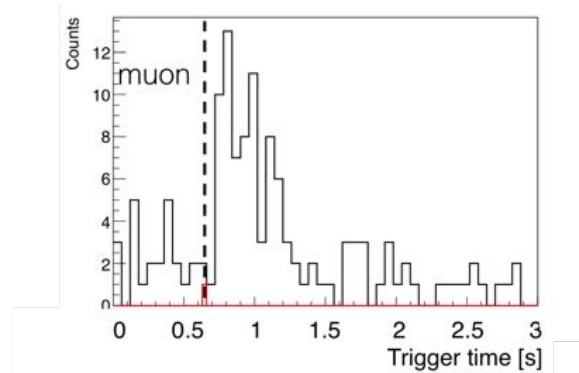


Figure 9.5: Potential phosphorescent event observed at Fermilab with a decay time of ~ 300 ms.

9.1.2 Boulby Run

DM-Ice37 was moved from Fermilab to the Boulby Underground Laboratory (Boulby) in November 2014. The detector came online at Boulby on December 10th, 2014, and it has been in operation ever since. Boulby, shown in Figure 9.6, provides 2850 m.w.e. (1070 m of rock) of overburden. In addition to a large overburden, the environmental backgrounds at Boulby are lower than in most labs, as illustrated in the comparison between Boulby, LNGS, and a typical surface environment, measured at Bochum, in Figure 9.7 [191]. The contamination components are compiled in Table 9.1. U-chain, Th-chain, and K values were measured with Ge surveys of local rock; Rn has been measured by experiments at the laboratory; neutron values are based on simulation for the measured U- and Th-chain contamination; muon measurements are from the ZEPLIN collaboration measurement [192]. Radon and neutrons are particularly important to reduce, and Boulby has significantly lower radon than other laboratories due to the location geology: the Boulby environment is made of salt, which results in significantly lower radon levels than rock environments.

The DM-Ice37 detector setup is shown in Figure 9.8. Both crystals are running within a nitrogen-flushed, copper-lined lead castle. The castle lid is in multiple sections so that one piece may be removed for source runs while keeping the remaining pieces installed. A mylar sheet is placed over the missing castle area as a light seal during source runs.

Detectors were upgraded in January 2015, when the PMTs models were changed from the Hamamatsu R877 model to the Hamamatsu R12699 model. Quartz light guides were also removed at this time. These upgrades produced a significant decrease in the overall rate, as shown in Figure 9.9. Crystal AS2 fell from 2.27 ± 0.01 to 2.17 ± 0.01 Hz, while AS1, which triggers much more efficiently on PMT noise, fell from 3.04 ± 0.01 to 2.37 ± 0.01 Hz. With these upgrades, a background rate directly above the region of interest (~ 8 keV) of 3 dru has been achieved. With the development of noise removal in the region of interest, this flat background will

Table 9.1: Potential background-producing particle counts at underground laboratories. U-chain, Th-chain, and K values from rock. Ice measurements are shown for glacial ice, designated by †, and drill ice. LNGS measurements were taken in both Hall A and Hall B; LSC measurements were taken at three locations in Hall A.

Laboratory	U-chain	Th-chain	⁴⁰K	²²⁸Rn	Muons	Neutrons
Reference	[ppb]	[ppb]	[ppm]	[Bq/m ³]	[cm ⁻² s ⁻¹]	[m ⁻² s ⁻¹] ¹
Boulby [191, 193]	67±6	127±10	1130±200	2.5±1.6	(3.75±0.09)×10 ⁻⁸	(1.2±0.99)×10 ⁻²
LNGS Hall A	6800±67	2167±74	160	20-120	2.87×10 ⁻⁸	(3.78±0.25)×10 ⁻²
[191, 194, 195] B	420±100	62±20				
LSC	30±3	60±6	880±36	70±8	(3±1)×10 ⁻⁷	(3.44±0.35)±10 ⁻²
[191, 196–198]	4.5±0.2	9.8±0.3	31±1			
	8.5±0.3	23±1	76±2			
Y2L [199–201]	1770 - 2820	11100-14500	270	40 - 80	2.7×10 ⁻⁷	8×10 ⁻³
South Pole [154]	0.076±0.046	0.47±0.14	<0.262	~0	2×10 ⁻⁷	-
(2200 m.w.e.)	10 ^{-4†}	10 ^{-4†}	0.1† (<i>nat</i> K)			

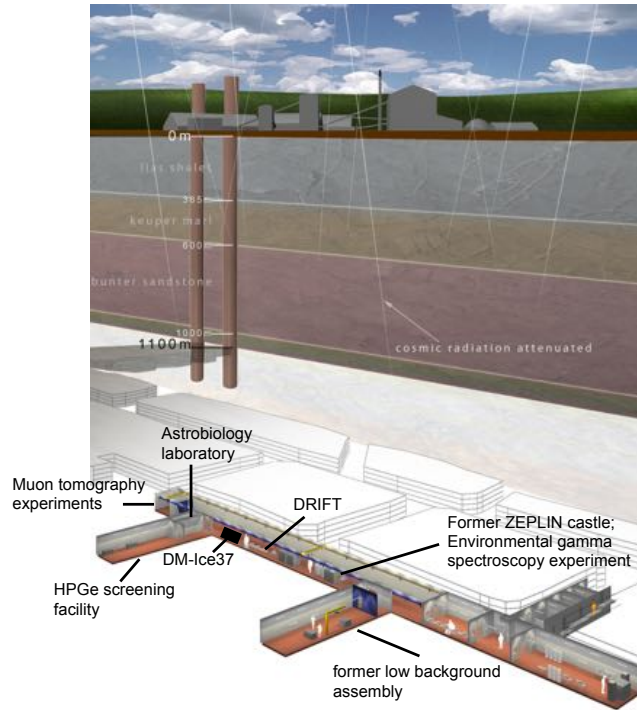


Figure 9.6: Boulby Underground Laboratory and experimental locations within the laboratory. DM-Ice37 and DRIFT are active direct detection dark matter experiments. ZEPLIN and NaIAD ran previously in the laboratory. The HPGe testing facility is used by a number of experiments for screening, including LZ and SuperNEMO.

remain as the estimated background for these crystals. Levels of ^{210}Pb continue to increase due to ^{222}Rn decays, increasing by 23% from Fermilab data from July 2014 to Boulby data from December 2014 and January 2015. Current work focuses on the development of cleaner crystals, as described in §3.5.

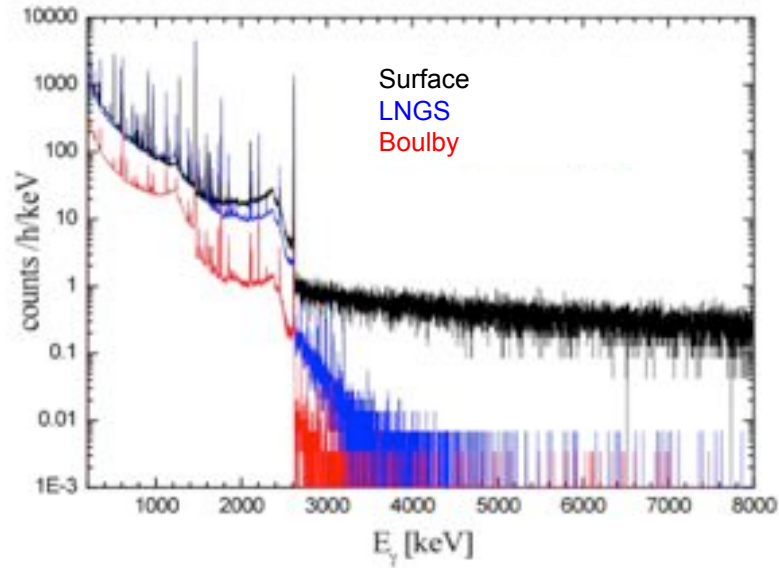


Figure 9.7: Lab background comparison. U-chain, Th-chain, and K values are from Ge surveys; Rn was measured by experiments at the laboratory; neutron values are from simulation from U-chain and Th-chain contamination; muon values are from the ZEPLIN collaboration measurements Figure from [191].

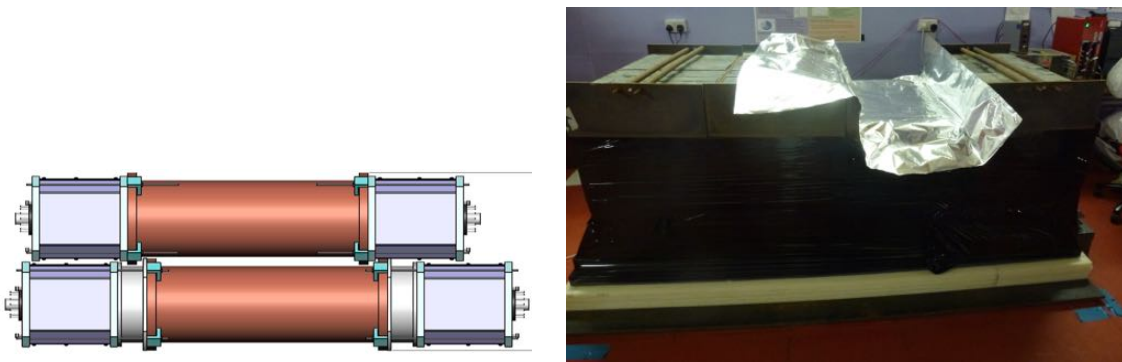


Figure 9.8: DM-Ice37 detector at Boulby. Both crystals are deployed inside a copper-lined lead castle and attached to two PMTs. Sections of the castle roof are removed for source runs; a mylar blanket is used as a light seal during these runs.

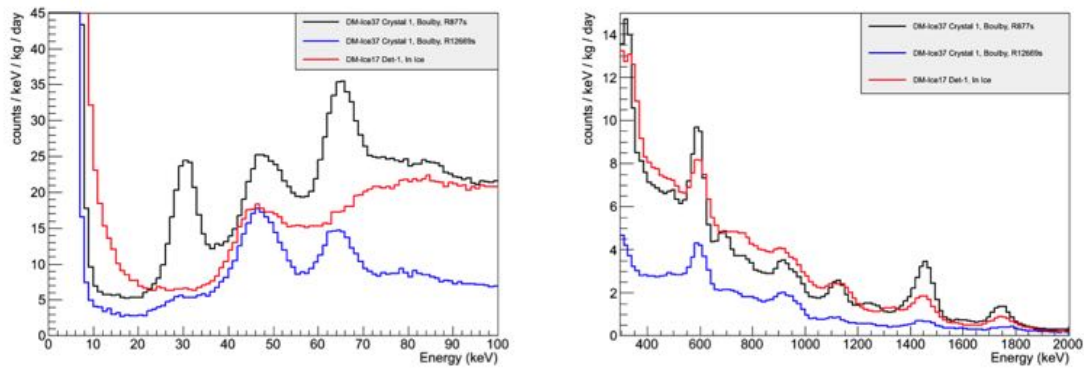


Figure 9.9: Background comparison of DM-Ice17, DM-Ice37 (R877 PMTs) and DM-Ice37 (R12699 PMTs) at Boulby. Left: low energy region (0-100 keV); right: high energy gamma region (300 - 2000 keV). Improvements in crystal purification has reduced backgrounds originating from the crystals. Combined with PMT choice, the background rate in DM-Ice37 has been significantly reduced.

9.2 DM-Ice250

DM-Ice250 will run an annual modulation search with a transportable detector run in both the Northern and Southern Hemispheres. The first phase of DM-Ice250 will be deployed inside the XENON100 shielding at LNGS. DM-Ice250 North and DAMA will run simultaneously at LNGS, providing a valuable comparison between data from the two experiments. The XENON100 shielding components have been previously radio-assayed and well-simulated, providing a well-understood environment for the detector [202]. Operating at LNGS offers the opportunity to perform calibration runs and additional detector testing, which are significantly more difficult at the South Pole. If a modulation is not observed with DM-Ice250 North, the DM-Ice250 South phase may not be required. DM-Ice250 will be able to exclude or confirm the DAMA signal with two years of data, as shown in Figures 5.5 and 5.6 for multiple background scenarios. If a modulation is observed with DM-Ice250 North, then DM-Ice250 South will be deployed to provide a unique set of complementary data for the most complete understanding of the annual modulation signal.

DM-Ice250 will be comprised of two 125 kg detectors, each containing a seven-crystal array, as shown in Figures 5.4 and 9.10. The array of low-background NaI(Tl) crystals will veto the 3 keV ^{40}K peak as described in §3.5.1. The veto is projected to be 67% efficient in removing the 3 keV peak in the inner crystal and 37% efficient in the outer crystals. This veto capability will significantly reduce the background rate in the region of interest, which is dominated by the ^{40}K peak.

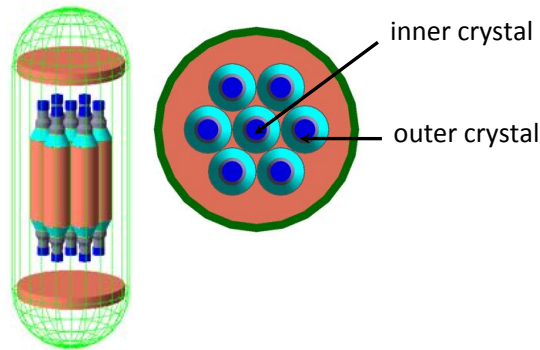


Figure 9.10: Crystal array for the DM-Ice250 detector. The crystal arrangement allows for a multi-crystal veto of the 3 keV ^{40}K peak (as shown in Figure 3.13 for DAMA), leading to a lower background rate in the region of interest.

9.3 DM-Ice Experiment

DM-Ice17 is the only dark matter experiment currently running in the Southern Hemisphere. It has been successfully running at the South Pole since December 2010. It continues to amass data and provide

important information on detector stability, response, and muon interactions. DM-Ice37 is actively taking data and pushing the development of cleaner crystals, optimized PMT and electronics configurations, and shielding. Once a background level below that of the DAMA crystals has been achieved, the experiment will progress to the full-scale, 250 kg detector. DM-Ice250 North will deploy in the Northern Hemisphere and may provide the key to resolving the inconsistencies between the DAMA signal and other experiments. The detector will be deployed in the Southern Hemisphere with PINGU for the DM-Ice250 South phase, which will run continuously. This combination of locations will provide additional confirmation of the DM-Ice250 North results by providing a definitive statement on any modulating backgrounds. DM-Ice250 South will also provide a calibration tool for PINGU and IceCube, as evidenced by the success of the DM-Ice17 coincidence study with IceCube. As the only Southern Hemisphere dark matter experiment running or planned, DM-Ice will provide a decisive contribution to the suite of NaI(Tl) dark matter detectors evolving from prototypes to full-scale detectors, with improvements in crystal purification and background reduction developing at a continuously accelerating rate.

Chapter 10

Conclusions

DM-Ice17 has demonstrated the feasibility and exciting potential of a dark matter detector in the South Pole ice. Three experimental challenges were explored and returned positive results: environmental compatibility, remote detector operation, and muon rejection. The seasonal stability and low radioactivity of the ice provide ideal conditions for an annual modulation search. In particular, negligible radon levels, neutron attenuation strength, and seasonal stability are far superior in the South Pole ice than in other underground locations.

Calibrating a detector that cannot be accessed presents a unique challenge, and DM-Ice17 illustrated the feasibility of relying on internal contamination lines for analysis. Calibration source runs prior to deployment provided an approximate energy calibration, and cosmogenic activation lines of varying decay times provide continuous verification of the calibration functions. The inability to perform regular source runs, while not ideal, is not a problem for this type of detector.

Muons are the only significant external background in DM-Ice17, and they are particularly important because they are known to modulate annually. DM-Ice17 identifies muon events through pulse shape and energy analysis, using events coincident with IceCube to validate the muon identification parameters. With an IceCube muon coincidence rate of up to 93% and a rate through DM-Ice17 that is consistent with expectation, muon identification in the crystal can be performed to high efficiency without external scintillators.

Of particular interest to low-energy, low-background NaI(Tl) experimental efforts, DM-Ice17 observes long-lived phosphorescence induced by high energy muons. These induced cascades of low energy events last for tens of seconds. While removed by DM-Ice17 noise cuts, this background has the potential to induce a low energy modulation following the phase of the muon modulation. Muon rejection is thus an important consideration for any direct detection dark matter experiment.

Development of the next generation of DM-Ice detectors focuses on reducing the largest sources of contamination in DM-Ice17, which are shown to be the crystal and the PMTs. Full-scale R&D efforts have

significantly reduced PMT and crystal backgrounds and currently focus on the further development of low-background crystals. A combined effort of NaI(Tl) experiments (DM-Ice, ANAIS, KIMS) and the Alpha-Spectra crystal-growing company continues to yield improved crystal purity, rapidly approaching the world's best contamination levels. Within this new generation of low-background NaI(Tl) experiments, the dual hemisphere operation of DM-Ice250 affords it a unique position to definitely confirm or reject the dark matter interpretation of the 9.5σ DAMA modulation.

LIST OF REFERENCES

- [1] J. Beringer, et al. Review of particle physics. *Phys. Rev. D*, 86:010001, Jul 2012. URL: <http://link.aps.org/doi/10.1103/PhysRevD.86.010001>, doi:10.1103/PhysRevD.86.010001.
- [2] V. M. Slipher. The radial velocity of the Andromeda Nebula. *Lowell Observatory Bulletin*, 2:56–57, 1913.
- [3] G. Lemaître. Un Univers homogène de masse constante et de rayon croissant rendant compte de la vitesse radiale des nébuleuses extra-galactiques. *Annales de la Societe Scietifique de Bruxelles*, 47:49–59, 1927.
- [4] Edwin Hubble. A relation between distance and radial velocity among extra-galactic nebulae. *Proceedings of the National Academy of Sciences*, 15(3):168–173, 1929. URL: <http://www.pnas.org/content/15/3/168.short>, arXiv:<http://www.pnas.org/content/15/3/168.full.pdf+html>, doi:10.1073/pnas.15.3.168.
- [5] P. Ade et al. Planck 2013 results. xvi. cosmological parameters. 2013. arXiv:1303.5076.
- [6] P.A.R. Ade et al. BICEP2 I: Detection Of B-mode Polarization at Degree Angular Scales. *Phys.Rev.Lett.*, 112(24):241101, 2014. arXiv:1403.3985, doi:10.1103/PhysRevLett.112.241101.
- [7] Glennys R. Farrar et al. Baryon asymmetry of the universe in the minimal Standard Model. *Phys.Rev.Lett.*, 70:2833–2836, 1993. arXiv:hep-ph/9305274, doi:10.1103/PhysRevLett.70.2833.
- [8] B.S. Ryden. *Introduction to cosmology*. Addison-Wesley, 2003. URL: <http://books.google.com/books?id=z27vAAAAAAAJ>.
- [9] Robert H. Sanders. *The Dark Matter Problem: A Historical Perspective*. Cambridge University Press, 1 edition, May 2010. URL: <http://www.amazon.com/exec/obidos/redirect?tag=citeulike07-20&path=ASIN/0521113016>.
- [10] ESA/Planck Collaboration. Planck reveals an almost perfect universe, 2013. URL: http://www.esa.int/Our_Activities/Space_Science/Planck/Planck_reveals_an_almost_perfect_Universe.
- [11] P. Ade et al. Planck 2013 results. xv. cmb power spectra and likelihood. 2013. arXiv:1303.5075.
- [12] C. L. Bennett, et al. Nine-year wilkinson microwave anisotropy probe (wmap) observations: Final maps and results. *The Astrophysical Journal Supplement Series*, 208(2):20, 2013. URL: <http://stacks.iop.org/0067-0049/208/i=2/a=20>.
- [13] C.L. Reichardt, et al. High resolution CMB power spectrum from the complete ACBAR data set. *Astrophys.J.*, 694:1200–1219, 2009. arXiv:0801.1491, doi:10.1088/0004-637X/694/2/1200.

- [14] P. de Bernardis, et al. A flat Universe from high-resolution maps of the cosmic microwave background radiation. *Nature*, 404:955–959, April 2000. [arXiv:astro-ph/0004404](#).
- [15] J.K. Cartwright, et al. Limits on the polarization of the cosmic microwave background radiation at multipoles up to $l = 2000$. *Astrophys.J.*, 623:11–16, 2005. [arXiv:astro-ph/0502174](#), [doi:10.1086/428384](#).
- [16] Marco Cirelli. Introduction to the dark components of the universe, 2011.
- [17] J.H. Oort. The force exerted by the stellar system in the direction perpendicular to the galactic plane and some related problems. *Bulletin of the Astronomical Institutes of the Netherlands*, 6:249, 1932.
- [18] F. Zwicky. Die rotverschiebung von extragalaktischen nebeln. *Acta Helvetica Physica*, 6:110–127, 1933.
- [19] H. W. Babcock. The rotation of the Andromeda Nebula. *Lick Observatory Bulletin*, 19:41–51, 1939.
- [20] W. A. Baum et al. A comparison of stellar populations in the Andromeda galaxy and its elliptical companion. *Astrophysical Journal*, 60:247, August 1955. [doi:10.1086/107222](#).
- [21] V.C. Rubin, et al. Rotational properties of 21 SC galaxies with a large range of luminosities and radii, from NGC 4605 ($R = 4$ kpc) to UGC 2885 ($R = 122$ kpc). *Astrophysical Journal*, 238:471–87, 1980. [doi:10.1086/158003](#).
- [22] Edvige Corbelli et al. The extended rotation curve and the dark matter halo of m33. *Monthly Notices of the Royal Astronomical Society*, 311(2):441–447, 2000. URL: <http://mnras.oxfordjournals.org/content/311/2/441.abstract>, [arXiv:http://mnras.oxfordjournals.org/content/311/2/441.full.pdf+html](#), [doi:10.1046/j.1365-8711.2000.03075.x](#).
- [23] M. Davis et al. A survey of galaxy redshifts. III - The density field and the induced gravity field. *Astrophysical Journal*, 254:437–450, March 1982. [doi:10.1086/159751](#).
- [24] C. P. Ahn, et al. The Tenth Data Release of the Sloan Digital Sky Survey: First Spectroscopic Data from the SDSS-III Apache Point Observatory Galactic Evolution Experiment. *Astrophysical Journal Supplements*, 211:17, April 2014. [arXiv:1307.7735](#), [doi:10.1088/0067-0049/211/2/17](#).
- [25] Volker Springel, et al. The large-scale structure of the universe. *Nature*, 440:1137–1144, 2006. [doi:10.1038/nature04805](#).
- [26] D. Walsh et al. 0957 + 561 a, c: twin quasistellar objects or gravitational lens? *Nature*, 279:381–384, 1979. [doi:10.1038/279381](#).
- [27] G. Chartas et al. Chandra looks over a cosmic four-leaf clover. *CXC Release*, 04-07, 2004. URL: <http://science.psu.edu/news-and-events/2004-news/Chartas6-2004.htm>.
- [28] Maxim Markevitch. Chandra observation of the most interesting cluster in the universe. *Proceedings of The X-ray Universe 2005, San Lorenzo de El Escorial, Spain, September 2005*, 2005. [arXiv:astro-ph/0511345](#).
- [29] Douglas Clowe, et al. A direct empirical proof of the existence of dark matter. *Astrophys.J.*, 648:L109–L113, 2006. [arXiv:astro-ph/0608407](#), [doi:10.1086/508162](#).

- [30] Bertone Gianfranco. Particle Dark Matter: Observations, Models and Searches. Cambridge University Press, 1 edition, February 2010. URL: <http://www.amazon.com/exec/obidos/redirect?tag=citeulike07-20&path=ASIN/0521763681>.
- [31] J. Diemand et al. The Structure and Evolution of Cold Dark Matter Halos. Advanced Science Letters, 4:297–310, February 2011. arXiv:0906.4340, doi:10.1166/asl.2011.1211.
- [32] Leszek Roszkowski. Particle dark matter, a theorist’s perspective. Pramana, 62(2):389–401, 2004. URL: <http://dx.doi.org/10.1007/BF02705097>, doi:10.1007/BF02705097.
- [33] Paolo Gondolo. Non-baryonic dark matter. NATO Sci.Ser.II, 187:279–333, 2005. arXiv:astro-ph/0403064.
- [34] H.J. de Vega et al. Dark matter in galaxies: the dark matter particle mass is about 7 keV. Based on Lectures by H J de V at NuMass 2013, Milano-Bicocca, Feb 2013; at Cosmic Frontiers, SLAC, March 2013 and by H J de V and N G S at the Chalonge Torino Colloquium 2013, Apr 2013 and The Paris Chalonge Colloquium July 2014., 2013. arXiv:1304.0759.
- [35] Matteo Viel, et al. Warm Dark Matter as a solution to the small scale crisis: new constraints from high redshift Lyman-alpha forest data. Phys.Rev., D88:043502, 2013. arXiv:1306.2314, doi:10.1103/PhysRevD.88.043502.
- [36] C. R. Watson, et al. Constraining sterile neutrino warm dark matter with Chandra observations of the Andromeda galaxy. Journal of Cosmology and Astroparticle Physics, 3:18, March 2012. arXiv:1111.4217, doi:10.1088/1475-7516/2012/03/018.
- [37] K. Abe et al. Search for bosonic superweakly interacting massive dark matter particles with the XMASS-I detector. Phys.Rev.Lett., 113:121301, 2014. arXiv:1406.0502, doi:10.1103/PhysRevLett.113.121301.
- [38] R. D. Peccei et al. CP conservation in the presence of pseudoparticles. Phys. Rev. Lett., 38:1440–1443, Jun 1977. URL: <http://link.aps.org/doi/10.1103/PhysRevLett.38.1440>, doi:10.1103/PhysRevLett.38.1440.
- [39] S. Asztalos, et al. Large-scale microwave cavity search for dark-matter axions. Phys. Rev. D, 64:092003, Oct 2001. URL: <http://link.aps.org/doi/10.1103/PhysRevD.64.092003>, doi:10.1103/PhysRevD.64.092003.
- [40] Karl van Bibber et al. Status of the ADMX and ADMX-HF experiments. Contribution to the 8th Patras Workshop on Axions, WIMPs and WISPs, Chicago, IL, 2013. arXiv:1304.7803.
- [41] Douglas Scott, et al. Cosmological difficulties with modified Newtonian dynamics (or, La Fin du MOND?). Mon.Not.Roy.Astron.Soc., 2001. arXiv:astro-ph/0104435.
- [42] Gordon Kane et al. Dark Matter and LHC: What is the Connection? Mod.Phys.Lett., A23:2103–2123, 2008. arXiv:0807.2244, doi:10.1142/S0217732308028314.
- [43] M. Aguilar, et al. Electron and positron fluxes in primary cosmic rays measured with the alpha magnetic spectrometer on the international space station. Phys. Rev. Lett., 113:121102, Sep 2014. URL: <http://link.aps.org/doi/10.1103/PhysRevLett.113.121102>, doi:10.1103/PhysRevLett.113.121102.
- [44] Oscar Adriani et al. An anomalous positron abundance in cosmic rays with energies 1.5-100 GeV. Nature, 458:607–609, 2009. arXiv:0810.4995, doi:10.1038/nature07942.

- [45] M. Ackermann, et al. Measurement of separate cosmic-ray electron and positron spectra with the fermi large area telescope. *Phys. Rev. Lett.*, 108:011103, Jan 2012. URL: <http://link.aps.org/doi/10.1103/PhysRevLett.108.011103>, doi:10.1103/PhysRevLett.108.011103.
- [46] J. Chang, et al. An excess of cosmic ray electrons at energies of 300-800 GeV. *Nature*, 456:362–365, 2008. doi:10.1038/nature07477.
- [47] P.A.R. Ade et al. Planck Intermediate Results. IX. Detection of the Galactic haze with Planck. 2012. [arXiv:1208.5483](https://arxiv.org/abs/1208.5483).
- [48] Benjamin Zitzer. Dark Matter Annihilation Limits from Dwarf Galaxies using VERITAS. *Proceedings of the 33rd International Cosmic Ray Conference (ICRC2013), Rio de Janeiro (Brazil), 2013*. [arXiv:1307.8367](https://arxiv.org/abs/1307.8367).
- [49] A. Abramowski, et al. Search for a dark matter annihilation signal from the galactic center halo with h.e.s.s. *Phys. Rev. Lett.*, 106:161301, Apr 2011. URL: <http://link.aps.org/doi/10.1103/PhysRevLett.106.161301>, doi:10.1103/PhysRevLett.106.161301.
- [50] M.G. Aartsen et al. The IceCube Neutrino Observatory Part IV: Searches for Dark Matter and Exotic Particles. *Papers submitted to the 33nd International Cosmic Ray Conference, Rio de Janeiro 2013, 2013*. [arXiv:1309.7007](https://arxiv.org/abs/1309.7007).
- [51] M. G. Aartsen, et al. Search for dark matter annihilations in the sun with the 79-string icecube detector. *Phys. Rev. Lett.*, 110:131302, Mar 2013. URL: <http://link.aps.org/doi/10.1103/PhysRevLett.110.131302>, doi:10.1103/PhysRevLett.110.131302.
- [52] M. Aguilar et al. First Result from the Alpha Magnetic Spectrometer on the International Space Station: Precision Measurement of the Positron Fraction in Primary Cosmic Rays of 0.5350 GeV. *Phys.Rev.Lett.*, 110(14):141102, 2013. doi:10.1103/PhysRevLett.110.141102.
- [53] R. W. Schnee. Introduction to Dark Matter Experiments. In C. Csaki et al., editors, *Physics of the Large and the Small: TASI 2009*, pages 775–829, March 2011. [arXiv:1101.5205](https://arxiv.org/abs/1101.5205), doi:10.1142/9789814327183_0014.
- [54] Katherine Freese, et al. *ijcolloquiumij*: Annual modulation of dark matter. *Rev. Mod. Phys.*, 85:1561–1581, Nov 2013. URL: <http://link.aps.org/doi/10.1103/RevModPhys.85.1561>, doi:10.1103/RevModPhys.85.1561.
- [55] R. Bernabei, et al. Dark matter search. *La Rivista del Nuovo Cimento*, 26N1:1 – 73, 2003. [arXiv:astro-ph/0307403](https://arxiv.org/abs/astro-ph/0307403).
- [56] G. Sciolla et al. Gaseous dark matter detectors. *New Journal of Physics*, 11(10):105018, October 2009. [arXiv:0905.3675](https://arxiv.org/abs/0905.3675), doi:10.1088/1367-2630/11/10/105018.
- [57] Michael F. Altmann, et al. Results and plans of the CRESST dark matter search. *Paper contributed to the X International Symposium on Lepton and Photon Interactions at High Energies, July 2001, Rome, Italy, 2001*. [arXiv:astro-ph/0106314](https://arxiv.org/abs/astro-ph/0106314).
- [58] E. Behnke et al. First Dark Matter Search Results from a 4-kg CF₃I Bubble Chamber Operated in a Deep Underground Site. *Phys.Rev.*, D86:052001, 2012. [arXiv:1204.3094](https://arxiv.org/abs/1204.3094), doi:10.1103/PhysRevD.86.052001.

- [59] E. Daw, et al. Spin-Dependent Limits from the DRIFT-II_d Directional Dark Matter Detector. Astropart.Phys., 35:397–401, 2012. arXiv:1010.3027, doi:10.1016/j.astropartphys.2011.11.003.
- [60] J Brack, et al. Long-term study of backgrounds in the drift-ii directional dark matter experiment. Journal of Instrumentation, 9(07):P07021, 2014. URL: <http://stacks.iop.org/1748-0221/9/i=07/a=P07021>.
- [61] G. Angloher, et al. Results from 730 kgdays of the cress_t-ii dark matter search. The European Physical Journal C, 72(4):1–22, 2012. URL: <http://dx.doi.org/10.1140/epjc/s10052-012-1971-8>, doi:10.1140/epjc/s10052-012-1971-8.
- [62] Andrew Brown, et al. Extending the cress_t-ii commissioning run limits to lower masses. Phys. Rev. D, 85:021301, Jan 2012. URL: <http://link.aps.org/doi/10.1103/PhysRevD.85.021301>, doi:10.1103/PhysRevD.85.021301.
- [63] C.E. Aalseth, et al. Search for An Annual Modulation in Three Years of CoGeNT Dark Matter Detector Data. 2014. arXiv:1401.3295.
- [64] Patrick J. Fox, et al. A cogent modulation analysis. Phys. Rev. D, 85:036008, Feb 2012. URL: <http://link.aps.org/doi/10.1103/PhysRevD.85.036008>, doi:10.1103/PhysRevD.85.036008.
- [65] The DAMIC Collaboration, et al. DAMIC: a novel dark matter experiment. ArXiv e-prints, October 2013.
- [66] R. Agnese et al. Search for Low-Mass Weakly Interacting Massive Particles with SuperCDMS. Phys.Rev.Lett., 112(24):241302, 2014. arXiv:1402.7137, doi:10.1103/PhysRevLett.112.241302.
- [67] R. Agnese, et al. Search for low-mass weakly interacting massive particles using voltage-assisted calorimetric ionization detection in the supercdms experiment. Phys. Rev. Lett., 112:041302, Jan 2014. URL: <http://link.aps.org/doi/10.1103/PhysRevLett.112.041302>, doi:10.1103/PhysRevLett.112.041302.
- [68] R. Agnese et al. Dark Matter Search Results Using the Silicon Detectors of CDMS II. Phys.Rev.Lett., 2013. arXiv:1304.4279.
- [69] D.S. Akerib et al. First results from the LUX dark matter experiment at the Sanford Underground Research Facility. Phys.Rev.Lett., 112:091303, 2014. arXiv:1310.8214, doi:10.1103/PhysRevLett.112.091303.
- [70] E. Aprile, et al. Dark matter results from 225 live days of xenon100 data. Phys. Rev. Lett., 109:181301, Nov 2012. URL: <http://link.aps.org/doi/10.1103/PhysRevLett.109.181301>, doi:10.1103/PhysRevLett.109.181301.
- [71] Z. Ahmed, et al. Combined limits on wimps from the cdms and edelweiss experiments. Phys. Rev. D, 84:011102, Jul 2011. URL: <http://link.aps.org/doi/10.1103/PhysRevD.84.011102>, doi:10.1103/PhysRevD.84.011102.
- [72] D.Yu. Akimov, et al. Wimp-nucleon cross-section results from the second science run of zeplin-iii. Physics Letters B, 709(12):14 – 20, 2012. URL: <http://www.sciencedirect.com/science/article/pii/S0370269312001050>, doi:http://dx.doi.org/10.1016/j.physletb.2012.01.064.

- [73] G.J. Alner, et al. Limits on {WIMP} cross-sections from the {NAIAD} experiment at the Boulby underground laboratory. *Physics Letters B*, 616(12):17 – 24, 2005. URL: <http://www.sciencedirect.com/science/article/pii/S0370269305005095>, doi:<http://dx.doi.org/10.1016/j.physletb.2000.09.001>.
- [74] C. E. Aalseth, et al. Cogent: A search for low-mass dark matter using p -type point contact germanium detectors. *Phys. Rev. D*, 88:012002, Jul 2013. URL: <http://link.aps.org/doi/10.1103/PhysRevD.88.012002>, doi:10.1103/PhysRevD.88.012002.
- [75] R. Bernabei, et al. First results from dama/libra and the combined results withdama/nai. *The European Physical Journal C*, 56(3):333–355, 2008. URL: <http://dx.doi.org/10.1140/epjc/s10052-008-0662-y>, doi:10.1140/epjc/s10052-008-0662-y.
- [76] Dan Hooper. The empirical case for 10-gev dark matter. *Physics of the Dark Universe*, 1(12):1 – 23, 2012. Next Decade in Dark Matter and Dark Energy: Next Decade in Dark Matter and Dark Energy. URL: <http://www.sciencedirect.com/science/article/pii/S2212686412000027>, doi:<http://dx.doi.org/10.1016/j.dark.2012.07.001>.
- [77] J. Cherwinka, et al. First data from DM-Ice17. *Physical Review D*, 90(9):092005, November 2014. arXiv:1401.4804, doi:10.1103/PhysRevD.90.092005.
- [78] R. Bernabei, et al. Dark matter particles in the galactic halo: Results and implications from dama/nai. *International Journal of Modern Physics D*, 13(10):2127–2159, 2004. URL: <http://www.worldscientific.com/doi/abs/10.1142/S0218271804006619>, arXiv:<http://www.worldscientific.com/doi/pdf/10.1142/S0218271804006619>, doi:10.1142/S0218271804006619.
- [79] R. Bernabei, et al. First results from dama/libra and the combined results withdama/nai. *The European Physical Journal C*, 56(3):333–355, 2008. URL: <http://dx.doi.org/10.1140/epjc/s10052-008-0662-y>, doi:10.1140/epjc/s10052-008-0662-y.
- [80] R. Bernabei, et al. Dama/libra results and perspectives of phase 2. *Nuclear Instruments and Methods in Physics Research Section A: Accelerators, Spectrometers, Detectors and Associated Equipment*, 742(0):177 – 180, 2014. 4th Roma International Conference on Astroparticle Physics. URL: <http://www.sciencedirect.com/science/article/pii/S0168900213014861>, doi:<http://dx.doi.org/10.1016/j.nima.2013.10.079>.
- [81] S. Cebrian, et al. Background model for a nai (tl) detector devoted to dark matter searches. *Astroparticle Physics*, 37(0):60 – 69, 2012. URL: <http://www.sciencedirect.com/science/article/pii/S0927650512001454>, doi:<http://dx.doi.org/10.1016/j.astropartphys.2012.07.009>.
- [82] J. Amar, et al. Preliminary results of ANAIS-25. *Nucl.Instrum.Meth.*, A742:187–190, 2014. arXiv:1308.3478, doi:10.1016/j.nima.2013.09.019.
- [83] Clara Cuesta for the ANAIS collaboration. Background analysis and status of the anais dark matter project, 2015. Slides of a talk given at LRT 2015, March 18 - 20, 2015, Seattle, WA. URL: <https://www.npl.washington.edu/indico/getFile.py/access?contribId=18&sessionId=10&resId=0&materialId=slides&confId=5>.
- [84] K. W. Kim, et al. Tests on NaI(Tl) crystals for WIMP search at the Yangyang Underground Laboratory. *Astroparticle Physics*, 62:249–257, March 2015. arXiv:1407.1586, doi:10.1016/j.astropartphys.2014.10.004.

- [85] Hyun Su Lee for the KIMS collaboration. Development of low background csi(tl) and nai(tl) crystals for wimp search, 2015. Slides of a talk given at LRT 2015, March 18 - 20, 2015, Seattle, WA. URL: <https://www.npl.washington.edu/indico/getFile.py/access?contribId=52&sessionId=4&resId=0&materialId=slides&confId=5>.
- [86] Jingke Xu for the SABRE collaboration. Sabre a test of dama/libra with ultra-high purity nai(tl) crystals, 2015. Slides of a talk given at LRT 2015, March 18 - 20, 2015, Seattle, WA. URL: <https://www.npl.washington.edu/indico/getFile.py/access?contribId=87&sessionId=4&resId=0&materialId=slides&confId=5>.
- [87] R. Bernabei, et al. The dama/libra apparatus. Nuclear Instruments and Methods in Physics Research Section A: Accelerators, Spectrometers, Detectors and Associated Equipment, 592(3):297 – 315, 2008. URL: <http://www.sciencedirect.com/science/article/pii/S016890020800675X>, doi:<http://dx.doi.org/10.1016/j.nima.2008.04.082>.
- [88] Clara Cuesta. ANAIS-0: Feasibility study for a 250 kg NaI(Tl) dark matter search experiment at the Canfranc Underground Laboratory. PhD thesis, Universidad de Zaragoza, 2013. URL: <http://gifna.unizar.es/anais/?cat=4>.
- [89] R. Bernabei, et al. Final model independent result of DAMA/LIBRA-phase1. European Physical Journal C, 73:2648, December 2013. arXiv:1308.5109, doi:10.1140/epjc/s10052-013-2648-7.
- [90] R. Bernabei, et al. New limits on {WIMP} search with large-mass low-radioactivity nai(tl) set-up at gran sasso. Physics Letters B, 389(4):757 – 766, 1996. URL: <http://www.sciencedirect.com/science/article/pii/S0370269396800207>, doi:[http://dx.doi.org/10.1016/S0370-2693\(96\)80020-7](http://dx.doi.org/10.1016/S0370-2693(96)80020-7).
- [91] John P. Ralston. One Model Explains DAMA/LIBRA, CoGENT, CDMS, and XENON. 2010. arXiv:1006.5255.
- [92] David Nygren. A testable conventional hypothesis for the DAMA-LIBRA annual modulation. 2011. arXiv:1102.0815.
- [93] Dan Hooper, et al. A Consistent Dark Matter Interpretation For CoGeNT and DAMA/LIBRA. Phys.Rev., D82:123509, 2010. arXiv:1007.1005, doi:10.1103/PhysRevD.82.123509.
- [94] R. Bernabei, et al. No role for muons in the DAMA annual modulation results. Eur.Phys.J., C72:2064, 2012. arXiv:1202.4179, doi:10.1140/epjc/s10052-012-2064-4.
- [95] G. Bellini et al. Cosmic-muon flux and annual modulation in Borexino at 3800 m water-equivalent depth. JCAP, 1205:015, 2012. arXiv:1202.6403, doi:10.1088/1475-7516/2012/05/015.
- [96] Jonathan H. Davis. Fitting the annual modulation in DAMA with neutrons from muons and neutrinos. Phys.Rev.Lett., 113:081302, 2014. arXiv:1407.1052, doi:10.1103/PhysRevLett.113.081302.
- [97] R. Bernabei, et al. No role for neutrons, muons and solar neutrinos in the DAMA annual modulation results. Eur.Phys.J., C74(12):3196, 2014. arXiv:1409.3516, doi:10.1140/epjc/s10052-014-3196-5.
- [98] N.J.T. Smith, et al. A possible mechanism for anomalous pulses observed in sodium iodide crystals. Physics Letters B, 485(13):9 – 15, 2000. URL: <http://www.sciencedirect.com/science/article/pii/S0370269300006407>, doi:[http://dx.doi.org/10.1016/S0370-2693\(00\)00640-7](http://dx.doi.org/10.1016/S0370-2693(00)00640-7).

- [99] V.A. Kudryavtsev, et al. Study and suppression of anomalous fast events in inorganic scintillators for dark matter searches. *Astropart.Phys.*, 17:401–408, 2002. arXiv:hep-ex/0109013, doi:10.1016/S0927-6505(01)00167-0.
- [100] Matthew Robinson. *The NaIAD Dark Matter Experiment: Backgrounds and Analysis*. PhD thesis, University of Sheffield, 2003. URL: <http://www.hep.shef.ac.uk/research/dm/theses/thesis-robinson.pdf>.
- [101] S. C. Kim, et al. New limits on interactions between weakly interacting massive particles and nucleons obtained with csi(tl) crystal detectors. *Phys. Rev. Lett.*, 108:181301, Apr 2012. URL: <http://link.aps.org/doi/10.1103/PhysRevLett.108.181301>, doi:10.1103/PhysRevLett.108.181301.
- [102] Frank Calaprice. *The Princeton NaI Experiment (SABRE)*, 2013. Slides of a talk given at Cosmic Frontier Workshop, March 2013, Stanford, CA. URL: <https://indico.fnal.gov/materialDisplay.py?contribId=135&sessionId=12&materialId=slides&confId=6199>.
- [103] Elena Aprile. Search for dark matter with xenon, 2014. Slides of a talk given at UCLA Dark Matter 2014, February 26, 2014, Los Angeles, California.
- [104] Xiangdong Ji. Status of pandax, 2014. Slides of a talk given at UCLA Dark Matter 2014, February 28, 2014, Los Angeles, California. URL: <http://www.pa.ucla.edu/sites/default/files/webform/pandaX.pdf>.
- [105] Harry Nelson. Lux-zeplin (lz): Part of the g2 proposals, 2014. Slides of a talk given at UCLA Dark Matter 2014, February 28, 2014, Los Angeles, California. URL: <http://www.pa.ucla.edu/sites/default/files/webform/HNelsonLZ.pdf>.
- [106] T Alexander, et al. Darkside search for dark matter. *Journal of Instrumentation*, 8(11):C11021, 2013. URL: <http://stacks.iop.org/1748-0221/8/i=11/a=C11021>.
- [107] John L. Orrell. Cogent-4: An expanded search for low-mass wimps, 2014. Slides of a talk given at TAUP 2011, September 5 - 9, 2011, Munich, Germany. URL: <http://www.taup-conference.to.infn.it/2011/day2/orrell.pdf>.
- [108] Ben Loer. Supercdms snolab, 2014. Slides of a talk given at UCLA Dark Matter 2014, February 28, 2014, Los Angeles, California. URL: http://www.pa.ucla.edu/sites/default/files/webform/loer_cdms_UCLA2014v2.pdf.
- [109] H Kraus, et al. Eureka the european future of cryogenic dark matter searches. *Journal of Physics: Conference Series*, 39(1):139, 2006. URL: <http://stacks.iop.org/1742-6596/39/i=1/a=031>.
- [110] Miguel Ardid. Dark matter searches with coupp bubble chambers, 2014. Slides of a talk given at SUSY 2013, August 26 - 31, 2013, Trieste, Italy. URL: http://susy2013.ictp.it/lecturenotes/04_Thursday/Dark_Matter_and_Cosmology/Ardid.pdf.
- [111] S. Archambault et al. Constraints on Low-Mass WIMP Interactions on ^{19}F from PICASSO. *Phys.Lett.*, B711:153–161, 2012. arXiv:1202.1240, doi:10.1016/j.physletb.2012.03.078.
- [112] Russell Neilson. Pico-2l: A bubble chamber to search for light wimps, 2014. Slides of a talk given at UCLA Dark Matter 2014, February 28, 2014, Los Angeles, California. URL: http://www.pa.ucla.edu/sites/default/files/webform/Neilson_PICO-2L_UCLA2014.pdf.
- [113] G.F. Knoll. *Radiation detection and measurement*. Wiley, 2000.

- [114] William R. Leo. Techniques for Nuclear and Particle Physics Experiments: A How-to Approach. Springer, Berlin, 2., überarb. a. edition, February 1994. URL: <http://www.amazon.com/exec/obidos/redirect?tag=citeulike07-20&path=ASIN/3540572805>.
- [115] P.A. Rodnyi. Physical Processes in Inorganic Scintillators. Laser & Optical Science & Technology. Taylor & Francis, 1997. URL: <https://books.google.com/books?id=BxgNoWH6aPAC>.
- [116] H.B. Dietrich et al. Kinetics of the diffusion of self-trapped holes in alkali halide scintillators. Journal of Luminescence, 5(3):155 – 170, 1972. URL: <http://www.sciencedirect.com/science/article/pii/0022231372900397>, doi:[http://dx.doi.org/10.1016/0022-2313\(72\)90039-7](http://dx.doi.org/10.1016/0022-2313(72)90039-7).
- [117] J. B. Birks. The theory and practice of scintillation counting. Pergamon Press, 1964.
- [118] R.B. Murray. Energy transfer in alkali halide scintillators by electron-hole diffusion and capture. Nuclear Science, IEEE Transactions on, 22(1):54–57, Feb 1975. doi:10.1109/TNS.1975.4327614.
- [119] H Chagani, et al. Measurement of the quenching factor of na recoils in nai(tl). Journal of Instrumentation, 3(06):P06003, 2008. URL: <http://stacks.iop.org/1748-0221/3/i=06/a=P06003>.
- [120] J. I. Collar. Quenching and channeling of nuclear recoils in nai(tl): Implications for dark-matter searches. Phys. Rev. C, 88:035806, Sep 2013. URL: <http://link.aps.org/doi/10.1103/PhysRevC.88.035806>, doi:10.1103/PhysRevC.88.035806.
- [121] Nassim Bozorgnia, et al. Channeling in direct dark matter detection i: channeling fraction in nai (tl) crystals. Journal of Cosmology and Astroparticle Physics, 2010(11):019, 2010. URL: <http://stacks.iop.org/1475-7516/2010/i=11/a=019>.
- [122] C. Sailer, et al. Low temperature light yield measurements in nai and nai(tl). The European Physical Journal C, 72(6), 2012. URL: <http://dx.doi.org/10.1140/epjc/s10052-012-2061-7>, doi:10.1140/epjc/s10052-012-2061-7.
- [123] Yutaka Toyozawa. A proposed model of excitonic mechanism for defect formation in alkali halides. Journal of the Physical Society of Japan, 44(2):482–488, 1978. URL: <http://dx.doi.org/10.1143/JPSJ.44.482>, arXiv:<http://dx.doi.org/10.1143/JPSJ.44.482>, doi:10.1143/JPSJ.44.482.
- [124] S. Kyropoulos. Ein verfahren zur herstellung groer kristalle. Zeitschrift fr anorganische und allgemeine Chemie, 154(1):308–313, 1926. URL: <http://dx.doi.org/10.1002/zaac.19261540129>, doi:10.1002/zaac.19261540129.
- [125] P.W. Bridgman. The compressibility of thirty metals as a function of pressure and temperature. Proceedings of the American Academy of Arts and Sciences, 58:165–242, 1923. arXiv:<http://www.biodiversitylibrary.org/item/28039>.
- [126] Donald C. Stockbarger. The production of large single crystals of lithium fluoride. Review of Scientific Instruments, 7(3):133–136, 1936. URL: <http://scitation.aip.org/content/aip/journal/rsi/7/3/10.1063/1.1752094>, doi:<http://dx.doi.org/10.1063/1.1752094>.
- [127] Alineason Materials & Technology. Crystal growth. Technical report, Alineason Materials & Technology, 2013. URL: <http://www.alineason.com/index.php/en/knowhow/crystal-growth>.
- [128] H.J. Scheel, et al. Crystal Growth Technology: Semiconductors and Dielectrics. Wiley, 2011. URL: <https://books.google.com/books?id=HxyKYTNo8cEC>.

- [129] Hans J. Scheel. The Development of Crystal Growth Technology, pages 1–14. John Wiley & Sons, Ltd, 2004. URL: <http://dx.doi.org/10.1002/0470871687.ch1>, doi:10.1002/0470871687.ch1.
- [130] R.G. Kaufman, et al. The scintillation mechanism in thallium doped alkali halides. Nuclear Science, IEEE Transactions on, 17(3):82–88, June 1970. doi:10.1109/TNS.1970.4325679.
- [131] Saint-Gobain Crystals. Nai(tl) and polycrin[®] nai(tl) sodium iodide scintillation material. Technical report, Saint-Gobain, 06 2012. URL: [http://www.detectors.saint-gobain.com/uploadedFiles/SGdetectors/Documents/Product_Data_Sheets/NaI\(Tl\)-Data-Sheet.pdf](http://www.detectors.saint-gobain.com/uploadedFiles/SGdetectors/Documents/Product_Data_Sheets/NaI(Tl)-Data-Sheet.pdf).
- [132] H. B. Dietrich, et al. Kinetics of self-trapped holes in alkali-halide crystals: Experiments in nai(tl) and ki(tl). Phys. Rev. B, 8:5894–5901, Dec 1973. URL: <http://link.aps.org/doi/10.1103/PhysRevB.8.5894>, doi:10.1103/PhysRevB.8.5894.
- [133] T. R. Waite. Theoretical treatment of the kinetics of diffusion-limited reactions. Phys. Rev., 107:463–470, Jul 1957. URL: <http://link.aps.org/doi/10.1103/PhysRev.107.463>, doi:10.1103/PhysRev.107.463.
- [134] B. S. Alexandrov, et al. Branching transport model of NaI(Tl) alkali-halide scintillator. Nuclear Instruments and Methods in Physics Research A, 586:432–438, March 2008. arXiv:0705.3703, doi:10.1016/j.nima.2007.12.010.
- [135] Hitoshi Nishimura et al. Hopping motion of self-trapped excitons in nai. Journal of Luminescence, 4041(0):429 – 430, 1988. URL: <http://www.sciencedirect.com/science/article/pii/0022231388902669>, doi:http://dx.doi.org/10.1016/0022-2313(88)90266-9.
- [136] Eiichi Matsui. Optical properties of the thalious ion center in sodium iodide-thallium crystals. Journal of the Physical Society of Japan, 22(3):819–830, 1967. URL: <http://dx.doi.org/10.1143/JPSJ.22.819>, arXiv:http://dx.doi.org/10.1143/JPSJ.22.819, doi:10.1143/JPSJ.22.819.
- [137] F. S. Eby et al. Fluorescent response of nai (tl) to nuclear radiations. Phys. Rev., 96:911–920, Nov 1954. URL: <http://link.aps.org/doi/10.1103/PhysRev.96.911>, doi:10.1103/PhysRev.96.911.
- [138] D. R. Tovey, et al. Measurement of scintillation efficiencies and pulse-shapes for nuclear recoils in NaI(Tl) and CaF₂(Eu) at low energies for dark matter experiments. Physics Letters B, 433:150–155, August 1998. doi:10.1016/S0370-2693(98)00643-1.
- [139] Th. Jagemann, et al. Measurement of the scintillation light quenching at room temperature of sodium recoils in nai(tl) and hydrogen recoils in {NE} 213 by the scattering of neutrons. Nuclear Instruments and Methods in Physics Research Section A: Accelerators, Spectrometers, Detectors and Associated Equipment, 564(1):549 – 558, 2006. URL: <http://www.sciencedirect.com/science/article/pii/S0168900206005377>, doi:http://dx.doi.org/10.1016/j.nima.2006.03.029.
- [140] The scintillation efficiency of sodium and iodine recoils in a nai(tl) detector for dark matter searches. Physics Letters B, 321(12):156 – 160, 1994. URL: <http://www.sciencedirect.com/science/article/pii/0370269394903433>, doi:http://dx.doi.org/10.1016/0370-2693(94)90343-3.
- [141] Jingke Xu, et al. Scintillation efficiency measurement of Na recoils in NaI(Tl) below the DAMA/LIBRA energy threshold. 2015. arXiv:1503.07212.
- [142] C. R. Emigh et al. The long-lived phosphorescent components of thallium-activated sodium iodide. Phys. Rev., 93:1190–1194, Mar 1954. URL: <http://link.aps.org/doi/10.1103/PhysRev.93.1190>, doi:10.1103/PhysRev.93.1190.

- [143] J C Robertson et al. The luminescent decay of various crystals for particles of different ionization density. Proceedings of the Physical Society, 77(3):751, 1961. URL: <http://stacks.iop.org/0370-1328/77/i=3/a=326>.
- [144] C. Cuesta, et al. Bulk NaI(Tl) scintillation low energy events selection with the ANAIS-0 module. ArXiv e-prints, July 2014. arXiv:1407.5125.
- [145] C. Cuesta, et al. Slow scintillation time constants in NaI(Tl) for different interacting particles. Optical Materials, 36:316–320, December 2013. arXiv:1307.1398, doi:10.1016/j.optmat.2013.09.015.
- [146] S. Koiki, et al. The investigation of the 0.15s phosphorescent component of nai(tl) and its application in scintillation counting. Nuclear Instruments and Methods, 108(2):297 – 299, 1973. URL: <http://www.sciencedirect.com/science/article/pii/0029554X73906034>, doi:http://dx.doi.org/10.1016/0029-554X(73)90603-4.
- [147] J. Bonanomi et al. Scintillations de luminescence dans les iodures d'alcalins. Helvetica Physica Acta, 25(7):725 – 752, 1952. URL: <http://retro.seals.ch/digbib/view?pid=hpa-001:1952:25::837>, doi:http://dx.doi.org/10.5169/seals-112332.
- [148] O. Fronka. Long-wave excitation of phosphorescence in nai(tl) and csi(tl). physica status solidi (a), 6(2):K89–K92, 1971. URL: <http://dx.doi.org/10.1002/pssa.2210060248>, doi:10.1002/pssa.2210060248.
- [149] V.G. Volkov. Assessing the phosphorescence generated in nai(tl) after excitation by betatron bremsstrahlung. Pribory i Tekhnika Eksperimenta, 2:65–67, 1981.
- [150] William W. Managan. Application of scintillation counters to reactors. Nuclear Science, IRE Transactions on, 5(3):171–177, Dec 1958. doi:10.1109/TNS2.1958.4315650.
- [151] Saint-Gobain Crystals. Effects of ultraviolet (uv) light on nai, csi and bgo crystals. Technical report, Saint-Gobain, 05 2012. URL: www.detectors.saint-gobain.com.
- [152] C.F.G. Delaney et al. Long-lived phosphorescent components in nai(tl) and csi(tl). The International Journal of Applied Radiation and Isotopes, 19(2):169 – 170, 1968. URL: <http://www.sciencedirect.com/science/article/pii/0020708X68900926>, doi:http://dx.doi.org/10.1016/0020-708X(68)90092-6.
- [153] Serap Tilav, et al. Atmospheric Variations as observed by IceCube. Proceedings of the 31st ICRC, 2009. arXiv:1001.0776.
- [154] J. Cherwinka, et al. A search for the dark matter annual modulation in south pole ice. Astroparticle Physics, 35(11):749 – 754, 2012. URL: <http://www.sciencedirect.com/science/article/pii/S0927650512000564>, doi:http://dx.doi.org/10.1016/j.astropartphys.2012.03.003.
- [155] B Ahmed, et al. The {NAIAD} experiment for {WIMP} searches at boulby mine and recent results. Astroparticle Physics, 19(6):691 – 702, 2003. URL: <http://www.sciencedirect.com/science/article/pii/S0927650503001154>, doi:http://dx.doi.org/10.1016/S0927-6505(03)00115-4.
- [156] Icecube Collaboration. South Pole glacial climate reconstruction from multi-borehole laser particulate stratigraphy. Journal of glaciology, 59(218):1117 – 1128, 2013. URL: <https://bib-pubdb1.desy.de/record/167632>, doi:10.3189/2013JoG13J068.

- [157] J Amar, et al. Neutrons from rock radioactivity in the new canfranc underground laboratory. *Journal of Physics: Conference Series*, 39(1):151, 2006. URL: <http://stacks.iop.org/1742-6596/39/i=1/a=035>.
- [158] R. Abbasi, et al. The icecube data acquisition system: Signal capture, digitization, and timestamping. *Nuclear Instruments and Methods in Physics Research Section A: Accelerators, Spectrometers, Detectors and Associated Equipment*, 601(3):294 – 316, 2009. URL: <http://www.sciencedirect.com/science/article/pii/S0168900209000084>, doi:<http://dx.doi.org/10.1016/j.nima.2009.01.001>.
- [159] E. Sakai. Recent Measurements on Scintillator-Photodetector Systems. *IEEE Transactions on Nuclear Science*, 34:418–422, February 1987. doi:10.1109/TNS.1987.4337375.
- [160] J. Amare, et al. Study of scintillation in natural and synthetic quartz and methacrylate. *ArXiv e-prints*, January 2014. arXiv:1401.3118.
- [161] D. Engelkemeir. Nonlinear Response of NaI(Tl) to Photons. *Review of Scientific Instruments*, 27:589–591, August 1956. doi:10.1063/1.1715643.
- [162] J.F. Ziegler. Terrestrial cosmic rays. *IBM Journal of Research and Development*, 40(1):19–39, Jan 1996. doi:10.1147/rd.401.0019.
- [163] I. Basile N.I. Barkov, J.-M. Barnola et al. Climate and atmospheric history of the past 420,000 years from the Vostok ice core, Antarctica. *Nature*, 399:429–436, 1999. URL: http://www.nature.com/nature/journal/v399/n6735/suppinfo/399429a0_S1.html, doi:10.1038/20859.
- [164] T. K. Gaisser. *Cosmic Rays And Particle Physics*. Cambridge University Press, 1990.
- [165] P. Desiati. Seasonal Variations of High Energy Cosmic Ray Muons Observed by the IceCube Observatory as a Probe of Kaon/Pion Ratio. In *International Cosmic Ray Conference*, volume 1 of *International Cosmic Ray Conference*, page 78, 2011.
- [166] Jakob van Santen. Neutrino Interactions in IceCube above 1 TeV Constraints on Atmospheric Charmed-Meson Production and Investigation of the Astrophysical Neutrino Flux with 2 Years of IceCube Data taken 2010–2012. PhD thesis, University of Wisconsin, 2014. URL: <http://search.proquest.com.ezproxy.library.wisc.edu/docview/1637727437?accountid=465>.
- [167] V.A. Kudryavtsev. Muon simulation codes {MUSIC} and {MUSUN} for underground physics. *Computer Physics Communications*, 180(3):339 – 346, 2009. URL: <http://www.sciencedirect.com/science/article/pii/S0010465508003640>, doi:<http://dx.doi.org/10.1016/j.cpc.2008.10.013>.
- [168] Eun-Joo Ahn, et al. Cosmic ray interaction event generator sibyll 2.1. *Phys. Rev. D*, 80:094003, Nov 2009. URL: <http://link.aps.org/doi/10.1103/PhysRevD.80.094003>, doi:10.1103/PhysRevD.80.094003.
- [169] Joerg R. Hoerandel. On the knee in the energy spectrum of cosmic rays. *Astropart.Phys.*, 19:193–220, 2003. arXiv:astro-ph/0210453, doi:10.1016/S0927-6505(02)00198-6.
- [170] Marco Bazzotti. *Studies of the atmospheric muon flux with the ANTARES detector*. PhD thesis, Università degli studi di Bologna, 2009. URL: http://amsdottorato.unibo.it/1906/1/bazzotti_marco_tesi.pdf.

- [171] X. Bai, et al. Response of AMANDA-II to cosmic ray muons. Proceedings of the 28th ICRC, Tsukuba, Japan, August 2003, pages 1373–1376, 2003.
- [172] E. Andres, et al. Observation of high-energy neutrinos using Cherenkov detectors embedded deep in Antarctic ice. Nature, 410:441–443, 2001. doi:10.1038/35068509.
- [173] P. Desiati et al. Seasonal Variation of Atmospheric Leptons as a Probe of Charm. Physical Review Letters, 105(12):121102, September 2010. arXiv:1008.2211, doi:10.1103/PhysRevLett.105.121102.
- [174] X. Bai, et al. Muon flux at the geographical south pole. Astroparticle Physics, 25(6):361 – 367, 2006. URL: <http://www.sciencedirect.com/science/article/pii/S0927650506000363>, doi:<http://dx.doi.org/10.1016/j.astropartphys.2006.03.005>.
- [175] D. Pengra. Cosmic ray counting. University Lecture, 2008. URL: http://courses.washington.edu/phys433/muon_counting/counting_telescope.pdf.
- [176] M.G. Aartsen et al. Evidence for High-Energy Extraterrestrial Neutrinos at the IceCube Detector. Science 342., 1242856, 2013. arXiv:1311.5238, doi:10.1126/science.1242856.
- [177] B.B. Govorkov. Cherenkov detectors in cherenkov’s laboratory. Nuclear Instruments and Methods in Physics Research Section A: Accelerators, Spectrometers, Detectors and Associated Equipment, 553(12):9 – 17, 2005. Proceedings of the fifth International Workshop on Ring Imaging Detectors Fifth International Workshop on Ring Imaging Detectors. URL: <http://www.sciencedirect.com/science/article/pii/S0168900205015627>, doi:<http://dx.doi.org/10.1016/j.nima.2005.08.088>.
- [178] I. Frank et al. Coherent radiation of fast electrons in a medium. Doklady Akad. Nauk SSSR, 14(07), 1937.
- [179] Jakob van Santen. Markov-chain monte-carlo reconstruction for cascade-like events in icecube. Master’s thesis, Humboldt-Universitat zu Berlin, 2010.
- [180] R. Abbasi, et al. Icetop: The surface component of icecube. Nuclear Instruments and Methods in Physics Research Section A: Accelerators, Spectrometers, Detectors and Associated Equipment, 700(0):188 – 220, 2013. URL: <http://www.sciencedirect.com/science/article/pii/S016890021201217X>, doi:<http://dx.doi.org/10.1016/j.nima.2012.10.067>.
- [181] Christopher Wiebusch. Physics Capabilities of the IceCube DeepCore Detector. Proceedings of the 31st ICRC, Lodz, Poland, July 2009, 2009. arXiv:0907.2263.
- [182] Benedikt Riedel. Modeling and Understanding Supernova Signals in the IceCube Neutrino Observatory. PhD thesis, University of Wisconsin, 2014. URL: <http://search.proquest.com.ezproxy.library.wisc.edu/docview/1625677515?accountid=465>.
- [183] T. Glüsenskamp et al. Muon filter proposal ic86-2012. Technical report, IceCube Collaboration, 2008. URL: https://docushare.icecube.wisc.edu/dsweb/Get/Document-59906/MuonFilter2012_v3_with_addendum.pdf.
- [184] The IceCube collaboration. Internal note: Slc hit cleaning. Technical report, IceCube Collaboration, 2010. URL: https://wiki.icecube.wisc.edu/index.php/SLC_hit_cleaning.

- [185] A. Karle et al. Proposal for an extended dst pole stream in 2011 (ic86). Technical report, IceCube Collaboration, 2010. URL: https://docushare.icecube.wisc.edu/dsweb/Get/Document-56552/dst_proposal_2011.pdf.
- [186] Sebastian Euler. Observation of oscillations of atmospheric neutrinos with the IceCube Neutrino Observatory. PhD thesis, RWTH Aachen University, 2014. URL: <http://darwin.bth.rwth-aachen.de/opus3/volltexte/2014/5089/pdf/5089.pdf>.
- [187] Christopher Weaver. Project documentation: Muex energy resolution, 2014. URL: http://icecube.wisc.edu/~cweaver/random/muex_energy_resolution.pdf.
- [188] Brian Rebel et al. Status of noa. Journal of Physics: Conference Series, 375(4):042072, 2012. URL: <http://stacks.iop.org/1742-6596/375/i=4/a=042072>.
- [189] P. Adamson, et al. Observation of muon intensity variations by season with the minos near detector. Phys. Rev. D, 90:012010, Jul 2014. URL: <http://link.aps.org/doi/10.1103/PhysRevD.90.012010>, doi:10.1103/PhysRevD.90.012010.
- [190] L.N. Bogdanova, et al. Cosmic muon flux at shallow depths underground. Phys.Atom.Nucl., 69:1293–1298, 2006. arXiv:nucl-ex/0601019, doi:10.1134/S1063778806080047.
- [191] Sean Paling. Horizon2020 DULIA Proposal, 2014.
- [192] H.M. Arajo, et al. Measurements of neutrons produced by high-energy muons at the Boulby underground laboratory. Astroparticle Physics, 29(6):471 – 481, 2008. URL: <http://www.sciencedirect.com/science/article/pii/S092765050800073X>, doi:<http://dx.doi.org/10.1016/j.astropartphys.2008.05.004>.
- [193] P.F. Smith, et al. Simulation studies of neutron shielding, calibration and veto systems for gaseous dark matter detectors. Astroparticle Physics, 22(56):409 – 420, 2005. URL: <http://www.sciencedirect.com/science/article/pii/S0927650504001586>, doi:<http://dx.doi.org/10.1016/j.astropartphys.2004.09.005>.
- [194] H. Wulandari, et al. Neutron flux underground revisited. Astropart.Phys., 22:313–322, 2004. arXiv:hep-ex/0312050, doi:10.1016/j.astropartphys.2004.07.005.
- [195] L. Pandola. Overview of the European Underground Facilities. AIP Conf.Proc., 1338:12–19, 2011. arXiv:1102.0208, doi:10.1063/1.3579554.
- [196] D. Jordan, et al. Measurement of the neutron background at the canfranc underground laboratory {LSC}. Astroparticle Physics, 42(0):1 – 6, 2013. URL: <http://www.sciencedirect.com/science/article/pii/S0927650512002046>, doi:<http://dx.doi.org/10.1016/j.astropartphys.2012.11.007>.
- [197] I. Bandac, et al. Radon y radiacion ambiental en el Laboratorio Subterraneo de Canfranc (LSC). Radioproteccion, 21(77):24, 2014. written in Spanish. URL: <http://www.lsc-canfranc.es/images/News/Labac.pdf>.
- [198] J. Puimedon. Neutrons from rock radioactivity in the new canfranc underground laboratory, 2005. Slides of a talk given at TAUP 2005, September 2005, Zaragoza, Spain. URL: <http://www.unizar.es/ilias/JRA1/Conferencias/TAUP05/Puimedon.pdf>.
- [199] MyeongJae Lee, et al. Radon Environment in the Korea Invisible Mass Search Experiment and Its Measurement. J. Korean Phys.Soc., 58(4):713, 2011. doi:10.3938/jkps.58.713.

- [200] Alessandro Bettini. New underground laboratories: Europe, asia and the americas. Physics of the Dark Universe, 4(0):36 – 40, 2014. {DARK} {TAUP2013}. URL: <http://www.sciencedirect.com/science/article/pii/S2212686414000181>, doi:<http://dx.doi.org/10.1016/j.dark.2014.05.006>.
- [201] Sun Kee Kim. Underground experimental program in korea, 2011. Slides of a talk given at the ASPERA Workshop, July 2011, Zaragoza, Spain. URL: <https://indico.cern.ch/event/130734/material/slides/1?contribId=19>.
- [202] Xenon100 Collaboration, et al. The XENON100 dark matter experiment. Astroparticle Physics, 35:573–590, April 2012. arXiv:1107.2155, doi:10.1016/j.astropartphys.2012.01.003.
- [203] L.N. Kalousis, et al. Cosmic Muon Flux Measurements at the Kimballton Underground Research Facility. JINST, 9:P08010, 2014. arXiv:1406.2641, doi:10.1088/1748-0221/9/08/P08010.
- [204] T.A. Girard, et al. Neutron and alpha backgrounds in the LSBB. Proceedings of i-DUST, Apt, France, June 2010, page 03003, 2011.
- [205] Tim Daniels. The enriched xenon observatory (exo), 2011. Slides of a talk given at DPF 2011, August 2011, Providence, RI. URL: <https://www-project.slac.stanford.edu/exo/Talks/dpf2011.pdf>.
- [206] Alessandro Bettini. The World underground scientific facilities: A Compendium. Proceedings from TAUP 2007, 2007. arXiv:0712.1051.
- [207] D Speller et al. Dark matter direct detection with supercdms soudan. Journal of Physics: Conference Series, 606(1):012003, 2015. URL: <http://stacks.iop.org/1742-6596/606/i=1/a=012003>.
- [208] Reina Maruyama. Dm-ice: A search for dark matter in the antarctic ice, 2011. Slides of a talk given at Indirect and Direct Detection of Dark Matter 2011, February, 2011, Aspen, CO. URL: https://www.physics.wisc.edu/~maruyama/talks/Maruyama_Aspen2011.pdf.
- [209] Hiroyuki Sekiya. Low energy investigations at kamioka observatory. Journal of Physics: Conference Series, 460(1):012017, 2013. URL: <http://stacks.iop.org/1742-6596/460/i=1/a=012017>.
- [210] Lucia Votano. Underground Laboratories. Proceedings of 6th Patras Workshop on Axions, WIMPs and WISPS, July 2010, Zurich, Switzerland, pages 172–175, 2010. doi:10.3204/DESY-PROC-2010-03/votano_lucia.
- [211] Melisa Luca. Status and Outlook of the EDELWEISS WIMP Search. Proceedings of the 41st Rencontres de Moriond, March 2006, La Thuile, Italy, 2006. arXiv:astro-ph/0605496.
- [212] R. Ford. SNOLAB: Review of the facility and experiments. In S. G. Steadman, et al., editors, American Institute of Physics Conference Series, volume 1441 of American Institute of Physics Conference Series, pages 521–524, September 2012. doi:10.1063/1.3700605.
- [213] Yu-Cheng Wu, et al. Measurement of Cosmic Ray Flux in China JinPing underground Laboratory. Chin.Phys., C37(8):086001, 2013. arXiv:1305.0899, doi:10.1088/1674-1137/37/8/086001.
- [214] T. J. Radcliffe. Fast neutrons from muon spallation in the sno detector. SNO Technical Reports, 93(043), 1993.
- [215] A. Lindote, et al. Simulation of neutrons produced by high-energy muons underground. Astroparticle Physics, 31(5):366 – 375, 2009. URL: <http://www.sciencedirect.com/science/article/pii/S0927650509000577>, doi:<http://dx.doi.org/10.1016/j.astropartphys.2009.03.008>.

- [216] V.A. Kudryavtsev, et al. Neutron- and muon-induced background in underground physics experiments. The European Physical Journal A, 36(2):171–180, 2008. URL: <http://dx.doi.org/10.1140/epja/i2007-10539-6>, doi:10.1140/epja/i2007-10539-6.
- [217] H.M. Arajo et al. μ -induced neutron production comparing geant4 and fluka simulations, 2004. Slides of a talk given at IDM 2004, September 6 - 10, 2004, Edinburgh, Scotland, UK.
- [218] Department of Energy Fundamentals Handbook. Doe-hdbk-1019/1-93 nuclear physics and reactor theory; module 2; reactor theory (neutron characteristics), 1993.
- [219] P. Rinard. Neutron interaction with matter. In D. Reilly et al., editors, Passive Nondestructive Assay of Nuclear Materials NUREG/CR-5550, page 357. U.S. Nuclear Regulatory Commission, 1991.
- [220] Cross Section Evaluation Working Group. Report bnl-ncs-17541 (endf-201), 1991.
- [221] D.S. Akerib, et al. The large underground xenon (lux) experiment. Nuclear Instruments and Methods in Physics Research Section A: Accelerators, Spectrometers, Detectors and Associated Equipment, 704(0):111 – 126, 2013. URL: <http://www.sciencedirect.com/science/article/pii/S0168900212014829>, doi:<http://dx.doi.org/10.1016/j.nima.2012.11.135>.

GLOSSARY

ANAIS	Annual modulation with NaI Scintillators experiment <i>NaI(Tl) dark matter experiment operating in Canfranc, Spain</i>
ATWD	Analog Transient Waveform Digitizer <i>3 DM-Ice17 readout channels, each with varying gain for dynamic range</i>
Boulby	Boulby Underground Laboratory <i>DM-Ice37 location in UK (2850 m.w.e.)</i>
CDM	Cold Dark Matter <i>Class of dark matter candidates, including the WIMP</i>
CORSIKA	CORSIKA <i>Muon propagation simulation</i>
DAMA	DARkMatter experiment <i>NaI(Tl) dark matter experiment that observes a 9.5σ modulation</i>
DOM	Digital Optical Module <i>IceCube detectors</i>
EMI	ElectroMagnetic Interference <i>Noise induced by hardware monitoring</i>
FADC	Flash Analog to Digital Converter <i>DM-Ice17 readout channel</i>
FNAL	Fermi National Accelerator Laboratory <i>DM-Ice37 initial testing site in Illinois</i>
HLC	Hard Local Coincidence <i>IceCube trigger condition: neighbors or next-to-neighbors must both trigger</i>
KIMS	Korean Invisible Matter Search <i>CsI(Tl) and NaI(Tl) dark matter experiment in Yangyang, South Korea</i>
LC	Local Coincidence <i>DM-Ice17 trigger condition: coupled PMTs on a crystal must both trigger</i>

LNGS	Laboratori Nazionali del Gran Sasso <i>Underground laboratory housing the DAMA experiment in Italy</i>
MIP	Minimum Ionizing Particle <i>Particle that loses the minimum mean energy passing through a medium</i>
MPEFit	IceCube reconstruction <i>Reconstruction that uses the Cherenkov photon arrival time and charge deposited</i>
MuEx	IceCube energy reconstruction <i>Converts energy loss to incoming particle energy to within a factor of ~ 2</i>
MUSIC	MUSIC <i>Muon propagation simulation</i>
MUSUN	MUSUN <i>Muon propagation simulation</i>
NaIAD	NaI Advanced Detector <i>NaI(Tl) experiment that ran at Boulby, 2000-2003</i>
PSD	Pulse Shape Discrimination <i>Technique to distinguish interaction types</i>
PMT	PhotoMultiplier Tube <i>Detector component that converts scintillation photons to amplified charge signals</i>
SABRE	Sodium iodide with Active Background REjection <i>Proposed NaI(Tl) experiment at LNGS</i>
sDST	super Data Storage and Transfer <i>IceCube data stream</i>
SLC	Soft Local Coincidence <i>IceCube classifications when a triggered DOM does not pass HLC</i>
SPEFit	IceCube reconstruction <i>Reconstruction that uses first photon arrival time</i>
SRTCleaning	Seeded Radius-Time Cleaning <i>IceCube processing that removes events outside a central radius and time window</i>
SRTInIcePulses	IceCube processed data stream <i>Events have undergone SRTCleaning</i>
WIMP	Weakly Interacting Massive Particle <i>Dark matter candidate particle sought by DM-Ice</i>

Appendix A: Underground Laboratories

Table A.1: Summary of overburdens at underground laboratory housing current (and former, designated with *) dark matter experiments. They are listed in order of depth in meters water equivalent (m.w.e.).

Laboratory	Experiment(s)	Overburden [m]	Overburden [m.w.e.]	Ref.
Fermilab (FNAL)	-	100	225	[189]
Kimballton	MALBEK	520	1450	[203]
LSBB	SIMPLE	505	1500	[204]
WIPP	DMTPC	650	1600	[205]
Yangyang (Y2L)	KIMS	700	2000	[206]
Soudan	CDMS, CoGeNT	780	2090	[207]
South Pole Ice	DM-Ice17	2450	2200	[208]
Canfranc (LSC)	ANAIS	850	2450	[145]
Kamioka	XMASS, PICO-LON	1000	2700	[209]
Boulby (BUL)	DM-Ice37, DRIFT NaIAD* , ZEPLIN*	1070	2850	[192]
Gran Sasso (LNGS)	DAMA, DarkSide XENON	1400	3400	[210]
Sanford (SURF)	LUX	1500	4300	[69]
Modane	EDELWEISS	1700	4800	[211]
SNOLAB	CLEAN, COUPP DAMIC, DEAP PICASSO, PICO	2070	6010	[212]
Jinping	CDEX, PandaX	2400	6720	[213]

Appendix B: Neutron Background

B.1 Neutron Production

The neutron production rate from cosmic muons varies with energy and target material. A ~ 300 GeV muon in ice has a neutron production rate of $\sim 3.5 \times 10^{-4}$ neutrons/ μ /(g/cm²), as shown in Figure B.1 [215]. Using $\rho_{ice} = 0.9196$ g/cm³ and $\Phi_{\mu} = 2 \times 10^{-7}$ μ /cm²/s yields a neutron production rate, R_n , of:

$$R_n = \frac{3.5 \times 10^{-4} \text{ neutrons}/\mu}{\text{g}/\text{cm}^2} \times \frac{0.9196 \text{ g}}{\text{cm}^3} \times \frac{2 \times 10^{-7} \mu}{\text{cm}^2 \cdot \text{s}} = 6.5 \times 10^{-11} \text{ neutrons}/\text{cm}^3 \cdot \text{s} \quad (\text{B.1})$$

This value is consistent with literature [214].

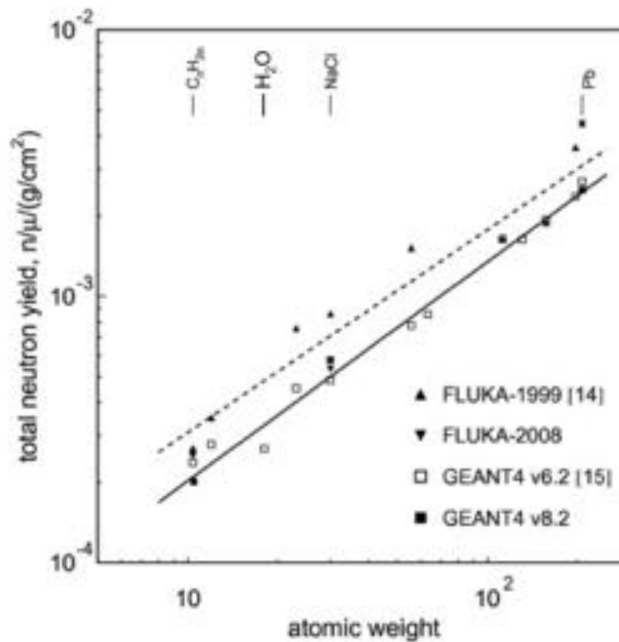


Figure B.1: The target material atomic mass dependence of spallation neutron production from cosmic muons [215].

Simulations have shown that above a neutron energy of 20 MeV, the energy distribution is virtually target-independent, as shown in Figure B.2 for a 270 GeV muon [216, 217]. The inset shows the spectrum from CH₂, which is similar to atomic weight to ice and is thus a comparable model for DM-Ice17. Neutrons of energy ≤ 10 MeV are the most probable, with a second break in the spectrum ~ 100 MeV. Neutrons at higher energies are significantly less probable. Spallation neutrons hit a kinematic high energy cutoff at the energy of the incident particle.

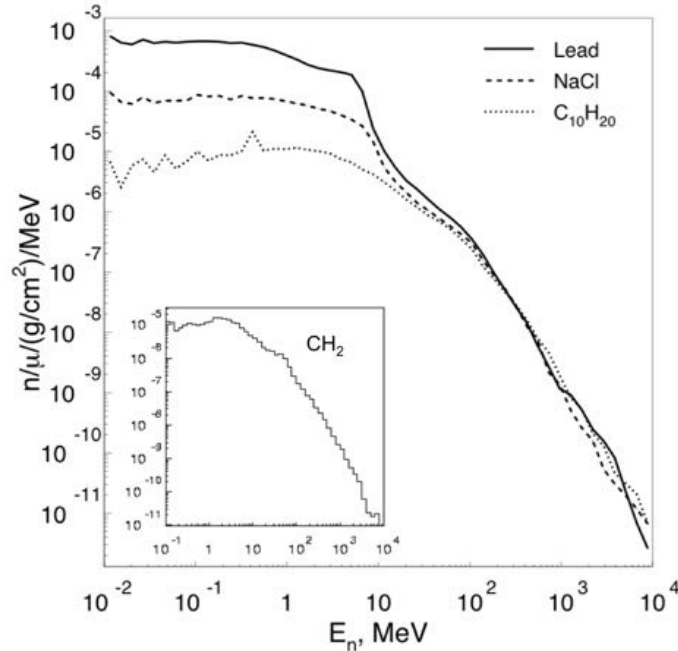


Figure B.2: The neutron energy spectrum for a variety of targets from ~ 270 GeV muon spallation [216]. Above 20 MeV, the spectrum becomes target-independent. Inset: The neutron energy spectrum for in CH_2 for a 280 GeV muon [217]. Water, of similar atomic weight to CH_2 , has a very similar distribution.

B.2 Neutron Propagation in Ice

Neutrons propagate until thermalization, at which point they fall into thermal equilibrium with the surrounding material. In the case of -20°C ice, thermalization corresponds to a neutron energy of 0.022 eV ($E = 3kT/2$). The distance that neutrons travel before thermalization depends on the number of collisions they undergo and the neutron cross-section in ice. A neutron of energy E_0 will undergo a number of collisions, n , determined by [218]:

$$n = \frac{\log\left(\frac{0.022\text{ eV}}{E_0}\right)}{\xi}, \quad \xi_{\text{water}} = 0.948 \quad (\text{B.2})$$

A 10 MeV neutron will thus undergo 21.0 collisions, and a 100 MeV neutron 23.5, before thermalization.

The total path length from production to thermalization depends on the interaction cross-section, mean free path, neutron energy loss in the interaction for a neutron of a given energy. The macroscopic cross-section for each interaction, Σ , is a function of the target density (ρ), the molecular weight of the target (M), the number of atoms of element i in a target molecule, (n_i), and the cross-section for that element (σ_i).

The macroscopic cross-section accounts for interactions with both hydrogen and oxygen in ice [219]:

$$\Sigma = \frac{\rho N_a}{M} (n_{\text{H}} \times \sigma_{\text{H}} + n_{\text{O}} \times \sigma_{\text{O}}) = \frac{0.9196 \text{ g/cm}^3 \times 6.022131 \times 10^{23} / \text{mol}}{18.0153 \text{ g/mol}} (\sigma_{\text{H}} + 2\sigma_{\text{O}}) \quad (\text{B.3})$$

where N_a is Avogadro's number. This equation dictates that a 10 MeV neutron will travel 13.5 cm before its first interaction:

$$\Sigma = \frac{0.9196 \text{ g/cm}^3 \times 6.022131 \times 10^{23} / \text{mol}}{18.0153 \text{ g/mol}} (0.93 \times 10^{-24} \text{ cm}^2 + 2 \times 0.74 \times 10^{-24} \text{ cm}^2) = 7.408 / \text{m} \quad (\text{B.4})$$

$$\frac{1}{\Sigma} = \frac{1}{7.408 / \text{m}} = 13.5 \text{ cm} \quad (\text{B.5})$$

Similarly, a 100 MeV neutron will travel 41.25 cm before its first interaction.

The mean free path calculation is repeated for each interaction until thermalization; the cross-sections and energy-loss are energy-dependent. The energy loss in interaction n is determined by:

$$E_{n+1} = E_n e^{-\xi} = E_n e^{-0.948} \quad (\text{B.6})$$

Each of the 21 collisions for a 10 MeV neutron can be calculated as shown in Table B.1.

Adding the mean free paths at each stage of thermalization produces a total expected distance traveled for a 10 MeV neutron of 48 cm in the ice. The same procedure for a 100 MeV neutron leads to ~ 1.1 meters traveled before thermalization. The volume of interest for spallation neutrons is thus 1.5 meters from the DM-Ice17 detector. Neutrons produced beyond this distances will be attenuated before they can reach DM-Ice17.

B.3 Neutrons in DM-Ice17

The volume of interest for neutron propagation is estimated to be 1.5 m out from the (7.3 cm radius, 16.5 cm height) crystal. This cylindrical volume of interest has a radius of (7.3 cm + 1.5 m) and height of (3 m + 16.5 cm) to produce a vertical cross-section of 7.74 m^2 and a total volume of interest of 24.54 m^3 . This volume will contain a neutron production rate of:

$$\Phi_n \times V = (4 \times 10^{-6} \text{ neutrons/m}^3/\text{s}) \times (24.54 \text{ m}^3) = 8.5 \text{ neutrons/day} \quad (\text{B.7})$$

Most of the 8.5 neutrons/day produced in the volume of interest will be attenuated in the ice before they reach DM-Ice. A GEANT4 simulation was run to determine the neutron flux in the DM-Ice17 detector. A 2 m volume of production was conservatively taken. A predicted neutron rate of 4 / crystal / year was derived, with 0.3 / crystal / year depositing $<100 \text{ keV}$ in the crystal, as shown in the simulated spectrum in Figure B.3. The neutron background is thus considered to be negligible for this experimental setup.

Table B.1: Propagation of a 10 MeV Neutron in Ice

Neutron energy	Mean free path	Hydrogen cross-section [220]	Oxygen cross-section [220]
10 MeV	13.5 cm	0.93 b	0.74 b
3.88 MeV	5.7 cm	1.9 b	1.9 b
1.50 MeV	4.3 cm	3.4 b	2.1 b
581 keV	2.7 cm	5.7 b	3.2 b
225 keV	2.1 cm	9.0 b	3.4 b
87.2 keV	1.6 cm	13.2 b	3.5 b
33.8 keV	1.3 cm	17.4 b	3.6 b
13.1 keV	1.3 cm	17.2 b	3.6 b
5.08 keV	1.3 cm	17.6 b	3.6 b
1.97 keV	1.3 cm	17.6 b	3.7 b
763 eV	1.3 cm	18.2 b	3.7 b
295.7 eV	1.2 cm	18.6 b	3.8 b
114.6 eV	1.2 cm	18.9 b	3.8 b
44.4 eV	1.2 cm	19.2 b	3.8 b
17.2 eV	1.2 cm	19.6 b	3.9 b
6.67 eV	1.2 cm	19.8 b	3.9 b
2.58 eV	1.2 cm	20.2 b	3.9 b
1.00 eV	1.1 cm	20.8 b	3.9 b
0.388 eV	1.1 cm	21.1 b	3.9 b
0.150 eV	1.0 cm	22.2 b	3.9 b
0.058 eV	1.0 cm	24.8 b	3.9 b
0.022 eV	thermalized	thermalized	thermalized

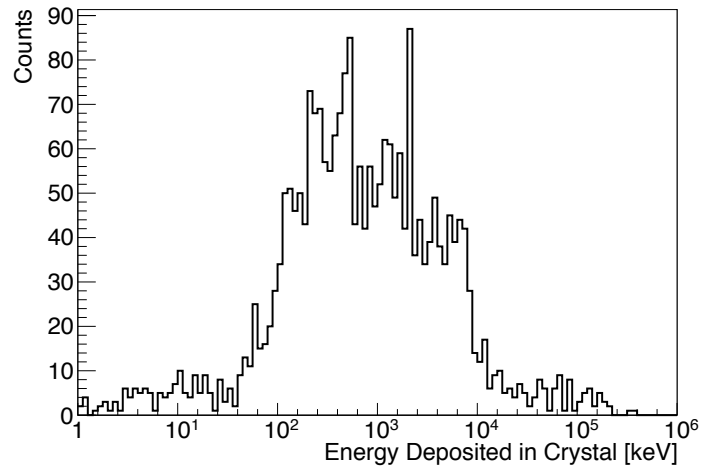


Figure B.3: Neutron energy deposition in DM-Ice17 as simulated by GEANT4.

Appendix C: IceCube Coincident Events

Select event displays of coincident DM-Ice17/IceCube events are shown for a series of conditions. The DM-Ice17 detector is located 7.5 m below the bottom IceCube DOM on the associated string; the bottom DOM is designated by a red box.

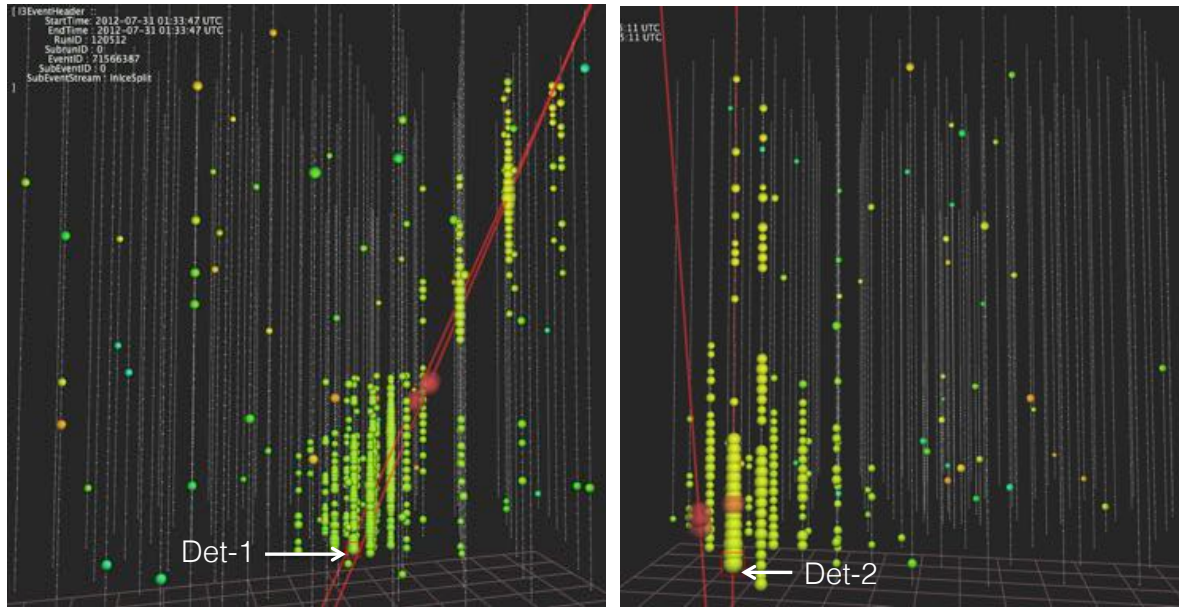


Figure C.1: Event display of a coincident muon passing through both IceCube and Det-1 (left) and Det-2 (right). Each dot represents a DOM; the large DOMs with colors triggered during the event. The red lines follow the reconstructed tracks of MPEFit and SPEFit. The red balls indicate the vertex of the interaction in IceCube according to each reconstruction.

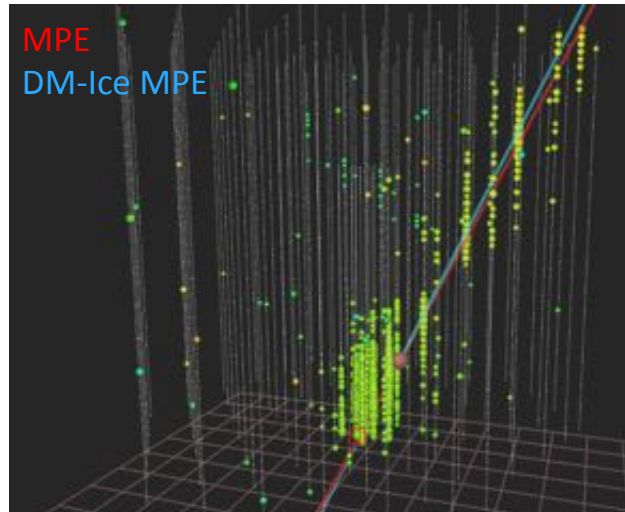


Figure C.2: Det-1 coincident event in which both the SPEFit seeded (red) and DM-Ice17 seeded (blue) MPEFit reconstruction pass. In this event, the difference in the reconstructed paths is within the resolution of the reconstructions.

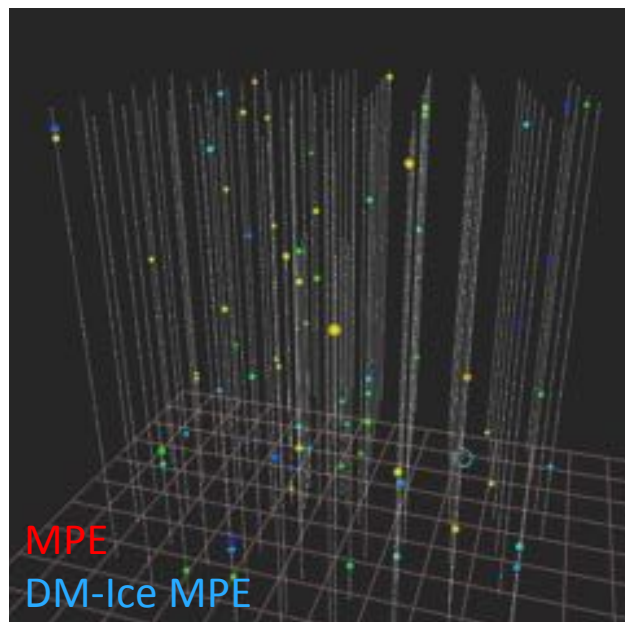


Figure C.3: Det-1 coincident event in which both the SPEFit seeded and DM-Ice17 seeded MPEFit reconstruction fail. This event triggered on noise in the detector.

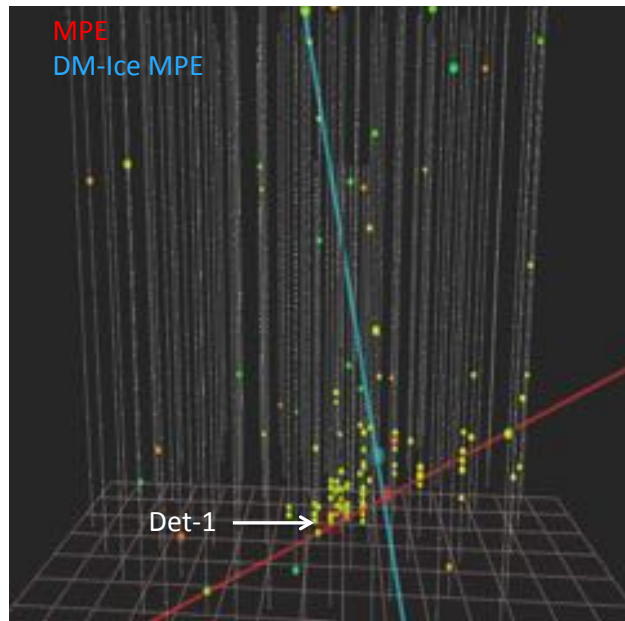


Figure C.4: Det-1 coincident event in which the DM-Ice17 seeded MPEFit reconstruction (blue) failed and the SPEFit seeded reconstruction (red) passed.

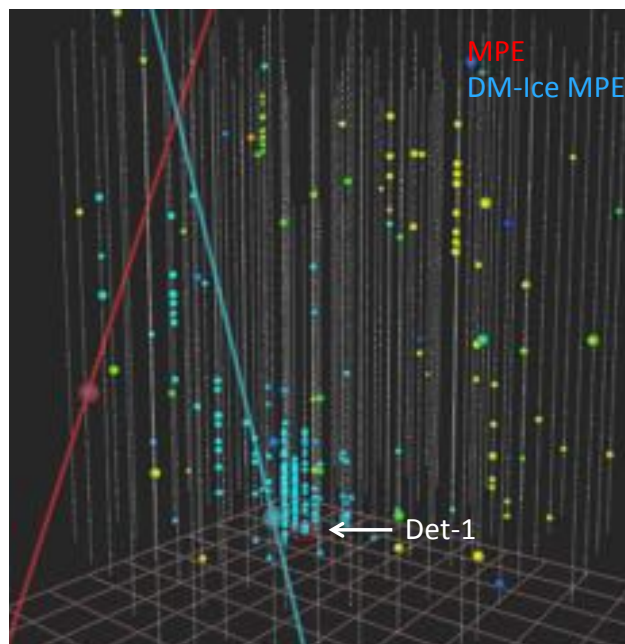


Figure C.5: Det-1 coincident event in which the DM-Ice17 seeded MPEFit reconstruction (blue) passed and the SPEFit seeded reconstruction (red) failed.